*p*ISSN 2615-5109
*e*ISSN 2621-0541

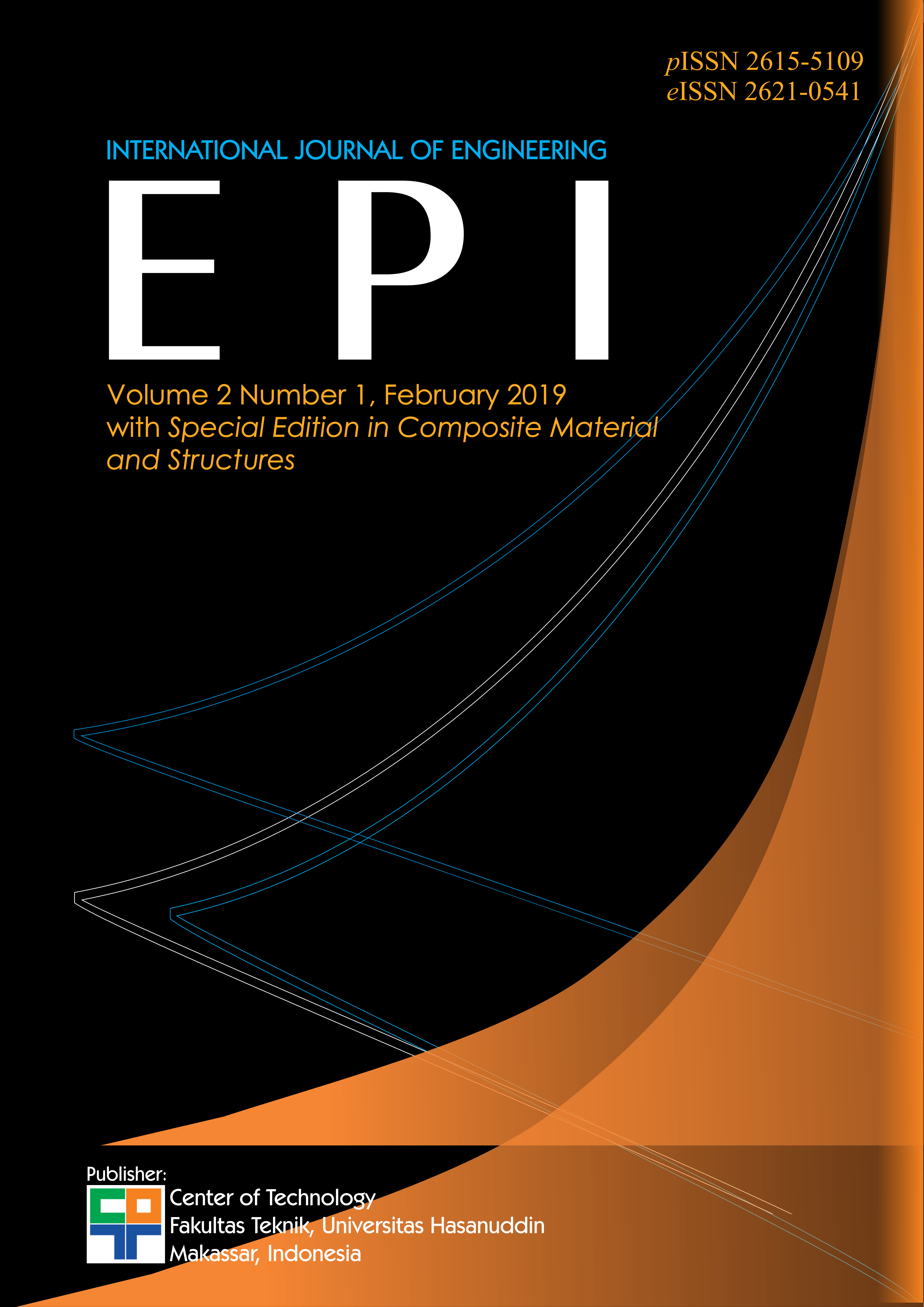

INTERNATIONAL JOURNAL OF ENGINEERING

EPI

Volume 2 Number 1, February 2019
with *Special Edition in Composite Material and Structures*

Publisher:
Center of Technology
Fakultas Teknik, Universitas Hasanuddin
Makassar, Indonesia

Print edition ISSN 2615-5109

Electronic edition ISSN 2621-0541

Publisher:
Center of Technology, Fakultas Teknik, Universitas Hasanuddin

Address:
Engineering Faculty Campus, Hasanuddin University
Jl. Poros Malino km. 6, Bontomarannu
Kabupaten Gowa, Sulawesi Selatan, Indonesia, 92171
Email : epi-ije@unhas.ac.id
Website : cot.unhas.ac.id/journals/index.php/epiije
Telp/Fax : +62-(0)411-58601

EPI International Journal of Engineering

Editor-in-Chief : **Prof. Baharuddin Hamzah**, Hasanuddin University (Makassar, Indonesia)
Associate Editors : **Dr. Faisal Mahmuddin**, Hasanuddin University (Makassar, Indonesia)
Prof. Yoshihiro Narita, Hokkaido University (Sapporo, Japan)
Guest Editor : **Dr. Andi Arwin Amiruddin**, Hasanuddin University (Makassar, Indonesia)
Editorial Board :

- Indonesia
  Dr. Muh. Arsyad Thaha, Hasanuddin University (Makassar, Indonesia)
  Prof. Hammada Abbas, Hasanuddin University (Makassar, Indonesia)
  Prof. M. Ramli Rahim, Hasanuddin University (Makassar, Indonesia)
  Prof. Herman Parung, Hasanuddin University (Makassar, Indonesia)
  Prof. Imran Umar, Hasanuddin University (Makassar, Indonesia)
  Dr. Rhiza S. Sadjad, Hasanuddin University (Makassar, Indonesia)
  Dr. Ganding Sitepu, Hasanuddin University (Makassar, Indonesia)
  Prof. Satriyo Brodjonegoro, Bandung Institute of Technology (Bandung, Indonesia)
  Prof. I Ketut Aria Pria Utama, Surabaya Institute of Technology (Surabaya, Indonesia)
  Dr. Arifuddin Idrus, Gadjah Mada University (Yogyakarta, Indonesia)
  Dr. Ngurah Nitya, Udayana University (Denpasar, Indonesia)
  Dr. Putu Wijaya Sunu, Bali State Polytechnic (Denpasar, Indonesia)
  Dr. Lukiyanto YB, Sanata Dharma University (Yogyakarta, Indonesia)

- Outside Indonesia
  Prof. Erasmo Carrera, Polytechnic University of Turin (Torino, Italy)
  Prof. Mark Ewing, University of Kansas (Lawrence, USA)
  Prof. Danna Ganbat, Mongol University of Science and Technology (Ulaanbaatar, Mongolia)
  Prof. Peter Hagedorn, Technical University of Darmstadt (Darmstadt, Germany)
  Prof. S. Ilanko, University of Waikato (Hamilton, New Zealand)
  Prof. David Kennedy, Cardiff University, (Cardiff, United Kingdom)
  Prof. Woo Il Lee, Seoul National University (Seoul, Korea)
  Prof. Oliver Polit, University Paris Ouest (Paris, France)
  Prof. Vasaka Visoottiviseth, Mahidol University, (Bangkok, Thailand)
  Dr. Jane Louie Fresco Zamora, Weathernews Inc. (Chiba, Japan)
  Dr. Kazunori Abe, Akita University (Akita, Japan)
  Prof. Jun Ando, Kyushu University (Fukuoka, Japan)
  Prof. Shun Chiyonobu, Akita University (Akita, Japan)
  Prof. Naohiro Hozumi, Toyohashi University of Technology (Toyohashi, Japan)
  Prof. Shigeru Kashihara, Nara Institute of Science and Technology (Nara, Japan)
  Prof. Akio Miyara, Saga University (Saga, Japan)
  Dr. Yusuke Mochida, University of Waikato (Hamilton, New Zealand)
  Prof. Prakash Bhandary Netra, Ehime Univ. (Matsuyama, Japan)
  Prof. Yoshiki Ohta, Hokkaido University of Science (Sapporo, Japan)
  Prof. Tsubasa Otake, Hokkaido University (Sapporo, Japan)
  Prof. Nobumasa Sekishita, Toyohashi University of Technology (Toyohashi, Japan)
  Prof. Hideaki Yasuhara, Ehime University (Matsuyama, Japan)

Foreword

We are pleased that EPI International Journal of Engineering (EPI-IJE) is presenting its 3rd issue. We are also excited that the numbers of authors' country of origin who published their papers in this issue has also increased. The country variety of submission will help to promote the journal globally. We are also delighted that this issue contains a special topic on Composite Materials & Structures.

Besides the special issue on Composite Materials & Structures, this issue also contains 5 (five) other major topics which are Naval Architecture, Ocean, and Marine Engineering, Electrical and Informatics Engineering, Civil and Environmental Engineering, Mechanical and Industrial Engineering and Multi-disciplinary Engineering. The first paper in Composite Materials & Structures Engineering group conduct a study on manufacture of continuous Glass Fiber/Polylactic Acid (PLA) composite and its properties. Then the second paper in this group studies the shear behavior of concrete beams strengthened with CFRP Grid and PCM Shotcrete. The third paper discuss the characteristics of activated carbon from the utilization of Red Chili Trees. The fourth paper studies the multi-objective optimization of variable-stiffness composites fabricated by tailored fiber placement machine. The last paper in this group studies the effect of using different elastic moduli on vibration of laminated CFRP rectangular plates. The group of Naval Architecture, Ocean, and Marine System Engineering contains 3 (three) papers. The first paper discusses the heave and pitch motion performances of a ship towing system incorporated with symmetrical bridle towline model. The second paper discusses the heave and pitch motions of a towed ship in waves incorporated with an asymmetrical bridle towline model. The last paper studies the influences of lengthening dimension of ro-ro ferry toward the considerations of hydrodynamics characteristic and loading capacity aspect.

In the next group which is Electrical and Informatics Engineering group, 2 (two) papers are published. The first paper studies the autonomy stemmer algorithm for legal and illegal affix detection use finite-state automata method. The second paper in this group studies the characteristic of current diffusion on double-plate conductor for smaller resistive load. The group of Civil and Environmental Engineering contains only one paper which conducts the experimental study of the use of pumice sand in the rigid pavement. The group of Mechanical and Industrial Engineering contains 3 (three) papers. The first paper in this group studies the free vibration analysis of L-shaped folded thin plates. The second paper developed a mathematical modeling in combining photovoltaic and thermoelectric generator using a spectrum splitter. The last paper investigates the harmonic response of strut fin on a planar motion mechanism. The last group contains one paper, which conducts a study on renewable energy developments in Indonesia; opportunities for improving local production energy for local consumption.

As the guest editor of this edition, I am greatly grateful to all authors for their outstanding papers and remarkable work. We hope these high-quality papers would give a contribution to knowledge development of their respective field of study. I also would like to express my gratitude to JICA C-BEST Project team, reviewers, editors, and all other people who have contributed to the publishing of this issue.

Warm regards,

Dr. Eng. A. Arwin Amiruddin
Editor-in-Chief of EPI-IJE

TABLE OF CONTENTS

<Mini-special Issue on Composite Materials and Structures>

<Naval Architecture, Ocean, and Marine System Engineering>

<Electrical and Informatics Engineering >

<Civil and Environmental Engineering>

<Mechanical and Industrial Engineering>

<Multi-disciplinary Engineering>

EPI International Journal of Engineering
Volume 2, Number 1, February 2019, pp. 1-4
DOI: 10.25042/epi-ije.022019.01

*p*ISSN 2615-5109
*e*ISSN 2621-0541

Manufacture of Continuous Glass Fiber/Polylactic Acid (PLA) Composite and Its Properties

Jeong U Roh[a], Woo Il Lee[b,]*

[a]Department School of Mechanical and Aerospace Engineering, Seoul National University.
[b]Department School of Mechanical and Aerospace Engineering, Seoul National University. Email: wilee@snu.ac.kr

---

Abstract

The continuous glass fiber reinforced polylactic acid (PLA) prepreg was manufactured by direct melt impregnation. The mechanical and thermal properties of PLA prepreg were observed. The properties of PLA prepreg were compared with the neat PLA and the injection molded glass fiber/PLA composite. The PLA prepreg having a fiber volume fraction of 27.7 % shows well enhanced tensile strength of 331.1 MPa, flexural strength of 528.6 MPa, and flexural modulus of 24.0 GPa. The enhancement in the heat deflection temperature (HDT) and the crystallinity were also observed. The fracture interface was inspected by FE-SEM. The degree of impregnation as a function of pulling speed was measured. The degree of impregnation at the pulling speed of 5 m/min reached over 90 % in this research.

Keywords: Continuous glass fiber; prepreg; fiber reinforced thermoplastic; heat deflection temperature (HDT); mechanical properties; polylactic acid (PLA)

---

1. Introduction

Polylactic acid (PLA) is one of bio-degradable polymers being used widely from as packaging material to medical applications [1, 2]. In these days, applications to automobiles have attracted industrial attention. However, eco-friendly materials, in many cases, have weak thermal stability to be used for vehicles. PLA, on the other hand, has better performance than other bio-degradable polymers. Nevertheless, it has disadvantages of low crystallinity and low heat deflection temperature (HDT). For example, the HDT of PLA (NatureWorks LLC, 4032D) is 50.4 ℃ while the HDT of polypropylene (PP) is 108 ℃ [3, 4]. PP is one of the most widely used polymers for automotive applications and the HDT of PLA is much lower than the value required for automotive industry. In order to increase the HDT of a polymer, there are several ways such as increasing the glass transition temperature, Tg, applying reinforcement, and increasing the crystallinity. Generally, higher aspect ratio of reinforcement in the matrix gives better reinforcing effect. Furthermore, it is well known that the crystallinity can be increased at high shear rates [5]. Therefore, in this study, continuous glass fiber was chosen for the reinforcement and the melted PLA resin was impregnated into the continuous fiber tow by using the direct melt impregnation method to induce high shear rates. The direct melt impregnation method is common technique and there are several variations in the process by combining elements such as fixed pin, porous impregnation wheel and freely rotating pin [6]. In this study, the melt pool with fixed pins was applied to impregnate PLA resin into the continuous fiber tow.

Higher shear rate can be applied to the PLA resin by forcing the resin to flow between the continuous fibers. This can be achieved by inducing resin pressure through pulling the fiber tow over the impregnation pin. For the PLA prepreg thus manufactured, degree of impregnation as a function of pulling speed was observed as well as mechanical properties, crystallinity, HDT, and the fracture surface.

2. Experiment

2.1. Materials

PLA resin (NatureWorks LLC, 4032D) was used for the matrix of prepreg. The glass fiber (Owens Corning, 2400 tex) was used for the reinforcement. The fiber diameter was 22.4 µm and the width of the fiber bundle was 6 mm. The roving was treated with the same sizing for PP matrix.

---

*Corresponding author. Tel.: +82-2-880-7008
School of Mechanical and Aerospace Engineering,
Seoul National University, Seoul 151-742, Korea
This manuscript has been reproduced from a paper published in Korean in Composites Research, The Journal of the Korean Society for Composite Materials, 26(4): 230-234, 2013.

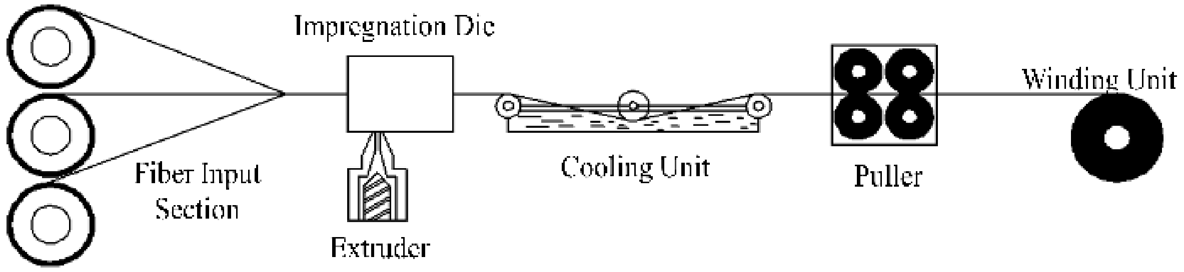

Figure 1. Illustration of the setup for manufacturing PLA prepreg.

Table 1. Thermal properties of neat PLA and PLA prepreg

	T_g (℃)	T_c(℃)	T_m (℃)	ΔH_m (J/g)	X_c (%)
Neat PLA	59.03	105	166	17.1	18.2
PLA prepreg	58.2	110.9	165.2	16.85	32.4

2.2. Setup for manufacturing of PLA prepreg

The setup consisted of 5 components: unwinding unit, pin impregnation die, cooling unit, puller and winding unit. Fiber bundle was unwound with a constant tension by using the unwinding unit. The constant tension is important to control the input position of fiber bundle [7, 8]. The guided fiber bundle was impregnated by using the direct impregnation method. The pin impregnation die consisted of three 10 mm diameter cylindrical pins and two 8 mm diameter cylindrical pins. At the bottom and upper plate of the pin impregnation die, the heaters were introduced to maintain the preset temperature for the resin at 220℃. The consumed resin was replenished by the extruder continuously. A single screw extruder (Uenoyama Kiko) was used to deliver the molten resin into the pin impregnation die. The impregnated fiber bundle after the pin impregnation die was cooled by using a water cooling vat. The caterpillar type puller was applied to pull the fiber bundle. The pulling speed was controlled from 0.5 m/min to 5 m/min. After the puller, the prepreg was wound with a constant torque by the winding unit. The illustration of the setup for manufacturing of the PLA prepreg is shown in Fig. 1.

2.3. Characterization

The tensile strength, the flexural modulus and strength, and the inter-laminar shear strength of the manufactured specimens were measured using a universal testing machine (UTM) (Lloyd Instruments, LR 50K). In order to obtain a data point, at least five tests were done and the results were averaged.

The tensile strength was measured following ASTM D 3039/D 3039M standard with the crosshead speed of 2 mm/min. The flexural strength and modulus were measured according to ASTM D 790 with the crosshead speed of 5 mm/min. Testing of the inter-laminar shear strength of the specimens was done following the ASTM D 5379/D 5379M with the crosshead speed of 2 mm/min.

The fiber volume fraction of PLA prepreg was observed by a close inspection of polished cross-sections of impregnated samples with five test values per one condition. A microscope (Leica, Type 020-520.008 DM/LM) with a mounted CCD camera (Nikon, Coolpix 950) was used to observe the polished cross-section of the prepreg. The test specimens were mounted with epoxy resin and the cross-sections were polished using a series of sand papers with increasing finish (400, 800, 1200, 2400 and 4000 grains/in).

The crystallization behavior was observed by differential scanning calorimetry (DSC) (Perkin Elmer, DSC7) in N2 atmosphere. In the DSC analysis, the samples were first heated to 200 °C with the temperature increasing at a rate of 10 °C/min. After complete melting, the samples were cooled down to 30 °C at a rate of 10 °C/min. They were then heated again to 200 °C at a rate of 10 °C per a minute. In this way, the crystallization as well as the melting curves of the composite was obtained. The crystallinity of PLA prepreg could be evaluated using the following equation:

$$X_c = \frac{\Delta H_m}{W_p \Delta H_m^0} \tag{1}$$

where *W*p is the weight fraction of the polymer, Δ*H*m the measured melting enthalpy, and ΔH0m the melting enthalpy of the 100% crystalline PLA. ΔH0mis taken as 93.7 kJ/kg from the literature [9].

The heat deflection temperature (HDT) was measured following ASTM D648 using the heat distortion tester (Toyoseiki, M-2). For the test, a constant load of 0.46 MPa was applied at the center of the three-point bending flexural coupon bar sample. The sample was heated from the room temperature to 200 °C at a rate of 2 °C/min.

The specimens used for the tests were made from the prepreg prepared using the manufacturing setup mentioned above. For producing the prepreg continuously, the pulling speed of 1 m/min and the setting temperature of 220 °C were applied.

3. Results and Discussion

3.1. Degree of impregnation

The degree of impregnation as a function of pulling speed was observed by using the microphotographs of the cross-sections of samples. It was defined as the ratio between the number of impregnated fibers and the total number of fibers in a tow. The results are shown in Fig.2. From the 1 m/min to the 5 m/min of pulling speed, the degree of impregnation was over 90 %. Especially, the degree of impregnation at the pulling speed of 5 m/min reached 92.5 %.

3.2. Mechanical properties

The incorporation of continuous glass fibers into PLA matrix produces an enhanced tensile and flexural strengths and a higher flexural modulus in the fiber axis direction. The average tensile strength of PLA prepreg was 331.1 MPa, the average flexural strength of PLA prepreg was 528.6 MPa, and the average flexural modulus of PLA prepreg was 24.0 GPa. Compared with the neat PLA and the injection molded glass fiber/PLA composite having a fiber volume fraction (Vf) of 17.0 %, the PLA prepreg having a fiber volume fraction (Vf) of 27.7 % shows much higher strength than the neat PLA (tensile strength: 62.9 MPa, flexural strength: 98.8 MPa) and the injection molded glass fiber / PLA composite (tensile strength: 80.2 MPa, flexural strength: 108.9 MPa) [10].

The flexural modulus was about 7.3 times larger than that of the neat PLA (flexural modulus: 3.3 GPa), about 2.9 times larger than the injection molded glass fiber/PLA composite (flexural modulus: 8.2 GPa). The average inter-laminar shear strength of PLA prepreg composite in the perpendicular direction of fiber axis was 33.2 MPa. The results are shown in Fig. 3.

3.3. Crystallization

The glass transition temperature (Tg), the crystallization temperature (Tc), and the melting temperature (Tm) of the PLA prepreg composite were observed by the DSC. The results are shown in Table 1.

As can be seen, Tg and Tm of the PLA prepreg were not changed notably from the neat PLA, while Tc and the crystallinity were increased. Crystallinity of the PLA prepreg was increased to 32.4 % from 18.25 % of the neat PLA. The increase in the crystallinity is likely due to the high shear rate applied during impregnation. The application of shear is known to increase the orientation of the molecular chain in the polymer melt and the nucleation rate [5] and thus to facilitate crystallization. Ultimately, the increase in the crystallinity of PLA prepreg is believed to affect the increase of mechanical properties.

Table 2. HDT of neat PLA and PLA prepreg

	HDT (°C)
Neat PLA [3]	50.4
PLA prepreg	100

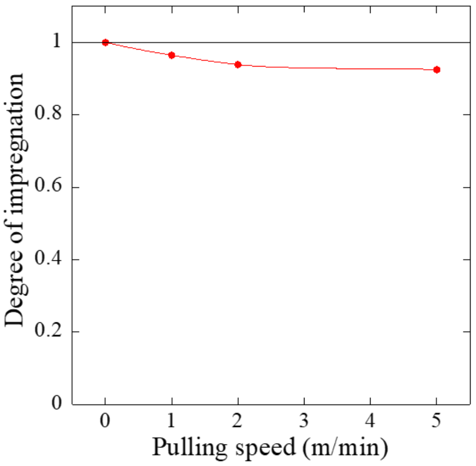

Figure 2. Degree of impregnation as a function of pulling speed

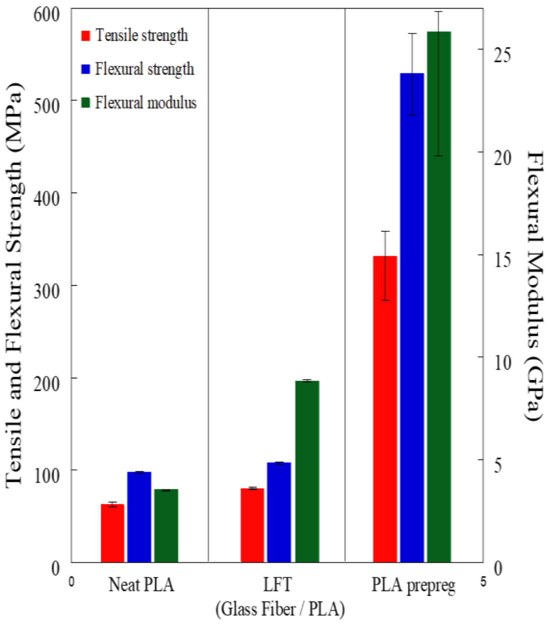

Figure 3. Mechanical properties of the composite specimen made with PLA prepreg

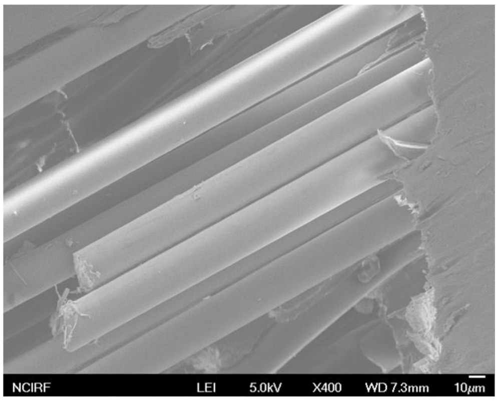

Figure 4. Fracture interface of tensile test specimen made with PLA prepreg

3.4. Heat deflection temperature (HDT)

The HDT of PLA prepreg composite was enhanced as shown in Table 2. The HDT of PLA prepreg composite was 100 °C while the HDT of neat PLA was 50.4 °C. There are several reasons for the increase in the HDT of polymer; increase of Tg, presence of the reinforcement, and increase in the crystallinity. Above all, the introduction of high aspect ratio reinforcement and the increase in crystallinity were considered as main reasons for the increase in HDT in this study.

3.5. The fracture interface

The fracture interface of tensile test specimen of PLA prepreg composite was observed with FE-SEM (JSM-6700F, JEOL) as shown in Fig.4. As can be seen, surface of glass fibers was clean and the PLA was not elongated well. It shows that the adhesion between the PLA and glass fiber is weak.

4. Conclusions

The manufacture and evaluation of PLA prepreg were considered. At the pulling speed of 5 m/min, the degree of impregnation was over 90 %. For the PLA prepreg, the mechanical properties were considerably increased. Besides the high aspect ratio of reinforcement, the high shear rate during the processing and the resulting crystallinity were thought to be responsible for the increase in mechanical properties and thermal stability. For the manufacturing of PLA prepreg, the direct melt impregnation method seemed to be working and served the purpose. The necessity of modification of the interface between the fiber and the matrix was evident.

Acknowledgement

This work was supported by the WCU(World Class University) program through the National Research Foundation funded by the Ministry of Education, Science and Technology (R31-2008-000-10083-0).

References

[1] Drumright R.E., Gruber P.R., Henton D.E.. (2000). Polylactic Acid Technology, Adv. Mater., 12(23); pp.1841-1846.

[2] Athanasiou K.A., Niederauer G.G., Mauliagrawal C. (1996). Sterilization, toxicity, biocompatibility and clinical applications of polylactic acid/polyglycolic acid copolymers, Biomoterids, 17; pp. 93-102.

[3] Shi Q.F., Mou H.Y., Li Q.Y., Wang J. K., and Guo W.H.. (2012). Influence of heat treatment on the heat distortion temperature of poly(lactic acid)/bamboo fiber/talc hybrid biocomposites, Journal of Applied Polymer Science, 123; pp.2828–2836.

[4] Jarus D., Scheibelhoffer A., Hiltner A. and Baer E. (1996). The Effect of "skin-core" morphology on the heat-deflection temperature of polypropylene, Journal of Applied Polymer Science, 60; pp.209-219.

[5] Fritzsche A.K. and Price F.P. (1974). Crystallization of polyethylene oxide under shear, Polymer Engineering and Science, 14(6); pp. 401-412.

[6] Proefschrift. (2008). PhD thesis, Delft University of Technology, The Netherlands

[7] Gaymans R.J. and Wevers E. (1998). Impregnation of a glass fibre roving with a polypropylene melt in a pin assisted process, Composites Part A, 29A; pp.663-670.

[8] Bijsterbosch, H., Gaymans R.J. (1993). Impregnation of glass rovings with a polyamide melt. Part 1: Impregnation bath, Composites Manufacturing, 4(2); pp.85-92.

[9] Nam J.Y., Ray, S.S., Okamoto M., (2003). Crystallization Behavior and Morphology of Biodegradable Polylactide/Layered Silicate Nanocomposite, Macromolecules, 36; pp.7126-7131.

[10] Huda M.S., Drzal L.T., Mohanty A.K., Misra, M. (2006). Chopped glass and recycled newspaper as reinforcement fibers in injection moulded poly(lactic acid) (PLA) composite: A comparative study, Composites Science and Technology, 66; pp.1813-1824.

EPI International Journal of Engineering
Volume 2, Number 1, February 2019, pp. 5-8
DOI: 10.25042/epi-ije.022019.02

*p*ISSN 2615-5109
*e*ISSN 2621-0541

Shear Behavior of Concrete Beams Strengthened with CFRP Grid and PCM Shotcrete

Andi Arwin Amiruddin[a]*

[a]Department of Civil Engineering, Hasanuddin University, Makassar, Indonesia. Email: a.arwinamiruddin@yahoo.com

---

Abstract

The results of an experimental and analytical study of the shear behavior of damaged or under-strength concrete beams strengthened with carbon fiber reinforced plastics (CFRP) grid and polymer cement mortar (PCM) shotcrete describes in this paper. The aim of this study is to evaluate shear performances of reinforced concrete beams retrofitted by using PCM shotcrete and CFRP grid. Four concrete beams reinforced internally with steel and externally with both PCM and CFRP grid (longitudinal direction used CR-10 and transversal direction used CR-6) applied to the specimens were tested under three-point bending. The shear failure is initiated by a major diagonal crack within the beam shear span. This diagonal crack extended horizontally at the level of the CFRP grid. Results show that PCM shotcrete with CFRP grid is very effective for shear strengthening. Increases in strength of 140% for PGB over the RCB as control, un-retrofitted beams were noted.

Keywords: Carbon Fiber Reinforced Plastics (CFRP) grid; Polymer Cement Mortar (PCM) shotcrete; shear behavior; strengthened

---

1. Introduction

Retrofit approaches may employ any innovative or economical scheme to prevent a RC bridge pier from collapsing during a design earthquake. One of the retrofit approaches is the strengthening of critical components [1, 2]. Strengthening is a widely used to retrofit approach that calls for increasing the force or moment capacity of selected components along the lateral load path to prevent premature or brittle failure [3]. An ideal strengthening should not alter the stiffness. However, since this is usually difficult to achieve, a re-evaluation of the seismic forces for the retrofitted RC bridge pier is required [4, 5]. Nowadays, retrofit materials with fiber reinforced polymer (FRP) and polymer cement mortar (PCM) are being used for a large variety of applications such as, bridge pier, bridge slab overlays, aqueduct tunnel, and box culvert. The prediction of mechanical properties of those materials plays an important role in the selection of materials and the design of each application case. Fiber reinforced plastics (FRP) have been considered as a substitute for conventional steel reinforcement owing primarily to their high corrosion resistance [6]. In addition, high strength, lightweight and non-conductivity of FRP composites have attracted the attention of researchers, as well as the industry. Although FRP reinforcements are more expensive than conventional steel reinforcements, the potential savings in maintenance costs make FRP reinforcements a viable alternative. Moreover, polymer cement mortar (PCM) consists of polymer cement mortar with polymer modified added is used to wrapping around RC bridge piers. In Japan, industrial companies produce many product types of PCM. For example, SABU 15 and SABU 15D, RIS SHOT, RFSP and ARMOR, respectively. On the other hand, there are some methods usually used to compact PCM as retrofit material in the fieldwork such as plasterer method and shotcrete method. In this research, PCM with high strength is used to retrofit RC beams by the shotcrete method. Strengthening reinforced concrete (RC) beams with fiber-reinforced polymer (FRP) composites is becoming an attractive for the construction industry [7, 8]. Commercially available FRP reinforcements are made of inorganic or organic fibers, such as glass (GFRP), carbon (CFRP) and aramid (AFRP), embedded in thermosetting resin matrix (polyesters, vinyl esters, and epoxies) and inorganic fillers. Unidirectional CFRP grid materials used in concrete reinforcement applications are linear elastic up to failure, and CFRP grid does not exhibit the yielding behavior that is typically displayed by conventional reinforcing steel [9, 10]. CFRP grid (high strength and high elasticity carbon fiber) materials generally have much higher strength than the yield strength of steel, although CFRP grid does not exhibit yield. Nowadays in Japan, CFRP grid and polymer cement mortar (PCM) shotcrete had been developed to retrofitting of RC structures such as to increase the shear capacity of RC beams [11, 12]. The contribution of the

---

*Corresponding author. Tel.: +62-821-9042-3578
Jl. Poros Malino, Borongloe, Bontomarannu, Kabupaten Gowa, Sulawesi Selatan 92171

CFRP grid (CR-6 and CR-10, high strength) transverse strengthening to the shear capacity on retrofit of RC beams is studied in this research. PCM (high strength and low elasticity) generally contains cement, fine aggregates, lightweight aggregate and polymer. PCM has the excellent bond strength, cohesiveness, improved resistance to freezing and thawing, reduced permeability, increased electrical resistivity and improved resistance to chemical attack [13].

2. Experimental Program

2.1. Test specimens and FRP strengthening system

The test specimens consisted of four RC beams classified into two types according to FRP strengthening system is shown in Fig.1. Two beams were tested without strengthening (RCB) and served as a control specimen for comparison purposes to evaluate the improvement in shear strength provided by externally bonded FRP reinforcements and PCM high strength shotcrete method. Two beams (RGB) were strengthened with FRP systems using Carbon Fiber-Reinforced Plastics (CFRP) grid rebars. A summary of these beams is given in Table 1.

2.2. Material properties

A design and experiment of material properties values of the concrete and PCM are given in Table 2. Moreover, Table 3 shows kinds of steel reinforcement were used in the experiment. The CFRP grid properties as reported by the manufacturers with linear stress strain behavior up to failure in longitudinal and transversal directions are shown in Table 4.

2.3. Test set-up

All beams were loaded in three-point bending that the subjected to static load is shown in Fig. 2. The beams were instrumented with a displacement meter at the mid-span and both of loading point to monitor displacement, as well as strain gauges bonded on concrete, PCM, and CFRP grid surface to measure the strain values. A 500 kN load cell was used to measure the applied load.

Table 1. Summary of specimen types

Type	PCM	CFRP Grid
RCB	-	-
PGB	High strength	High strength

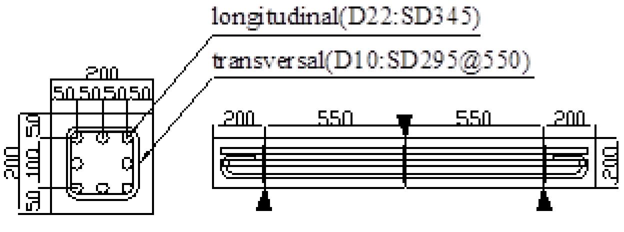

(a) RCB

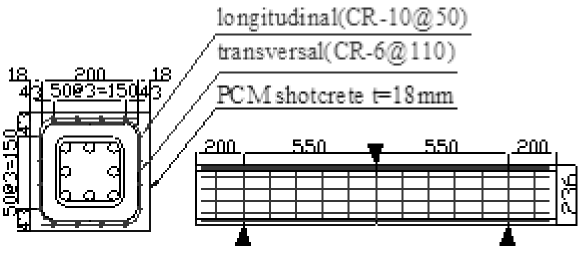

(b) PGB

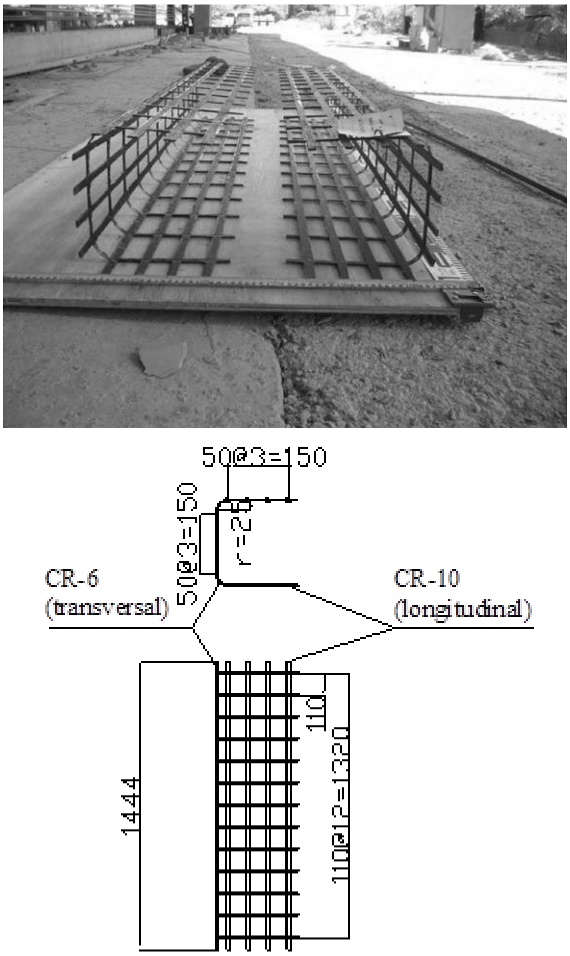

Figure 1. Test specimens and FRP grid strengthening system

Table 2. Material properties of concrete and PCM

CF grid	Direction	A_{cf} (mm^2)	f_t (N/mm^2)	E_{cf} (N/mm^2)
CR-10	Longitudinal	39.2	1400	1.0 x 10^5
CR-6	Transversal	17.5		

Table 3. Material properties of steel reinforcement

Type	Item	First Crack P_{cr} (kN)	First Yield P_{y0} (kN)	Ultimate P_u (kN)	Shear Strength P_s (kN)	Comparison of P_s Experiment / Analysis
RCB	Experiment	15.1	-	-	147	1.3
	Analysis	19.3	211	216	112	
PGB	Experiment	29.0	-	-	352	0.9
	Analysis	24.7	535	438	376	

Table 4. Material properties of CFRP grid

Type	Materials	Design values		Experiment values	
		f'_c (N/mm^2)	E_c (N/mm^2)	f'_c (N/mm^2)	E_c (N/mm^2)

RCB	Concrete	30.0	2.80×10^4	35.0	3.06×10^4
PGB	PCM-high strength	68.2	2.70×10^4	69.5	2.61×10^4

Table 5. Comparison of experiment and analysis values

Diameter	Standard	Direction	f_y (N/mm^2)	f_t (N/mm^2)	E_s (N/mm^2)
D22	SD345	Longitudinal	395	582	2.0×10^5
D10	SD345	Transversal	323	455	

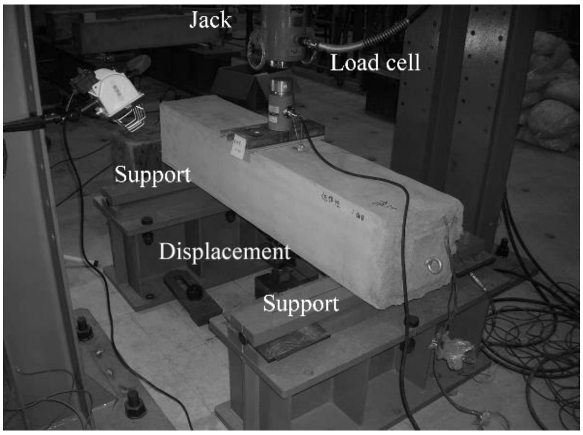

Figure 2. Specimen under testing and loading system

3. Results and Discussions

3.1. Comparison of experiment and analysis values of Ps

The design of load is divided into four parts, load at first crack (P_{cr}), first yield at steel reinforcement in tension area (P_{y0}) so that steel bars was separated with concrete, ultimate strength (P_u), and shear strength (P_s). In particular for P_s, the analysis was carried out based on Japan Road Association (JRA) Bridge Part V method. In design, the shear failure was proposed on $P_{y0} / P_s > 1.5$. In experiment result, it was obtained that for all of specimen types had propagation of cracks showed shear failure behavior. Especially for PGB type, slip between CFRP grid and PCM was occurred so that obtained CFRP grid was not broken but separate with PCM and experiment value become less than design value. The comparison of experiment and analysis value is given in Table 5 and Fig. 3, respectively.

3.2. Load – deflection relationship

The load deflection as showed in Fig. 4 plot for beam PGB along with that of the shear control beam, RCB. The control beam failed in shear and also for PGB type. PGB type had shear strength more than RCB type and increases in shear strength of 140% for PGB over the RCB、un-retrofitted beams.

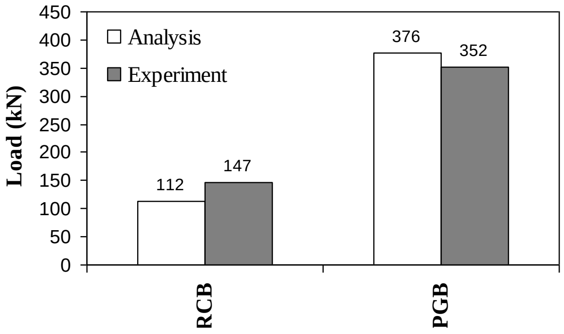

Figure 3. Shear strength values

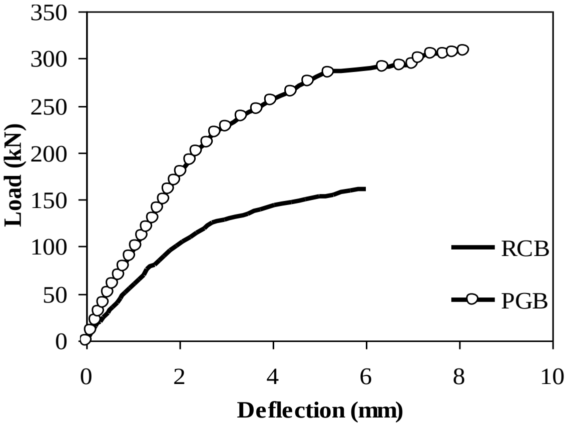

Figure 4. Load deflection relationship

3.3. Load – strain relationship

Figure 5 shows relationship of shear load with compressive strain of concrete/PCM and tensile strain of steel bars/CFRP grid. Tensile strain of steel bars of RCB was achieved up to about 1,300 µ at the maximum of shear load. On the other hand, tensile strain of PGB type was achieved up to 4,500 µ but less than 14,000 µ as a design value for tensile strain of CFRP grid. Therefore, all of beams the specimens had shear failure modes. Figure 6 shows the crack pattern and failure mode of the beam under test.

4. Conclusions

In three-point bending test results, RCB type as control beam or un-retrofit type failed by shear. However, the retrofit specimens (PGB) also were failed at shear and these conditions parallel with design concept. PGB type was failed by separation with epoxy adhesive from PCM. CFRP grid had not enough adhesive strength to prevent relative slip to PCM. Based on experiment results, the retrofit of RC beams (PGB) by industrial method (SRS) have revealed that shear strength increase 140% as significantly to control beam.

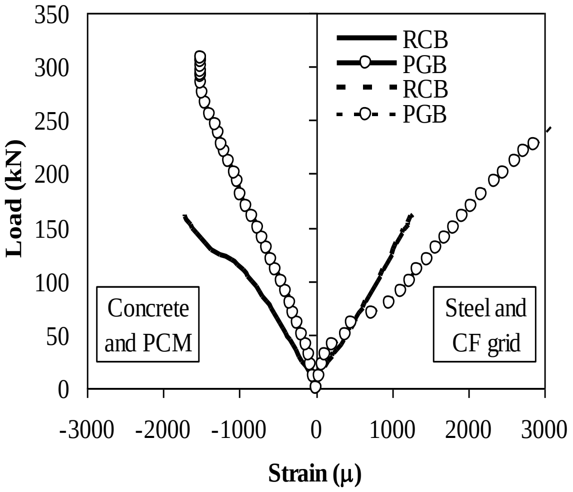

Figure 5. Load strain relationship

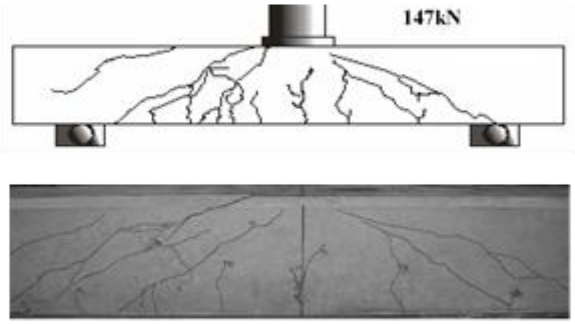

(a) RCB

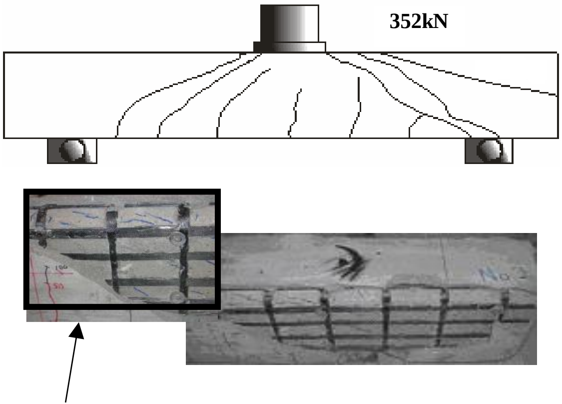

(b) PGB

Figure 6. Crack pattern and failure mode of beam under test

Acknowledgments

I kindly would like to express my sincere gratitude to Prof. Shinichi Hino for his valuable help. The authors also wish to express the gratitude to Association of PCM shotcrete method for RC structures in Japan and FRP Grid Engineering Association for the finance support of this research as well as to the Laboratory of the Bridge and structural aesthetic design of the Kyushu University, Japan.

References

[1] Kawashima, K., “Seismic Design and Retrofit of Bridges”, 12 WCEE 2000, pp.16, 2000.

[2] Theodorakopoulos, D. D., Swamy, R. N., “A Design for Punching Shear of FRP-Reinforced Slab-Column Connections”, Cement and Concrete Composites Journal, Vol.30, Elsevier Ltd, pp.544-555, 2007

[3] Priestley, M. J. N., Seible, F., Calvi, G. M., “Seismic Design and Retrofit of Bridges”, A Wiley-Interscience Publication, John Wiley & Sons, Inc., New York, United States of America, pp.308-310, 1996.

[4] Kitada, T., Yamaguchi, T., Matsumara, M., Okada, J., Ono, K., Ochi, N., “New Technology of Steel Bridges in Japan”, Journal of Constructional Steel Research, Vol.58, Elsevier, pp.21-70, 2002.

[5] Kitada, T., Matsumura, M., Otoguro, Y., “Seismic Retrofitting Techniques Using an Energy Absorption Segment for Steel Bridge Piers”, Journal of Engineering Structures, Vol.25, Elsevier, pp.621-635, 2003.

[6] Chagnon, N., Massicotte, B., “Seismic Retrofitting of Rectangular Bridge Piers with CFRP”, ConMat’05 Third International Conference on Construction Material, Canada, pp.1-10, 2005.

[7] Fujikura, S., Bruneau, M., “Blast Resistance of Seismically Designed Bridge Piers”, The 14th World Conference on Earthquake Engineering, Beijing, China, pp.12-16, 2008.

[8] Japan Road Association (JRA). (2003). Specification for Highway Bridge Part V, Seismic Design, Japan. (English Translation)

[9] Iemura, H., Takahashi, Y., Sogabe, N., “Development of Unbonded Bar Reinforced Concrete Structure”, 13th World Conference on Earthquake Engineering, Vancouver, B.C., Canada, pp.1-15, 2004.

[10] Shima, H., Chou, L., Okamura, H., “Micro and Macro Models for Bond in Reinforced Concrete, Journal Faculty of Engineering, The University of Tokyo (B); XXXIX (2), pp.133-194, 1987.

[11] Liang, J.; Kimitaka, A.; Takanashi, Y. (2008). Shear Strengthening of RC Beam with CFRP grid and Sprayed Mortar, Japan Concrete Institute (JCI), Vol.30, No.2, Fukuoka, Japan, pp. 1609-1614. (English Translation)

[12] Saatci, S.; Vecchio, F. J. (2009). Effect of Shear Mechanism on Impact Behavior of Reinforced Concrete Beams, ACI Structural Journal, Vol.106, No.1, pp. 78-86.

[13] Kasakura, R.; Uji, K.; Liang, J.; Sato, K. (2007). Shear Resisting Mechanism of RC Beam Strengthened with CFRP grid and Sprayed Mortar, Japan Concrete Institute (JCI), Vol.29, No.2, Sendai, Japan, pp. 853-858. (English Translation)

EPI International Journal of Engineering
Volume 2, Number 1, February 2019, pp. 9-13
DOI: 10.25042/epi-ije.022019.03

*p*ISSN 2615-5109
*e*ISSN 2621-0541

Characteristics of Active Carbon from Utilization of Red Chili Trees (Capsicum annuum L)

Ni Made Dwidiani[a], Putu Wijaya Sunu[b], Gusti Ngurah Nitya Santhiarsa [c,]*

[a]Udayana University, Indonesia. Email: dwidiani@gmail.com
[b]Bali State Politechnic, Indonesia. Email: wijayasunu@pnb.ac.id
[c]Udayana University, Indonesia. Email: santhiarsa@yahoo.com

---

Abstract

This work studies the use of red chilli tree (capsicum anuumm L) waste as material of activated carbon and examines the morphological structure and elemental composition of the activated chili trees. The morphological structure was measured at TekMIRA (Pusat Penelitian dan Pengembangan Teknologi Mineral dan Batubara, Bandung) by using the scanning electron microscope (SEM), and the composition of the elements of carbon, hydrogen, nitrogen and ash is determined by the ultimate testing analysis with the ASTM D5373 standard. In the testing procedure, activated carbon is made from red chili tree waste by dehydration with a temperature of 2000 C for 1 hour and carbonized with a temperature of 3750 C for 1 hour. Then, the chemical activation (NaOH) is made in variation of concentration of 1%, 3%, and 5% with soaked time 24 hours, and dried at 2000 C for one hour. The carbonization at a concentration of 1% (NaOH) gave the best result on activated carbon from red chili trees.

Keywords: Activated carbon; capsicum annuum L.; carbonization; red chili tree waste

---

1. Introduction

Activated carbon is a type of carbon with low-volume pores that is formed to increase the surface area, and mostly used to adsorb other substances or to cause chemical reactions. Since the activated carbon has high degree of micro-porosity, one particle has considerable surface area, for example, in excess of a few square meters. With such large surface area, useful application may be obtained solely from porosity, but also additional chemical treatment increases adsorption property.

In this research, activated carbon is made from red chili tree by utilizing waste from the harvest done by farmers in Bangli, a regency (kabupaten) of Bali, Indonesia. Stems of chili trees have round and smooth, hard and woody structure with color of dark green and have many branches. In scientific classification of biology (botany), capsicum annuum is classified as Kingdom: Plantae, Clade: Angiosperms, Eudicots, Asterids, Order: Solanales, Family: Solanaceae, Genus: Capsicum, Species: C. annuum. In the binomial name (i.e., naming using a combination of Genus and Species), it is called "Capsicum annuum L.".

Chili plants belong to plants that produce seeds (Spermatophyta). Chili seeds are covered by the skin of the fruit, so then they are included in the group of closed seed plants (Angiosperms). The institution on chili seeds is divided into two leaf institutions, so it is included in the class of split seed plants (Dicotyledoneae). Leaves of chili plants are light green to dark, leaves are supported by leaf stalks. Pinnate leaf bone. Overall the leaf shape of a large chili plant is oval with tapered leaf tips [1]. Based on this, red chili trees are included in hardwood or hardwood with a composition of 43% cellulose, 25% hemicellulose, 16% lignin, 0.6% ash and 15.4% are other extractive parts [2]. With this composition the red chili tree waste is expected to have characteristics and good quality for active carbon material.

2. Basic Approach

In general terms, activated carbon is an amorphous compound that is produced from material containing carbon or charcoal that specially induces high adsorption power. Activated carbon can adsorb gases and certain chemical compounds or selective adsorption properties, depending on the size or volume of pores and surface area. The absorption of activated carbon is very large, which is 25-100% of the weight of activated carbon [3].

2.1. Scanning electron microscope (SEM)

Scanning Electron Microscope (SEM) is an electron microscope used as a means of detecting objects on a very small scale. In this study, SEM is used to determine the structure and pore size. The working principle of SEM is the detection of electrons scattered from a continuous high-energy electron beam accelerated in an

---

*Corresponding author. Tel.: +82-2-880-7008
Fakultas Teknik Jimbaran, Udayana University, Jl. Kampus Bukit Jimbaran, Bali, Indonesia

electromagnetic coil, and the coil is connected to a cathode ray tube so that information is generated about the surface state of a compound sample.

Before applying SEM, sample preparation was carried out by solvent removal, sample selection and coating. When electrons with sufficiently large energy pound on the sample, it causes X-ray emissions whose energy and intensity depend on the elemental composition of the sample [4]. The detector inside SEM collects reflected electrons and determines the location of the signals with the highest intensity. The direction of detected signals informs the surface profile of the object.

2.2. Ultimate analyzer (UA)

The objective of using Ultimate Analyzer (UA) is to measure the amount of carbon (C), hydrogen (H), oxygen (O), and other elements. The measurement test was conducted by TekMIRA(Bandung) for ash on activated carbon.

3. Research Method

3.1. Materials and tools

The materials used in this study were red chili trees, NaOH solution, aquades and silica sand. The tools used were knives, earthenware jars, ovens, scales, thermocouples, mortals, 35 mesh sieves, pH meters, ovens, furnaces. Scanning Electron Microscope (SEM) was used to determine the pore structure of activated carbon, and Ultimate Analyzer to find out carbon, nitrogen and hydrogen content.

3.2. Testing methods

After the necessary treatment on the material samples in 3.1, Scanning Electron Microscope (SEM) was applied to find out the morphology of activated carbon. As mentioned, the measurement was done at TekMIRA (Bandung). The ultimate test was carried out based on a standard procedure described in ASTM D5373 to find out carbon (C), hydrogen (H), and nitogen (N) in the ash content.

4. Results and Discussion

4.1. Scanning electron microscope (SEM)

Scanning Electron Microscope (SEM) testing aims to determine the morphology of activated carbon including pores, and to determine the amount of volatile (impurity). The SEM test results are shown in Fig. 1(A) with 1% NaOH, (B) 3% NaOH and (C) 5% NaOH. These SEM image show the carbon morphology of the active red chili tree with a magnification of 1,500 x the scale of the image is 10 µm.

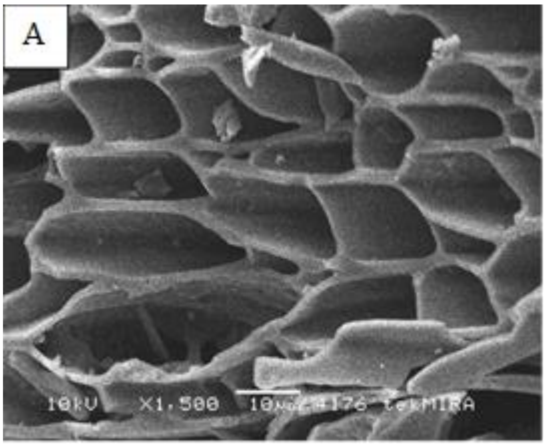

(A) 1% NaOH

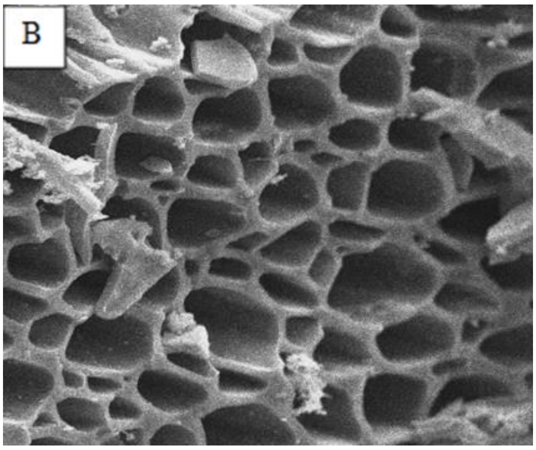

(B) 3% NaOH

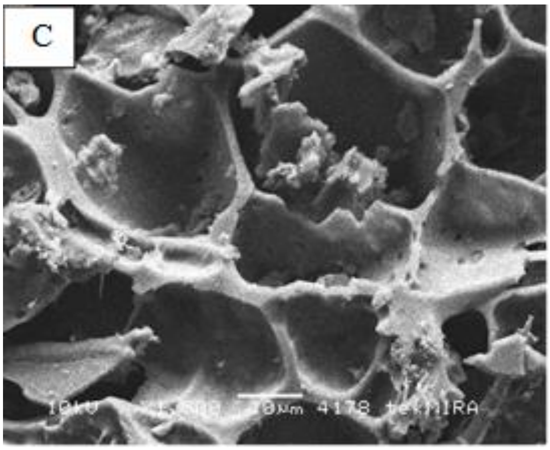

(C) 5% NaOH

Figure 1. Photo of surface observed by SEM

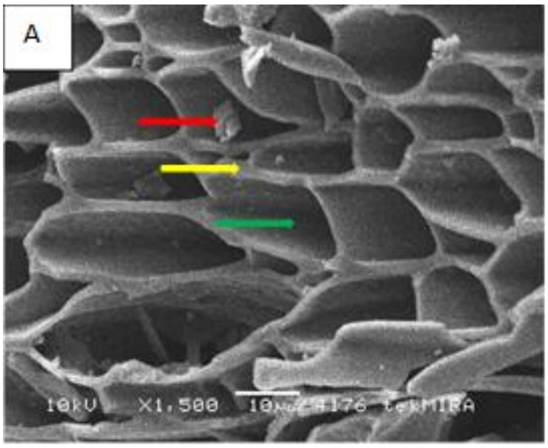

(A) 1% NaOH

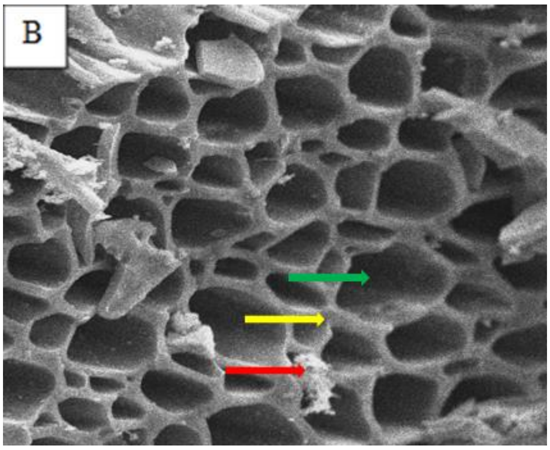

(B) 3% NaOH

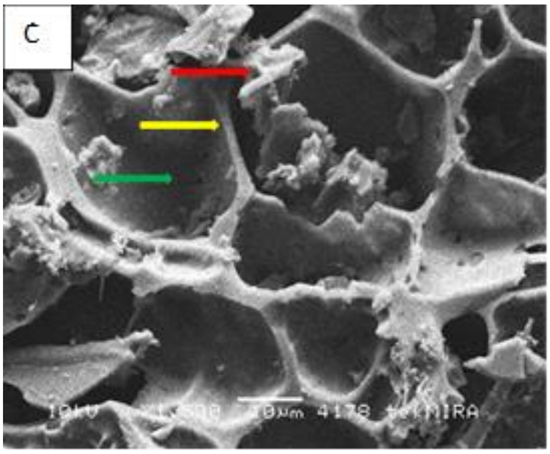

(C) 5% NaOH

Figure 2. Volatile, pore wall and pore on the surface

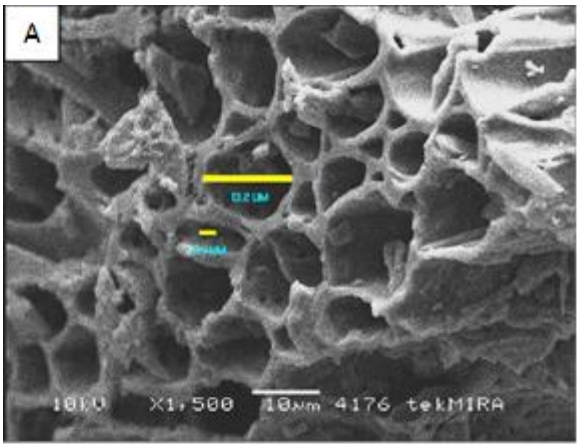

(A) 1% NaOH

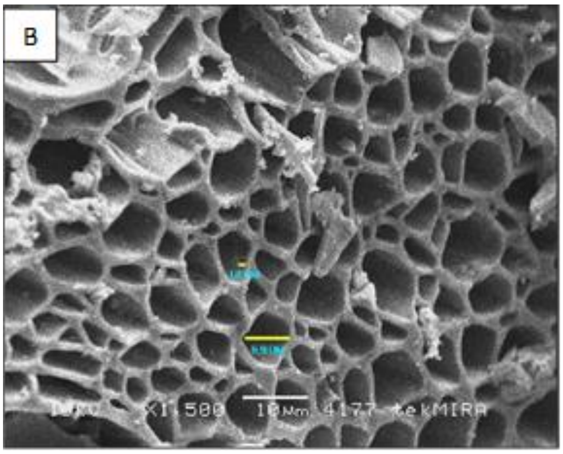

(B) 3% NaOH

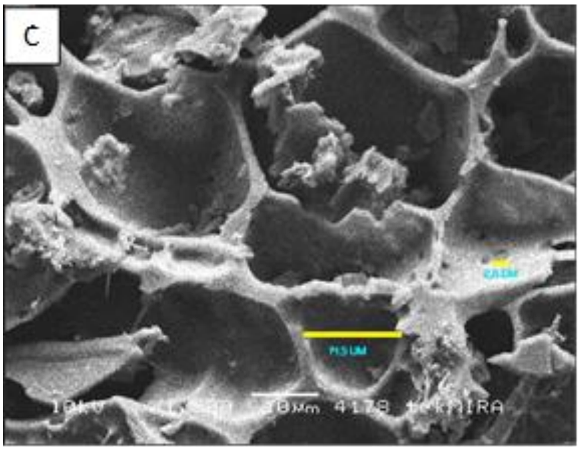

(C) 5% NaOH

Figure 3. Measurement of sizes on the surface

4.2. Shape

In Fig. 1(A) with the 1% NaOH activation, it appears that the pores formed are predominantly squares and the walls of the pores are thin. In Fig. 1(B) with the NaOH activation 3%, the pores form circles dominantly and the wall of the pores are thicker. For maximum NaOH in Fig. 1(C), the pores formed begin to be irregular and the walls of the pores are very thin. Based on the shapes of the pores in the image, activation with NaOH with increasing concentration can affect the amount of pores formed on the activated carbon observed surfaces of the samples after treatment of different NaOH concentration.

4.3. Analysis of section

There are several parts in the image of SEM Scanning Electron Microscope activated carbon from the waste of the red chili tree shown in the image of Fig. 2(A), (B) and (C) for 1% NaOH, 3% NaOH and 5% NaOH activated carbon, respectively. In the figure, red arrow indicates volatile, yellow arrow does the pore wall, and green line does pores.

4.4. Size

In SEM image the activated carbon from the waste of red chili tree (capsicum annuum L.) has a magnitude, among others, is the large pore diameter. Based on the picture in Fig. 3 with SEM photos from different angles in part (A) with NaOH activation 1% the average pore diameter is 13.2 µm and the largest pore diameter on the pore wall is 2.4 µm, for Fig. 3(B) with the activation of 3% Na0H the average pore size is 6.9 µm, and the pore diameter on the pore wall is 1.2 µm. In Fig.3(C) activation with 5% NaOH with a large pore diameter averaged 14.5 µm, and the pore diameter on the pore wall is 2.5 µm.

4.5. Ultimate test

The ultimate test aims to determine the content of elements that exist in activated carbon. Tests include carbon content (C), hydrogen content (H), nitrogen (N), and ash content.

Table 1. Test data of the ultimate analyzer

Elements	Content (%)		
	Treatment		
	1%	3%	5%
Carbon	67.73	53.92	51.40
Nitrogen	1.38	1.57	1.29
Hidrogen	4.03	3.51	3.29
Ash	6.28	20.30	22.23

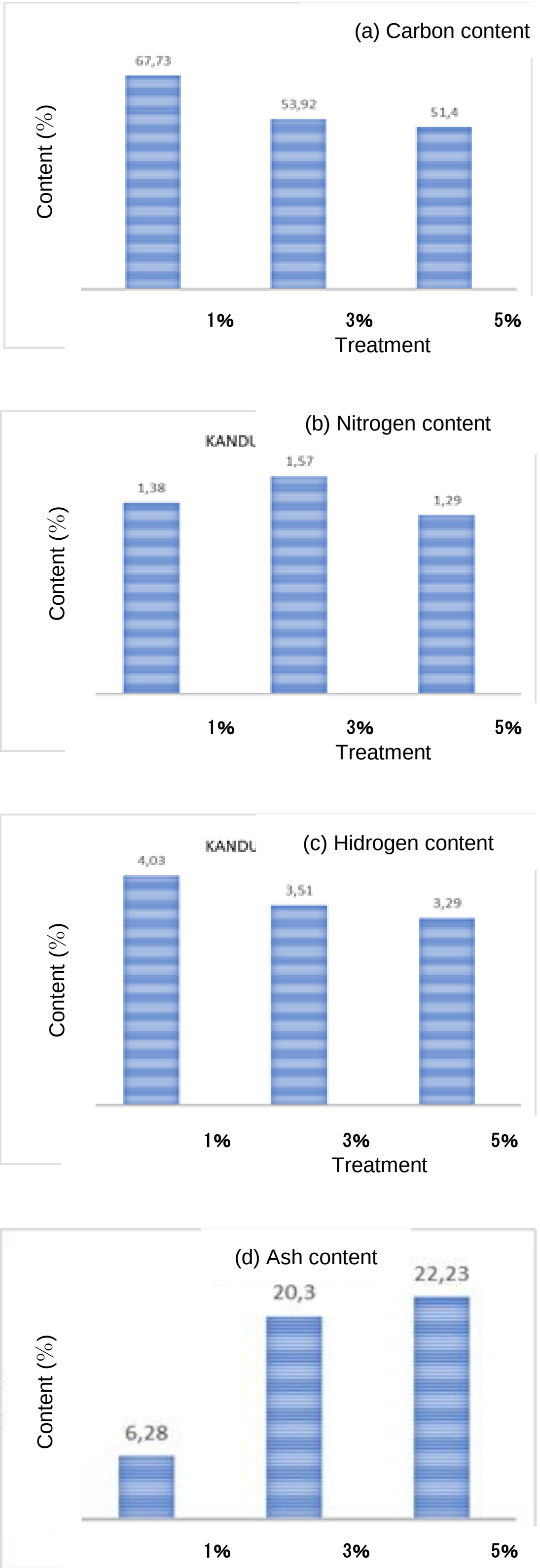

Figure 4. Variation of contents with NaOH concentration

(i) Carbon Content (C)

The results of the analysis showed that the lower the use of NaOH activator concentration, the more activated charcoal carbon produced. This is due to the high concentration can give excessive reactions so that it can damage the structure of the pores in activated charcoal [6].

Based on the ultimate test results shown by Table 1 activated carbon with 1% NaOH activation has the most Carbon (C) content of 67.73%, while the activated carbon with 5% NaOH activation contains the smallest Carbon (C) value with a value of 51.40 %. The carbon content in the activated carbon of the red chilli tree (Capsicum Anuumm L) waste will be addressed in Fig. 4(a) of Carbon Content.

Based on the graph, the carbon content for activation with 1% NaOH activator fulfills the requirements of activated carbon SNI 06-3730-1995.

(ii) Nitrogen (N) content

The value of Nitrogen (N) with activation of 1% NaOH has a value of 1.38%, and the value of Nitrogen (N) for activated carbon with activation of 3% NaOH has the highest Nitrogen (N) value of 1.57%, for Nitrogen (The smallest N) is found on activated carbon with activation of 5% NaOH with a value of 1.29%. The content of Nitrogen (N) in activated carbon will be directed to Fig. 4(b) of Nitrogen content.

(iii) Hydrogen content

For the largest Hydrogen (H) value found on activated carbon with 1% NaOH activation with a value of 4.03%, the smallest Hydrogen (H) value is found on activated carbon with 5% NaOH activation of 3.29%, and for Hydrogen value (H) with the activation of 3% NaOH having a value of 3.51%, the Hydrogen (H) content in the activated carbon of the red chilli tree (Capsicum Anuumm L) waste will be shown in Fig. 4(c) of Hydrogen content.

(iv) Ash content

The highest ash level is found on activated carbon with 5% NaOH activation with a value of 22.23% for the smallest level of ash found on activated carbon with 1% NaOH activation with an ash value of 6.28%, and for activation with 3% NaOH having ash value of 20.30%, the content of ash in the activated carbon of the red chilli tree (Capsicum Anuumm L) waste will be addressed in Fig. 4(d) of the ash content graph.

The highest ash content found in activated carbon soaked with NaOH is due to the presence of Na^+ cations from activating materials that are bound to activated carbon, so that during heating a certain amount of Na^+ becomes ash. On the other hand, it can be caused when activation occurs in contact with the air so that a further combustion process occurs where the activated carbon formed turns to ash. This ash level indicates the purity of the activated carbon produced [6].

5. Conclusions

The conclusions from the study "Characteristics of Active Carbon from Utilization of Red Chili Tree Waste (Capsicum annuum L) are as follows:

(i) The characteristics of activated carbon from the capsules of red chili (Capsicum annuum L.) analyzed using SEM observations and Ultimate testing are as follows: Test results on SEM for activated carbon from the red chili tree, at a concentration of NaOH 1%-5% higher concentration of NaOH activation, the pores formed will increase but make a lot of damaged pore walls, and the more voletile formed.

(ii) The Ultimate test results, the concentration of NaOH 1% -5% the higher the concentration of NaOH activation, the level of carbon (C) in activated carbon decreases, and the variation of NaOH activation concentration to nitrogen (N) levels is fluctuating, the higher the concentration of NaOH activation in hydrogen (H) in activated carbon will decrease, and the higher the concentration of NaOH variation, the higher the ash content in activated carbon.

References

[1] Hewindati, Y.T. et al. *Hortikultura*. Universitas Terbuka. Jakarta, 2006.

[2] Kuhad R.C., Singh A. and Ericksson K.E., Microorganisms and enzymes involved in the degradation of plant fiber cell walls. Delhi; *Adv Biochem Eng Biotechnol,* 1997.

[3] Darmawan S., Sifat arang aktif tempurung kemiri dan pemanfaatannya sebagai penyerap emisi formaldehida papan serat berkerapatan sedang. [tesis]. *Bogor: Sekolah Pasca Sarjana*. Institut Pertanian Bogor, 2008.

[4] Abdullah, Mikrajuddin and Khairurrijal. *Karakterisasi Nanomaterial Jurnal Nanoscience dan Teknologi,* 2008.

[5] Gusti Gilang Ramadhan Maulana, Lya Agustina, and Susi, Proses aktivasi arang aktif dari cangkang kemiri (aleurites moluccana) dengan variasi jenis dan konsentrasi aktivator kimia, *Jurusan Teknologi Industri,* Pertanian Fakultas Pertanian Universitas Lambung Mangkurat, 2017.

[6] i Setiawat and Suroto, Pengaruh bahan aktivator pada pembuatan karbon aktif tempurung kelapa, *Jurnal Riset Industri Hasil Hutan* Vol. 2, No. 1, 2010.

EPI International Journal of Engineering
Volume 2, Number 1, February 2019, pp. 14-18
DOI: 10.25042/epi-ije.022019.04

*p*ISSN 2615-5109
*e*ISSN 2621-0541

Multi-objective Optimization of Variable-stiffness Composites Fabricated by Tailored Fiber Placement Machine

Shinya Honda[a,*]

[a]Department of Human Mechanical Systems and Design, Faculty of Engineering, Hokkaido University. Email: honda@eng.hokudai.ac.jp

Abstract

A multi-objective optimization method for the laminated composite fabricated by a tailored fiber placement machine that is an application of embroidering machine is presented. The mechanical properties of composite with curvilinear fibers including stiffness, volume fraction, and density are variable depending on curvatures of fibers. The present study first measures the relation between curvatures and mechanical properties. The measured results indicate that the stiffness of composite decreases linearly as the curvature increases. Then, the obtained relation is applied to the multi-objective optimization where the maximum principal strain and magnitude of curvature are employed as objective functions. Obtained Pareto optimum solutions are widely distributed ranging from the solutions with curvilinear fibers to those with straight fibers, and the curvilinear fiber has still advantages over straight fiber even its weakened stiffness.

Keywords: Laminated composite; multi-objective optimization; variable-stiffness composites; tailored fiber placement

1. Introduction

Due to the development of fabrication process of composite materials, it has become possible to produce composites with curved reinforcing fibers. Since curvilinear fibers indicate locally varying anisotropic property in the same layer, it is possible to design with larger degree-of-freedom in terms of anisotropy compared with straight fibers. This results in that the laminated composites with optimally designed curved reinforcing fibers possess higher mechanical properties to the specific occasion than the conventional composite with straight fibers.

Many studies about composites with curvilinear fibers are reported in the past [1-5], and the authors also propose an optimization method of composite with curvilinear fibers [6, 7] where it was revealed that there is a trade-off relationship between mechanical properties and curvature of reinforcing fibers. Moreover, it was also found from experimental studies by using a tailored fiber placement (TFP) machine that the fiber volume fraction and layer thickness varies depending on curvature since fiber tows shrink and become thick along the curved path. This causes a gap between fiber tows and overlapping of adjacent tows.

The present study first reveals the relationship among curvature, volume fraction, and stiffnesses of composite with curved fibers by measuring densities of test specimens with various curvatures fabricated by the TFP machine. Then, obtained relationship is applied to the multi-objective optimization problem that has two conflicting objective functions including in-plane mechanical properties and fiber curvatures.

2. Experiment

2.1. Experimental methods

The tailored fiber placement (TFP) machine is employed to fabricate composites with curvilinear fibers. The TFP machine is an application of embroidering machine and its sewing head is shown in Fig. 1 (a). Fiber tows (TR50S12L) are provided from horizontally rotating bobbin, and they are fixed by sewing thread in a zigzag manner to the base material as indicated in Fig. 1 (b) where peel-ply cross is used as a base material. Then, the fabricated preform is molded by using the vacuumed resign transfer molding (VaRTM) method with unsaturated polyester.

Six kinds of test specimens with constant curvatures are prepared to reveal the relationship between curvature and fiber volume fraction. The dimension of composite is 150 mm × 150 mm with four layers, and fiber shapes are defined by an equation of arc, $y = -\sqrt{R^2 - x^2}$. Distance between adjacent tow is 2.5 mm at the center line of plate. Curvatures of each specimen are κ = 1/100, 1/150, 1/200, 1/250, 1/300, and 0 mm^{-1} (straight). As an example, design of fiber shape and preform before molding are indicated in Fig. 2(a) and (b).

---

*Corresponding author. Tel.: +81-11-706-6415
Kita-13, Nishi-8, Kita-ku
Sapporo, Hokkaido, Japan, 060-8628

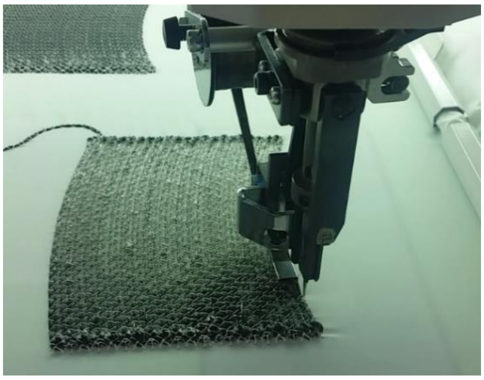

(a) Sewing head

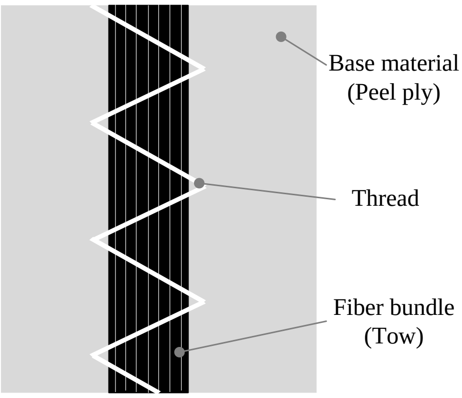

(b) Fiber tow and zigzag thread

Figure 1. Sewing head of TFP machine and schematic diagram of fiber placement

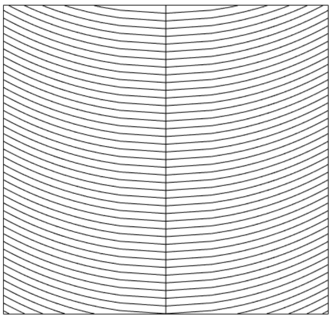

(a) Fiber design

(b) Preform

Figure 2. Example of (a) fiber shape and (b) preform of test specimen $\kappa = 1/100\mathrm{mm}^{-1}$

2.2. Experimental results

Figure 3 indicates measured relation between (a) thickness and curvature, and (b) density and curvature. Three test specimens are prepared for each curvature. Blue diamonds show averaged values and error bars are standard deviations. Red lines are linear regression equations for both results and they are determined as follows.

$$h = 30.0\kappa + 2.10 \text{ [mm]} \tag{1}$$

$$\rho_c = -5.9 \times 10^3\kappa + 1405 \text{ [kg/m}^3\text{]} \tag{2}$$

where ρ_c is a density of composite. Coefficients of determination are 0.814 and 0.917, respectively. Using Eq. (2) and the mixture rule of composites, the fiber volume fraction V_f is estimated with densities of fiber $\rho_f = 1820\ \mathrm{kg/m^3}$ and matrix $\rho_m = 1180\ \mathrm{kg/m^3}$. Finally, variable stiffnesses E_1 and E_2 and Poisson's ratio ν_{12} depending on curvature are calculated by using mixture rule again. As with the density, the stiffness decreases linearly as the curvature increases. That is, a part with curved fiber has lower mechanical properties than straight ones. In the next chapter, it will be confirmed by the optimization problem if the curvilinear fiber nevertheless has advantages over straight fibers.

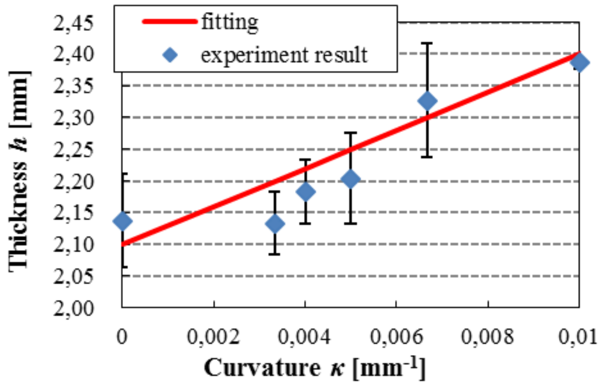

(a) Thickness vs curvature

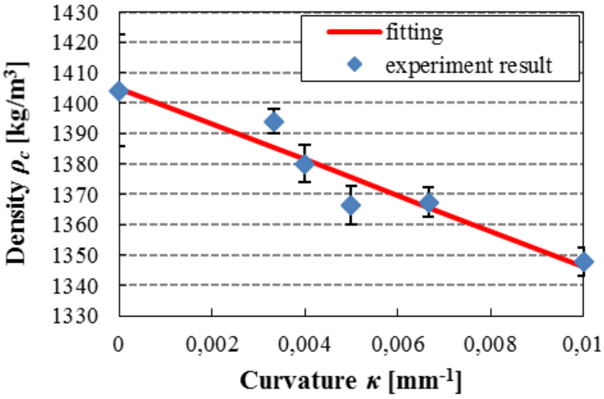

(b) Density vs curvature

Figure 3. Experimentally obtained relationship between (a) thickness and curvature, and (b) density and curvature

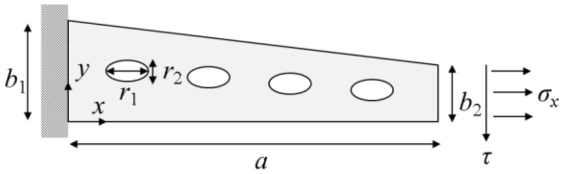

(a) Dimensions and loading condition

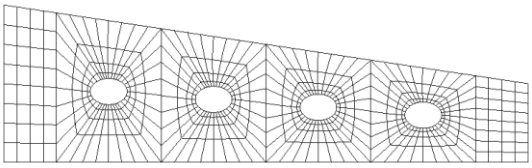

(b) Meshing

Figure 4. Numerical model for the optimization

3. Optimization

3.1. Optimization conditions

The present study employs a cantilever wing-shaped plate with four elliptical holes under in-plane loading as an optimized numerical model (Fig. 4 (a)). Its dimensions are $a = 1000$ mm, $b_1 = 300$ mm, $b_2 = 150$ mm, $r_1 = 70$ mm, $r_2 = 50$ mm, and each elliptical hole is located at $x = 200, 400, 600, 800$ mm, respectively. Loading conditions are $\sigma_x = 175$ MPa, $\tau = 17.5$ MPa. The number of layer is fixed to 16. The finite element model is shown in Fig. 4(b), and numbers of element and node result in 576 and 1949.

For an expression of arbitral curvilinear reinforcing fibers, a surface defined by a cubic polynomial function is employed as follows [6-7].

$$f(x,y) = c_{10}x + c_{01}y + c_{20}x^2 + c_{11}xy + c_{02}y^2 + c_{30}x^3 + c_{21}x^2y + c_{12}xy^2 + c_{03}y^3 \quad (3)$$

For example, Eq. (3) gives a surface shown in Fig. 5(a). Contour lines of the surface projected to the horizontal plane is indicated in Fig. 5 (b). By varying the values of c_{ij} $(i,j = 1,2,3)$ arbitrary, various shapes of curves are expressed with Eq. (3), and these coefficients are employed as the design variables in the optimization. When these curved fibers are implemented in the finite element analysis, tangential directions of contour lines are calculated at center of each element by following equation.

$$\theta_{n,p}(x_c, y_c) = \tan^{-1}\left(-\frac{\partial f/\partial x}{\partial f/\partial y}\right)\Bigg|_{x=x_c,\, y=y_c} \quad (4)$$

where x_c and y_c is the coordinate of center of element, and $\theta_{n,p}$ is the fiber orientation angle at p-th element in the n-th layer. Thus, curved fibers are discretized and approximated by the continuously changing short straight fibers in the FEA. Figure 6 (a) shows discrete fiber shape corresponding with Fig. 5. This fiber shape defined by Eq. (3) explicitly is referred as $+\theta$ layer, and a fiber shape which has symmetric fiber shape with respect to horizontal line at each element is $-\theta$ layer as shown in Fig. 6 (b).

Then, the present optimization problem can be formulated as follows.

Objectives:	Maximizing P, Minimizing $\varepsilon_{1,max}$
Design variables:	c_{ij} $(i,j = 1,2,3)$, θ_k $(k = 1,2,\ldots nl)$, ncl
Constraints:	$-2.0 \le c_{ij} \le 2.0$ $(\Delta c_{ij} = 0.1)$, $-75° \le \theta_k \le 90$ $(\Delta\theta_k = 15°)$, $0 \le ncl \le 16$ $(\Delta ncl = 2)$, $P \ge 0$, $\varepsilon_{1,max} \le 11000\mu$ (around hole), $\varepsilon_{1,max} \le 5000\mu$ (other area)

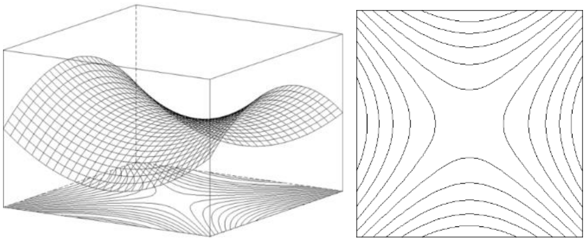

(a) Surface (b) Curvilinear shapes

Figure 5. (a) An example of a curved surface, and (b) the curvilinear fiber shape corresponding with curved surface of (a)

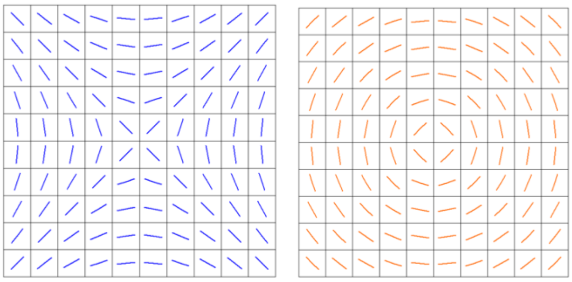

(a) $+\theta$ layer (b) $-\theta$ layer

Figure 6. The discrete curvilinear fiber shapes of $+\theta$ and $-\theta$ layers in FEA corresponding with Fig. 5

The objectives are minimizing the maximum principal strain $\varepsilon_{1,max}$ and maximizing the productivity index P which is defined as a function of curvature as follows.

$$P = -3.5 \times 10^5 \kappa^2 + 200\kappa + 30 \quad (5)$$

This relation is apporoximated by the experimental experiences and when the layer is composed of straight fibers, $P = 31$.

The design variables are coefficients of cubic polynomial function c_{ij} $(i,j = 1,2,3)$, fiber orientation angle θ_k in the k-th layer which has straight fibers only, and number of layer with curvilinear reinforcing fibers ncl.

Two elements adjacent to the hole are regarded as around hole elements and a less-restricted constraint is imposed compared with other parts. As an optimizer, the improved non-dominated sorted genetic algorithm (NSGA-II) [8] are used due to its high searching ability and versatility.

3.2. Optimization results

Obtained optimum solutions are shown in Fig. 7. The vertical and horizontal lines indicate the productivity *P* and the maximum principal strain $\varepsilon_{1,max}$. The number of layers with curved fibers is distinguished by colors. It is known from Fig. 7 that the present study found widely distributed Pareto optimum solutions.

For example, the lay-up configuration of the solution A is $[+\theta/-\theta/0°/+\theta/-30°/-\theta/15°/+\theta]_S$ where the $+\theta$ layer has the optimized coefficients of cubic polynomial (c_{10}, c_{01}, c_{20}, c_{11}, c_{02}, c_{30}, c_{21}, c_{12}, c_{03}) = (-1.0, 0.1, 0.6, 1.0, -0.4, -0.4, -1.3, -2.0), and its fiber shapes are given in Fig. 8 (a). The $-\theta$ layer has symmetric fiber shape with respect to the horizontal line. Distribution of principal strain ε_1 is demonstrated in Fig. 8 (b). The maximum value $\varepsilon_{1,max}$ = 3976 μ that is the minimum value in all obtained non-dominated solutions, but the solution A has the lowest productivity *P* = 29.75. On the other hand, the solution B whose lay-up is $[-15°/+\theta/0°/-\theta/-15°/0°/30°/-45°]_S$ and coefficients are c_{ij} = (-2.0, 0.5, 0.2, -1.7, -0.5, -1.9, -1.5, -1.0) gives the higher principal strain $\varepsilon_{1,max}$ = 4225 μ and productivity *P* = 30.75 than the solution A. The solution C is only solution which is composed of straight fibers for all layers and its lay-up is $[-15°/0°/-15°/0°/0°/0°/30°/-45°]_S$ with $\varepsilon_{1,max}$ = 4232 μ. This is the highest value in the obtained solutions even the straight part has mechanical properties superior to curvilinear fiber path. Therefore, the effectiveness of the curvilinear fibers with variable stiffnesses depending on curvature is confirmed from above.

4. Conclusions

The present study first experimentally revealed the relationship between curvature of reinforcing fiber and fiber volume fraction of laminated composites fabricated by the tailored fiber placement machine. It was found that the stiffness of the composite decrease as the curvature increases. Then, the obtained results are applied to the multi-objective optimization problem. From numerical results, it became clear that the composites with curved fibers have still advantages over those with straight fibers even their weakened stiffnesses due to fiber curvatures.

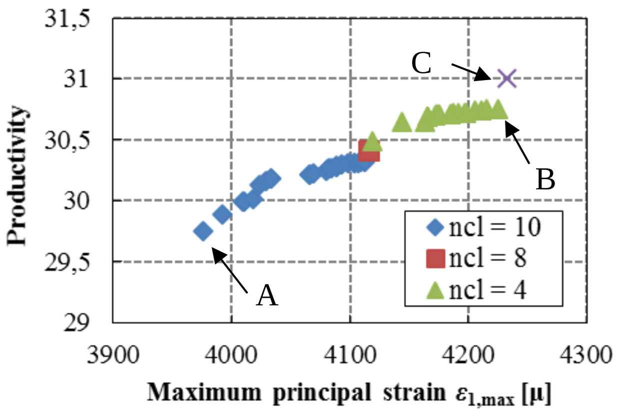

Figure 7. Obtained Pareto optimum solutions

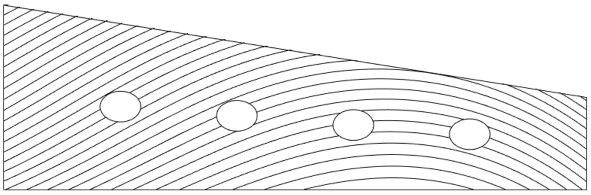

(a) Fiber shape for + layer, *P* = 29.75

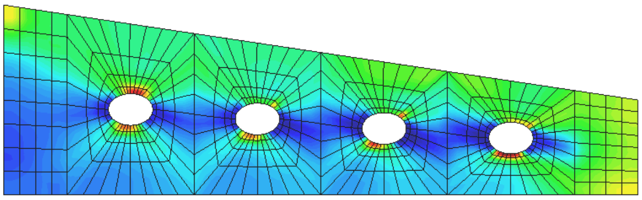

(b) Principal strain ε_1 distribution, $\varepsilon_{1,max}$ = 3976 μ

Figure 8. Fiber shape of + layer and strain distribution for solution A

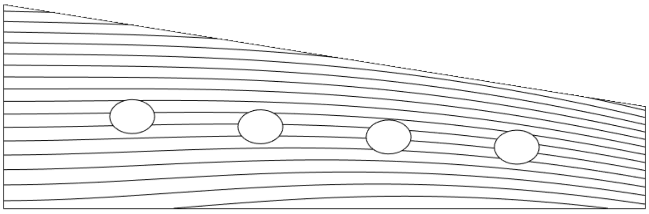

(a) Fiber shape for + layer, *P* =30.75

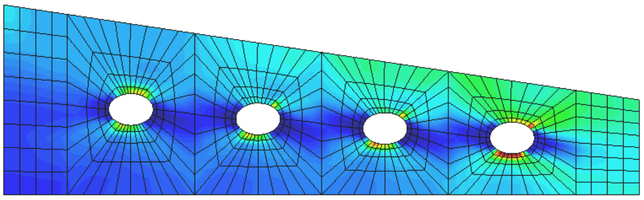

(b) Principal strain ε_1 distribution, $\varepsilon_{1,max}$ = 4225 μ

Figure 9. Fiber shape of + layer and strain distribution for solution B

References

[1] Hyer, M. H. and Lee, H. H., The Use of Curvilinear Fiber Format to Improve Buckling Resistance of Composite Plates with Central Circular Holes, Composite Structures, Vol. 18(1991), pp. 239-261.

[2] Huang, J. and Haftka, R. T., Optimization of Fiber Orientation near a Hole for Increased Load-carrying Capacity of Composite Laminates, Structural Multidisciplinary Optimization, Vol. 30(2005), pp. 335-341.

[3] Parnas, L., Oral, S., and Ceyhan, Ü., Optimum Design of Composite Structures with Curved Fiber Courses, Composites Science and Structures, Vol. 63 (2003), pp. 8493-8516.

[4] Lopes, C. S., Gürdal, Z., and Camanho, P. P., Variable-stiffness Composite Panels: Buckling and First-ply Failure Improvements over Straight-fibre Laminates, Computer & Structures, Vol. 86 (2008), pp. 897-907.

[5] Lopes, C. S., Camanho, P. P., Gürdal, Z., and Tatting B. F., Progressive Failure Analysis of Tow-placed, Variable-stiffness Composite Panels, International Journal of Solids and Structures, Vol. 44(2007), pp. 8493-8516.

[6] Honda, S., and Narita, Y., Vibration Design of Laminated Fibrous Composite Plates with Local Anisotropy Induced by Short Fibers and Curvilinear Fibers, Composite Structures, Vol. 93 (2011), pp. 902-910.

[7] Honda, S., Igarashi, T., and Narita, Y., Multi-Objective Optimization of Curvilinear Fiber Shapes for Laminated Composite

Plates by Using NSGA-II", Composites Part B: Engineering, Vol. 45, 2013, 1071-1078.

[8] Deb, K., Multi-objective Optimization Using Evolutionary Algorithms, John Wiley and Sons Ltd, (2001).

EPI International Journal of Engineering
Volume 2, Number 1, February 2019, pp. 19-27
DOI: 10.25042/epi-ije.022019.05

*p*ISSN 2615-5109
*e*ISSN 2621-0541

The Effect of Using Different Elastic Moduli on Vibration of Laminated CFRP Rectangular Plates

Yoshihiro Narita [a]*, Michio Innami[b], Daisuke Narita[c]

[a]Hokkaido University (Professor Emeritus), C-BEST Project, Center of Technology, Hasanuddin University. Email: ynarita@eng.hokudai.ac.jp
[b]Hokkaido Polytechnic College, Otaru, Japan. Email: innami@hokkaido-pc.ac.jp
[c]Hokkaido University of Science Junior College, Sapporo, Japan. Email: narita@hus.ac.jp

Abstract

This paper deals with effects of using different sets of material constants on the natural frequencies of laminated composite rectangular plates. The plate is symmetrically laminated by thin layers composed of recently developed carbon fiber reinforced plastic (CFRP) materials. Numerical experiments are conducted by using a semi-analytical solution based on the thin plate theory and the lamination theory. The displacements are assumed to accommodate any combination of classical boundary conditions. The material property is expressed by a set of four elastic constants, and some typical sets of values are cited from the recent literature. Furthermore, a new standard set of discretized constants is proposed to uncover the underlying characteristics of the existing constants. The convergence study is carried out first, and the lowest five natural frequencies are calculated for five sets of classical boundary conditions including totally free through totally clamped cases. Next, a new definition of frequency parameters is introduced to promote more physically meaningful comparison among the obtained results, and the effect of using slightly different constants is clarified for unified comparison and insights. It is also discussed to derive approximate frequency formulas by linear regression analysis and to test accuracy of the formulas.

Keywords: Carbon fiber reinforced plastic; laminated composite plate; material constants; natural frequency; vibration

1. Introduction

Structural components in the form of flat plates are found practically in all fields of industry, and the literatures related to free vibration of flat plates are numerous. Leissa [1] compiled in 1969 a monograph "Vibration of Plates" and it is still cited in many papers. For isotropic rectangular plates, he published a comprehensive set of natural frequencies for all possible combinations of classical boundary conditions [2]. Since in the 1970's, advanced fibrous composite materials have been developed and served as plate components in many industrial applications, such as airplane, automobile and marine structures. Generally, fiber reinforced plastics have microstructures made of reinforcing fiber and matrix material. There are various fibers, ranging from natural fibers to chemical fibers such as glass, boron and carbon fibers. When such constituents merge into one material, it shows anisotropic characteristics. Among various types of fibers, the use of carbon fibers in reinforced plastics (CFRP) is becoming more increasingly dominant in weight-sensitive structures. For the reason, some books [3-5] dealing with mechanics of the composites have been published to serve for analysis and design, and review papers have appeared, for example [6].

Since the publication of journal papers in the 1970's, researchers such as Bert [7] published papers on vibration of laminated composite plates, and it has led to improvement of lamination theories to the first order and higher order plate theories [5, 8]. For rectangular plates with arbitrary edges, combination of classical boundary conditions became possible to be analyzed [9] in good accuracy. Application of the finite element method has also been active in analyzing laminated plates [10, 11].

For defining elastic problem of laminated CFRP plates, four independent elastic constants are necessary, unlike isotropic plates with only two independent constants being needed. Previous literatures have used different values of the constants, because the improvement of fiber stiffness is in progress, and many past researchers have used elastic constants obtained from measurement tests supplied from different chemical companies. This fact makes direct comparison difficult among the published results, and was also obstacles preventing from compiling design date book.

Despite such practical needs, however, there is no literature to discuss the influence caused by using different elastic constants. The present study takes up this problem for studying the effect when slightly different constants are used in the vibration analysis of laminated CFRP plates. In doing so, numerical experiments are conducted

---

*Corresponding author.
Kita-13, Nishi-8, Kita-ku, Sapporo, Japan, 060-8628

to calculate natural frequencies of laminated CFRP rectangular plates by using various sets of constants [3, 12-14], and for effective insights, new standard constants are proposed to understand vibration behaviors in the comprehensive way.

2. Analytical Method

Figure 1 shows a laminated rectangular plate in the coordinate system and in each layer the major and minor principal axes are denoted by the *L* and *T* axes. The dimension of the whole plate is given by $a \times b \times h$ (thickness). The plate considered is limited to symmetric laminate, and the total number of layers is defined as $2N$ (i.e., N layers in the upper(lower) half cross-section).

Free vibration of a macroscopic model for such thin symmetric plates is governed in the classical lamination (plate) theory by

$$D_{11}\frac{\partial^4 w}{\partial x^4}+2\left(D_{12}+2D_{66}\right)\frac{\partial^4 w}{\partial x^2 \partial y^2}+D_{22}\frac{\partial^4 w}{\partial y^4}$$
$$+4D_{16}\frac{\partial^4 w}{\partial x^3 \partial y}+4D_{26}\frac{\partial^4 w}{\partial x \partial y^3}+\rho h\frac{\partial^2 w}{\partial t^2}=0 \qquad (1)$$

where w is a deflection and ρ is a mean mass per unit volume of the plate. The D_{ij} (i, j = 1, 2, 6) are the bending stiffness of the symmetric laminate defined by

$$D_{ij}=\frac{2}{3}\sum_{k=1}^{N}\bar{Q}_{ij}^{(k)}\left(z_k^3-z_{k-1}^3\right) \qquad (2)$$

with z_k being a thickness coordinate measured from the mid-surface and $\bar{Q}_{ij}^{(k)}$ being elastic constants [3, 4] in the k-th layer, obtained from

$$Q_{11}=\frac{E_L}{1-\nu_{LT}\nu_{TL}},Q_{12}=\frac{E_L\nu_{TL}}{1-\nu_{LT}\nu_{TL}},$$
$$Q_{22}=\frac{E_T}{1-\nu_{LT}\nu_{TL}},Q_{16}=\frac{G_{LT}}{1-\nu_{LT}\nu_{TL}} \qquad (3)$$

(superscript (k) is omitted) by considering a fiber orientation angle θ_k in the layer. The E_L and E_T are moduli of longitudinal elasticity in the *L* and *T* directions, respectively, G_{LT} is a shear modulus and ν_{LT} is a Poisson ratio.

For the small amplitude (linear) free vibration, the deflection w of a thin plate may be written by

$$w(x,y,t)=W(x,y)\sin\omega t \qquad (4)$$

where W is the amplitude and ω is a radian frequency. Natural frequency is normalized as a frequency parameter

$$\Omega=\omega a^2\left(\rho h/D_0\right)^{1/2} \qquad (5)$$

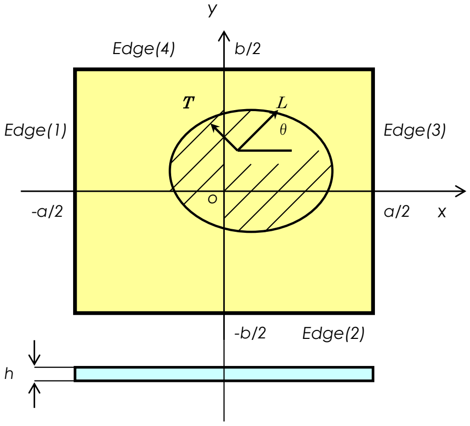

Figure 1. Laminated rectangular plat

where ω is a radian frequency of the laminated plate and D_0 is a reference bending stiffness.

Then, the maximum strain energy due to the bending is expressed by

$$U_{max}=\frac{1}{2}\iint_A \{\kappa\}^T\begin{bmatrix} D_{11} & D_{12} & D_{16}\\ D_{12} & D_{22} & D_{26}\\ D_{16} & D_{26} & D_{66}\end{bmatrix}\{\kappa\}dA \qquad (6)$$

and $\{\kappa\}$ is a curvature vector

$$\{\kappa\}=\left\{-\frac{\partial^2 W}{\partial x^2} \quad -\frac{\partial^2 W}{\partial y^2} \quad -2\frac{\partial^2 W}{\partial x \partial y}\right\}^T \qquad (7)$$

The maximum kinetic energy is given by

$$T_{max}=\frac{1}{2}\rho h\omega^2\iint_A W^2 dA \qquad (8)$$

In the Ritz method the amplitude is assumed in the form

$$W(x,y)=\sum_{m=0}^{M-1}\sum_{n=0}^{N-1}A_{mn}X_m(x)Y_n(y) \qquad (9)$$

where A_{mn} are unknown coefficients, and $X_m(x)$ and $Y_n(y)$ are the functions modified so that any kinematical boundary conditions are satisfied at the edges with applying “boundary indices” [9, 15, 16]. To simplify the analysis, the normalized co-ordinate system O-$\xi\eta$ ($-1 \le \xi, \eta \le 1$) is defined in equation

$$\xi=2x/a,\ \eta=2y/b \qquad (10)$$

and $X_m(\xi)$ and $Y_n(\eta)$ are the displacement functions

$$X_m(\xi)=\xi^m(\xi+1)^{bc1}(\xi-1)^{bc2}$$
$$Y_n(\eta)=\eta^n(\eta+1)^{bc3}(\eta-1)^{bc4} \qquad (11)$$

The bci (i = 1, 2, 3 and 4) is the boundary index which is used to satisfy the kinematical boundary conditions on each edge, and they are defined as

$$bc1, bc2, bc3, bc4 = \begin{cases} 0 & (\text{free}) \\ 1 & (\text{simple support}) \\ 2 & (\text{clamp}) \end{cases} \tag{12}$$

on each of four edges.

After substituting Eq.(9) into the sum of energies (6) and (8), the stationary value is obtained by

$$\frac{\partial}{\partial A_{\overline{m}\overline{n}}}\left(T_{max} - U_{max}\right) = 0 \qquad (13)$$
$$\left(\overline{m} = 0,1,..,M-1; \overline{n} = 0,1,..,N-1\right)$$

The minimizing process gives a set of linear simultaneous equations in terms of the coefficients A_{mn}, and the eigenvalues Ω may be extracted by using existing computer subroutines. This analytical procedure is a standard routine of the Ritz method but the special form of polynomials (13) can satisfy any kinematical boundary conditions [9, 15, 16].

3. Numerical Examples and Accuracy of Solution

3.1. Numerical examples

Symmetrically laminated square (*a/b*=1) and rectangular plates (*a/b*=2) are considered as numerical examples. The number of layers is eight and a lamination sequence is denoted by $[\theta_1/\theta_2/\theta_3/\theta_4]$s, where θ_1 is a fiber orientation angle of the outer most layer measured from *x* axis (as shown in Fig.1) and θ_4 is the angle of inner most layer. In the examples, the lamination sequence is limited to two typical types:

Cross-ply plate [0°/90°/0°/90°]s, (i.e., $[(0°/90°)_2]$s),

Angle-ply [30°/-30°/30°/-30°]s, ($[(30°/\text{-}30°)_2]$s)

(s: symmetric lamination), (hereafter, "°" is omitted). The boundary conditions are denoted by four capital letters, such as CSFF, labelling counter-clockwise starting from Edge(1) in Fig. 1. Here, "C" denotes a clamped edge (i.e., deflection and rotation are both rigidly constrained), "S" does a simply supported edge (deflection is constrained but bending moment is zero) and "F" does a free edge (bending moment and shear force are both zero). By using this notation, natural frequencies for SSSS (totally simply supported plate) are presented in both Table 3 and 4, and those for FFFF (totally free plate), CFFF (cantilever plate), CSFF (combination of C,S,F) and CCCC (totally clamped plate) are presented for square planform (*a/b*=1) in Tables 5, 6, 7 and 8, respectively. Results of rectangular plates (*a/b*=2) are in Tables 9 and 10.

3.2. Elastic constants of different CFRP materials

For a fixed geometry (*a,b,h*) and boundary condition (C,S,F) of plate, it is easily understandable that frequency parameters are governed only by the values of elastic constants, and it is the main topic of this work to study the effect from the constants. As shown in Eq. (3), there are four independent elastic constants in Q_{ij}: E_L and E_T being modulus of longitudinal elasticity (Young's modulus) in the *L* (fiber) and *T* directions, respectively, G_{LT} being a shear modulus and a Poisson's ratio ν_{LT}, and there is a relation of $E_L/\nu_{LT} = E_T/\nu_{TL}$ among the constants.

The survey by the authors showed that a little different value of elastic constants has been employed previously, as listed in Table 1. It is observed that the difference is mainly caused by values of E_L but not by E_T and G_{LT}, because Young modulus of the fibers is a key factor in controlling the stiffness in the longitudinal direction within lamina, while the matrix material is almost the same, mostly epoxy material. In the table, Mat.1 indicates values used by Stanford and Jutte [12] in NASA and shows the lowest anisotropy rate E_L/E_T=11.6 among the listed sets of constants. Mat.2 and 3 are medium values listed in [3] and [13], respectively. Mat.4 indicates those used by Panesar and Weaver [14], a group in Bristle University, and it shows the highest anisotropy E_L/E_T=18.7. Finally, Mat.5 is introduced to represent the mean values of recently used CFRP materials and used as the standard reference for comparison. This set of discretized values is fictious and not measured in experiment, but it will be shown that it is useful as the representative constants for CFRP. When one measures deviation of listed materials from Mat.5, the differences in the constants show ranges of

Table 1. Elastic constants of carbon fiber reinforced plastic (CFRP) materials

	E_L [Gpa]	E_T [Gpa]	(E_L/E_T)	G_{LT} [Gpa]	ν_{LT}
Mat.1 [12]	**128**	**11**	**(11.6)**	**4.5**	**0.25**
Mat.2 [3]	**138**	**8.96**	**(15.4)**	**7.1**	**0.30**
Mat.3 [13]	**139**	**8.76**	**(15.9)**	**4.57**	**0.32**
Mat.4 [14]	**168.980**	**9.050**	**(18.7)**	**5.00**	**0.288**
Mat.5	**150.0**	**10.0**	**(15.0)**	**5.00**	**0.30**

Table 2. Convergence of the solution for cross-ply and angle-ply square plates (Mat.5)

Number of term					
m×n	Ω_1	Ω_2	Ω_3	Ω_4	Ω_5
Cross-ply plate $[(0/90)_2]$s, CSFF					
6x6	12.55	40.36	73.06	90.49	119.9
8x8	12.55	40.36	73.06	90.48	118.7
10x10	12.55	40.36	73.06	90.48	118.7
Cross-ply plate $[(0/90)_2]$s, SSSS					
6x6	42.55	102.1	134.5	170.2	217.2
8x8	42.55	102.1	134.5	170.2	213.9
10x10	42.55	102.1	134.5	170.2	213.8
Exact sol.	42.55	102.1	134.5	170.2	213.8
(m,n)	(1,1)	(1,2)	(2,1)	(2,2)	(1,3)
Angle-ply plate $[(30/-30)_2]$s, CCCC					
6x6	88.50	143.7	209.1	225.8	273.9
8x8	88.50	143.7	209.1	225.6	273.8
10x10	88.50	143.7	209.1	225.6	273.8

-15% (Mat.1)≦0% (Mat.5)≦15%(Mat.4) for E_L,
-12%(Mat.3)≦0%(Mat.5)≦11%(Mat.1) for E_T,
-10%(Mat.1)≦0%(Mat.5)≦42%(Mat.2) for G_{LT}, and
-17%(Mat.1)≦0%(Mat.5)≦7%(Mat.3) for ν_{LT}.

The following comparison is made by a frequency parameter, but two types of reference bending rigidity are used as

$$\Omega = \omega a^2 \left(\rho h / D_0\right)^{1/2}, D_0 = E_T h^3 / 12\left(1-\nu_{LT}\nu_{TL}\right) \quad (14)$$

with E_T, ν_{LT} for each material in Table 1, and

$$\Omega^* = \omega a^2 \left(\rho h / D_0^*\right)^{1/2}, D_0^* = E_T^* h^3 / 12\left(1-\nu_{LT}^*\nu_{TL}^*\right) \quad (15)$$

with E_T^* =10 GPa, ν_{LT}^* =0.3. Note $\nu_{TL}^* = \left(E_T^* / E_L^*\right)\nu_{LT}^*$ of Mat.5, for global comparison among different materials listed in the table.

3.3. Convergence and comparison of the solution

Before the natural frequencies are compared to discuss the discrepancy stemming from different CFRP materials, validity of the solution should be established. Table 2 presents frequency parameters of laminated square plates with Mat.5 (i.e., D_0= D_0* in Es.(14)(15)). Number of terms M, N in Eq.(9) is increased from six to ten for cross-ply (CSFF, SSSS) and angle-ply (CCCC) plates. They converge well within four significant figures.

For a special case of cross-ply (i.e., D_{16}= D_{26}=0) simply supported rectangular plate (SSSS), the exact solution can be written in the form

$$\Omega = \pi^2 \left[\left(\frac{D_{11}}{D_0}\right) m^4 + 2\left(\frac{b}{a}\right)^2 \left(\frac{D_{12}+2D_{66}}{D_0}\right) m^2 n^2 + \left(\frac{b}{a}\right)^4 \left(\frac{D_{22}}{D_0}\right) n^4 \right]^{1/2} \quad (16)$$

with m and n being half wave numbers in x and y direction, respectively. The results from this formula exactly agree with the present solution within four significant figures in Table 2. All the frequency parameters listed hereafter will be obtained by using 10×10 solution.

4. Results and Discussions

4.1. Unified parameter for different CFRP

Table 3 presents lowest five frequency parameters Ω, defined in Eq.(14) by using E_T of each material, for simply supported (SSSS) square plate. The results are given for Mat.1～Mat.5, and the differences (%) in frequency measured from Mat.5 are also written in the table. The frequency parameter Ω is non-dimensional and it does not include the plate geometry (a, b, h) and mass density ρ. So for the fixed geometry and density, values of the frequency parameters depend on ω itself and E_T and ν_{LT}.

From observation in the table, no significant differences (%) exist among the frequency orders (i.e., from the first to fifth frequency) and between the lamination schemes of cross-ply and angle-ply. The increasing (or decreasing) trend of the frequencies is unclear with respect to the constant E_L, which should be the most influential factor on the frequency values. Next, the degree of influence by E_L will be quantitatively focused.

Table 3. Frequency parameters Ω (Eq.(14)) of symmetric 8-layer square plates (SSSS)

	Ω_1	Ω_2	Ω_3	Ω_4	Ω_5
Cross-ply	$[(0/90)_2]$s				
Mat.1	37.92	91.53	119.2	151.7	191.8
(%)	-10.9	-10.3	-11.4	-10.9	-10.3
Mat.2	44.31	105.3	137.8	177.2	218.5
(%)	4.1	3.2	2.5	4.1	2.2
Mat.3	43.67	104.6	138.2	174.7	219.1
(%)	2.6	2.5	2.7	2.6	2.5
Mat.4	46.76	111.9	149.0	187.0	234.9
(%)	9.9	9.7	10.8	9.9	9.9
Mat.5	42.55	102.1	134.5	170.2	213.8
Angle-ply	$[(30/-30)_2]$s				
Mat.1	46.13	91.04	127.7	156.8	185.4
(%)	-11.0	-10.0	-11.4	-9.2	-10.9
Mat.2	52.71	103.7	147.0	178.4	212.2
(%)	1.8	2.5	2.0	3.3	2.0
Mat.3	53.16	103.60	148.1	176.6	213.5
(%)	2.6	2.4	2.7	2.3	2.6
Mat.4	57.28	110.7	159.9	187.6	229.9
(%)	10.6	9.5	10.9	8.6	10.5
Mat.5	51.80	101.1	144.1	172.7	208.1

Table 4. Frequency parameters Ω* (Eq.(15)) of symmetric 8-layer square plates (SSSS)

	Ω_1^*	Ω_2^*	Ω_3^*	Ω_4^*	Ω_5^*
Cross-ply	**$[(0/90)_2]$s**				
Mat.1	**39.76**	**95.97**	**125.0**	**159.0**	**201.1**
(%)	**-6.6**	**-6.0**	**-7.1**	**-6.6**	**-5.9**
Mat.2	**41.94**	**99.70**	**130.4**	**167.7**	**206.8**
(%)	**-1.5**	**-2.3**	**-3.0**	**-1.5**	**-3.3**
Mat.3	**40.89**	**97.96**	**129.4**	**163.5**	**205.1**
(%)	**-3.9**	**-4.0**	**-3.8**	**-3.9**	**-4.0**
Mat.4	**44.45**	**106.4**	**141.7**	**177.8**	**223.3**
(%)	**4.5**	**4.2**	**5.3**	**4.5**	**4.4**
Mat.5	**42.55**	**102.1**	**134.5**	**170.2**	**213.8**
Angle-ply	**$[(30/-30)_2]$s**				
Mat.1	**48.37**	**95.45**	**133.8**	**164.4**	**194.4**
(%)	**-6.6**	**-5.6**	**-7.1**	**-4.8**	**-6.6**
Mat.2	**49.89**	**98.11**	**139.2**	**168.8**	**200.8**
(%)	**-3.7**	**-3.0**	**-3.5**	**-2.3**	**-3.5**
Mat.3	**49.77**	**96.96**	**138.6**	**165.4**	**200.0**
(%)	**-3.9**	**-4.1**	**-3.8**	**-4.3**	**-3.9**
Mat.4	**54.45**	**105.2**	**152.0**	**178.3**	**218.5**
(%)	**5.1**	**4.1**	**5.5**	**3.2**	**5.0**
Mat.5	**51.80**	**101.1**	**144.1**	**172.7**	**208.1**

Table 5. Frequency parameters Ω* (Eq.(15)) of symmetric 8-layer square plates (FFFF)

	Ω_1^*	Ω_2^*	Ω_3^*	Ω_4^*	Ω_5^*
Cross-ply $[(0/90)_2]$s					
Mat.1	15.76	48.72	58.25	67.64	74.65
(%)	-5.2	-6.0	-5.7	-7.3	-6.9
Mat.2	19.66	49.62	63.55	69.93	80.21
(%)	18.3	-4.2	2.9	-4.1	0.0
Mat.3	15.89	49.71	59.23	70.17	77.06
(%)	-4.4	-4.1	-4.2	-3.8	-3.9
Mat.4	16.64	54.28	63.89	77.12	84.04
(%)	0.1	4.80	3.4	5.7	4.8
Mat.5	16.62	51.82	61.79	72.93	80.18
Angle-ply $[(30/-30)_2]$s					
Mat.1	23.67	33.64	60.88	70.96	73.45
(%)	-1.4	-6.4	-6.9	-2.7	-5.9
Mat.2	25.90	35.14	64.11	74.19	77.31
(%)	7.9	-2.3	-1.9	1.8	-1.0
Mat.3	22.78	34.52	62.83	69.40	74.89
(%)	-5.1	-4.0	-3.9	-4.8	-4.1
Mat.4	23.64	37.79	68.58	73.23	81.65
(%)	-1.5	5.1	4.9	0.5	4.6
Mat.5	24.00	35.95	65.37	72.90	78.09

Table 6. Frequency parameters Ω* (Eq.(15)) of symmetric 8-layer square plates (CFFF)

	Ω_1^*	Ω_2^*	Ω_3^*	Ω_4^*	Ω_5^*
Cross-ply $[(0/90)_2]$s					
Mat.1	10.63	14.34	53.23	66.61	71.40
(%)	-7.3	-6.4	-6.0	-7.3	-7.0
Mat.2	10.99	16.22	55.72	68.86	75.94
(%)	-4.1	5.9	-1.6	-4.1	-1.1
Mat.3	11.02	14.70	54.29	69.10	73.80
(%)	-3.8	-4.0	-4.1	-3.8	-3.9
Mat.4	12.12	15.83	59.03	75.95	80.66
(%)	5.8	3.4	4.3	5.8	5.1
Mat.5	11.46	15.31	56.60	71.82	76.77
Angle-ply $[(30/-30)_2]$s					
Mat.1	9.212	22.31	46.28	60.04	78.55
(%)	-7.3	-6.7	-5.5	-6.9	-6.2
Mat.2	9.740	23.25	48.83	62.89	82.95
(%)	-1.9	-2.7	-0.4	-2.4	-1.0
Mat.3	9.553	22.96	46.94	61.96	80.35
(%)	-3.8	-4.0	-4.2	-3.9	-4.1
Mat.4	10.46	25.16	50.92	67.71	87.45
(%)	5.3	5.3	3.9	5.0	4.4
Mat.5	9.933	23.90	49.00	64.46	83.76

Table 7. Frequency parameters Ω* (Eq.(15)) of symmetric 8-layer square plates (CSFF)

	Ω_1^*	Ω_2^*	Ω_3^*	Ω_4^*	Ω_5^*
Cross-ply $[(0/90)_2]$s					
Mat.1	11.68	37.95	67.81	84.51	111.6
(%)	-6.9	-6.0	-7.2	-6.6	-6.0
Mat.2	12.54	39.93	70.64	91.10	114.7
(%)	-0.1	-1.1	-3.3	0.7	-3.4
Mat.3	12.06	38.72	70.28	86.91	113.9
(%)	-3.9	-4.1	-3.8	-4.0	-4.1
Mat.4	13.16	42.08	77.12	94.42	124.1
(%)	4.9	4.3	5.6	4.4	4.6
Mat.5	12.55	40.36	73.06	90.48	118.7
Angle-ply $[(30/-30)_2]$s					
Mat.1	14.42	36.15	66.51	80.68	110.1
(%)	-6.7	-5.5	-6.6	-4.6	-6.6
Mat.2	15.03	37.82	70.11	83.64	114.7
(%)	-2.8	-1.2	-1.6	-1.1	-2.7
Mat.3	14.85	36.67	68.40	80.90	113.3
(%)	-3.9	-4.2	-4.0	-4.3	-3.9
Mat.4	16.27	39.79	74.56	87.13	123.9
(%)	5.2	4.0	4.7	3.0	5.1
Mat.5	15.46	38.27	71.23	84.56	117.9

Table 8. Frequency parameters Ω* (Eq.(15)) of symmetric 8-layer square plates (CCCC)

	Ω_1^*	Ω_2^*	Ω_3^*	Ω_4^*	Ω_5^*
Cross-ply $[(0/90)_2]$s					
Mat.1	85.47	154.8	196.1	240.3	277.2
(%)	-6.7	-6.2	-7.1	-6.7	-6.0
Mat.2	88.65	159.7	203.7	250.9	284.5
(%)	-3.3	-3.2	-3.5	-2.6	-3.6
Mat.3	88.08	158.4	203.0	247.5	283.0
(%)	-3.9	-4.0	-3.8	-3.9	-4.0
Mat.4	96.31	172.6	222.6	270.0	308.4
(%)	5.1	4.6	5.5	4.9	4.6
Mat.5	91.64	165.0	211.1	257.5	294.9
Angle-ply $[(30/-30)_2]$s					
Mat.1	82.66	135.8	194.2	214.9	255.8
(%)	-6.6	-5.5	-7.1	-4.7	-6.6
Mat.2	85.84	140.2	202.4	221.4	265.2
(%)	-3.0	-2.4	-3.2	-1.9	-3.2
Mat.3	85.04	137.7	201.1	215.9	263.1
(%)	-3.9	-4.1	-3.8	-4.3	-3.9
Mat.4	92.85	149.2	220.4	232.4	287.3
(%)	4.9	3.8	5.4	3.0	4.9
Mat.5	88.50	143.7	209.1	225.6	273.8

Therefore, use of Ω* defined in Eq. (15) is considered next to make effective comparison and to provide with clear physical interpretation. Table 4 is in the same format as Table 3 for the same square plate, except that a new reference stiffness

$D_0^*=E_T^*h^3/12(1-\nu_{LT}^*\nu_{TL}^*)$ (E_T^*, ν_{LT}^* for Mat.5) is used for all the materials (i.e, even for Mat.1,2,3 and 4). Therefore, the frequency parameters for Mat.5 are identical as those in Table.3.

The idea here is that by using the identical elastic constants E_T^* and ν_{LT}^* in the frequency parameter, the differences are caused only by ω in the new frequency parameters. Actually, it is observed in Tables 4-8 that the increasing order of E_L (Mat.1<Mat.2 ≒ Mat.3<Mat.4) among the materials basically reflects the order in the difference, except for FFFF plate, and the differences only for Mat.4 are positive, i.e. session Ω* (Mat.5)< Ω* (Mat.4) due to E_L (Mat.5)< E_L (Mat.4), unlike unnatural findings in Table 3.

The frequency parameters listed in Tables 5 (FFFF), 6 (CFFF), 7 (CSFF) and 8 (CCCC) are based on the same idea, and Ω* uses the identical values of E_T^*=10GPa and ν_{LT}^*=0.3. In Table 5 (FFFF), it is seen that the differences for Mat.2 take alternatively positive and negative values, but those of Mat 3 show only all negative differences. This unpredicted behavior may be caused by the fact that in the FFFF case, there are three rigid body motions (elastic frequencies become zero) and the vibrations take complicated mode shapes to satisfy the self-equilibrium. Such strange behavior is found when the plate edges involve a number of free edges, such as FFFF, CFFF and CSFF, and it decreases as the number of free edges (F) diminished.

For Mat.1 with E_L being the smallest in Table 1, all the differences are negative in Tables 4-8 for ten cases (cross-ply and angle-ply plates with 5 different combinations of boundary conditions), and the average differences of the lowest five Ω for the ten cases stay within the range of -6.8～-4.6%. Similarly, for Mat.5 with E_L being the largest in the table, all the differences are positive for the ten cases.

By using the data in Tables 4 and 8, Figure 2 presents comparison of percentage differences for two lamination types (cross-ply, angle-ply) and two sets of boundary conditions (SSSS, CCCC). The lowest five frequency parameters are presented for the four cases with material constants for Mat.4. These differences are located between 3.0 and 5.5 percentages, and it is observed that there are no significant differences for different modes, laminations and boundary conditions.

Figure 3 presents also the lowest five frequency parameters for different sets of boundary conditions. The differences stay within the range of 3.0 and 5.5 percent, and no significant difference is observed, except for the FFFF case. As previously mentioned, the FFFF plate shows three rigid body motions and the vibration modes presented take very different shapes from the other sets (CFFF, CSFF, SSSS, CCCC).

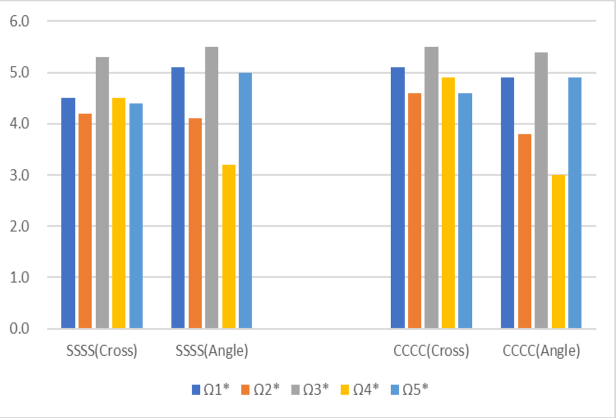

Figure 2. Comparison of percentage differences between cross-ply and angle-ply square plates with SSSS and CCCC boundary conditions (Mat.4)

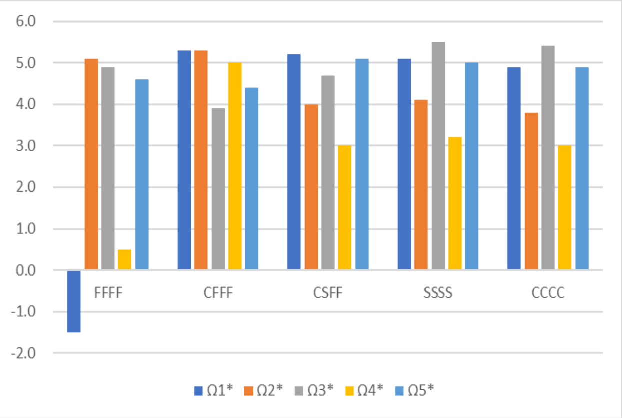

Figure 3. Comparison of percentage differences in angle-ply square plates among five sets of boundary conditions (Mat.4)

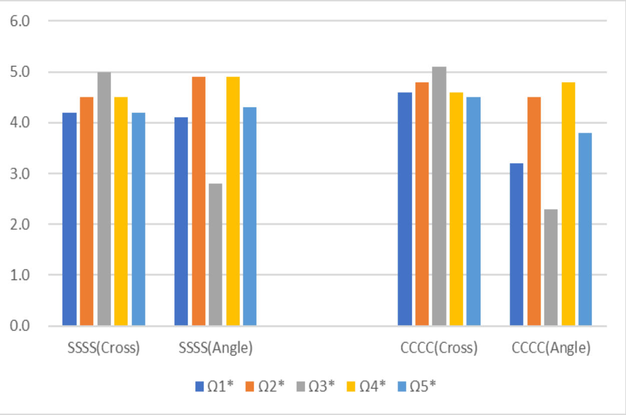

Figure 4. Comparison of percentage differences between cross-ply and angle-ply rectangular plates with SSSS and CCCC boundary conditions (Mat.4)(a/b=2)

Table 9. Frequency parameters Ω* (Eq.(15)) of symmetric 8-layer rectangular plate (*a*/*b*=2, SSSS)

	Ω_1^*	Ω_2^*	Ω_3^*	Ω_4^*	Ω_5^*
Cross-ply $[(0/90)_2]$s					
Mat. 1	95.97	159.0	296.2	350.8	383.9
(%)	-6.0	-6.6	-6.9	-5.9	-6.0
Mat. 2	99.70	167.7	310.7	359.3	398.8
(%)	-2.3	-1.5	-2.4	-3.7	-2.3
Mat. 3	97.96	163.5	306.0	357.9	391.8
(%)	-4.0	-3.9	-3.8	-4.1	-4.0
Mat. 4	106.4	177.8	334.3	389.9	425.6
(%)	4.2	4.5	5.0	4.5	4.2
Mat. 5	102.1	170.2	318.3	373.0	408.3
Angle-ply $[(30/-30)_2]$s					
Mat. 1	96.63	192.1	265.3	330.1	390.5
(%)	-5.7	-6.4	-4.6	-6.6	-5.8
Mat. 2	99.32	197.7	273.8	340.9	401.8
(%)	-3.0	-3.7	-1.5	-3.5	-3.1
Mat. 3	98.22	197.1	265.9	339.4	397.7
(%)	-4.1	-4.0	-4.3	-3.9	-4.1
Mat. 4	106.7	215.3	285.6	370.7	432.4
(%)	4.1	4.9	2.8	4.9	4.3
Mat. 5	102.4	205.2	277.9	353.3	414.6

Table 10. Frequency parameters Ω* (Eq.(15)) of symmetric 8-layer rectangular plates (*a*/*b*=2, CCCC)

	Ω_1^*	Ω_2^*	Ω_3^*	Ω_4^*	Ω_5^*
Cross-ply $[(0/90)_2]$s					
Mat. 1	209.9	279.4	427.7	546.8	586.2
(%)	-6.1	-6.5	-6.9	-6.0	-6.0
Mat. 2	215.3	290.1	445.4	558.7	604.3
(%)	-3.6	-2.9	-3.0	-3.9	-3.2
Mat. 3	214.4	287.0	441.4	558.0	598.8
(%)	-4.0	-3.9	-3.9	-4.1	-4.0
Mat. 4	233.8	313.1	482.7	608.4	651.9
(%)	4.6	4.8	5.1	4.6	4.5
Mat. 5	223.4	298.8	459.2	581.5	623.9
Angle-ply $[(30/-30)_2]$s					
Mat. 1	164.4	272.6	384.1	431.7	512.2
(%)	-4.9	-6.1	-4.2	-6.5	-5.4
Mat. 2	169.9	281.8	397.2	447.2	528.3
(%)	-1.7	-3.0	-0.9	-3.1	-2.4
Mat. 3	165.6	278.8	383.1	443.5	518.9
(%)	-4.3	-4.0	-4.4	-4.0	-4.2
Mat. 4	178.4	303.4	409.9	483.8	561.7
(%)	3.2	4.5	2.3	4.8	3.8
Mat. 5	172.9	290.4	400.8	461.7	541.4

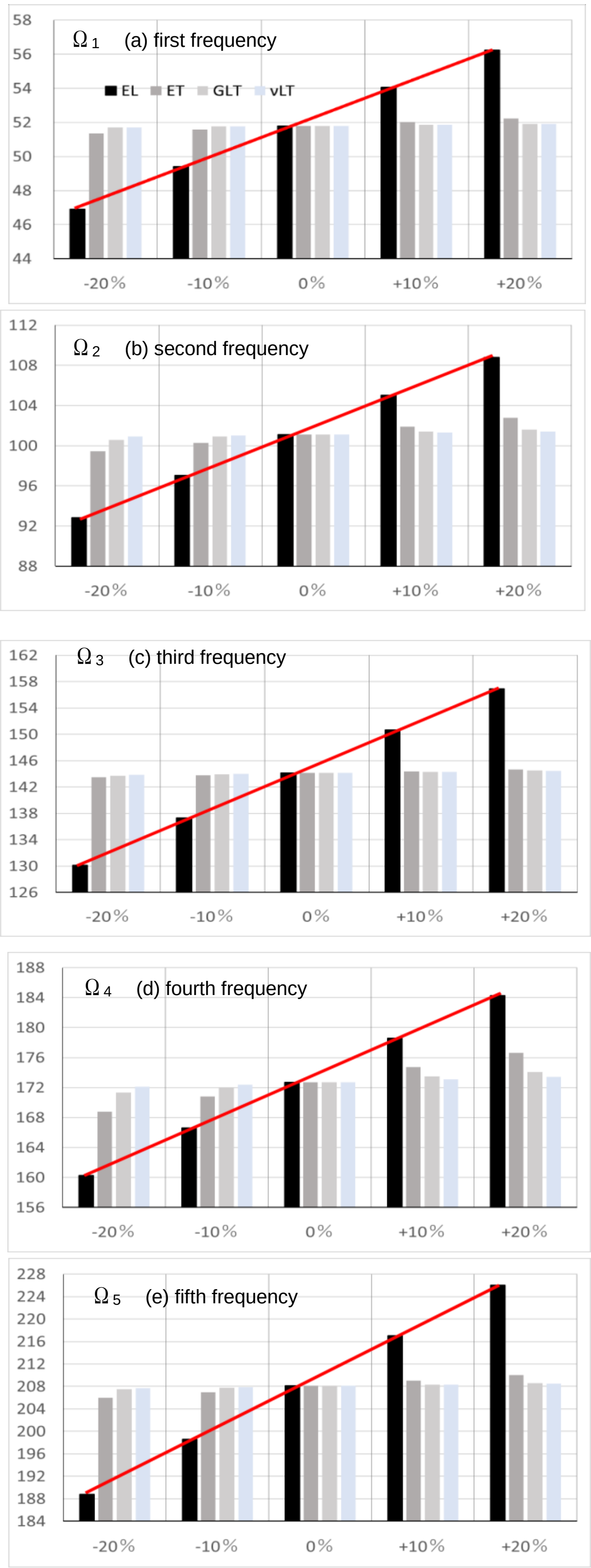

Figure 5. Variations of the lowest three frequency parameter with change (-20%～+20%) of the four elastic constants (E_L, E_T, G_{LT}, ν_{LT}) for square plate (SSSS) with $[(30/-30)_2]$s lamination

4.2. Effect of aspect ratio on frequency parameters

Numerical experiment is extended to include the frequency parameters of rectangular plate (*a/b*=2) to see the effect of aspect ratio. Table 9 present the lowest five frequency parameters of cross-ply and angle-ply rectangular plates with SSSS boundary conditions. The results in the same format is given in Table 10 for CCCC boundary condition. The data for Mat.4 is plotted in Fig.4 with the same format in Fig.2. When one compares results in Fig.4 with those in Fig.2, there is no difference globally and one can conclude that the differences do not exist for different aspect ratios.

4.3. Effect of each material constant on frequency parameters

From the results in Tables 4-8, it is obvious that Young's modulus E_L in the fiber direction is the most decisive controlling factor among the four constants to determine the frequency parameters. Therefore, numerical experiment is done in Fig.5 to calculate the lowest five frequencies Ω_1～Ω_5 for the angle-ply square plate (SSSS) [(30/-30)$_2$]s by changing independently each of the four elastic constants in the range of 80 %～120 % from the reference value of Mat.5 (i.e., E_L=150GPa, E_T=10GPa, G_{LT}=5GPa, ν_{LT}=0.3). In the figure, the values with change of E_L are denoted by black solid columns and those with other three constants E_T, G_{LT}, ν_{LT} are by lighter grey columns. As clearly seen, the frequency values increase significantly in linear fashion with change of E_L, while those values for change of the other three constants stay almost unchanged. Thus, the straight line can be used to approximate the frequency values, as indicated by red straight lines in the figure, for laminated plates with different CFRP materials under specified lamination condition of fixed aspect ratio and lamination scheme (in this case, cross-ply or angle-ply laminates).

A simple linear regression is applied by using

$$\Omega_i^* = C_1\left(E_L / 10^9\right) + C_0 \tag{17}$$

where C_1 and C_0 indicate slope (sensitivity) and constant (intercept), respectively. Those constants are listed in Table 11 for two boundary conditions (SSSS, CCCC) and aspect ratios (*a/b*=1,2) of angle-ply plates [(30/-30)$_2$]s. By using these coefficients, approximate frequency parameters are evaluated by Eq. (17) for Mat.1-Mat.4 of square plates (SSSS, CCCC), and are compared to the values from Table 4 and 8. The values of difference in percentage are also listed in the table to assess accuracy of the formula. Except for three cases (Ω_2 and Ω_4 for Mat.3, and Ω_4 for Mat.4) of 20 frequencies presented, absolute values in discrepancies are less than one percent, and the accuracy of formula is demonstrated. Physically speaking, it is verified that Young's modulus E_L is dominant explanatory variable in the frequency evaluation of laminated plates.

Table 11. Coefficients of frequency formula in Eq. (17) for square and rectangular (*a/b*=2) plates [(30/-30)$_2$]s

	Ω_1^*	Ω_2^*	Ω_3^*	Ω_4^*	Ω_5^*
SSSS (*a/b*=1)					
C_1	0.155	0.266	0.446	0.401	0.616
C_0	28.38	61.06	76.86	112.31	115.27
CCCC (*a/b*=1)					
C_1	0.257	0.363	0.641	0.506	0.797
C_0	49.80	88.94	112.50	149.50	153.68
SSSS (*a/b*=2)					
C_1	0.272	0.603	0.595	1.040	1.122
C_0	61.53	114.45	188.35	196.46	245.70
CCCC (*a/b*=2)					
C_1	0.393	0.803	0.782	1.330	1.351
C_0	113.70	169.50	283.10	261.25	337.98

Table 12. Comparison of frequency parameters between the formula estimation (17) and fully computed values for square and rectangular (*a/b*=2) plates [(30/-30)$_2$]s

	Ω_1^*	Ω_2^*	Ω_3^*	Ω_4^*	Ω_5^*
SSSS (*a/b*=1)					
Mat.1	48.37	95.45	133.8	164.4	194.4
Eq.(14)	48.22	95.11	133.9	163.6	194.1
(%)	-0.3	-0.4	0.1	-0.5	-0.2
Mat.2	49.89	98.11	139.2	168.8	200.8
Eq.(14)	49.77	97.77	138.4	167.6	200.3
(%)	-0.2	-0.3	-0.6	-0.7	-0.2
Mat.3	49.77	96.96	138.6	165.4	200.0
Eq.(14)	49.93	98.03	138.9	168.0	200.9
(%)	0.3	1.1	0.2	1.6	0.5
Mat.4	54.45	105.2	152.0	178.3	218.5
Eq.(14)	54.57	106.0	152.2	180.1	219.4
(%)	0.2	0.8	0.1	1.0	0.4
CCCC (*a/b*=1)					
Mat.1	82.66	135.8	194.2	214.9	255.8
Eq.(14)	82.70	135.40	194.5	214.3	255.7
(%)	0.0	-0.3	0.2	-0.3	0.0
Mat.2	85.84	140.2	202.4	221.4	265.2
Eq.(14)	85.27	139.0	201.0	219.3	263.7
(%)	-0.7	-0.9	-0.7	-0.9	-0.6
Mat.3	85.04	137.7	201.1	215.9	263.1
Eq.(14)	85.52	139.4	201.6	219.8	264.5
(%)	0.6	1.2	0.2	1.8	0.5
Mat.4	92.85	149.2	220.4	232.4	287.3
Eq.(14)	93.23	150.3	220.8	235.0	288.4
(%)	0.4	0.7	0.2	1.1	0.4

5. Conclusions

It has been demonstrated that, for symmetrically laminated CFRP rectangular plates having slightly different elastic constants, there is a underlying relation among calculated values of frequency parameters when the frequency parameters are properly defined. The Ritz method was used as an analytical tool in numerical experiments for solving free vibration of the plates. In numerical results, examples were given for cross-ply and angle-ply square plates. The frequency parameters for four different sets of materials were calculated and compared to those of new hypothetical material with the averaged and discretized constants. It turned out that, despite the difference of CFRP materials, the frequency parameters show unified behaviors with the change of Young's modulus in the fiber direction. It was demonstrated that it is feasible to derive approximate formulas to simultaneously predict the frequency parameters for laminated plates composed of different CFRP materials. The coefficients in the linear formula were tabulated and used to estimate the frequency parameters for limited cases, and it is hoped that this formula will be extended and used in many design situations.

References

[1] Leissa, A.W. 1993 *Vibration of Plates*, Acoustical Society of America; previously, 1969 NASA SP-160, U.S. Government Printing Office, Washington D.C.

[2] Leissa, A.W. 1973 The free vibration of rectangular plates, J. Sound Vib., vol.31, pp.257-293.

[3] Vinson, J.R., Sierakowski R.L. 1986 *The Behavior of Structures Composed of Composite Materials.* Martinus Nijhoff Publishers, Dardrecht, The Netherlands.

[4] Jones, R.M. 1999 *Mechanics of Composite Materials*, 2nd ed. Taylor & Francis.

[5] Reddy J.N. 1997 *Mechanics of Laminated Composite Plates: Theory and Analysis*, CRC Press, Boca Raton, FL.

[6] Sharma A.K., Mittal N.D. 2010 Review on stress and vibration analysis of composite plates, J. of Appl. Sci., vol.10(23), pp.3156-3166.

[7] Bert C.W., Mayberry B.L. 1969 Free vibration of unsymmetrically laminated anisotropic plate with clamped edges, J. Compos. Mater. vol.3 pp.282-293.

[8] Reddy, J.N. 1984 A simple higher-order theory for laminated composite plates, Trans. ASME J. Appl. Mech., vol.51, pp.745-752.

[9] Narita, Y. 2000 Combinations for the free-vibration behaviors of anisotropic rectangular plates under general edge conditions, Trans. ASME J. Appl. Mech., vol.67, pp.568-573.

[10] Narita, Y. 2006 Maximum frequency design of laminated plates with mixed boundary conditions, Int. J. Solids Struct., vol.43, pp.4342-4356.

[11] Narita, Y. 2006 Maximum frequency design of laminated plates with mixed boundary conditions, Int. J. Solids Struct., vol.43, pp.4342-4356.

[12] Pandit, M.K., Haldar, S., Mukhopadhyay, M. 2007 Free vibration analysis of laminated composite rectangular plate using finite element method, J. of Reinforced Plastic Compo., vol.26, p.69-80.

[13] Stanford B.K., Jutte C.V. 2017 Comparison of curvilinear stiffeners and tow steered composites for aeroelastic tailoring of aircraft wings, Comput Struct, vol.183, pp.48-60.

[14] Ogasawara T., Ishikawa T. 2010 Proposal of a convenient compressive test method for carbon fiber reinforced plastics composites (in Japanese), J. Japan Soc. Comp. Mat., vol.36, pp.33-40.

[15] Panesar A.S., Weaver P.M. 2012 Optimisation of blended bistable laminates for a morphing flap, Compos Struct, vol.94, pp.3092-3105.

[16] Narita, Y., et a. 1992 Analytical method for vibration of angle-ply cylindrical shells having arbitrary edges, AIAA J., vol.30, pp.790–796.

[17] Narita, Y. 1995 Series and Ritz-type buckling analysis, in: G.J. Turvey, I.H. Marshall (Eds.), Buckling and Postbuckling of Composite Plates, Chapman & Hall, London, pp. 33–57 (Chapter 2).

EPI International Journal of Engineering
Volume 2, Number 1, February 2019, pp. 28-33
DOI: 10.25042/epi-ije.022019.06

*p*ISSN 2615-5109
*e*ISSN 2621-0541

Heave and Pitch Motion Performances of a Ship Towing System Incorporated with Symmetrical Bridle Towline Model

Ahmad Fitriadhy[a,*], Nur Adlina Aldin[b], Nurul Aqilah Mansor[c], Nur Aqilah Hanis[d]

[a]Programme of Maritime Technology, School of Ocean Engineering, University Malaysia Terengganu. Email: naoe.afit@gmail.com
[b]Programme of Maritime Technology, School of Ocean Engineering, University Malaysia Terengganu. Email: nuradlina1910@gmail.com
[c]Programme of Maritime Technology, School of Ocean Engineering, University Malaysia Terengganu. Email: n.aqilahmansor@gmail.com
dProgramme of Maritime Technology, School of Ocean Engineering, University Malaysia Terengganu. Email: aqilahzaniza@gmail.com

---

Abstract

An investigation on vertical motion characteristics of a ship towing system incorporated with symmetrical bridle towline configuration set a real challenge for the naval architect engineer. This paper presents a Computational Fluid Dynamic (CFD) approach to analyse heave and pitch motion performances in waves. Several towing parameters such as various towline length and towing's velocity have been taken into account. Here, 1B (barge) is employed in the simulation; and designated as a towed ship. The results revealed that the subsequent increase of the towline lengths has been basically proportional with the increase of her heave motion; while inversely decrease in pitch motions. In addition, the effect of the extending towline length l' = 1.0 to 3.0 resulted in insignificant effect to the towline tension. However, the increase of the towing's velocity from 0.509 m/s to 0.728 m/s has led to significantly increase her heave motion and the towline tension by 40.46% and 24%, respectively; meanwhile, the pitch motion barge has sufficiently decreased by 35.94%. This simulation has been beneficial for the towing operator to ensure a higher level of the safety navigation of ship towing system.

Keywords: Bridle towline model; CFD; heave motion; pitch motion; towline tension

---

1. Introduction

Development of the global economics and drastic growth of shipping industries leads to heavy congestion due to abundant of ships in the waterways which threaten the safety of towed barge. Towing system is less course-keeping stable than the conventional single ships and it is dangerous when it runs in harsh environmental conditions. Therefore, an extensive investigation on towline tension is then required to observe the behaviour of towed barge using symmetrical bridle towline during towing operations.

Several researchers have attempted various approaches to investigate the performance of the ship towing system in calm water. Inoue et al [1], Lee [2], Kijima et al [3], Fitriadhy et al. [4] and Fitriadhy et al. [5] analysed the towed barge by numerical approaches. Lee [2] studied the tension of the towline using different material of towline, polyester and nylon while the effect of the towline length, tow point location on barge and tug proposed by Fitriadhy et al [4]. Experimental approach was conducted by Im et al [6] to investigate the effect of different towline configuration and employing active thruster to the barge. Im et al extended their research experiment using Computational Fluid Dynamics (CFD) for further validation.

Since numerical calculation and experiment have limitation in accurately reflecting the effect of interference and viscosity that affect the motion of vessel, CFD is employed to analyze the effects of nonlinearities, such as generation of 3D vortices [6]; computed the sway force and yaw moment during drift and steady yaw motion and analysed the flow field around the barge. Nonaka et al. [7] determine the fluid motion around the hull of a vessel and the hydrodynamics force exerted on a drifting vessel as well as presence of strong nonlinearities and complex flowfield [7]. CFD approach had been widely applied in maritime technology field such as estimating the vessel performance [8-10], resistance [11-15], and ship motions characteristics [16-21].

The assessment of ship motion characteristics is carried out in calm water conditions, but evaluation of ship in waves is more realistic since sea-going ships sails through waves. The effects of waves alter the water particle kinematics around the ship hydrodynamic forces acting on it, resulting in change of ship motions as stated by Rameesha and Krishnankutty in 2018. Hence, for the safety of towed barge during towing operations, it is important to include wave effects on the motion of barge to assess the motion of barge during ocean going towing. Waves from different headings particularly induce motion responses of the vessels and this may limit the

---

*Corresponding author. Tel.: +6-09-668-3350
Programme of Maritime Technology, School of Ocean Engineering, Universiti Malaysia Terengganu, 21030 Kuala Terengganu, Terengganu, Malaysia.

operability of the towing process [22]. Nam [22], Das [23] and Lee [24] studied the barge motion characteristics in waves using CFD approach. Their studies show that CFD can interpret turbulent free surface considering the viscosity and prove that the pressure changes around the barge affect the motion characteristics of the barge.

Thus, this paper presents a CFD simulation to predict heave and pitch motion performance of a ship towing system in waves incorporated with the symmetrical bridle towline configuration. Several effects such as towline length and towing's velocity have been mainly considered in the simulation. 1B (barge) is the symbol of the towed ship that employed in the simulation. Here, a commercial CFD so called Flow3D v11.2 is utilized by applying unsteady Reynolds-Averaged Navier Stokes Equation (RANSE). Flow3D incorporates different technique (TruVOF) to capture the free surface and computes flow variable only within one fluid. The heave and pitch motion performances are then clearly discussed.

2. Governing Equation

The CFD flow solver on FLOW-3D version 11.2 is based on the incompressible unsteady RANS equations in which the solver applies the Volume of Fluid (VOF) to track the free surface elevation. The interface between fluid and solid boundaries is simulated with the fractional area volume obstacle representation favor method. This method computes open area and volume in each cell to define the area that is occupied by obstacle.

2.1. Continuity and momentum equation

The continuity and momentum equations for a moving object and the relative transport equation for VOF function are

$$\frac{V_f}{\rho}\frac{\partial\rho}{\partial t}+\frac{1}{\rho}\nabla.\left(\rho\vec{u}A_f\right)=-\frac{\partial V_f}{\partial t} \tag{1}$$

$$\frac{\partial\vec{u}}{\partial t}+\frac{1}{V_f}\left(\vec{u}A_f.\nabla\vec{u}\right)=-\frac{1}{\rho}\left[\nabla_\rho+\nabla.\left(\tau A_f\right)\right]+\vec{G} \tag{2}$$

$$\frac{\partial F}{\partial t}+\frac{1}{V_f}\nabla.\left(F\vec{u}A_f\right)=-\frac{F}{V_f}\frac{\partial V_f}{\partial t} \tag{3}$$

where ρ is the density of the fluid, $\vec{u}$ is the fluid velocity, V_f is the volume fraction,A_f is the area fraction, p is the pressure, τ is the viscous stress tensor, G denotes gravity and F is the fluid fraction.

In the case of coupled GMO's motion, Eqs.(1) and (2) are solved at each time step and the location of all moving objects is recorded and the area and volume fractions updated using the FAVOR technique. Equations (3) are solved with the source term $\left(-\frac{\partial V_f}{\partial t}\right)$ on the right-hand side which is computed as

$$-\frac{\partial V_f}{\partial t}=\vec{U}_{obj}\vec{n}S_{obj}/\,V_{cell} \tag{4}$$

where S_{obj} is the surface area, $\vec{n}$surface normal vector, $\vec{U}_{obj}$ is the velocity of the moving object at a mesh cell and V_{cell} is the total volume of the cell [25].

2.2. Turbulence model

The RNG turbulence model was used for the simulation of the exchange flow between open water and floating object since it accounts for low Reynolds number effects [26-28]. Applying the double averaging strategy to the transport equations for TKE and its dissipation rate produces the turbulence model for the flow. The resulting equations are:

$$\frac{\delta k}{\delta t}+U_j\frac{\delta k}{\delta x_j}=\frac{\delta}{\delta x_j}\left[\left(v+\frac{v_t}{\sigma_k}\right)\frac{\delta k}{\delta x_j}\right]+P_k+B_k+W_k \tag{5}$$

$$\frac{\delta\varepsilon}{\delta t}+U_j\frac{\delta\varepsilon}{\delta x_j}=\frac{\delta}{\delta x_j}\left[\left(v+\frac{v_t}{\sigma_\varepsilon}\right)\frac{\delta\varepsilon}{\delta x_j}\right]+C_{1\varepsilon}\frac{\varepsilon}{k}(P_k+B_k)\big(1+C_{3\varepsilon}R_f\big)+W_\varepsilon-C_{2\varepsilon}^{*}\frac{\varepsilon^2}{k} \tag{6}$$

$$P_k=v_tS^2=v_t\left(\frac{\delta U_i}{\delta x_j}+\frac{\delta U_j}{\delta x_i}\right)\frac{\delta U_i}{\delta x_j} \tag{7}$$

$$B_k=\beta g_i\frac{v_t}{\sigma_s}\frac{\delta s}{\delta x_i} \tag{8}$$

where P_k is the shear production term of TKE, $S=\sqrt{2S_{ij}S_{ji}}$ is the modulus of the mean rate of strain tensor and $S_{ij}=\frac{1}{2}\left(\frac{\delta U_i}{\delta x_j}+\frac{\delta U_j}{\delta x_i}\right)$, B_k is the buoyant production term of TKE, W_k is the wake production tern of TKE, W_ε is the wake production term in ε, σ_k and σ_ε are the turbulent Prandtl numbers for k and ε, and $C_{i\varepsilon}$, $C_{3\varepsilon}$ and $C_{2\varepsilon}^{*}$ are model coefficients.

2.3. Body motion equation

The body motion was analysed in a space-fixed Cartesian coordinate system, the global coordinate system. The governing equation of the six degree of freedom (DOF) of a rigid body motion can be expressed in this coordinate system as

$$\frac{d}{dt}(m\vec{v}_c)=\vec{f} \tag{9}$$

$$\frac{d}{dt}(M_c.\vec{w}_c)=\vec{m}_c \tag{10}$$

The index C denotes the centre of mass of the body, m denotes the mass of the body, $\vec{v}_c$ the velocity vector, M_c is the tensor of the moments of inertia, $\vec{\omega}_c$ is the angular velocity vector, $\vec{f}$ denotes the resulting force vector and $\vec{m}_c$ denotes the resultant moment vector acting on the body [12]. The resultant force $\vec{f}$ has three components; surface force, field forces and external forces:

$$\vec{f}=\int_S(T-\rho I).\vec{n}dS+\int_V\rho_b\vec{b}dV+\vec{f}E \tag{11}$$

Here, $\rho_b$is the density of the body. The only field force considered is the gravity, so the volume integral of above equation (right hand side) reduces to $m\vec{g}$, where g is the gravity acceleration vector. The vector $f\vec{E}$ denotes the external forces acting in the body [29].

2.4. Waves

The model is based on Airy's linear wave theory. The linear wave is assumed to come from flat bottom reservoir into the computational domain [30]. The linear wave theory is based on the following assumptions; fluid is incompressible, inviscid, irrational, two-dimensional flow and the wave amplitude (A) is small compared to the mean water depth (h) and wavelength (λ). With the assumption, the problem can be reduced to a linear potential flow problem. The free surface elevation $\eta(x,t)$ measured in the vertical direction from mean water surface, the velocity potential $\varphi(x,z,t)$ and velocity components in x and z directions $u(x,z,t)$ and $w(x,z,t)$ are obtained as

$$\eta = A\ \cos(kx - \omega t + \phi) \tag{12}$$

$$\varphi(x,z,t) = xU + \frac{A\omega \cosh[k(z+h)]\sin(kx-\omega t+\phi)}{k\sinh(kh)} \tag{13}$$

$$u(x,z,t) = U + \frac{A\omega \cosh[k(z+h)]\cos(kx-\omega t+\phi)}{\sinh(kh)} \tag{14}$$

$$w(x,z,t) = \frac{A\omega \sinh[k(z+h)]\sin(kx-\omega t+\phi)}{\sinh(kh)} \tag{15}$$

where ϕ is the phase shift angle, t is time.

The dispersion equation in terms of wave speed $c = \omega/k$ is given by

$$(c-U)^2 = \frac{g}{k}\tanh(kh) \tag{16}$$

3. Simulation Conditions

The CFD flow solver on FLOW-3D version 11.2 is based on the incompressible unsteady RANS equations in which the solver applies the Volume of Fluid (VOF) to track the free surface elevation. The interface between fluid and solid boundaries is simulated with the fractional area volume obstacle representation favor method. This method computes open area and volume in each cell to define the area that is occupied by obstacle.

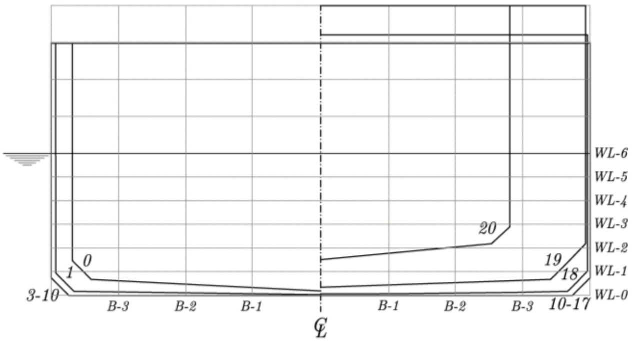

Figure 1. Body plan of barge

Table 1. Principal dimensions of barge (1B)

Description	1B	
	Full-scale	Model
Length, $L(m)$	60.96	1.219
Breadth, $B(m)$	10.67	0.213
Draft, $d(m)$	2.74	0.0548
Volume, $V(m^3)$	1646.2	0.01317
L/B	5.71	5.71
Block coefficient, C_b	0.92	0.92
k_{yy2}/L	0.3266	0.3266
$X_{G\ abaft\ the\ midship}, (m)$	-1.04	-0.0208

Table 2. Various towline length, l'

Towing velocity, V_s (m/s)	Towline length, l'	Wavelength, λ/lpp
0.509	1.0	1.0
	2.0	
	3.0	

3.1. Principal data of ships

The principal dimensions barge (1B) are presented in Table 1. Her respective body plan is shown in Fig.1.

3.2. Parametric studies

Table 2 presents various towline length employed in the simulations. Towing's velocity, V_s is kept constant by 0.509 m/s. Various towing's velocity, V_s used in the simulation are shown in Table 3 with fixed towline length, l'=1.0 L. Towing point location is set to l_b'=0.5 for both cases.

Table 3. Various towing's velocity, V_s.

Towing velocity, V_s (m/s)	Towline length, l'	Wavelength, λ/lpp
0.509	1.0	1.0
0.582		
0.655		
0.728		

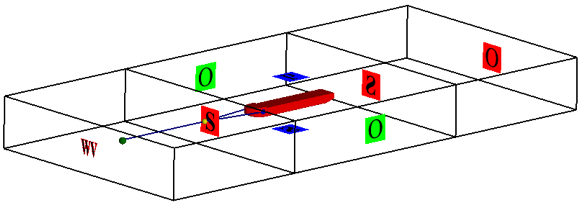

Figure 2. Boundary conditions

Table 4. Various towing's velocity, V_s.

Boundary	Mesh block 1	Mesh block 2
X_{min}	Wave	Symmetry
X_{max}	Outflow	Symmetry
Y_{min}	Outflow	Symmetry
Y_{max}	Outflow	Symmetry
Z_{min}	Symmetry	Symmetry
Z_{max}	Specified pressure	Symmetry

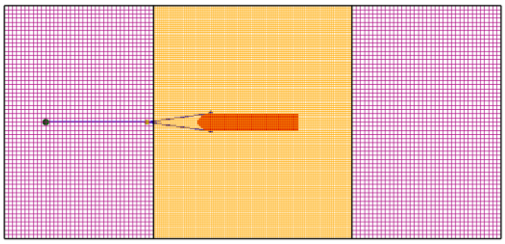

Figure 3. Meshing generation

3.3. Computational domain and boundary conditions

The computational domain uses a structured mesh that is defined in a Cartesian. Referring to Fig.2, the boundary condition is mark in the mesh block 1 and mesh block 2. The boundary condition at X-max boundary is wave, linear wave so that there is wave generated into the simulation. In order to save computational time, wave is assigned to water at X-max boundary. As for X-min, Y-max and Y-min boundary, outflow is assigned to prevent reflection while Z-min is symmetry and Z-max is specified pressure. The boundary conditions for this simulation are shown in Table 4.

The meshing generation is created in Flow3D v11.2 as shown in Fig.3. An extra refinement of the mesh called nested block is added to increase meshing resolution in this study. The barge is coupled through a towline. A virtual tug, a sphere model is assigned prescribed motion while barge as towed ship was set as coupled motion in X-translational, Z-translational and Y-rotational motions (surge, heave and pitch motions). The barge was in 5° inclination arrangement initially. The towline is set as polyester mooring line with spring coefficient of 7.347 N/m^2.

Based on the applications of Flow3D v11.2, the average duration of every simulation was about 70-80 hours (4 parallel computations) on a HP Z820 workstation PC with processor Intel (R) Xeon (R) CPU ES-2690 v2 @ 3.00 GHz (2 processors) associated with the installed memory (RAM) of 32.0 GB and 64-bit Operating System.

4. Results and Discussions

Referring to Figs.4-7, the CFD simulation has been successfully carried out to predict the course stability of the towing system in various towline lengths and towing's velocity. The simulations results of heave and pitch motion performances of the barge associated with the towline tension are presented.

4.1. Effect of various towline lengths

The characteristics of heave and pitch motion characteristics at various towline lengths have been displayed in Fig.4. Here, the extending towline length from l' = 1.0 to 3.0 resulted in the increase of the heave motion of the barge by 17.7%; meanwhile her pitch motion decreased 7.4%. This could be explained the CFD simulation that the free surface elevation around the barge subsequently increased, which indicated by high pressure region (red color) as the towline extended up l' = 3.0. However, this extending towline was insignificant to the increase of the maximum towline tension about 8.5% as the increase the towline from l' = 1.0 to 2.0.

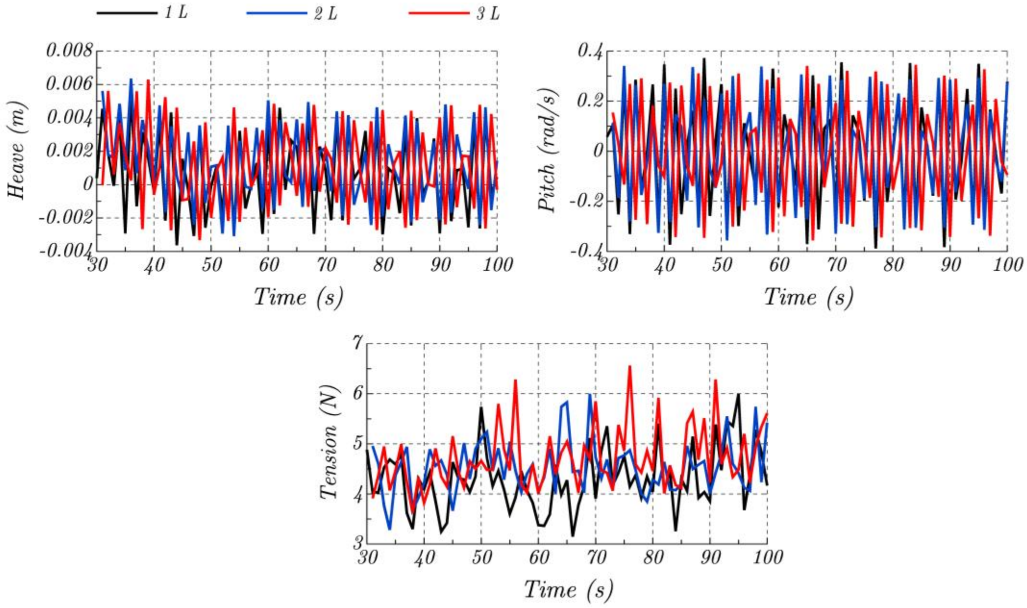

Figure 4. Characteristics of heave and pitch motion of 1B associated with the towline tension at various towing's velocity

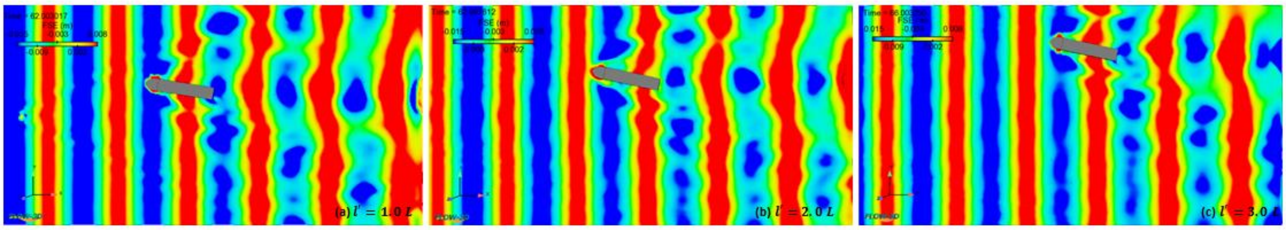

Figure 5. Free surface elevation, V_s= 0.509 m/s, l'=1.0 (a), 2.0 (b) and 3.0 (c)

4.2. Efect of various towing's velocity

The characteristics of heave and pitch motion performances with the symmetrical bridle towline model associated with dynamic towline tension in various towing's velocity have been displayed in Figure 6. The subsequent increase of the towing's velocity from V_s =0.509 to 0.582 m/s and 0.655 m/s to 0.728 m/s resulted in the increment of heave motion by 24% and 29.9%, respectively. However, the pitch motion of the barge decreased by 35.9% as towing's velocity increased from V_s = 0.509 m/s to 0.728 m/s; meanwhile the towline tension increased by 24%. This can be explained by the CFD simulation (see Figure 7) that the heave motions at the maximum towing's velocity of 0.728 m/s has been the highest ones due to the higher pressure phenomenon indicated by the subsequent increase of the red color at the aft region as compared to the towing velocity of 0.582 m/s and 0.655 m/s. On the other hand, the effects of resonance and exciting forces due to the incoming waves have also contributed to the increase of the larger vertical motion responses of the barge (the towed ship) [20].

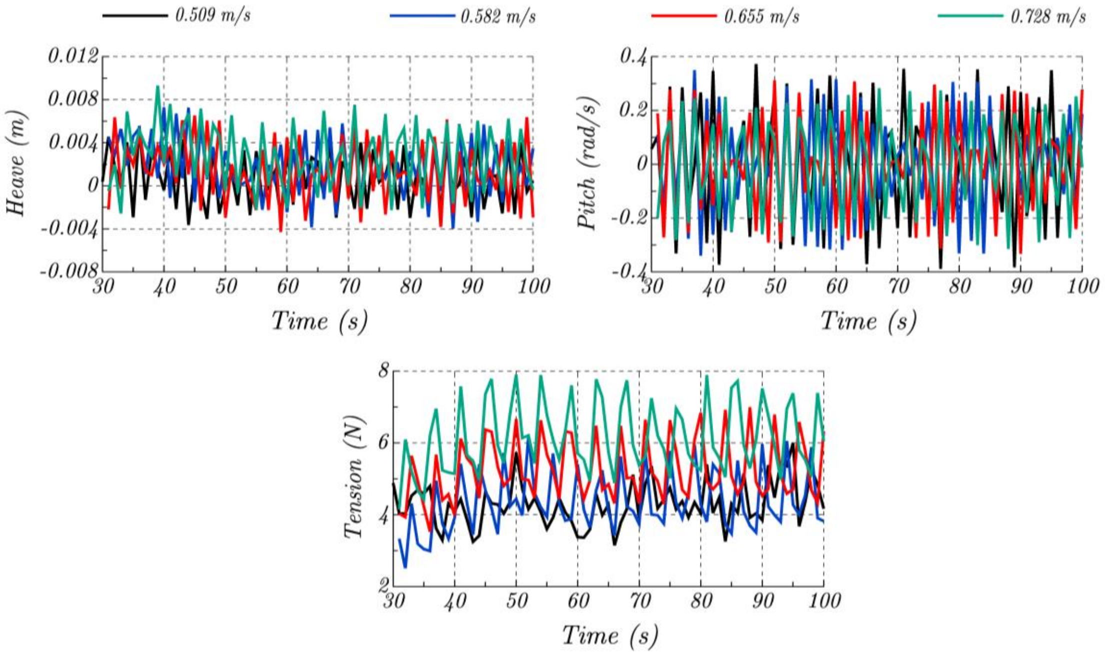

Figure 6. Characteristics of heave and pitch motion of 1B associated with the towline tension at various towing's velocity

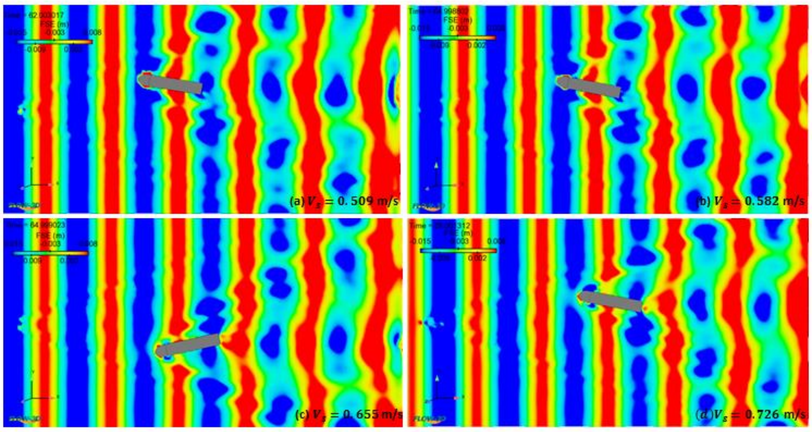

Figure 7. Free surface elevation , l'=1.0, V_s= 0.509 m/s (a), 0.582 m/s (b) 0.655 m/s (c) and 0.728 m/s (d)

5. Conclusions

The Computational Fluid Dynamics (CFD) analysis on the heave and pitch motion characteristics of barge incorporated with the symmetrical towline model has been successfully performed using Flow3D v11.2 software. The effect of various towline length and towing's velocity have taken into the simulation. The simulations results can be drawn as follow:

- Basically, the extending towline length from l' = 1.0 to 3.0 results in the increase of the heave motion of the barge by 17.7%; while her pitch motion decreases by 7.4%. It should be merely noted here that the towline tension exhibits insignificant effect when the towline length increases.
- The effect of the towing velocity has led to increase the heave motion of the barge by 40.46%; and inversely decreases her pitch motion by 35.94% as the towing velocity increases from 0.582 m/s to 0.728 m/s; meanwhile, the towline tension increases by 24%.

Refrences

[1] Inoue, S., Hirano, M. and Mukai, K. (1979). *The Nonlinear Terms of Lateral Force and Moment Acting on Ship Hull in the Case of Manoeuvering*. Trans. West-Japan Soc. Nav. Archit(58).

[2] Lee, M.-L. (1989). *Dynamic Stability of Nonlinear Barge-towing System*. Applied mathematical modelling, 13(12), 693-701.

[3] Kijima, K., Katsuno, T., Nakiri, Y. and Furukawa, Y. (1990). *On the manoeuvring performance of a ship with theparameter of loading condition*. Journal of the Society of Naval Architects of Japan, 1990(168), 141-148.

[4] Fitriadhy, A. and Yasukawa, H. (2011). *Course Stability of a Ship Towing System*. Ship Technology Research, 58(1), 4-23.

[5] Fitriadhy, A., Yasukawa, H., Wan Nik, W.B. and Abu Bakar, A. (2016). *Numerical Simulation of Predicting Dynamic Towline Tension on a Towed Marine Vehicle*. International Conference on Ships and Offshore Structures ICSOS 2016 31 August - 2 September 2016, Hamburg, Germany.

[6] Im, N., Lee, S. and Lee, C. (2015). *The influence of skegs on course stability of a barge with a different configuration*. Ocean Engineering, 97, 165-174.

[7] Nonaka, K., Fuwa, T. and Nimura, T. (1986). *Measurement of wake flow and hydrodynamic force distribution on a ship model with drift angle (2nd report, Tanker model)*. J. Soc. Naval Architects of West Japan, 72, 197-212.

[8] van Oers, B. and Toxopeus, S. (2006). *On the relation between flow behaviour and the lateral force distribution acting on a ship in oblique motion*. 10th International Cooperation on Marine Engineering Systems ICMES, London, UK.

[9] Miyazaki, H., Ueno, M. and Tsukada, Y. *Numerical study about effects of stern skeg on course stability*. in *The Twenty-first International Offshore and Polar Engineering Conference*. 2011. International Society of Offshore and Polar Engineers.

[10] Broglia, R., Dubbioso, G., Durante, D. and Di Mascio, A. (2013). *Simulation of turning circle by CFD: Analysis of different propeller models and their effect on manoeuvring prediction*. Applied Ocean Research, 39, 1-10.

[11] Tezdogan, T., Demirel, Y.K., Kellett, P., Khorasanchi, M., Incecik, A. and Turan, O. (2015). *Full-scale Unsteady RANS CFD Simulations of Ship Behaviour and Performance in Head Seas due to Slow Steaming*. Ocean Engineering, 97, 186-206.

[12] Maki, K.J., Broglia, R., Doctors, L.J. and Di Mascio, A. (2013). *Numerical investigation of the components of calm-water resistance of a surface-effect ship*. Ocean Engineering, 72, 375-385.

[13] Fitriadhy, A., Jamaluddin, A., Norsani, W.M., Wan Nik, W.B., Bakar, A., Azlan, M. and W. M. Noor, C. (2014). *Frictional Resistance's Prediction of a Trimaran Ship in Calm Water using Computational Fluid Dynamic (CFD) Approach*.

[14] Fitriadhy, A., Lim, P.S. and Jamaluddin, A., *CFD Investigation on Total Resistance Coefficient of Symmetrical and Staggered Catamaran Configurations through Quantifying Existence of an Interference Factor*, in *The First International Conference on Ships and Offshore Structures ICSOS 2016*. 2016: Hamburg, Germany. p. 1-20.

[15] Fitriadhy, A., Azmi, S., Mansor, N.A. and Aldin, N.A. (2017). *Computational fluid dynamics investigation on total resistance coefficient of a high-speed" deep-V" catamaran in shallow water*. International Journal of Automotive and Mechanical Engineering, 14, 4369-4382.

[16] Tezdogan, T., Incecik, A. and Turan, O. (2016). *A Numerical Investigation of the Squat and Resistance of Ships Advancing through a Canal using CFD*. Journal of marine science and technology, 21(1), 86-101.

[17] Sadat-Hosseini, H., Kim, D.-H., Carrica, P.M., Rhee, S.H. and Stern, F. (2016). *URANS simulations for a flooded ship in calm water and regular beam waves*. Ocean Engineering, 120, 318-330.

[18] Cercos-Pita, J.L., Bulian, G., Pérez-Rojas, L. and Francescutto, A. (2016). *Coupled simulation of nonlinear ship motions and a free surface tank*. Ocean Engineering, 120, 281-288.

[19] Zhang, G., Zhang, X. and Pang, H. (2015). *Multi-innovation auto-constructed least squares identification for 4 DOF ship manoeuvring modelling with full-scale trial data*. ISA transactions, 58, 186-195.

[20] Fitriadhy, A. and Adam, N.A. (2017). *Heave and pitch motions performance of a monotricat ship in head-seas*. International Journal of Automotive and Mechanical Engineering, 14, 4243-4258.

[21] Fitriadhy, A., Razali, N. and AqilahMansor, N. (2017). *Seakeeping performance of a rounded hull catamaran in waves using CFD approach*. Journal of Mechanical Engineering and Sciences, 11(2), 2601-2614.

[22] Nam, B.W., Kim, Y. and Hong, S.Y. (2015). *Hydrodynamic interaction between two barges during berthing operation in regular waves*. Ocean Engineering, 106, 317-328.

[23] Das, S., Das, S.K. and Kariya, J. (2012). *Simulation of return flow in restricted navigation channel for barge-tow movements*. Open Ocean Engineering Journal, 5, 34-46.

[24] Lee, S.-M., Jeong, U.-C. and Kim, H.-S. (2010). *Study on the Flow Characteristics around a Barge in Still Water*. Journal of Navigation and Port Research, 34(6), 417-422.

[25] *FLOW-3D 10.1.1 User Manual*. (2013). Flow Science Inc.

[26] Yakhot, V. and Orszag, S.A. (1986). *Renormalization group analysis of turbulence. I. Basic theory*. Journal of scientific computing, 1(1), 3-51.

[27] Yakhot, A., Rakib, S. and Flannery, W. (1994). *Low-Reynolds number approximation for turbulent eddy viscosity*. Journal of scientific computing, 9(3), 283-292.

[28] Koutsourakis, N., Bartzis, J.G. and Markatos, N.C. (2012). *Evaluation of Reynolds stress, k-ε and RNG k-ε turbulence models in street canyon flows using various experimental datasets*. Environmental fluid mechanics, 1-25.

[29] Yan, S. and Huang, G. (1996). *Dynamic Performance of Towing System-Simulation and Model Experiment*. Proceedings, OCEAN, 96.

[30] *Flow3D 10.1.1 User Manual*. (2013). Flow Science Inc.

EPI International Journal of Engineering
Volume 2, Number 1, February 2019, pp. 34-40
DOI: 10.25042/epi-ije.022019.07

*p*ISSN 2615-5109
*e*ISSN 2621-0541

Heave and Pitch Motions of a Towed Ship in Waves Incorporated with an Asymmetrical Bridle Towline Model

Ahmad Fitriadhy[a]*, Nurul Aqilah Mansor[b], Nur Adlina Aldin[c]

[a]Programme of Maritime Technology, School of Ocean Engineering, University Malaysia Terengganu, Malaysia. Email: naoe.afit@mail.com
[b]Programme of Maritime Technology, School of Ocean Engineering, University Malaysia Terengganu, Malaysia. Email: n.aqilahmansor2@gmail.com
[c]Programme of Maritime Technology, School of Ocean Engineering, University Malaysia Terengganu, Malaysia. Email: nuradlina1910@gmail.com

---

Abstract

Investigation of a ship towing system performance in waves incorporated with an asymmetrical towline configuration is necessarily to be studied to ensure a towing safety of navigation. To achieve the objective, this paper presents the ship towing motion performance in waves using Computational Fluid Dynamic (CFD) approach. Here, the heave and pitch motions of the towed ship so-called barge has been analysed, where several effects of the towing angle and towing speeds have been taken into account. In the calm water condition, the results revealed that the increase of tow angle was proportional with the sufficient reduction of the sway amplitude motion and inversely proportional to her yaw motion. The increase of the asymmetrical tow angle, however, has led to increase her sway motion amplitude in wave condition and conversely reduced the tow speed increased. In addition to the pitch motion characteristic, it subsequently increased by 12.1% as the tow angle raised from 25° to 35°; meanwhile the pitch motion of barge has by 10.2% as the tow speed increased from 0.655 m/s to 0.728 m/s. This CFD simulation is very useful as the preliminary prediction on the heave and pitch motion characteristics ensure a safety navigation of a towed ship in waves

Keywords: CFD; heave; pitch; towed ship; waves

---

1. Introduction

Ensuring a safety ship navigation is very crucial to avoid any negative impact during towing of barge such as collision with other ship or onshore structure. The towing instability in term of large heave and pitch motion may occur when the towing of ship exposed to various sea conditions such as wave and wind. Therefore, it is necessary for the barge to keep at steady state for its safety during towing [1] since it do not equipped with active surface control to keep it stable [2].

Several researchers had investigated on the ship towing system configuration of towline model. The study shows that the asymmetrical bridle towline configuration [3, 4] has better course stability compared to single [2] [5, 6] and symmetrical bridle towline model [3, 7-8]. These course stability of barge had focused on the sway and yaw motion of barge. [9, 10] had predicting the course stability of barge by considering the hydrodynamic forces acting on it. However, the motion characteristic of barge is also important to ensure its safety navigation in waves [11]. The external factor such as waves had significant effect on the course stability of towing system, thus can affect the crew safety [12] and harm goods on board. Few researchers had researched on seakeeping of ship in waves such as [12-15] while [16] had focused more on ship towing in various wave conditions.

Few research methods had been used to investigate the heaving and pitching motion of ship in waves. Those includes numerical approach by [16, 17] who studied the seakeeping of ship in waves while [18, 19] use the experimental approach. [20] had investigating the heave and pitch motion of structure using experimental approach before simulating the seakeeping analysis by using Computational Fluid Dynamics (CFD). CFD is a reliable and practical tool to solve maritime problem such as ship towing, seakeeping and analysing the ship resistance. There are researchers such as those in [8, 13, 21, 22], [1, 3, 23, 24] that have been using the CFD since it can capture the hydrodynamic force and non-linear phenomenon during the simulation [1, 9].

This paper proposes an analysis on heave and pitch motion of a towed ship in wave using an asymmetrical bridle towline model by using CFD. The CFD software give more advantages compared to numerical and analytical method as it can capture the non-linear phenomenon during the computation. Besides, it also reduces the computation time and provides more accurate results. Tow angle and tow speed of the barge are taken into account during the simulation to investigate the heave and pitch motion of barge using asymmetrical bridle towline configuration.

---

*Corresponding author. Tel.: +6-09-668-3350
Programme of Maritime Technology, School of Ocean Engineering, Universiti Malaysia Terengganu, 21030 Kuala Terengganu, Terengganu, Malaysia.

2. Governing Equation

FAVOR technique has been applied in Flow3D simulation. In this technique, the computational domain can have multiple moving object which must be in term of solid with no porosity. The tug and barge are both moving object which allow it to be in the same computational domain. Besides, the FAVOR technique treats the complex geometries very efficiently.

A body system (x, y, z) has been set up for each moving object where the coordinate axes parallel with the space system at time=0. The origin of the six ° of freedom (6DOF) objects have been set up at the object mass center, G. the coordinate transformation between space system (x,y,z) and body system (x', y', z') is

$$\overrightarrow{x_s} = [R] \cdot \overrightarrow{x_b} + \overrightarrow{x_G} \qquad (1)$$

where $\overrightarrow{x_s}$ and $\overrightarrow{x_b}$ are position vectors of a point in space and body systems, respectively, $\overrightarrow{x_G}$ is position vector of the mass center in space system, and $[R]$ is an orthogonal transformation tensor,

$$[R] = \begin{bmatrix} R_{11} & R_{12} & R_{13} \\ R_{21} & R_{22} & R_{23} \\ R_{31} & R_{32} & R_{33} \end{bmatrix} \qquad (2)$$

where $R_{ij}, R_{jk} = \delta_{ik}$ and δ_{ik} is the Kronecker δ symbol. It is a property of [R] that its inverse and transposed matrices are identical. For a space vector Ar, the transformation between the space and body systems is

$$A_s = [R] \cdot A_b \qquad (3)$$

where $\overrightarrow{A_s}$ and $\overrightarrow{A_b}$ denote the A expressions in space and body systems, respectively. [R] is calculated by solving

$$\frac{d[R]}{dt} = [\Omega] \cdot [R] \qquad (4)$$

where

$$[\Omega] = \begin{bmatrix} 0 & -\Omega_z & \Omega_y \\ \Omega_z & 0 & -\Omega_x \\ -\Omega_y & \Omega_x & 0 \end{bmatrix} \qquad (5)$$

and Ω_x, Ω_y and Ω_z are the x-, y- and z-components of the angular velocity of the object in space system, respectively.

FLOW-3D solves Navier-stokes type equations embedded with various turbulence models. This simulation used the RNG turbulence model since it consider the low Reynold number effects. [25-27]. Applying the double averaging strategy to the transport equations for TKE and its dissipation rate produces the turbulence model for the flow. The resulting equations are:

$$\frac{\delta k}{\delta t} + U_j \frac{\delta k}{\delta x_j} = \frac{\delta}{\delta x_j}\left[\left(v + \frac{v_t}{\sigma_k}\right)\frac{\delta k}{\delta x_j}\right] + P_k + B_k + W_k - \varepsilon \qquad (6)$$

$$\frac{\delta \varepsilon}{\delta t} + U_j \frac{\delta \varepsilon}{\delta x_j} = \frac{\delta}{\delta x_j}\left[\left(v + \frac{v_t}{\sigma_\varepsilon}\right)\frac{\delta \varepsilon}{\delta x_j}\right] + C_{1\varepsilon}\frac{\varepsilon}{k}\left(P_k + B_k\right)\left(1 + C_{3\varepsilon}R_f\right) + W_k - C^*_{2\varepsilon}\frac{\varepsilon^2}{k} \qquad (7)$$

$$P_k = v_t S^2 = v_t\left(\frac{\delta U_i}{\delta x_j} + \frac{\delta U_j}{\delta x_j}\right)\frac{\delta U_i}{\delta x_j} \qquad (8)$$

$$B_k = \beta g_i \frac{v_t}{\sigma_s}\frac{\delta s}{\delta x_j} \qquad (9)$$

where P_k is the shear production term of TKE, $S = \sqrt{2S_{ij}S_{ji}}$ is the modulus of the mean rate of strain tensor and $S_{ij} = \frac{1}{2}\left(\frac{\delta U_i}{\delta x_j} + \frac{\delta U_j}{\delta x_i}\right)$, B_k is the buoyant production term of TKE, W_k is the wake production tern of TKE, W_ε is the wake production term in ε, σ_k and σ_ε are the turbulent Prandtl numbers for k and ε, and $C_{i\varepsilon}$, $C_{3\varepsilon}$ and $C^*_{2\varepsilon}$ are model coefficients.

Stokes and Cnoidal wave generator (Fourier Series Method) is used since it both provides higher-order accuracy. The wave speed c and the angular wave frequency are related to other parameters as

$$c = \frac{\lambda}{T} \qquad (10)$$

$$\omega = \frac{2\pi}{T} = ck \qquad (11)$$

where:

- λ is the wavelength,
- k is the wave number, $k = \frac{2\pi}{\lambda}$
- T is the wave period.

Table 1. Barge dimension

Description	Dimension
Length *l*,(m)	1.221
Breadth *b*, (m)	0.213
Draft *d*, (m)	0.0548
Volume *V*,(m^3)	0.02634
L/B	2.86
Block coefficient C_b	0.92

(a) Barge model

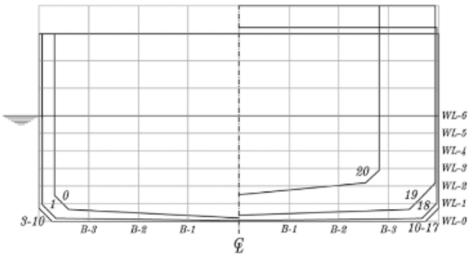

b) Barge body plan

Figure 1. Barge model and body plan used in CFD simulation

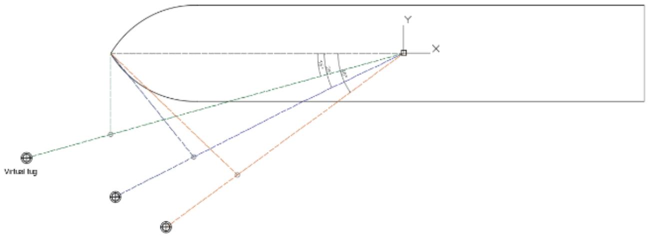

Figure 2. Simulation condition of barge

Table 2. Barge's towing parameter in various tow angle

Tow angle	Wavelength (λ/Lpp)	Tow speed (m/s)
5°	1.0	0.509
15°		
25°		
35°		

Table 3. Barge's towing parameter in various tow speed

Tow speed (m/s)	Wavelength (λ/Lpp)	Tow angle
0.509	1.0	25°
0.582		
0.655		
0.728		

3. Simulation Condition

3.1. Principle data of ship

The dimension of the barge is presented in Table 1 while the barge model used in the CFD simulation is shown in Fig.1.

3.2. Simulation parameters

Figure 2 shows the towing condition of the towed barge. The tug is replaced with the sphere body by using similar characteristics of tug to reduce the computational time during simulation. The simulation parameters used in this analysis are shown in Table 2 and 3. The tow angle used are 5°, 15°, 25° and 35° with tow speed 0.509 m/s, 0.582 m/s, 0.655 m/s and 0.728 m/s. The wavelength (λ/Lpp) used is 1.0 L in constant wave height at 0.03m.

3.3. Computational domain and meshing generation

The computational domain of the barge associated with the number of meshing cell in the CFD. The total number of cells used in the simulation is 1 million cells. Referring to Fig.3, the boundary conditions are mark in the mesh blocks. For mesh block 1, the boundary condition at X-max boundary is defined by wave to allow the wave to enter the boundary. The velocity used in the simulation is constant by 0.509 m/s for the sphere model. X-min, Y-max and Y-min is defined by outflow boundary to absorb the wave motion which will reduce the reflection from the boundary while Z-min using symmetry boundary which it applies zero-gradient condition at the boundary and Z-max using specified pressure to create a uniform pressure in the boundary. All mesh boundary for mesh block 2 are defined by symmetry. The boundary conditions for this simulation are as shown in Table 4 and Fig.3(a). The meshing scheme is also shown in Fig.3(b).

The barge is coupled through a towline. Sphere model which acted as the tow ship is assigned as prescribed motion while barge as towed ship is set as coupled motion in X translational, Y translational and Z rotational motions (surge, sway and yaw as this simulation is considering 3 degree of freedom. The towline is set as mooring line characteristic with spring coefficient of 7.347 kg/s^2.

Based on the applications of FLOW3D v11.0.4, the average duration of every simulation was about 70-80 hours (4 parallel computations) on a HP Z820 workstation PC with processor Intel (R) Xeon (R) CPU ES-2690 v2 @ 3.00 GHz (2 processors) associated with the installed memory of 32.0 GB and 64-bit Operating System.

Table 4. Boundary Conditions

Boundary	Mesh block 1	Mesh block 1
X_{min}	Wave	Symmetry
X_{max}	Outflow	Symmetry
Y_{min}	Outflow	Symmetry
Y_{max}	Outflow	Symmetry
Z_{min}	Symmetry	Symmetry
Z_{max}	Specified pressure	Symmetry

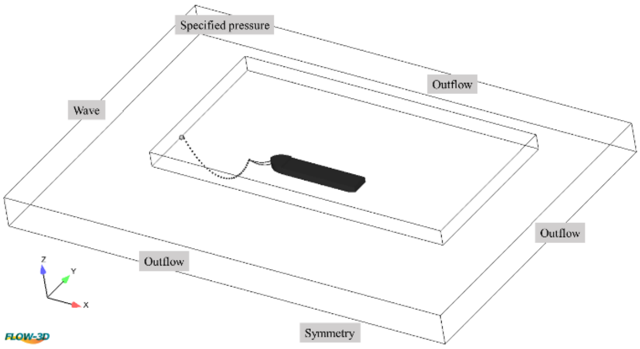

a) Boundary condition

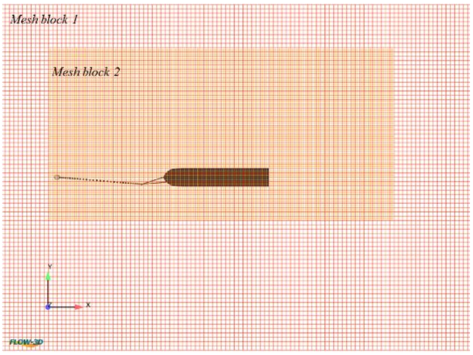

b) Meshing generation

Figure 3. Boundary condition (a), and meshing generation (b) of barge

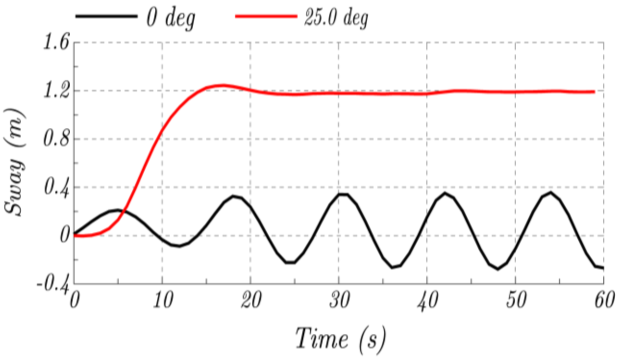

Figure 4. Effect of sway motion using single towline (0°) and asymmetrical bridle towline (25°)

3.4. Analysis of results of tow angle 0° and 25°

Applying asymmetrical bridle towline configuration during towing will reduce the sway motion of the towed ship. Figure 4 shows the sway motion graph of tow angle 0° and 25°.

Comparing this asymmetrical bridle towline configuration and straight tow (0° of the tow angle), the results show significant different of the slewing motion of barge. this can be proven by the researches from [3] [4] who stated that the increase of tow angle had reduce the slewing motion of barge. Even though their research is in calm water, the results of the sway motion show similar trend when the barge is towing in waves. The simulation of tow angle 0° and 25° had been run to prove that the theory that the increase of tow angle had reduce the slewing motion of barge.

4. Results and Discussions

4.1. Effect of tow angle on heave and pitch motions of barge

The simulation of heave and pitch motion on asymmetrical bridle towline configuration has been done by using CFD. The simulation result is presented along with the effect of sway, heave, pitch, yaw and towline tension of barge. Figure 5 shows the results of the sway, heave, pitch, yaw and towline tension of barge during towing in waves.

The average sway motion amplitude of barge has decreased as the tow angle increases from 5° to 35°. It should be noted here that the barge has the higher sway motion amplitude of 0.31 m at the tow angle of 5° as compared to the larger tow angles. This can be validated by the research from [3] who stated that the increase of tow angle has decreased the sway motion of barge. In addition, the heave motion amplitude of barge has decreased as the tow angle increases. Here, the results show that the maximum decrement of heave motion occurred when the tow angle subsequently increases from 15° up to 25°. Besides, the average yaw motion of barge also increased as the tow angle increase from 15° to 35°. The significant increase of the average yaw motion of the barge by 32.4% occurred as the tow angle increased from 15° to 25°.

Referring to Fig.6, the CFD visualization has been presented in the form of the wave fluid elevation of fluid at various tow angles. Here, the ratio of λ/Lpp has been constant of 1.0. As seen, the increase of the tow angle resulted in the higher wave crest (red color) at the barge's port. This means that the pressure at the port side increased. Consequently, the resistance of barge increases, which inherently resulted in the increment of the towline tension as the tow angle subsequently increases up to 35°.

4.2. Effect of tow speed on heave and pitch of barge

As seen in Fig.7, the effect of the tow speed on the sway, heave, pitch and yaw motions of barge incorporated with the asymmetrical bridle towline model have been analysed. The results showed that the sway motion amplitude of the barge has led to be steady at the tow angle of 25°. Besides, the yaw motion has gradually decreased, where the maximum reduction of the sway motion amplitude of the barge by 5.4% as the tow speed increases from 0.582 m/s to 0.655 m/s. Meanwhile, the heave and pitch motion amplitudes of the barge has decreased by 2.26% and 10.2%, respectively, as the tow speed increased from 0.655 m/s to 0.728 m/s. Referring to the results, the magnitude of the towline tension has proportionally increased with respect the increase of the tow speed, where its maximum increment of 19.54% occurred as the tow speed increased from 0.509 m/s to 0.582 m/s.

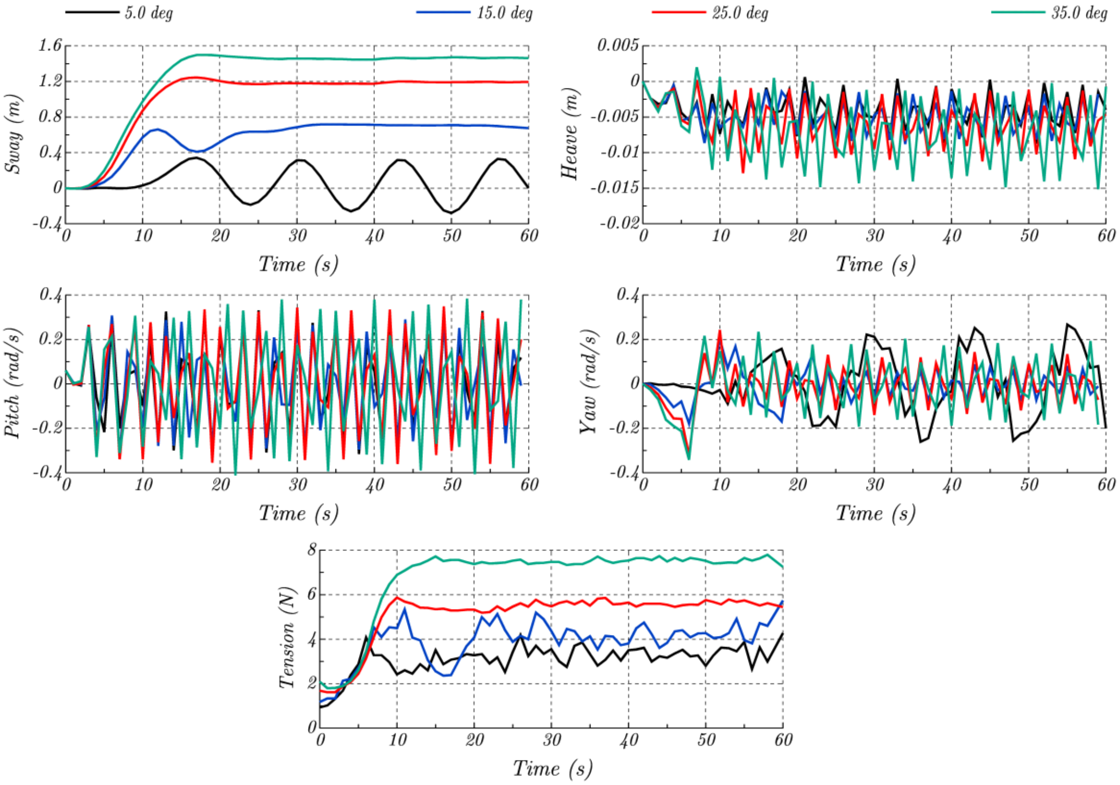

Figure 5. Effect of sway, heave, pitch, yaw and towline tension in various tow angle at constant tow speed 0.509 m/s

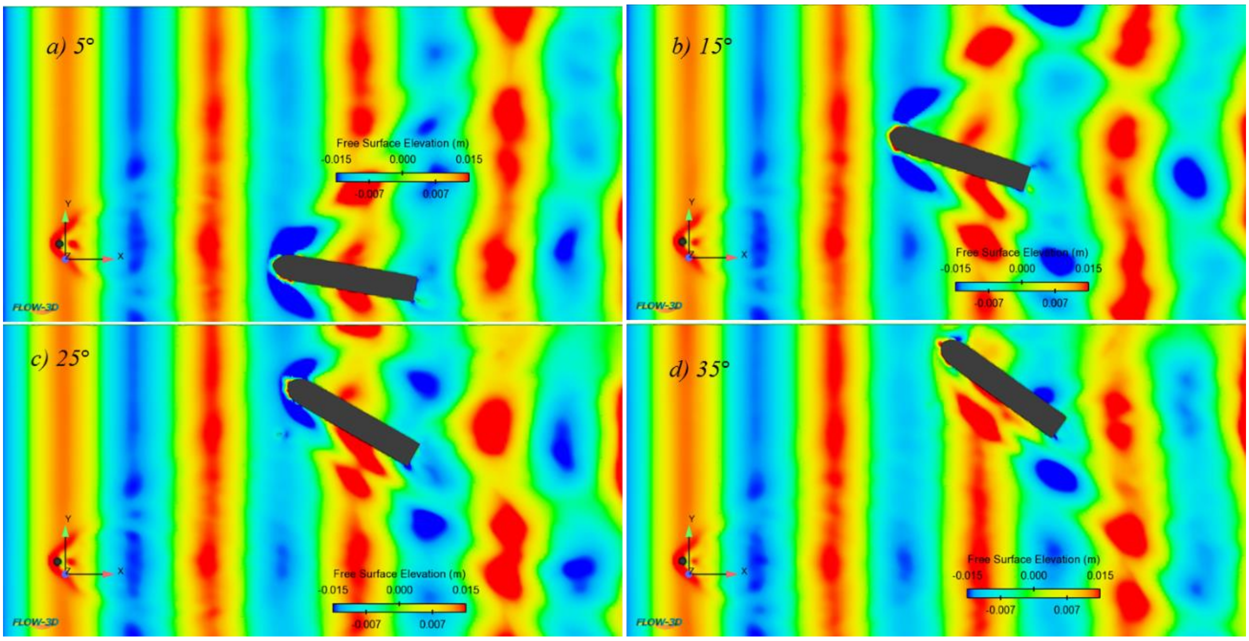

Figure 6. CFD visualisation of various tow angle in wavelength, λ/Lpp =1.0 at constant tow speed 0.509 m/s

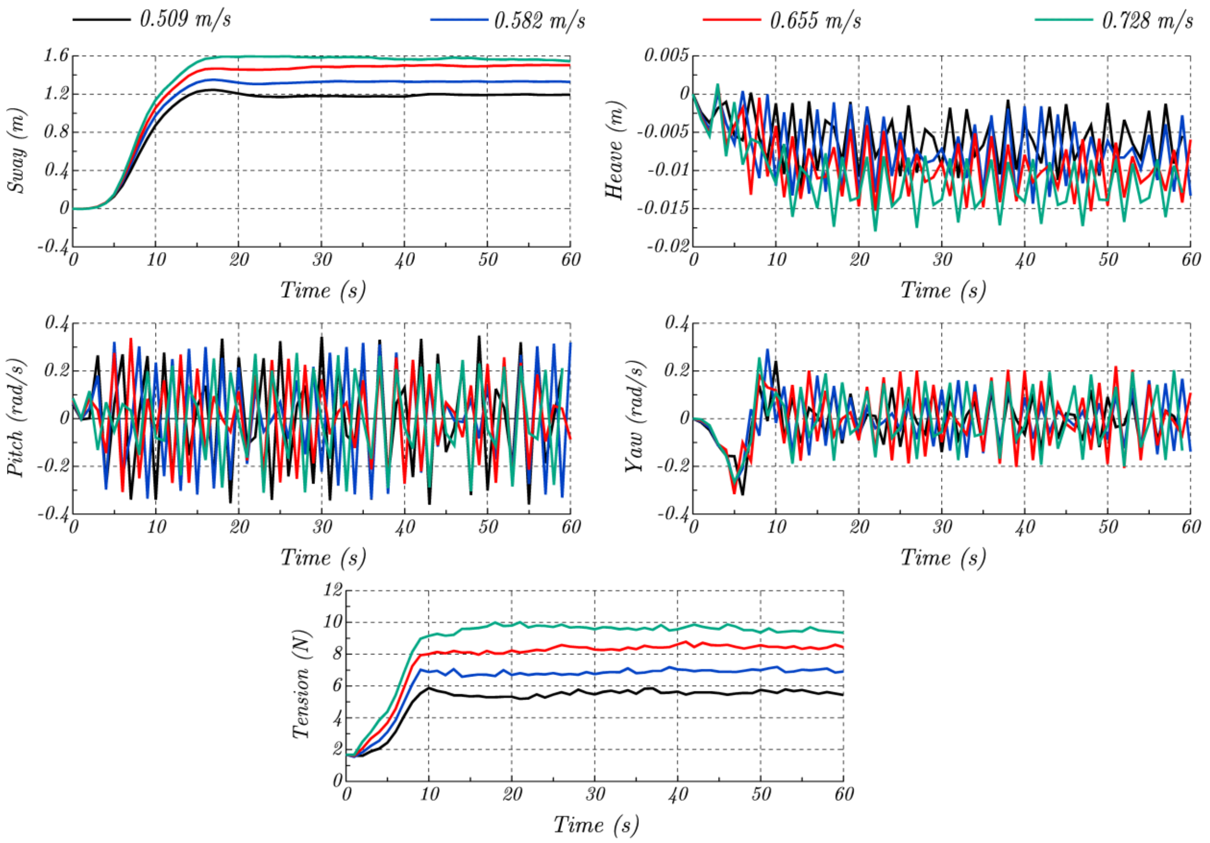

Figure 7. Effect of surge, sway, heave, pitch and towline tension in various tow speed at constant tow angle 25°

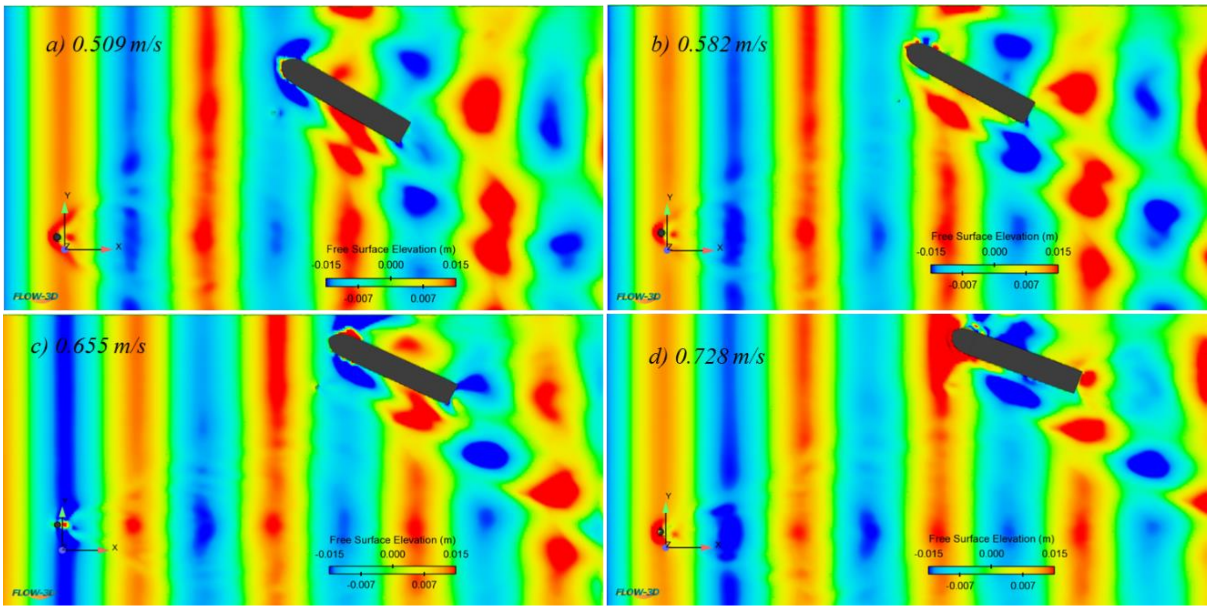

Figure 8. CFD visualisation of various tow speed in wavelength, λ/Lpp =1.0 at at constant tow angle 25°

Figure 8 shows the CFD visualisation of the barge during simulation at various tow speeds. The wave crest (red color) of the barge's bow increased as the tow speed increased from 0.509 m/s to 0.728 m/s. This is due to higher resistance (see Figure 7) which predominantly caused by the increase of pressure at the bow. As a result, this hydrodynamic phenomenon has resulted in the increase of towline tension to tow the barge during towing.

5. Conclusion

The analysis of heave and pitch motion of the towed ship incorporated with the asymmetrical bridle towline model has been carried out using the Computational Fluid Dynamic approach. Here, the effect of the tow angle and tow speed on the performance of the heave and pitch motions of the barge have been taken into account at a wide range of tow angles and tow speeds. Several simulation results have been concluded as follows;

- The characteristics of the sway and yaw motion amplitude of the barge in waves have seemed with in calm water condition.
- In addition to heave and pitch motions of the barge has decreased by 2.26% and 10.2%, respectively, as the tow speed increases from 0.655 m/s to 0.728 m/s.
- Besides, the increase of tow speed is also proportional with the increase of the towline tension magnitude, where the maximum increment of the towline tension is 19.54% as the tow speed increases from 0.509m/s to 0.582 m/s. This can be explained by the CFD visualization that the pressure increases, which result in the increase of her resistance.

References

[1] Lee, S. and C. Hong, *Study on the Course Stability of Very Large Vessels in Shallow Water Using CFD.* Ocean Engineering, 2017. 145: p. 395-405.

[2] Lee, M.-L., *Dynamic Stability of Nonlinear Barge-towing system.* Applied mathematical modelling, 1989. 13(12): p. 693-701.

[3] Zan, U.I., et al., *Model Experimental Study of a Towed Ship's Motion.* Journal, 2012.

[4] Fitriadhy, A., et al., *Analysis of an Asymmetrical Bridle Towline Model to Stabilise Towing Performance of a Towed Ship.* Jurnal Teknologi (Sciences & Engineering), 2014. 66(2): p. 151-156.

[5] Bernitsas, M. and N. Kekridis, *Simulation and Stability of Ship Towing.* International Shipbuilding Progress, 1985. 32(369): p. 112-123.

[6] Kijima, K. and Y. Wada, *Course stability of towed vessel with wind effect.* Journal of the Society of Naval Architects of Japan, 1983. 1983(153): p. 117-126.

[7] Fitriadhy, A. and H. Yasukawa, *Turning Ability of a Ship Towing System.* Ship Technology Research, 2011. 58(2): p. 112-124.

[8] Fitriadhy, A., et al., *Computational Fluid Dynamics Analysis on the Course Stability of a Towed Ship.* Journal of Mechanical Engineering and Sciences, 2017. 11(3): p. 2919-2929.

[9] Im, N., S. Lee, and C. Lee, *The Influence of Skegs on Course Stability of a Barge with a Different Configuration.* Ocean Engineering, 2015. 97: p. 165-174.

[10] Fitriadhy, A., H. Yasukawa, and K. Koh, *Course Stability of a Ship Towing System in Wind.* Ocean Engineering, 2013. 64: p. 135-145.

[11] Nakayama, Y., et al. *Time Domain Simulation OfWave-induced Motions of a Towed Ship In Head Seas*. in *The Twenty-second International Offshore and Polar Engineering Conference*. 2012. International Society of Offshore and Polar Engineers.

[12] McTaggart, K., et al., *Seakeeping of two ships in close proximity.* Ocean engineering, 2003. 30(8): p. 1051-1063.

[13] Fitriadhy, A. and N.A. Adam, *Heave and Pitch Motions Performance of a Monotricat Ship in Head-seas.* International Journal of Automotive and Mechanical Engineering, 2017. 14: p. 4243-4258.

[14] Skejic, R., *Maneuvering and seakeeping of a single ship and of two ships in interaction.* 2008.

[15] Fang, M.-C. and J.-H. Ju, *The dynamic simulations of the ship towing system in random waves.* Marine Technology, 2009. 46(2): p. 107-115.

[16] Milgram, J.H., M.S. Triantafyllou, and F.C. Frimm, *Seakeeping and extreme tensions in offshore towing.* Society of Naval Architects and Marine Engineers-Transactions, 1988. 96.

[17] Seo, M.-G. and Y. Kim, *Numerical analysis on ship maneuvering coupled with ship motion in waves.* Ocean engineering, 2011. 38(17-18): p. 1934-1945.

[18] Islam, M., F. Jahra, and S. Hiscock, *Data Analysis Methodologies for Hydrodynamic Experiments In Waves.* Journal of Naval Architecture & Marine Engineering, 2016. 13(1).

[19] Dumez, X. and S. Cordier. *Accuracy of wave pattern analysis methods in towing tanks.* in *21st Symposium on Naval Hydrodynamics*. 1997.

[20] Habekost, T., et al. *Experimental and Numerical Seakeeping Analysis of a Mobile Offshore Application Barge (MOAB®).* in *The Twenty-second International Offshore and Polar Engineering Conference*. 2012. International Society of Offshore and Polar Engineers.

[21] Fitriadhy, A., et al., *Computational Fluid Dynamics Investigation on Total Resistance Coefficient of a High-speed" Deep-V" Catamaran in Shallow Water.* International Journal of Automotive and Mechanical Engineering, 2017. 14: p. 4369-4382.

[22] Fitriadhy, A., P. Lim, and A. Jamaluddin. *CFD Investigation on Total Resistance Coefficient of Symmetrical and Staggered Catamaran Configurations through Quantifying Existence of an Interference Factor*. in *International Conference on Ships and Offshore Structures. Hamburg, Germany*. 2016.

[23] Oldfield, C., et al. *Prediction of Warship Manoeuvring Coefficients using CFD.* in *World Maritime Technology Conference*. 2015.

[24] Yaakob, O., et al., *Determining Ship Resistance Using Computational Fluid Dynamics (CFD).* Journal of Transport System Engineering, 2015. 2(1): p. 20-25.

[25] Yakhot, V. and S.A. Orszag, *Renormalization group analysis of turbulence. I. Basic theory.* Journal of scientific computing, 1986. 1(1): p. 3-51.

[26] Yakhot, A., S. Rakib, and W. Flannery, *Low-Reynolds Number Approximation for Turbulent Eddy Viscosity.* Journal of Scientific Computing, 1994. 9(3): p. 283-292.

[27] Koutsourakis, N., J.G. Bartzis, and N.C. Markatos, *Evaluation of Reynolds Stress, k-ε and RNG k-ε Turbulence Models in Street Canyon Flows Using Various Experimental Datasets.* Environmental fluid mechanics, 2012. 12(4): p. 379-403.

EPI International Journal of Engineering
Volume 2, Number 1, February 2019, pp. 41-45
DOI: 10.25042/epi-ije.022019.08

*p*ISSN 2615-5109
*e*ISSN 2621-0541

The Influences of Lengthening Dimension of Ro-Ro Ferry Toward the Considerations of Hydrodynamics Characteristic and Loading Capacity Aspect

Andi Rachmianty[a], Suandar Baso[b]*, Syamsul Asri[c]

[a]Department of Naval Architecture, Engineering Faculty, Hasanuddin University. Email: rachmianty@yahoo.co.id
[b]Department of Naval Architecture, Engineering Faculty, Hasanuddin University. Email: andar_baso@yahoo.co.id
[c]Department of Naval Architecture, Engineering Faculty, Hasanuddin University. Email: sa_tanri_kapal83@yahoo.com

---

Abstract

The ferry business has become an important business segment for ship designers, builders, and operators. Therefore, many ways have been done in order to increase ferry business through proper design or ship conversion by lengthening the hull. This research is focused on the influences of lengthening a Ro-Ro ferry to hydrodynamics characteristic and loading capacity aspects. 4 (four) ship models are investigated in the present study. The ships are fixed in the same width and draft dimensions. The difference of the Ro-Ro ferries length is indicated by the addition of one column of car space where one column car space is given by car size including the distance between car columns spaces which is an increment of every 5.88 meters. The total resistances of Ro-Ro ferries are obtained by ship model experiment in towing tank. There are 4 ship models that are made. The lengthening of a Ro-Ro ferry is described into non-dimensional parameter by the ratio of ship length and displacement volume ($L/V^{1/3}$). The hydrodynamics and the loading capacity of carried car aspects could be described in the ratio of resistance and loading capacity of the carried car (Rt/S_{UK}) with ship speed. The research result shows that the lengthening of a Ro-Ro ferry affects total resistance, speed, and loading capacity of the carried car. The increase of total resistance is caused by higher residual resistance at high speeds and this is experienced by smaller length size ship. Therefore by lengthening the Ro-Ro ferry, it could reduce total resistance at the same speed especially the residuary resistance but eventhough lengthening Ro-Ro ferry the effective speed should be considered. In additions, the effective speed for actual ships dimension in the same Rt/S_{UK} 0.05 i.e. B5L10 is about 13.85 knot, B5L11 14.33 knot, B5L12 14.94 knot, and B5L13 15.45 knot respectively.

Keywords: Hydrodynamics characteristic; loading capacity; ro-ro ferry; ship lengthening

---

1. Introduction

The main dimensions detemine many of the ship characteristics, e.g. stability, hold capacity, power requirements, and even economic efficiency [1]. These ship characteristics are interrelated with each other. The characteristics desired by the shipping company can usually be achieved with various combinations of dimensions. Therefore the main dimensions of a ship should be determined in the preliminary design and then another design stage which is needed to optimize those main dimensions in order to obtain proper design.

There are several types of ship which have a different approach to determine their dimensions. For example, a ferry which is a vessel to carry passengers, cars, and cargo on short sea routes. The ferry business has become an important business segment for ship designers, builders, and operators. In the current situation, the passenger car ferries have been growing in size and capacity. Different with Ro-Ro ferry case, the design concept is focused on Ro-Ro decks for cars, busses, and trucks. Its flexibility, ability to integrate with other transport systems and speed of operation has made it extremely popular on many shipping routes [2]. Then, the problem is the whole design concept that is different from that of traditional ships because of the introduction of a number of elements which make Ro-Ro ships unique. Therefore, the main dimensions of Ro-Ro ferries are important particularly on length and width value to be determined by deck plan consideration.

Researches related to Ro-Ro ferry have been carried out and devoted widely. This paper provides a brief review of that design history and illustrates how that knowledge is applied to new ferry projects. The RoPax concept was improved with high tech solutions where ship functions are divided into two main categories i.e. payload and ship systems, such as payload systems, Ro-Ro decks are arranged for cars [3]. A Ro-Ro ferry design has been optimized by investigation and simulation for hydrodynamics aspects [4]. The numerical, simulation, and safety based design method were described into

---

*Corresponding author. Tel.: +62 852 55625397
Jl. Poros Malino, Borongloe, Bontomarannu, Kabupaten Gowa, Sulawesi Selatan 92171

design and building of cruise ferries [5]. The development of a formalized design methodology was facilitated for safer Ro-Ro Ferry by promoting an integrated approach [6]. The multi-objective optimization procedure for the internal compartmentation of Ro-Ro Passenger ships has been formalized [7]. Then, it has been continued where the arrangements of Ro-Ro passenger ships have been optimized with genetic algorithms [8]. The developed optimization procedure could be used both at the conceptual design stage to generate from scratch the internal subdivision of a new design, and at later design stages to improve significantly the survivability of an existing design.

Concurrent with Ro-Ro ferry design research, there were also several studies related to the conversion of the Ro-Ro ferry that had been carried out. A number of ferry conversions were investigated especially their hydrodynamic aspect that has become a trend [9]. The lengthening of an existing vessel is a direct approach for achieving an increased payload. It could add displacement of the existing vessel and increase its stability but it does not automatically mean an increase in the required power. However, the hydrodynamics characteristics are not described and interpreted practically that could be used in design stage. A method for determination of a common transport unit for Ro-Ro passenger ships has been described in mixing cargos, such as passengers, passenger cars, trucks, lorries, busses, and other rolling transport units [10].

Moreover, the demand for transport capacity and ship speed are dependent on service transport demand and traject distance [11]. This research resulted in a model design of Ro-Ro ferry consist of design requirements such as loading capacity and ship speed. The main dimension is estimated base on required loading capacity. The maximum speed is determined to be used for validation with the required speed.

Therefore, this study further analizes the influences of lengthening of Ro-Ro ferry on the consideration of hydrodynamic and loading capacity aspects where the dimensions of width and draft are fixed.

2. Experimental Set-up

The model experiment for determining its resistance has been conducted in this research. The ship resistance in this research means water resistance. The towing tank belongs to the Naval Architecture Department, Faculty of Engineering, Hasanuddin University which has a size of 60 m in length, 4 m width, and 4 m depth as shown in Fig. 1. The towing tank is equipped by towing carriage with a maximum speed of 4 m/sec. Then, it is also equipped by resistance dynamometer R35E as shown in Fig. 2.

There are four Ro-Ro ferries models that were made namely B5L10, B5L11, B5L12, B5L13, and their dimensions are based on actual ship dimensions which are provided by previous research in [11]. Then the body lines plans of the actual ships are shown in Fig. 3. These have a similar geometry with the actual ship and the ships have only different in lenght size. Moreover, the ships also are fixed in the same width and draft dimensions. The difference of the Ro-Ro ferries length is indicated by the addition of one column of car space where one column car space is given by car size including the distance between car column spaces which is about 5.88 meters. The Ro-Ro ferry model is made of wood and fiberglass combination as shown in Fig. 4. The main dimensions of models are determined by using the geometry similarity with scale 1:43 where the actual ship and model dimensions are provided in Table 1. The dimension of the models considered also the width of the towing tank to avoid blockage effect.

The model speeds have been determined by using kinematic similarity with Froude number *(Fn)* based on the speed of actual ships and were set into five increased speeds i.e. 0.314 m/sec, 0.628 m/sec, 0.942 m/sec, 1.256 m/sec, 1.570 m/sec, respectively.

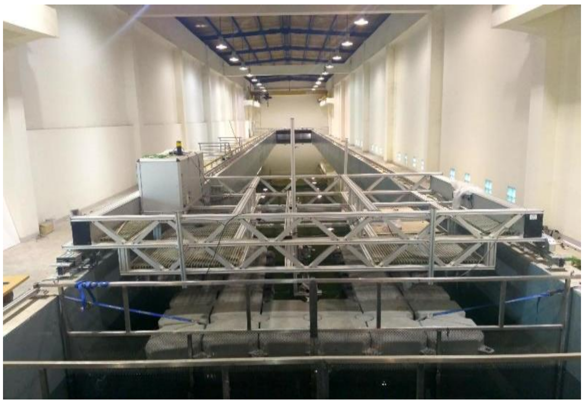

Figure 1. The towing tank facility, Naval Architecture Department, Faculty of Engineering, Hasanuddin University

Figure 2. The resistance dynamometer R35E as attached on model

Table 1. The main dimensions of actual ships and ship models

Dimension	Actual Ship (AS) and Model (M)							
	B5L10		B5L11		B5L12		B5L13	
	AS	M	AS	M	AS	M	AS	M
Lbp (m)	58.56	1.36	64.44	1.50	70.33	1.64	76.22	1.77
B (m)	17.10	0.39	17.10	0.39	17.10	0.39	17.10	0.39
H (m)	5.08	0.12	5.08	0.12	5.08	0.12	5.08	0.12
T (m)	3.37	0.08	3.37	0.08	3.37	0.08	3.37	0.08

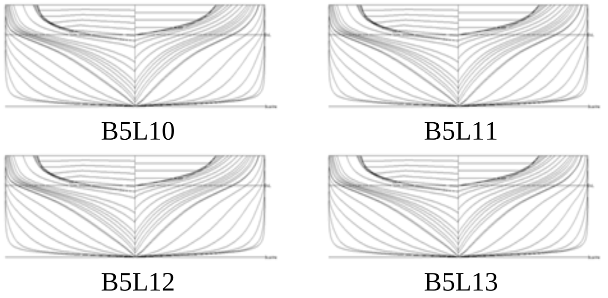

Figure 3. The body lines plan of the actual ships

Figure 4. The ship models B5L10, B5L11, B5L12, and B5L13

The resistance data were collected three times for each model speed and then the resistance values which are analyzed further were obtained in stable condition. Here, the total resistance has been analyzed further by using ITTC 1957 method [12] which is divided into two components which are friction resistance and residuary resistance. This is done to predict the magnitude dominance of friction resistance or cause of increasing speed by lengthening.

The lengthening the Ro-Ro ferry is described on increase length size as provided in Table 1 where the lengthening shows an increment of every 5.88 meters. In addition, it could be indicated by a non-dimensional parameter as well by the ratio of ship length and the cubed root of displaced volume $Lbp/\nabla^{1/3}$. Therefore, a relation between total resistance RT and lengthening ship $Lbp/\nabla^{1/3}$ could be interpreted further.

Moreover, the influence of speed on loading capacity of Ro-Ro ferry has been interpreted as well by using a graph of the relation between ship speed V and the ratio of total resistance with load capacity Rt/S_{UK} where S_{UK} is defined by loading capacity. The loading capacity S_{UK} of the Ro-Ro ferries is based on the number of carried cars in car deck.

3. Results and Discussions

The resistance experiment by using Ro-Ro ferries models in towing tank was successfully conducted. The models were adjusted to similar geometry and kinematics characteristics with the actual ship dimensions. This means that the models have the same hydrodynamics caracteristics with the actual ship. Therefore, the following furher explanations concerning on model experiment results are indicated the same with the actual ship. An example time history of resistance which was obtained from the conducted experiment is shown in Fig. 5. Then, the overall total resistance in increased speed for all models is provided in Table 2.

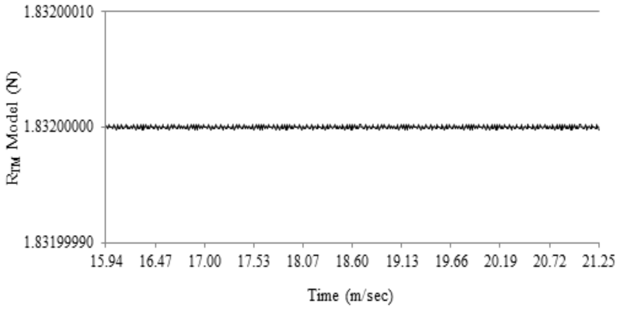

Figure 5. Time history of resistance, model B5L10, speed 0.942 m/sec

Table 2. The total resistance in increased speed of every model

Vm (m/sec)	R_{TM} Model (N)			
	B5L10	B5L11	B5L12	B5L13
0.314	0.231	0.232	0.257	0.270
0.628	0.803	0.806	0.898	0.945
0.942	1.833	1.807	1.997	2.084
1.256	4.109	3.881	4.232	4.311
1.570	10.687	9.485	8.838	8.179

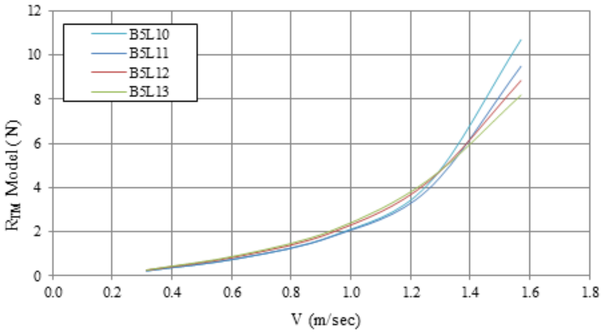

Figure 6. Total resistance of all ship models in increasing speed obtained by conducting the experiment

Based on Fig. 5, the resistance value R_{TM} shows quite stable data in a certain time and it shows also a small difference during the towing model process. The graph of the total resistance in increased speed Vm for all models is shown in Fig. 6 and it tends to increase in increasing speed. However, small length model which is B5L10 has the biggest resistance in speed Vm > 1.29 m/sec compared with others and then the big length B5L13 shows the lowest resistance in speed Vm > 1.36 m/sec. Moreover, the resistance significantly increases when speed reaches more than 1.20 m/sec for all models. This means that the effective speed of all ships are required properly where the increment of resistance is not significantly high or overestimated for every increasing speed.

Meanwhile, this total resistance would be derived and decomposed into two components such as friction resistance R_F and residuary resistance R_R. The overall friction resistance and residuary resistance of all models in increased speed are provided in Table 3 and 4 respectively.

Table 3. The friction resistance in increased speed for all models

Vm (m/sec)	Friction Resistance (N)			
	B5L10	B5L11	B5L12	B5L13
0.314	0.164	0.177	0.188	0.200
0.628	0.559	0.602	0.643	0.684
0.942	1.151	1.240	1.325	1.411
1.256	1.925	2.076	2.219	2.365
1.570	2.873	3.099	3.315	3.533

Table 4. The Residuary resisance in increased speed for all models

Vm (m/sec)	Residuary Resistance (N)			
	B5L10 (N)	B5L11 (N)	B5L12 (N)	B5L13 (N)
0.314	0.067	0.055	0.069	0.070
0.628	0.243	0.203	0.254	0.260
0.942	0.681	0.566	0.671	0.672
1.256	2.181	1.802	2.010	1.943
1.570	7.807	6.380	5.517	4.641

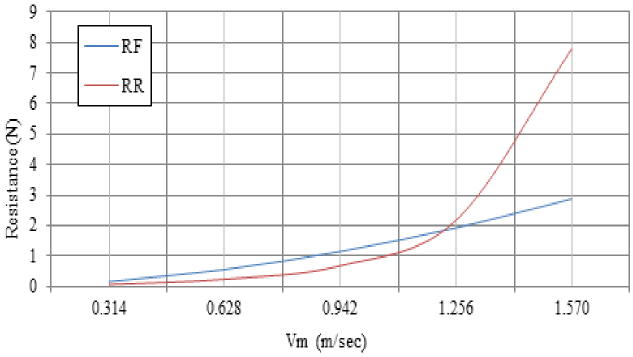

Figure 7. The friction resistance and the residuary resistance in increased speed for the model B5L10

Table 5. The composition of Friction and Residuary resistances in total resistance for each Ro-Ro ferry and increased speed

V_M (m/sec)	B5L10		B5L11		B5L12		B5L13	
	RF (%)	RR (%)	RF (%)	RR (%)	RF (%)	RR (%)	RF (%)	RR (%)
0.314	71.14	28.86	76.12	23.84	73.24	26.72	74.08	25.88
0.628	69.13	30.87	74.20	25.80	70.98	29.02	71.77	28.23
0.942	57.45	42.55	63.74	36.26	62.09	37.91	63.85	36.15
1.256	34.07	65.93	40.33	59.67	40.05	59.95	42.86	57.14
1.570	14.44	85.55	18.29	81.71	23.82	76.18	30.24	69.76

Table 6. The lengthening Ro-Ro ferry Lbp/$\nabla^{1/3}$ for each ship

Dimension/ non dimension	B5L10	B5L11	B5L12	B5L13
Lbp (m)	1.36	1.50	1.64	1.77
V (m^3)	0.024	0.026	0.029	0.031
L/$V^{1/3}$	4.72	5.06	5.32	5.64

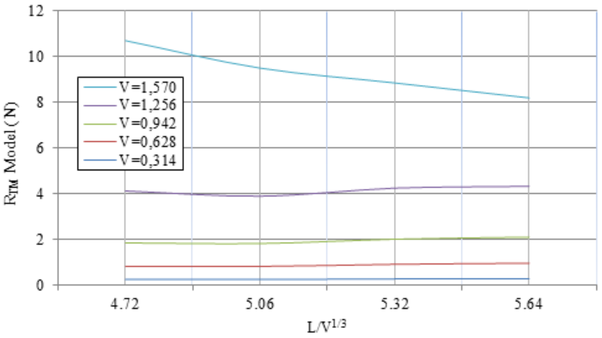

Figure 8. The total resistance in increased speed by lengthening Ro-Ro ferry Lbp/$\nabla^{1/3}$

One example of graph of friction resistance and residuary resistance in increased speed is shown in Fig. 7. The friction resistance has higher proportion compared with the residuary resistance into total resistance when *Vm* < 1.216 m/sec. However, the friction resistance is lower in *Vm* > 1.216 m/sec. The friction resistance tends to increase relatively linear and the residuary resistance is in exponential growth. The composition of friction and residuary resistances in total resistance for each Ro-Ro ferry and increased speed is shown in Table 5 where the lengthening affects on bigger residuary resistance when in high speed V ≥ 1.256 m/sec. This means that the high residuary resistance could be avoided for the lengthening ship and then it could be considered to determine an effective speed.

On the other hand, the lengthening Ro-Ro ferry *Lbp/*$\nabla^{1/3}$ for each B5L10, B5L11, B5L12, and B5L13 is shown in Table 6. The lengthening affects total resistance where it is relatively the same in small speeds which are in 0.314 and 0.628 m/sec as shown in Fig. 8. Moreover, the total resistance increases small in speeds 0.942 and 1.256 m/sec. Contrary, it decreases significantly in speed of 1.570 m/sec by leghtening ship. The increase of total resistance is affected by residual resistance at high speeds for the ship that have a small length. Therefore by lengthening the ship, it could reduce total resistance, especially in the residuary resistance. However, the effective speed for lengthening Ro-Ro ferry *Lbp/*$\nabla^{1/3}$ should consider the loading capacity of carried car *SUK* that is explained further.

Meanwhile, the lengthening Ro-Ro ferry should consider also the loading capacity of carried car associated with effective speed. The number of carried cars for every Ro-Ro ferry is shown in Table 7. Here, the ratio of total resistance with a loading capacity of carried car RT/S_{UK} is a parameter that could show a relation between increased speeds as shown in Fig. 9. Based on the figure, the loading capacity of carried car S_{UK} could be increased by lengthening which affects on increasing speed as well. Therefore, it seems that the ratio of total resistance with loading capacity of carried car Rt/S_{UK} increases in increasing speed for all ships.

Table 7. The number of carried cars for every Ro-Ro ferry

Loading Capacity of Carried Car (S_{UK})			
B5L10	B5L11	B5L12	B5L13
50	55	60	65

Table 8. The speed of each ship in the same R_{TM}/S_{UK}

R_{TM}/S_{UK}	Speed (m/sec)			
	B5L10	B5L11	B5L12	B5L13
0.03	0.914	0.945	0.986	1.020
0.04	1.011	1.046	1.090	1.128
0.05	1.086	1.124	1.172	1.212
0.06	1.148	1.188	1.238	1.281
0.07	1.200	1.241	1.294	1.339

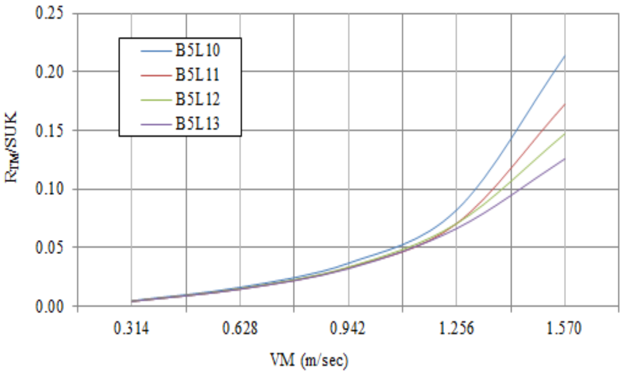

Figure 9. The ratio of total resistance with loading capacity of carried car in increased speeds

The ratio of total resistance with loading capacity of carried car increases gently in speed range *V* from 0.314 m/sec to 1.212 m/sec and it increases significant highly in a small range of increased speed at speed > 1.256. Table 8 provides the speed of each ship in the same Rt/S_{UK} where this shows only until 0.07. This could be as consideration to determine an effective speed of Ro-Ro ferry taking into account the loading capacity of carried car. Therefore, the effective speed for each ship is given at the same Rt/S_{UK} 0.05 where B5L10 is at 1.087 m/sec, B5L11 at 1.124 m/sec, B5L12 at 1.172 m/sec, and B5L13 at 1.212 m/sec. This speed also could be converted to speed for actual ship dimension where B5L10 is about 13.85 knot, B5L11 14.33 knot, B5L12 14.94 knot, and B5L13 15.45 knot, respectively.

4. Conclusions

The resistance experiment by using Ro-Ro ferries models in towing tank was successfully conducted. The models have the same hydrodynamics caracteristics with the actual ship. The increase in total resistance is caused by higher residual resistance at high speeds. This is experienced by small length size therefore by lengthening the ship it could reduce total resistance at the same speed especially the residuary resistance.

In additions, the effective speed for actual ships dimension in the same Rt/S_{UK} 0.05 i.e. B5L10 is about 13.85 knot, B5L11 14.33 knot, B5L12 14.94 knot, and B5L13 15.45 knot respectively. Therefore, the lengthening Ro-Ro ferry could be simulated in the preliminary ship design or analized in conversion ship but it should consider ship resistance, speed, and loading capacity of carried car for enhancing ferries business and safety.

Acknowledgement

We are very grateful to the undergraduate students namely Sahudin, Ardedi Yusuf, Bayu Anggara, Ardian, Abdul Wahid, Muh. Riky Adhitama, Muh. Taslim, Adi Rais Saputra who have helped in conducting the experiment.

References

[1] Schneekluth, H., Bertram, V. (1998). Ship Design for Efficiency and Economy. 2nd Edition, Butterworth-Heinemann.
[2] IMO, (1997). IMO and Ro-Ro Safety. Focus on IMO
[3] Levander, K., Yard, K.M. (2001). EUROCONFERENCE; Passenger Ship Desing, Construction, Operation and Safety, Crete, Greece, pp. 45-62.
[4] Krueger, S., Yard, F.S.G. (2001). Competitive RoRo-Ships by First Principle Design Tools. EUROCONFERENCE; Passenger Ship Desing, Construction, Operation and Safety, Crete, Greece, pp. 63-72.
[5] Kanerva, M., Poylio, E., Lindqvist, G. (2001). From Handy Size up to Cruise Ferries, Elements Required to Design and Build Successful Configuration. EUROCONFERENCE; Passenger Ship Desing, Construction, Operation and Safety, Crete, Greece, pp. 83-112.
[6] SAFER EURORO (2003). Design for Safety: An Integrated Approach to Safe European Ro-Ro Ferry Design. Available at http://research.dnv.com/skj/safereuroro/safer_euroro_1_final.pdf
[7] Zaraphonitis, G., Boulougouris, E., Papanikolaou, A. (2003). An Integrated Optimisation Procedure for the Design of Ro-Ro Passenger Ships of Enhanced Safety and Efficiency. Proc. IMDC 03, Athens, Vol. I, pp. 313-324.
[8] Boulougouris, E.K., Papanikolaou, A.D., Zaraphonitis, G. (2004). Optimization of Arrangements of Ro-Ro Passenger Ship with Genetic Algorithms. Ship Technology Research, 51(3):99-105.
[9] Richards, J.S., Reinholz, O. (2011). Hydrodynamic Trends in Ferry Design. The 11th International Conference on Fast Sea Transportation FAST 2011, Honolulu, Hawaii, September 2011.
[10] Kristensen, H.O.H., Hagemeister, C. (2012). Environmental Performance Evaluation of Ro-Ro Passenger Feery Transportation. Danish Information Paper for the Work in the MEPC committee under the International Maritime Organisation, IMO, London.
[11] Asri, S., Pallu, M.S., Thaha, M.A., Misliah. (2015). Model Design of Inter-Island Ships Base on Transport Demand and Port Facility. International Journal of Engineering Research & Technology, Vol. 4(12), pp. 643-651.
[12] ITTC (2002). Recommended Procedures, Resistance Uncertainty Analysis, Example for Resistance Test, Specialist Committee of 23rd ITTC.

EPI International Journal of Engineering
Volume 2, Number 1, February 2019, pp. 46-55
DOI: 10.25042/epi-ije.022019.09

*p*ISSN 2615-5109
*e*ISSN 2621-0541

Autonomy Stemmer Algorithm for Legal and Illegal Affix Detection Use Finite-State Automata Method

Ana Tsalitsatun Ni'mah[a]*, Dwi Ari Suryaningrum[b], Agus Zainal Arifin[c]

[a]Informatics Department, Faculty of Information Technology, Institut Teknologi Sepuluh Nopember. Email: anatsalits@gmail.com
[b]Informatics Department, Faculty of Information Technology, Institut Teknologi Sepuluh Nopember. Email: dwiari.suryaningrum@gmail.com
[c]Informatics Department, Faculty of Information Technology, Institut Teknologi Sepuluh Nopember. Email: agusza@cs.its.ac.id

---

Abstract

Stemming is the process of separating words from their affixes to get a basic word. Stemming is generally used when preprocessing in text-based applications. Indonesian Stemming has developed research which is divided into two types, namely, stemming without dictionaries and stemming using dictionaries. Stemming without dictionaries has a disadvantage in the results of removal of affixes which are sometimes inappropriate so that it results in over stemming or under stemming, while stemming using dictionaries has a disadvantage during the stemming process which is relatively long and cannot eliminate affixes to compound words. This study proposes a new stemming algorithm without a dictionary that is able to detect legal and illegal affixes in Indonesian using the Finite-State Automata method. The technique used is rule-based Stemmer based on Indonesian language morphology with Regular Expression. Test results were carried out using 118 news documents with 15792 words. The first test results on the autonomy stemmer algorithm obtain the correct word which amounts to 10449 of the total number of words processed, which means getting an average accuracy of 66%. The second test results on the autonomy stemmer algorithm get the results of the average speed of 0.0051 seconds. The third test result is being able to do the elimination of affixes to compound words.

Keywords: Autonomy stemmer; confix stripping stemmer; finite state method; porter Indonesian language; regular expression; stemming

---

1. Introduction

Stemming is a basic word separation process from its affixes based on the morphological mapping of various variants of affixed words [1]. Stemming in informatics is used in text processing which is generally when searching for information, translations, etc. [2-4]. Morphology is a very important thing in stemming algorithms. Morphology is a process of forming words [2, 5, 6]. Words that experience morphology in Indonesian is affixed words, rephrase words and compound words. English only has one type of affix word, suffix, whereas in the morphology of the Indonesian language there are several types of affixes, namely: prefix, insertion, suffix, combined prefix ending, and foreign affixes.

The Indonesian Stemming Algorithm was first developed by Nazief and Adriani [7]. The Stemming algorithm is called Confix Stripping (CS). The Confix Stripping (CS) algorithm performs the affix decapitation process by referring to the Indonesian dictionary at each step. The algorithm was developed again by Arifin and Setiono [8]. The development of this algorithm simplifies the affixing rule. Tala [1] conducted research on stemming Indonesian without using a dictionary [1]. The stemming algorithm refers to the Porter algorithm, that algorithm is a stemming algorithm used in English, Tala applies the algorithm to Indonesian. Furthermore, Putra et al. [7] doing research on various types of stemming in Indonesian. The study presents several Indonesian languages stemming algorithms, including Confix Stripping (Nazief and Adriani), Modified Confix Stripping (Arifin and Setiono), Vega etc. The research was conducted again on Confix Stripping by Adriani et al. [9]. The results of the study concluded that the most stable algorithm for stemming Indonesian at that time was Confix Stripping. Arifin, et al. [10] developed the Confix Stripping Algorithm. The algorithm is named Enhanced Confix Stripping Stemmer (ECS). ECS modifies the rules in Confix Stripping. Apart from some of there are still many more studies on Indonesian stemming [2, 3, 5, 6].

There are some researches on stemming, including carrying out the affixing process with the Brute Force technique/table lookup or stemming based dictionary, there are also some that use affix removal techniques. The basic research of Indonesian stemming with affix removal technique is the Indonesian Porter stemming algorithm [1], while the research basis for a dictionary-based stemming technique is Confix Stripping [7]. The development of the Porter stemming algorithm for Indonesian has been compared with the Confix Stripping stemming algorithm [12]. The study, developed by Agusta [12], has mentioned several comparisons. Among other

---

*Corresponding author. Tel.: +62 857 3612 4000
Jl. Raya Telang - Kamal
Bangkalan, Indonesia Postcode 69162

things, the Porter Stemming Algorithm process takes a shorter time than the Confix Stripping algorithm, the Porter stemming algorithm has a smaller accuracy compared to Confix Stripping Algorithm with an average difference of 20%. The process of Confix Stripping dictionary stemming algorithm is very influential on stemming results, the more complete the dictionary is used, the more accurate stemming results will be. According to Tahitoe and Purwitasari's research [11] the Enhanced Confix Stripping algorithm that they developed still lacked that is unable to stem compound words. According to Widjaja and Hansun research [6], the Indonesian Porter stemming algorithm also has its drawbacks, namely over stemming and under stemming. This, of course, will reduce the efficiency and performance of the stemming algorithm [6].

This study proposes a new stemming algorithm without a dictionary that is able to detect legal and illegal affixes in Indonesian using the Finite-State Automata method. The purpose of this study is to get stemming results that have high accuracy and speed by not relying on dictionaries during the removal process so that they can do the elimination of affixes to compound words.

2. Method

2.1. Finite-state automata and regular expression

Automata is a process sequence that automatically receives input and produces discrete output. The input circuit received is a string or language that is recognized by automata. If the input circuit is received and recognized, the engine produces output [5].

Finite-State Machine is an abstract machine in the form of mathematical theory by getting discrete outputs and inputs during the process that can recognize the simplest language (regular language) and can be implemented significantly where the system in an internal configuration called a state [5]. FSM works by means of the machine reading the input memory in the form of a tape, which is 1 character at a time (from left to right) using a read head which is controlled by a finite state control box where there are a number of finite states on the machine. The FSM is always in a condition called the initial state when starting to read a tape. State changes occur on the machine when the next character is read. When the head arrives at the end of the tape and the condition encountered is the final state, then the string contained on the tape is said to be received by FSM (Strings are the property of the language if the FSM language is accepted). FSM is stated simply by the regular expression language.

Regular expressions or often referred to as Regex are formulas for searching patterns of sentences or strings. Regex is very helpful in finding sentence patterns. So experiments with all possible sentence patterns need not be done. Regular expressions are generally used by many word processors or text editors and other tools to search for and manipulate sentences based on a certain pattern. At low levels, the regex can search for a word fragment. At a high level, the regex is able to control the data. Both searching, deleting and changing [5].

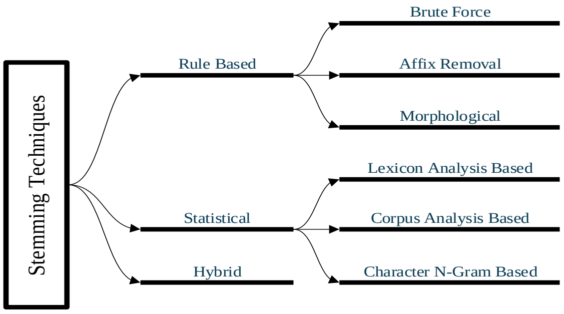

Figure 1. Stemming techniques

2.2. Stemming

The Stemming method can be classified into 3 techniques, namely [13]: rule-based, statistical, and hybrid can be seen in Fig. 1.

2.2.1. Rule-based stemmer

This stemmer is a more accurate stemmer compared to other stemmer techniques because this technique pays attention to the language rules in the stemming process. Stemmer is categorized into 3, namely: Brute Force method, Affix Removal method, and morphology method.

The Brute Force method is also known as the Table lookup techniques which is a stemming process carried out on the basis of a search table that contains a collection of basic words or basic word dictionaries.

Affix removal method is to delete the ending or prefix of words so that they turn them into basic words. Most stemmers currently used use this type of approach. The Affix removal method is based on two principles namely iteration and the other is the longest match [14]. This method starts at the end of the word and works towards the beginning. No more than one process is permitted in one class the deletion process. Some stemming algorithms that use this approach are Lovins and MF Porter [14]. In Basaha Indonesia, the stemming algorithm that uses this technique is the Indonesian Porter. The recharge process only occurs once every time the process.

Morphological methods are stemming techniques that use the language morphology rules in the process of eliminating affixes. This method allows the simultaneous removal of affixes in one deletion process, in contrast to the affix removal method.

2.2.2. Statistical stemmer

This Lexicon technique is a technique that groups words according to similarity. The process of stemming is done by finding the closest distance from the meaning of the word that has been collected. Corpus techniques are similar to the Lexicon Technique, the difference is that if Lexicon collects words based on meaning, the corpus collects morphologically or similarly written words.

The N-gram method was coined in 1974 by Adamson and Boreham. N-grams come from grams that are more than 2 or digram. A digram is a pair of consecutive letters [14]. This approach, linking the pair's words on the basis of the unique digram both have. To calculate this measurement using the Dice coefficient. For example, the term information and informative can enter into grams as follows [14]:

information => in nf fo or rm ma at ti io on
unique digrams = in nf fo or rm ma at ti io on
informative => in nf fo or rm ma at ti iv ve
unique digrams = in nf fo or rm ma at ti iv ve

Thus, "information" has ten digrams, all of which are unique, and "informative" also have ten digrams, all of which are unique. Two eight digram sharing words are unique: in, nf, fo, or, rm, ma, at, and ti. After the digram is unique for the pairs of words that have been identified and counted, the size of the similarity based on them is calculated. The similarity measure used is the Dice coefficient, which is expressed in Eq. 1.

$$S = \frac{2C}{A + B} \tag{1}$$

where A is the number of digrams unique in the first word, B the number of digram is unique in seconds, and C digram number is unique which is shared by A and B. For the example above, the dice coefficient will be the same (2 x 8) / (10 + 10) = 0.80. The size of the similarity is determined for all terms in the database. Once the similarities are calculated for all the words their partners are grouped as groups. The Dice Coefficient value gives us a clue that the basic word for this pair is in the first 8 digrams [14].

2.2.3. *Hybrid stemmer*

This Hybrid technique is a technique that combines several techniques. For example, the lookup table technique is combined with affix removal or something else. The stemming algorithm that uses this technique is Confix Stripping. Confix Stripping removes affixes based on Indonesian morphology and matches them into an Indonesian language dictionary table with the deletion process adjusted to an affix removal rule, one by one.

2.3. *Indonesian morphology*

The technique used in the Algorithm of this study is based on the word grammar contained in the Indonesian Grammar guidebook from the Ministry of Education and Culture [15]. The basic prefix is the most basic prefix and has not experienced developer. Consists of 6 affixes namely meng, peng-, ber-, di-, ter- and se-. There are some basic prefixes that have developed if strung together with a few basic words with several rules.

Meng- and peng- becomes me- and pe- if coupled with a basic word that starts with the letter /r, l, m, n, w, y, ng, ny/. Example :

- Meng-/peng- + rawat : care (merawat), nurse (perawat)
- Meng-/peng- + lamar : apply (melamar), applicant (pelamar)
- Meng-/peng- + minum : drink (meminum), drinker (peminum)
- Meng-…-i + nama : name (menamai)
- Peng-…-an + nama : naming (penamaan)
- Meng-…-i + waris : inherit (mewarisi)
- Peng- + waris : heir (pewaris)
- Meng-…-kan + yakin : convincing (meyakinkan)
- Peng-…-an + yakin : confidence (peyakinan)
- Meng- + nganga : gaping (menganga)

Meng- and peng- change into mem- and pem- if coupled with basic words that begin with the letters /b, f, v, pr/. Exceptions to the basic words beginning with /pr/ if they meet peng- then letter p melts, e.g. peng- + proses : pemroses. Example :

- Meng-/peng - + bawa : carry (membawa), carrier (pembawa)
- Meng-/peng - + fitnah : slander (memfitnah), slander (pemfitnah)
- Meng-/peng - + vonis : sentencing (memvonis), verdict (pemvonis)
- Meng- + produk + i : produce (memproduksi)

Meng- and peng- change into men- and pen- if coupled with basic word that begin with letter /d, c, j, z, s(consonant), t(consonant)/. Example :

- Meng-/peng - + dakwah : preaching (mendakwah), preacher (pendakwah)
- Meng-/peng - + curi : steal (mencuri), thief (pencuri)
- meN-/peN- + jual : sell (menjual), seller (penjual)
- Meng-…-i + ziarah : visit (menziarahi)
- Peng- + ziarah : pilgrims (penziarah)
- Meng-…-i + syukur : grateful (mensyukuri)
- Peng-…-an + syukur : thanksful (pensyukuran)

Meng- and peng- remain as meng- and peng- if coupled with basic word that begin with letters /k(konsonan), g, h, kh, and vokal/. Example :

- meng-/peng- + ganggu : disturb (mengganggu), disturber (penggangu)
- meng-/peng- + hasut : provoke (menghasut), provoker (penghasut)
- meng-/peng- + khitan : circumcise (mengkhitan), circumcision (pengkhitan)
- meng-/peng- + atur : arrange (mengatur), arranger (pengatur)
- meng-/peng- + ekor : follow (mengekor), follower (pengekor)
- meng-/peng- + inap : lodge (menginap), lodger (penginap)
- meng-…-i + obat : treat (mengobati)
- peng-…-an + obat : treatment (pengobatan)
- meng-/peng - + ukur : measure (mengukur), measure (pengukur)

Meng- and peng- change into meny- and peny- if coupled with basic word that begin with letters /s(vokal)/ and that letter s melts. Example :

- meng-/peng- + sayang : love (menyayang), loving (penyayang)
- meng-/peng- + sapa : greet (menyapa), greeter (penyapa)
- meng-/peng- + sulap : juggle (menyulap), juggler (penyulap)
- meng-/peng- + sikat : brushing (menyikat), brush (penyikat)

Meng- and peng- change into menge- and penge- if coupled with basic word which consists of only one syllable. Example :

- meng-/peng- + cat : paint (mengecat), painter (pengecat)
- meng-/peng- + bom : bomb (mengebom), bomber (pengebom)
- meng-/peng- + las : weld (mengelas), welder (pengelas)
- meng-/peng- + pel : swab (mengepel), swabber (pengepel)
- meng-/peng - + cek : check (mengecek), checker (pengecek)
- meng-/peng- + tes : test (mengetes), tester(pengetes)

Meng- and peng- change into mem- and pem- if coupled with basic word that begin with letters /p(vokal)/ and that letter p melts. Example, meng-/peng- + pukul : hit (memukul), hitter (pemukul).

Meng- and peng- remain as meng- and peng- if coupled with basic word that begins with letters /k(vocal)/ but the letter k melts. Example, meng-/peng- + kikis : scrape (mengikis), scraper (pengikis).

Meng- and peng- change into men- and pen- if coupled with basic word that begins with letters /t(vocal)/ and the letter t melts. Example, meng-/peng- + tukar : swap (menukar), swapper (penukar).

Ber- change into be- if coupled with basic word that begins with letters /r(vocal)/. Example, ber- + regu : team (beregu). Ber- change into bel- if coupled with the basic word /ajar/. Example, ber- + ajar : study (belajar). Ber- remain as ber- if coupled with basic word that begins with letters /all consonants except r/. Example, ber- + canda : joking (bercanda).

Per- remain as per- if coupled with basic word that begins with letter /consonant/. Example, per- + tanda : sign (pertanda). Per- change into pel- if coupled with the basic word /ajar/. Example, per- + ajar : student (pelajar). Per- change into pe- if coupled with basic word that begins with letter /r(vocal), tani, tinju/. Exceptions if per- is added to the –an suffix, then per- remain as per-. Example, per- + tani : farmer (petani).

Ter- change into te- if coupled with basic word /r(vokal)/. Example, ter- + rasa : feel (terasa). Ter- remain as ter- if coupled with all consonant or vocal letter /(vocal), (consonant)/. Example, ter- + indah : most beautiful (terindah).

The basic suffix is the most basic suffix. There is no development or change as in the prefix. The suffix is only three, namely -an, -kan, and -i.

The rules for the combined prefix and suffix are explained in a legal and illegal table Affix, can be seen in Table 1 [15]. The table describes the prefix rules and their derivatives combined with suffix suffixes. There are some that are the rules of Confix Stripping, other rules are obtained from Indonesian grammar from the 2015 graduation [15].

In line with the rules, a combination of words or commonly called compound words, including special terms, the elements are written separately. However, if the combination of words gets a prefix and suffix at the same time, the combined elements of the word are written in a series. The basic form of responsibility also must be written a series if you get the prefix and suffix at once. Therefore, writing the correct form of the word is accountability, not responsibility, accountability, or accountability. Combined payoffs on phrases have the same rules as affixes to compound words.

Table 1. Illegal and legal affix

Prefix		Suffix	
		Illegal	Legal
Ber	Ber	-i	-kan, -an
	Berke	-kan, -i	-an
Me	Me	-an	-kan, -i
	Mem	-an	-kan, -i
	Men	-an	-kan, -i
	Meng	-an	-kan, -i
	Menge	-an, -i	-kan
	Meny	-an	-kan, -i
Pe	Pe	-kan, -i	-an
	Pem	-kan, -i	-an
	Pen	-kan, -i	-an
	Penge	-kan, -i	-an
	Peng	-kan, -i	-an
	Peny	-kan, -i	-an
Per	Per	-	-kan, -an, -i
	Perse	-kan, -i	-an
	Pember	-kan, -i	-an
	Memper	-an	-kan, -i
	Diper	-an	-kan, -i
	Di	-an	-kan, -i
Ke	Ke	-kan, -i	-an
	Keter	-kan, -i	-an
	Kese	-kan, -i	-an
	Se	-kan, -i	-an
	Ter	-an	-kan, -i

2.4. *Indonesian stemming*

Indonesian stemming was first developed by Nazief and Adriani in 1996. The developed Stemming used a checking technique on the basic word dictionary in each process of removing the affix. Furthermore, there are also those who develop Indonesian stemming without using a dictionary in the process of eliminating the affix, the research was carried out by Tala in 2005. Stemming without the dictionary only uses affix removal techniques as Porter did.

2.2.1. *Nazief and Adriani (confix stripping)*

Nazief and Adriani [9] stemming algorithms were developed based on dictionary lookup table techniques of basic words and Indonesian language morphological rules which group affixes into prefixes (prefixes), insertions (infix), suffixes (suffixes) and combined prefixes (confixes). This algorithm uses a dictionary of basic words and supports recoding, namely the rearrangement of words that experience an excessive stemming process [11].

The Indonesian morphology rules used in the Confix Stripping algorithm are grouped into the following categories [11]:

a) Inflection suffixes are groups of endings that do not change the basic word form.
    1) Particle (P), which includes “-lah”, “-kah”, “-tah”, and “-pun”.
    2) Possessive Pronoun (PP), including “-ku” , “- mu”, and “-nya”.
b) Derivation Suffixes (DS) is a collection of original Indonesian endings which are directly added to the basic words, namely the ending “-i”, “-kan”, dan “-an”.

Table 2. Illegal affix of confix stripping

Prefix	Suffix
Be-	-i
Di-	-an
Ke-	-i, -kan
Me-	-an
Se-	-i, -kan

c) Derivation Prefixes (DP) is a collection of prefixes that can be directly given to pure base words, or to basic words that have received additions up to 2 prefixes.
   1) Prefixes that can be morphological ("me-", "be-", "pe-", and "te-")
   2) Prefixes that are not morphological ("di-", "ke-" and "se-")

These rules are used in the process of stemming algorithms by Nazief and Adriani. But not all composite prefixes are allowed by Confix Stripping [9]. Some affix combinations that are not allowed can be seen in Table 2.

The Confix Stripping algorithm has the following processes [16]:

a) Search for words that will be in the dictionary system. If it's found, it is assumed that the word is root word. Then the algorithm stops.
b) Inflection Suffixes ("-lah", "-kah", "-ku", "-mu", or "-nya") are discarded. If it is in the form of particles ("-lah", "-kah", "-tah" or "-pun") then this step is repeated again to delete obsessive pronouns ("-ku", "-mu", or "-nya"), if there is.
c) Remove Derivation Suffixes ("-i", "-an" or "-kan"). If the word is found in the dictionary, the algorithm stops. If not then go to step c1. Inflective affixes always in sequence. This algorithm first removes the inflection particle (P) suffix {"-kah", "-lah", "-tah", atau "-pun"}, and then each suffix change the ownership pronoun {"-ku", "-mu", or "-nya"}.
   1) If "-an" has been deleted and the last letter of the words Is "–k", the "-k" is also deleted. If the word is found in the dictionary, the algorithm stops. If not found then do step c2.
   2) The deleted suffix ("-i", "-an" or "-kan") is returned, proceed to step d.
d) Derivation Prefix is removed. If in step 3 there is a suffix that is deleted then go to step d2.
   1) Check prefix-suffix combination tables that are not permitted. If it is found, the algorithm stops, if it does not go to step 4b.
   2) For i = 1 to 3, specify the type of prefix then delete the prefix. If the root word has not been found, do step 5, if the algorithm has stopped. Note: if the second prefix equals the first prefix of the stop algorithm.
e) Recoding.
f) If all steps have been completed but it does not work, the initial word is assumed to be root word. Process complete.

After a number of experiments and analyses, several words that could not be stemmed using Confiz Stripping Stemmer were conducted. Analysis by the Enhanced Confix Stripping Stemmer algorithm for words that failed to be stemmed as follows:

a) Lack of decapitation of the word prefix rules in the format "mem+p...", "men+s...", and "peng+k...". This happened to word "mempromosikan", "memproteksi", "mensyaratkan", "mensyukuri", dan "pengkajian".
b) The lack of relevance of the rules for the decapitation of the word prefix in the format "menge+basic word" and "penge+basic word", as in the words "mengerem" and "pengeboman".
c) There are elements in some basic words that resemble an affix. Words like "pelanggan", "perpolitikan", and "pelaku" fail to be stemmed because the end of "-an", "-kan" and "-ku" should not be eliminated.

To correct the errors above, the ECS Stemmer algorithm performs several improvements as follow:

a) Make modifications and additions to the rules.
b) Add an additional algorithm to overcome end-chopping errors that should not be done. This algorithm is called Returns Suffix loop, and is done if the recoding process fails.
c) Return all prefixes that have been removed before, resulting in the word model as follows: [DP+[DP+[DP]]] + basic word. Decapitation of the prefix is followed by a search process in the dictionary then performed on the word that has been returned to that model.
d) Return the suffix according to the sequence of models in Indonesian. This means that the return starts from DS ("-i", "-kan", "-an"), then PP("-ku", "-mu", "-nya"), and finally P ("-lah", "-kah", "-tah", "-pun"). For each return, do steps 3) to 5) below. Especially for the "-kan" suffix, the first return starts with "k", then it continues with "an".
e) Check in the basic word dictionary. If found, the process is stopped. If it fails, then do the prefix process based on the rules.
f) Perform recoding if needed.
g) If checking in the base word dictionary still fails after recoding, then the omitted prefixes are returned again.

This algorithm still has several disadvantages that must be corrected, i.e.:

- Elimination of affixes to compound words that have combined additions.
- Over stemming and under stemming
- The speed of the stemming process

2.2.2. *Ledy Agusta (porter)*

According to Milutinovich, Porter's stemmer algorithm was first discovered in 1979 by Martin Porter in the computer lab. Porter stemming algorithm is a process of removing English morphology suffixes and inflections of words. The Porter algorithm, which was originally developed for English, was developed for Indonesian by Frakes [6]. Porter's stemmer works well in English [17]. Porter stemmer has become the standard stemmer for English and the same stemming approach has been adopted for other languages i.e. Romance (French, Italian, Portuguese and Spanish), Germanic (Dutch and German), Scandinavian languages (Danish, Norwegian and Swedish), Finnish and Russia [18]. Porter stemmer is a linear stemmer step, applying morphological rules sequentially allows the elimination of affixes gradually [19].

Table 3. Regular expression of autonomy stemmer

No	Prefix	Suffix	Deleted	Replacement	Example word
1	Belajar	[klt]ah|pun	Bel	-	Learn (Belajarkah)
2	Ber[eo][a-z]{3,}	[klt]ah|pun	Be	-	Swim (Berenang)
3	Ber[^eo][a-z]{3,}	Kan[km]u|nya|kah|pun	Ber	-	Together (Bersama)
4	Be[^aiueor][e][r][a-z]{2,}	[klt]ah|pun	Be	-	Work (Bekerja)
5	Keber[^e][a-z]{3,}	An|[km]u|nya|[klt]ah|pun	Keber	-	Success (Keberhasilan)
6	Mempelajar	I|[klt]ah|pun	Mempel	-	Learn (Mempelajari)
7	Memper[a-z]{3,}	Kan|an|[klt]ah|pun	Memper	-	Enslave (Memperbudakkan)
8	Mempe[^aiueor][e][r][a-z]{2,}	Kan|an|[km]u|nya|[klt]ah|pun	Mempe	-	Employ (Mempekerjakan)
9	Menyanyi	Kan|nya|[klt]ah|pun	Me	-	Sing (Menyanyi)
10	Meny[auieo][a-z]{2,}	Kan|i|[km]u|nya|[klt]ah|pun	Meny	S	Sweep away (Menyapu)
11	Menge[bcks][a-z]{3,}	Kan|nya|[klt]ah|pun	Menge	-	Validate (Mengesahkan)
12	Meng[ioeu][a-z]{3,}	Kan|i|[km]u|nya|[klt]ah|pun	Meng	K	Reduce (Mengurangi)
13	Men[aiueo][a-z]{3,}	Kan|i|[km]u|nya|[klt]ah|pun	Men	T	Dance (Menari)
14	Mem[aiueo][a-z]{3,}	Kan|i|[km]u|nya|[klt]ah|pun	Mem	P	Cut it off (Memotongkan)
15	Memper[a-z]{4,}|diper[a-z]{4,}|meng[akgh][a-z]{3,}|men[cdjt][a-z]{3,}|mem[bfvp][a-z]{3,}|me[lrwy][a-z]{3,}|di[a-z]{3,}	Kan|i|[km]u|nya|[klt]ah|pun	Memper|diper|meng|men|mem|me|di	-	Use (Mempergunakan), Used (Dipergunakan), Expect (Mengharapkan), Get (Mendapatkan), Justify (Membenarkan), Revealed (Mewahyukan), Delivered (Diantarkan)
16	Penge[bcks][a-z]{3,}	An|[km]u|nya|[klt]ah|pun	Pe|penge	-	Singer (Penyanyi), Verifier (Pengesah), Clicker (Pengeklik), Bomber (Pengebom), Checker (Pengecek)
17	Pe[m][a-z]{4,}	An|[km]u|nya|[klt]ah|pun	Pe	-	Entry (Pemasukan)
18	Peny[auieo][a-z]{2,}	An|[km]u|nya|[klt]ah|pun	Peny	S	Poet (Penyair)
19	Peng[ioeu][a-z]{3,}	An|[km]u|nya|[klt]ah|pun	Peng	K	Corrector (Pengoreksi)
20	Pen[aiueo][a-z]{3,}	An|[km]u|nya|[klt]ah|pun	Pen	T	Dancer (Penari)
21	Pem[aiueo][a-z]{3,}	An|[km]u|nya|[klt]ah|pun	Pem	P	Cutting (Pemotongan)
22	(ke*se[a-z]{10,}|keter[a-z]{3,}|ke[a-z]{3,}|peng[akgh][a-z]{3,}|pen[cdjt][a-z]{3,}|pem[bfvp][a-z]{3,}|pe[lrwyp][a-z]{5,}	An|[km]u|nya|[klt]ah|pun	Kese|se|keter|ke|peng|pen|pem|pe	-	Limitations (Keterbatasan), Negligence (Kelalaian), Barrier (Penghalang), Creation (Penciptaan), Generation (Pembangkitan), Throwing (Pelemparan)

The steps of this algorithm are as follows [12]:

a) Remove particle.
b) Remove obsessive pronoun.
c) Remove the first prefix. If it doesn't exist, then proceed to step d. Whereas if there is, then proceed to step e.
d) Delete the second prefix, then proceed to step f.
e) Delete suffix, if it is not found, the word is assumed to be root word. Whereas if found, then proceed to step g.
f) Remove suffix. Then the final word is assumed to be a basic word.
g) Remove the second prefix. Then the final word is assumed to be a basic word.

This algorithm still has several disadvantages, i.e. Over stemming and Under stemming.

2.2.3. *Autonomy stemmer*

The ECS Stemmer algorithm uses the basic word lookup table technique and the removal process using affix removal techniques. The Indonesian Porter algorithm only uses affix removal techniques. Both of them use Indonesian language morphology as the basis for deletion. The modification that we propose is to use the Indonesian Language morphology rules as a reference for eliminating affixes by applying them to the Regular Language Expression. The steps of the proposed stemming algorithm can be seen in Fig. 2.

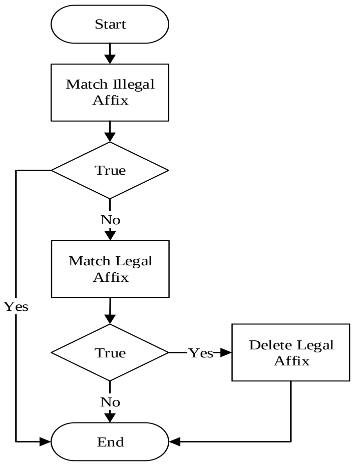

Figure 2. Flowchart autonomy stemmer

With the following information:

a) Analyzing the words that will be stemmed, if the word character is ≤ 3, then the process is complete.
b) Analyzing the words that will be stemmed, if it has an illegal compounding according to Table 1, the process is complete.
c) Analyzing the words that will be stemmed, if the word structure matches the regular expression formula in Table 3, then delete the affix.

The following is a description of Table 3:

a) If the word contains learning and or accompanied by particles, then the stemming process is carried out and has a teaching output.
b) If the word contains the prefix character “ber[eo][a-z]{3,}” and the suffix “[klt]ah|pun" which means the prefix meets letters e and o then meets the letters a to z with the number characters of at least 3 and or ending in particles. Then the stemming process is carried out, the output is the suffix prefix and the particle suffix is removed.
c) If the word contains the prefix character “ber[^eo][a-z]{3,}” and the ending “kan[km]u|nya|kah|pun” which means the prefix meets except the letters e and o then meets with letters a to z with a minimum number of characters of 3 and or ending in, substitutes for property and particles. Then the stemming process is carried out, the output is the prefix ber and the ending is deleted.
d) If the word contains the prefix character “be[^aiueor][e][r][a-z]{2,}” and the suffix “[klt]ah|pun” which means the prefix meets except letters a, i, u, e, o, r then meet with the letter e, then meet with the letter r, then meet with the letters a to z with a minimum number of characters 2 and or end of particles. Then the stemming process is carried out the output is the suffix prefix and the particle suffix is removed.
e) if the word contains the prefix character “keber[^e][a-z]{3,}” and the suffix “an|[km]u|nya|[klt]ah|pun" which means the prefix is met except letter e then meets with letters a to z with a minimum number of characters 3 and or ending in or ending –an, substitute for property and particles. Then the stemming process is carried out, the output is the suffix prefix of the succession and the ending is deleted.
f) And for the next number, how to read it is almost the same as the way above.

3. Result and Discussion

This chapter explains the results and discussion in our study. Our experiment is done in several processes, i.e. the first to input 118 news document, then the next step is to do preprocessing on punctuation and conjunctions. After preprocessing is done, the program separates paragraph into the table in every word to do the word stemming process. The amount from this process is 15792 words that will be in the system. The next step of the experiment in this research is to classify the results of the stemming. The following is a complete explanation of the trial process in this study:

3.1. News Document Dataset Input

The dataset used in this experiment is a crawl news document of some 118 online news sites. After preprocessing, the dataset obtained 15792 words stem.

3.2. Classification of Result of Stem Errors and Fixes

The process of classifying the results of errors and stemming improvements in our study uses a manual method by categorizing the types of words in the stem. Our truth is prediction by matching stemming words with the Indonesian language dictionary dataset. If the stemming yield word is not found in the dictionary database, the word trust counts 0. Here are some of the classifications:

Table 4. Example of compound word

Id	Word	Autonomy	ECS	Porter	Correct result
1	Notified (Diberitahukan)	Beritahu	Beritahu	Beritahu	Beritahu
2	Disseminate (Menyebarluaskan)	Sebarluas	Menyebarluaskan	Sebarluas	Sebarluas
3	Pulverization (Penghancurleburan)	Hancurlebur	Penghancurleburan	Nghancurlebur	Hancurlebur
4	Tell (Memberitahukan)	Beritahu	Beritahu	Beritahu	Beritahu
5	Responsibility (Pertanggungjawaban)	Tanggungjawab	Pertanggungjawaban	Rtanggungjawab	Tanggungjawab
6	Sign (Menandatangani)	Tandatangan	Menandatangani	Andatangan	Tandatangan
7	Underline (Menggarisbawahi)	Garisbawah	Menggarisbawahi	Garisbawah	Garisbawah
8	Accountable (Mempertanggungjawabkan)	Tanggungjawab	Mempertanggungjawabkan	Tanggungjawab	Tanggungjawab
9	Multiplied (Dilipatgandakan)	Lipatganda	Dilipatgandakan	Lipatganda	Lipatganda

Table 5. Example over stemming and under stemming

Id	Word	Autonomy	ECS	Porter	Correct Result
1	Policy (Kebijakan)	Bijak	Bija	Bija	Bijak
2	Agreed (Disetujuinya)	Setuju	Disetujui	Setujui	Setuju
3	Perpetrator (Pelaku)	Pelaku	Pela	Laku	Pelaku
4	Legislation (Perundang-undangan)	Undang-undang	Perundang-undangan	Rundang-undang	Undang-undang
5	Country (Negeri)	Negeri	Neger	Negeri	Negeri
6	Economy (Ekonominya)	Ekonomi	Ekonom	Ekonomi	Ekonomi

a) Improvements in stemming compound words

One of our aims to conduct research on modification of stemmer is to correct errors in compound word stem. Some of them are summarized in Table IV. In the table, there are 9 examples of compound words that are given combined additions. Can be seen in the results that the algorithm that we propose gets the best results among other algorithms.

b) Improvements to over stemming and under stemming

There are some over stemming and under stemming that can be corrected by the algorithm that is proposed. This is showed in Table V. In the table we only list 6 words that are successful in the algorithm that we propose, while the other words we include in Appendix A.

3.3. Calculation of Average Results

The calculation of the average stemming yield that described in this point. There are 3 calculations that are done, i.e. the number of word truth, the average speed of the process and the percentage of the word truth. Here is an explanation of how to calculate it:

a) Average word truth

The average truth of the word we counted from 118 datasets processed which produced 15,792 words. The results obtained from the word truth in the modification algorithm get 10,449 correct words, in the ECS algorithm get 11,530 correct words, and in the Porter, the algorithm gets as many as 9,043 words correctly. Word errors in the modification algorithm get 5,343 incorrect words, in the ECS algorithm get 4,262 incorrect words, and in the Porter, the algorithm gets 6,749 incorrect words. Can be seen in Table 6 and Fig. 3.

b) Average process speed

The average speed obtained to process 118 news documents with 15,792 words can be seen in Table 6. In the Modification algorithm the speed reaches 0.0051 seconds, at ECS it reaches 1.9195 seconds and the Porter algorithm reaches 0.0039 seconds.

c) Percentage of the word truth

We summarize the overall average in Table 6. The truth in the Modification algorithm that we propose is 66% word truth, the ECS algorithm gets 73% and the Porter algorithm gets 57%. We get a percentage of no more than 70% because in the dataset we use is not the whole standard language document, so there are still many non-standard words that are the results of the stem that we cannot match in the dictionary when the word truth calculation process.

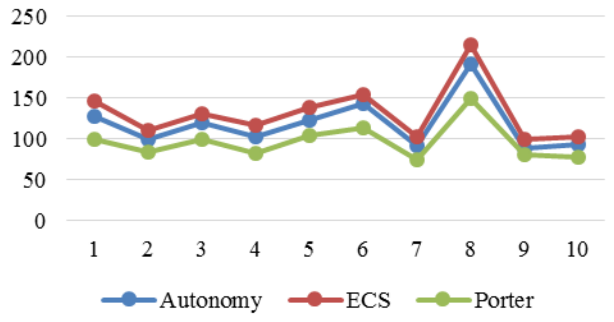

Figure 3. Comparison of true word

Table 6. Percentage of true word

Word	Autonomy	Porter	ECS
True Word	10.449	9.043	11.530
False Word	5343	6749	4262
Time (second)	0,0051	0,0039	1,9195
The precision of True Word (%)	66%	57%	73%
The precision of False Word (%)	34%	43%	27%

4. Conclusion

This study got the results of the initial goal of getting stemming results that have high accuracy and speed by not relying on the dictionary during the process of removing the additive so that it can do the elimination of affixes to compound words. From the results of the trial obtained accuracy of 10,449 true words with an accuracy of 66%, while Porter gets 9,043 correct words with an accuracy of 57%. The second objective of this study was to be able to get a faster stemming time from ECS which was equal to 0.0051, while ECS obtained a stem processing time for 15,792 words of 1.9195 seconds. This study has several shortcomings, so there is a need for further development, namely improvements to over stemming and under stemming in words that have foreign affixes, Sanskrit additions, and inserts.

Reference

[1] Tala, F. Z., A Study of Stemming Effect on Information Retrieval in Bahasa Indonesia, Master of Logic Project, Institute for Logic, Language and Computation, Universiteit van Amsterdam, Netherland. 2003.

[2] Purwarianti, A. A Non-Deterministic Indonesian Stemmer. International Conference on Electrical Engineering and Informatics 17-19 July, Bandung, Indonesia. 2011.

[3] Setiawan, R., Kurniawan, A., and Budiharto, W., Flexible Affix Classification for Stemming Indonesian Language. 13th International Conference on Electrical Engineering/Electronics, Computer, Telecommunications and Information Technology (ECTI-CON). 2016.

[4] Agbele K.K., Adesina A.O., Azeez N.A., and Abidoye A.P.Context-Aware Stemming Algorithm for Semantically Related Root Words. Afr J Comp & ICT Vol 5. No. 4, ISSN 2006-1781, June. 2012.

[5] Latt, T. M. and Thida, A., An Analysis of Myanmar Inflectional Morphology Using Finite-State Method. 17th International Conference on Computer and Information Science (ICIS). June 6-8, Singapore. 2018.

[6] Widjaja, M., and Hansun, S., Implementation Of Porter's Modified Stemming Algorithm In An Indonesian Word Error Detection Plugin Application. International Journal of Technology (IJTech) 2: 139-150 ISSN 2086-9614. 2015.

[7] Putra R. B. S. and Utami E., Non-formal Affixed Word Stemming in Indonesian Language. International Conference on Information and Communications Technology (ICOIACT). 2018.

[8] Arifin, A. Z., and Setiono, A. N. Classification of Event News Documents in Indonesian Language Using Single-Pass Clustering Algorithm. Proceedings of the Seminar on Intelligent Technology and its Applications (SITIA), Surabaya, Indonesia. 2002.

[9] Adriani, M., Nazief, B., Asian, J., Tahaghoghi, S. M. M., and Williams, H. E. 2007. Stemming Indonesian: A confix-stripping approach. ACM J. Educ. Resour. Comput. 6, 4, Article 13. 2007.

[10] Arifin, A.Z., dkk. Enhanced Confix Stripping Stemmer And Ants Algorithm For Classifying News Document In Indonesian Language. International Conference on Information & Communication Technology and Systems ISSN 2085-1944 : 149-156. 2009.

[11] Dwiyoga, A., dan Purwitasari, D. Implementasi Modifikasi Enhanced Confix Stripping Stemmer Untuk Bahasa Indonesia Dengan Metode Corpus Based Stemming. Skripsi Jurusan Teknik Informatika, Fakultas Teknologi Informasi Institut Teknologi Sepuluh Nopember (ITS). 2010.

[12] Agusta, L., Comparison of Porter Stemming Algorithm and Nazief & Adriani's Algorithm for Stemming Indonesian Text Documents. National Conference on Systems and Informatics. 2009.

[13] Kaur P. and Buttar P. K., Review On Stemming Techniques. International Journal of Advanced Research in Computer Science Volume 9, No. 5, September-October 2018 ISSN No. 0976-5697 DOI: http://dx.doi.org/10.26483/ijarcs.v9i5.6308. 2018.

[14] Sharma D., Stemming Algorithms: *A Comparative Study and their Analysis*. International Journal of Applied Information Systems (IJAIS) – ISSN : 2249-0868 Foundation of Computer Science FCS, New York, USA Volume 4– No.3, September. 2012.

[15] http://badanbahasa.kemdikbud.go.id/lamanbahasa/sites/default/files/Buku%20Penyuluhan%20BPK.pdf. 2015.

[16] Widayanto H. dan Huda A. F., *Comparison Nazief Adriani And CS Stemmer Algorithm For Stemm Real Data*. e-Proceeding of Engineering : Vol.4, No.3 ISSN : 2355-9365 page 5215 - 5222 Desember. 2017.

[17] Haroon M., *Comparative Analysis of Stemming Algorithms for Web Text Mining*. I.J. Modern Education and Computer Science, 2018, 9, 20-25 Published Online September 2018 in MECS (http://www.mecs-press.org/) DOI: 10.5815/ijmecs. 2018.

[18] Kassim M. N., Maarof M. A., Zainal A. and Wahab A. A., *Enhanced Affixation Word Stemmer with Stemming Error Reducer to Solve Affixation Stemming Errors.* Journal of Telecommunication, Electronic and Computer Engineering ISSN: 2180 – 1843 e-ISSN: 2289-8131 Vol. 8 No. 3. 2016.

[19] Karaa W. B. A., *A New Stemmer To Improve Information Retrieval*. International Journal of Network Security & Its Applications (IJNSA), Vol.5, No.4, July 2013 DOI : 10.5121/ijnsa.2013.5411. 2013.

Appendix A

No	Word	Autonomy	ECS	Porter	Current Result
1	Kebijakan	Bijak	Bija	bija	bijak
2	Disetujuinya	Setuju	Disetujui	setujui	setuju
3	Pemangkasan	Pangkas	Mangkas	mangkas	pangkas
4	Perbankan	Perbankan	Ban	rban	bank
5	Pertanggungjawaban	Tanggungjawab	Pertanggungjawaban	rtanggungjawab	tanggungjawab
6	Pergerakan	Pergerakan	Gera	rgera	gerak
7	Ketidakpastian	Tidakpasti	Ketidakpastian	tidakpasti	tidakpasti
8	Menahan	Menahan	Nah	ahan	tahan
9	Negeri	Negeri	Neger	negeri	negeri
10	Ekonominya	Ekonomi	Ekonom	ekonomi	ekonomi
11	Dibayangi-bayangi	Bayangi-bayang	Dibayangi-bayangi	bayangi-bayang	bayang-bayang
12	Kehandalan	Handal	Kehandalan	handal	handal
13	Perlahan	Perlahan	Perlahan	rlah	perlahan
14	Pelaku	Pelaku	Pela	laku	pelaku
15	Pemilu	Pemilu	Milu	milu	pemilu
16	Direspon	Respon	Direspon	respon	respon
17	Depannya	Dep	Dep	depan	depan
18	Menggerakan	Gera	Gera	gera	gerak
19	Terhadap	Hadap	Terhadap	hadap	hadap
20	Menjabarkan	Jabar	Menjabarkan	jabar	jabar
21	Ketidakstabilan	Tidakstabil	Ketidakstabilan	tidakstabil	tidakstabil
22	Kehati-hatian	Hati-hati	Kehati-hatian	hati-hati	hati-hati
23	Merespon	Respon	Merespon	respon	respon
24	Walaupun	Walau	Walaupun	walaupun	walau
25	Diekspektasikan	Ekspektasi	Diekspektasikan	ekspektasi	ekspektasi
26	Pemungutan	Pungut	Mungut	mungut	pungut
27	Dilipatgandakan	Lipatganda	Dilipatgandakan	lipatganda	lipatganda
28	Berjumlah	Jumlah	Berjum	jumlah	jumlah
29	Keikutsertaan	Ikutserta	Keikutsertaan	ikutserta	ikutserta
30	Mempertanggungjawabkan	Tanggungjawab	Mempertanggungjawabkan	tanggungjawab	tanggungjawab
31	Kepengurusan	Pengurus	Kepengurusan	pengurus	pengurus
32	Bekerjasama	Kerjasama	Bekerjasama	bekerjasama	kerjasama
33	Menutup-nutupi	Tutup-nutup	Menutup-nutupi	utup-nutup	tutup-tutup
34	Penghancurleburan	Hancurlebur	Penghancurleburan	nghancurlebur	hancurlebur
35	Sekian	Sekian	Kian	kian	sekian
36	Ditandatangani	Tandatangan	ditandatangani	tandatangan	tandatangan
37	Menghawatirkan	Hawatir	menghawatirkan	hawatir	hawatir
38	Buka-bukaan	Buka-buka	buka-bukaan	buka-buka	buka-buka
39	Walaupun	Walau	walaupun	walaupun	walau
40	Perundang-undangan	Undang-undang	perundang-undangan	rundang-undang	undang-undang
41	Ketidakstabilan	Tidakstabil	ketidakstabilan	tidakstabil	tidakstabil
42	Ketidakpastian	Tidakpasti	ketidakpastian	tidakpasti	tidakpasti
43	Menggarisbawahi	Garisbawah	menggarisbawahi	garisbawah	garisbawah
44	Menyebarluaskan	Sebarluas	menyebarluaskan	sebarluas	sebarluas
45	Beragam	Ragam	agam	agam	ragam

EPI International Journal of Engineering
Volume 2, Number 1, February 2019, pp. 56-60
DOI: 10.25042/epi-ije.022019.10

*p*ISSN 2615-5109
*e*ISSN 2621-0541

Characteristic of Current Diffusion on Double-Plate Conductor for Smaller Resistive Load

A. M. Shiddiq Yunus[a]*, Apollo[b], Muhammad Ruswandi Djalal[c], Ahmed Abu-Siada[d]

[a]Energy Conversion Engineering, State Polytechnic of Ujung Pandang, Indonesia, Email: shiddiq@poliupg.ac.id
[b]Energy Conversion Engineering, State Polytechnic of Ujung Pandang, Indonesia, Email: apollo@poliupg.ac.id
[c]Energy Conversion Engineering, State Polytechnic of Ujung Pandang, Indonesia, Email: wandy@poliupg.ac.id
[d]Electrical and Computing Engineering, Curtin University, Australia, Email: a.abusiada@curtin.edu.au

---

Abstract

Power transmission line is one of the pivotal parts of a power system. It connects power generation house with the consumer even in the long distances. Research on current diffusion on the conductor is inevitable to maximize the power dispatch on transmission line. The main purpose of this study is to recognize the behaviors and characteristics of current diffusion in double-plates conductor for further development in the future. The research outcomes would be very useful, particularly in the transmission line study. In this paper, study will be focused on the characteristic of current diffusion in conductor due to its variation impedance value of load particularly when resistive load is smaller than the conductor impedance (Z_o). This research is conducted by experimental test and carried out through extensive simulation using MATLAB and Visual Basic Program in MS. Excel. Poynting theory is employed as a validation approach. The simulation and experiment results show that if R_L is smaller than the line impedance Zo, deficiency current establish will occur where the electromagnetic energy is not sufficient for the load.

Keywords: Conductor; current diffusion; impedance

---

1. Introduction

Power transmission is one of the important parts of power system delivery due to its role in connecting power house to the loads centereven in very long distances [1]. One of the pivotal things on power transmission that should be taken into consideration is how to maximize the power delivery on the conductor through the current diffusion study on transmission line.

Research on current diffusion on conductor can be divided into two where the first case is investigation on impacts of current diffusion on conductor for resistive value larger than transmission line impedance, this study has been carried out in prior research in [2]. In this study, the second case of current diffusion on conductor is studied where the study is focused on the impacts of current diffusion on conductor for resistive value smaller than the transmission line impedance. The study of current diffusion could not be separated with the theory of energy storage where the storage process can be done in form of magnetic field and electric field processes. The energy storage that performed through magnetic field generally applied to inductor (L) which storing energy in Joule. The energy capacity is depending on the value of L and the current flow on it. The formula can be stated as follow:

$$W_m = \int_0^t P_L dt = \int_0^I LI \frac{dI}{dt} = \int_0^I LI \quad dI = \frac{1}{2} LI^2 \text{ (J)} \qquad (1)$$

The formula above becomes the fundamental of superconductor development where the coil is placed in the very extreme low temperature (cryogenic state). This superconducting coil could store energy in very high efficiency [3], applied in wind turbine generators [4-6], and in micro hydro [7, 8]. Meanwhile, energy storage that performed from electrical field normally occurs due to the difference capacitance among some parts including the difference on their voltages. The energy content that stored can be formulated as follow [9]:

$$W = \frac{1}{2C} Q^2 = \frac{1}{2} QV = \frac{1}{2} CV^2 \text{ (J)} \qquad (2)$$

It can be concluded from eq. (1) and (2), that electromagnetic energy can be determined by the flowing current in conductor while electrostatic energy is influenced by potential (V) at plates.

---

*Corresponding author. Tel.: +82-347-521-449
Jalan Perintis Kemerdekaan KM. 10
Makassar, Indonesia, 90245

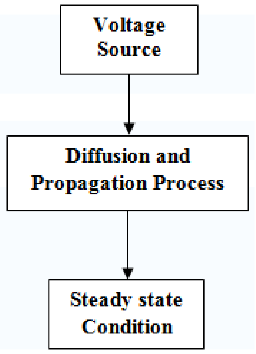

Figure 1. Process diagram of diffusion and propagation in a conductor

1.1. Poynting theory

John Henry Poynting (1852-1914) is the first person who introduced Poynting Vector as can be determined with the following equation [10]:

$$P = E \times H \; (\frac{W}{m^2}) \tag{3}$$

where:

E = Electric Field (V/m)
H = Magnetic Field (A/m)

Poynting theory allows the wave propagation of power flow to be easily calculated. The power flow can be calculated based on multiplication vector of the perpendicular of *E* and *H* (according to the "Right Hand Rule").

1.2. Parallel plate voltage at transmission line

In this paper, research is focused on the diffusion and propagation process of current flow in a conductor after connected to a voltage source as illustrated in Fig. 1, where load is applied in condition of smaller than line impedance.

When voltage is applied at the first point of the conductor with two identical plates, a magnetic field will across the conductor in V/m and simultaneously, there is a current flow (I_D) in the conductor. According to the "Right Hand Rule", when a current flow in the conductor, it will generate a magnetic field (H) where the direction is dictated by the current flow. The movement of magnetic field, H is determined by I_D and current velocity (*v*) which can be determined according to the equation (4):

$$v = \frac{1}{\sqrt{\varepsilon\mu}} \; (\frac{m}{s}) \tag{4}$$

When magnetic field moves, a back electric field simultaneously will be appeared in opposite direction, limiting the velocity of magnetic field movement itself. This phenomenon can be written in the following equation:

$$E_B = -Bv \tag{5}$$

$$V_B = E_B \times g = -B \times g \times v \quad \text{(V)} \tag{6}$$

where: g is distance between plates conductors (m)

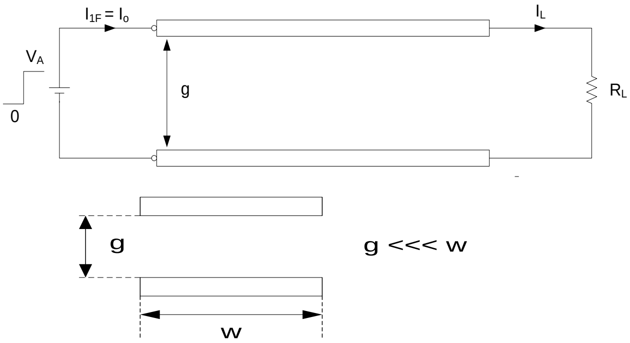

Figure 2. Conductor configuration with identical plates

Figure 2 is the equivalent circuit represents the experiment test for current diffusion at conductors with parallel plates where distance between plates (*g*) is very small compared to the wide (*w*).

2. Research Methodology

This research is conducted by experimental test and carried out through extensive simulation using MATLAB and Visual Basic Program in MS. Excel. Poynting theory is employed as a validation approach. In this paper, a smaller resistive load than the line impedance is employed. The value of resistive load is 5x smaller than the line impedance. However, for comprehensive study an equal value of resistive load and line impedance is formerly conducted.

3. Results and Discussion

3.1. Current characteristic in line

When wave front reach the load, there are three form of energies produced, electric field (*E*) which generates electrostatic; magnetic field resultant (*H*) which generates mechanical energy; and sustainable power that is determined by $V_A \times I_o$.

3.1.1. R_L Equal with line impedance (Z_0)

Discussion on R_L equal with the line impedance (Z_0) has been provided in the prior paper in [2]. If the value of R_L is equal with Z_0, the value of I_0 will bring a small negative V_A (ohmic voltage drop) from source to the load as illustrated in Fig. 3.

From Fig. 4, it can be seen that the magnitude of voltage along the conductor has the same value as simulated with MATLAB in the case of R_L=Z_0. Meanwhile, the V_{fr}–forward and V_b-backward calculated using Excel Visual Basic is listed in Table 1.

3.1.2. R_L Smaller Than Line Impedance (Z_0)

The propagation process will show a different response when R_L is smaller than Z_0. There will be a current deficiency where electromagnetic value is too small for the load. The propagation diffusion process can be seen in Fig. 5.

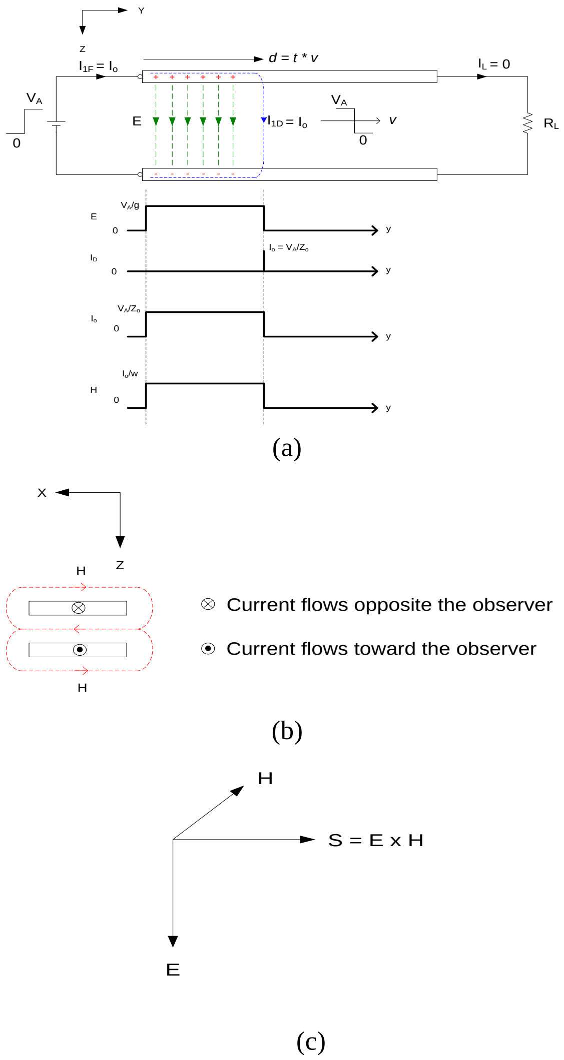

(a)

(b)

(c)

Figure 3.Process of diffusion and propagation in a conductor; (a) Equivalent Circuit (b) Magnetic Field and (c) Poynting Vector [2]

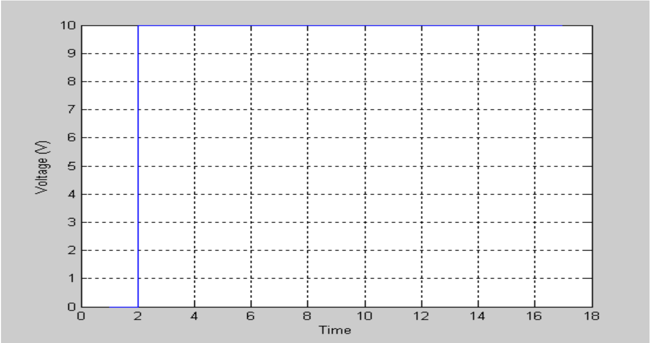

Figure 4. Matlab plot for $R_L = Z_o$

Table 1. V_{fr}–forward and V_b-backward for R_L=Zo [2]

V_A	:	10	V		
Z_o	:	10	Ohm		
R_L	:	10	Ohm		
V_{fr} (V)	I_{fr} (A)	I_e (A)	ΔV (V)	V_b (V)	I_b (A)
10	1	0	0	10	1
10	1	0	0	10	1
10	1	0	0	10	1
10	1	0	0	10	1
10	1	0	0	10	1
10	1	0	0	10	1
10	1	0	0	10	1
10	1	0	0	10	1
10	1	0	0	10	1
10	1	0	0	10	1
10	1	0	0	10	1
10	1	0	0	10	1
10	1	0	0	10	1
10	1	0	0	10	1
10	1	0	0	10	1

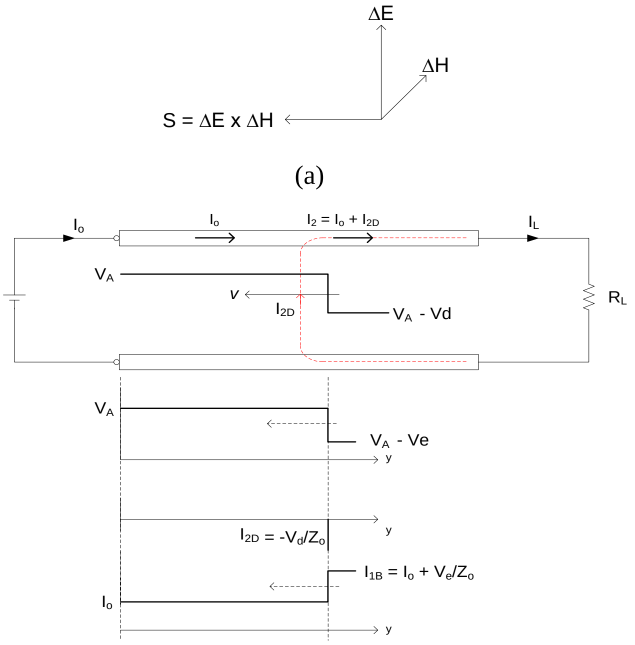

(a)

(b)

Figure 5. Process diffusion of propagation of first backward wave for R_L<Zo, (a) Poynting Vector (b) Equivalent Circuit [2]

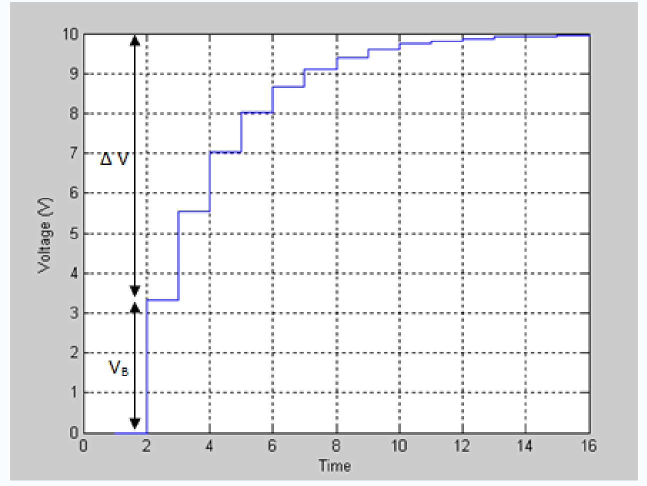

Figure 6. Matlab plot for R_L < Zo

As can be seen in Fig. 6, from time to time the V backward becomes larger until the transition of the voltage propagation reach the same value with V_A. The equation to determine the V-backward and ΔV can be stated as follow:

1st Forward

$$V_{1F} = V_A \text{ and } I_{1F} = \frac{V_A}{R_L} \tag{7}$$

1st Backward

$$V_{1B} = V_A + \Delta V_1 \text{ and } I_{1B} = I_{1F} - \frac{\Delta V_1}{Z_o} \tag{8}$$

Nth transition

$$V_{nF} = V_A, I_{nF} = I_{(n-1)B} + \frac{\Delta V_{(n-1)}}{Z_o}, I_{nd} = \frac{\Delta V_n}{R_L} - I_{nF}$$

,

$$\Delta V_n = -I_{nd}(Z_o // R_L), \tag{9}$$

$$V_{nB} = V_{nF} + \Delta V_n, \tag{10}$$

$$I_{nB} = I_{nF} - \frac{\Delta V_n}{Z_o} \tag{11}$$

3.2. Laboratory experiment

In this experiment, parallel plate conductors are used and sourced with 2V, this value is selected because if the input voltage larger than noise it will influence the voltage characteristic of the load.

As shown in Fig. 7, there is a time delay between V_{in} and V_{out}. This is occur due to propagation wave that move forward toward the load required certain time where its velocity depends on conductivity, permeability and physical properties of the conductor. In this research, time delay has reach about 100 ns.

To calculate the load impedance, a simple circuit is assembled as shown in Fig. 8 to measure the current flow (I_0).

By calculating the voltage value between R_1 = 1 Ohm, we could obtain the measured current by $V_{R1} = I_o \times R_1$ or can be written $V_{R1} = I_o$. As shown in Fig. 9, the initial voltage value is 2 V and the measured current is 165 mA, therefore the line impedance is:

$$Z_0 = \frac{V_A}{I_0} = \frac{2}{0.165} = 12.12 \approx 12 \text{ Ohm}$$

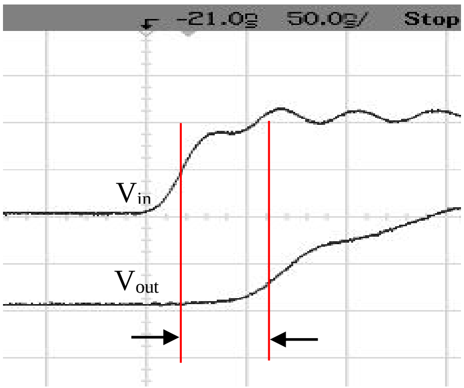

Figure 7. V_{in} versus V_{out}

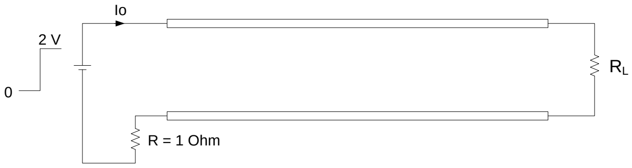

Figure 8. A simple circuit to measure the current flow in conductor

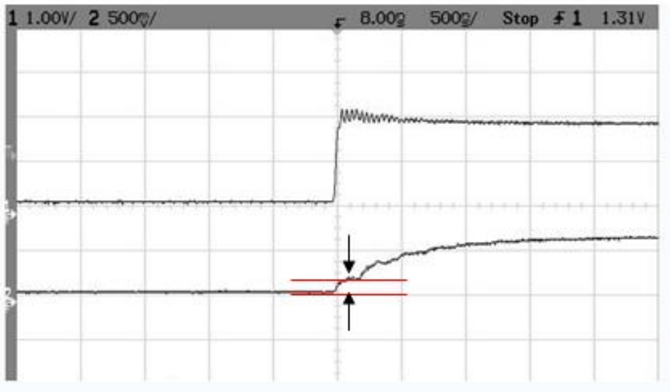

Figure 9. V_{in} and current flow (I_o)

The next measurement is to investigate the current diffusion characteristic in conductor when the R_L is smaller than the line impedance (Zo). The comparison between calculation and measurement can be seen in Figs. 6 and 9.

It can be concluded from simulation and laboratory measurement that if R_L is smaller than the line impedance Zo, deficiency current establish will occur where the electromagnetic energy is not sufficient for the load. As a result, the load voltage become smaller than V_A which in turn reduce the $-V_d$ that is propagated back toward the source with current displacement of $I_{D2} = -V_d/Zo$. By using the nth transition equation, it is clearly shown that voltage backward increased gradually from time to time until matching the voltage source V_A.

Table 2. Forward and backward voltage for $R_L=Zo/5$ (computed using VB-Excel)

V_A : 10 Volt
Z_o : 10 Ohm
R_l : 2 Ohm

V_{Fr} (V)	I_{fr} (A)	I_d (A)	ΔV (V)	V_b (V)	I_b (A)
10	1	4	-6.66667	3.333333	1.666667
10	2.333333	2.666667	-4.44444	5.555556	2.777778
10	3.222222	1.777778	-2.96296	7.037037	3.518519
10	3.814815	1.185185	-1.97531	8.024691	4.012346
10	4.209877	0.790123	-1.31687	8.683128	4.341564
10	4.473251	0.526749	-0.87791	9.122085	4.561043
10	4.648834	0.351166	-0.58528	9.414723	4.707362
10	4.765889	0.234111	-0.39018	9.609816	4.804908
10	4.843926	0.156074	-0.26012	9.739877	4.869939
10	4.895951	0.104049	-0.17342	9.826585	4.913292
10	4.930634	0.069366	-0.11561	9.88439	4.942195
10	4.953756	0.046244	-0.07707	9.922927	4.961463
10	4.969171	0.030829	-0.05138	9.948618	4.974309
10	4.979447	0.020553	-0.03425	9.965745	4.982873
10	4.986298	0.013702	-0.02284	9.977163	4.988582

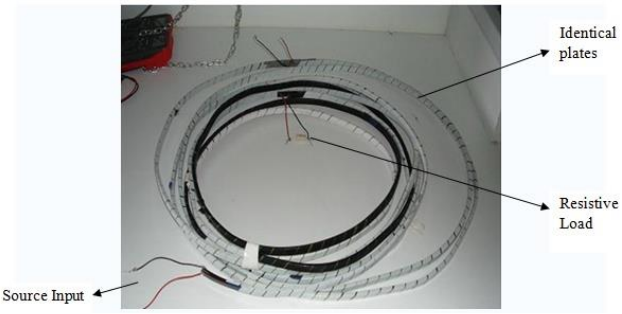

Figure 10. Experiment circuit set up for current diffusion study [2]

For study validation, the experimental set up is conducted as shown in Fig. 10. Using oscilloscope, the wave propagation diffusion of the experiment is measured as depicted in Figs. 7 and 9. The experiment set up as shown in Fig. 10 consists of identical plates where resistor terminals is designed to allow measurement conducted at the middle and the end of the identical plates.

4. Conclusion

Study of current diffusion characteristic in a conductor involves several parameters including propagation velocity of the current flow. The propagation is influenced by permeability, conductivity and the physical properties of the conductor. If the initial voltage is given, there will be an electric field (E) that related to current wave front I_D. Meanwhile, the magnetic field (H) that is also depending on I_D, will generate back electrostatic (E_b) which limit the electromagnetic velocity. The comparison value between R_L and Z_0 will determine the diffusion and propagation characteristic in the system. It can be drawn a conclusion from simulation and laboratory measurement that if R_L is smaller than the line impedance Z_0, deficiency current establish will occur where the electromagnetic energy is not sufficient for the load. As a result, the load voltage become smaller than V_A which in turn reduce the $–V_d$ that is propagated back toward the source with current displacement of $I_{D2}=-V_d/Zo$. By using the n^{th} transition equation, it is clearly shown that voltage backward increased gradually from time to time until matching the voltage source $V_{A.}$

References

[1] M. Saini, A. A. B. M. Zin, M. W. B. Mustafa, and A. R. Sultan, "An accurate fault detection and location on transmission line using wavelet based on Clarke's transformation," *PRZEGLĄD ELEKTROTECHNICZNY,* vol. 90, pp. 156-161, 2014.

[2] A. M. S. Yunus and A. Apollo, "Dampak Difusi Arus dalam Konduktor untuk Nilai Beban Resistif Lebih Besar dari Impedansi Saluran," *Jurnal Teknik Mesin SINERGI,* vol. 11, pp. 63-73, 2013.

[3] A. M. S. Yunus, A. Abu-Siada, and M. Masoum, "Effect of SMES unit on the performance of type 4 wind turbine generator during voltage sag," 2011.

[4] A. M. S. Yunus, A. Abu-Siada, and M. A. Masoum, "Improvement of LVRT capability of variable speed wind turbine generators using SMES unit," in *Innovative Smart Grid Technologies Asia (ISGT), 2011 IEEE PES,* pp. 1-7. 2011.

[5] I. Hussain, S. Ranjan, D. C. Das, and N. Sinha, "Performance Analysis of Flower Pollination Algorithm Optimized PID Controller for Wind-PV-SMES-BESS-Diesel Autonomous Hybrid Power System," *International Journal of Renewable Energy Research (IJRER),* vol. 7, pp. 643-651, 2017.

[6] M. Y. Khamaira, A. S. Yunus, and A. Abu-Siada, "Improvement of DFIG-based WECS performance using SMES unit," in *Power Engineering Conference (AUPEC), 2013 Australasian Universities*, 2013, pp. 1-5.

[7] M. R. Djalal, S. Sonong, and M. Marhatang, "Superconducting Magnetic Energy Storage Optimization for Load Frequency Control in Micro Hydro Power Plant using Imperialist Competitive Algorithm," *International Journal of Engineering and Manufacturing (IJEM),* vol. 8, pp. 1-9, 2018.

[8] M. R. Djalal, H. Setiadi, and A. Imran, "Frequency stability improvement of micro hydro power system using hybrid SMES and CES based on Cuckoo search algorithm," *Journal of Mechatronics, Electrical Power, and Vehicular Technology,* vol. 8, pp. 76-84.

[9] Boylestad, *Introductory Circuit Analysis*. New Jersey: Mc. Milan Publishing Company, 1990.

[10] https://www.britannica.com. (2018). Available: https://www.britannica.com/science/Poynting-vector.

EPI International Journal of Engineering
Volume 2, Number 1, February 2019, pp. 61-66
DOI: 10.25042/epi-ije.022019.11

*p*ISSN 2615-5109
*e*ISSN 2621-0541

Experimental Study on the Use of Pumice on the Rigid Pavement

Abdul Gaus[a]*, Imran[b], Chairul Anwar[c], Liska Novianti[d]

[a]Department of Civil Engineering, Faculty of Engineering, Khairun University. Email: gaussmuhammad@gmail.com
[b]Department of Civil Engineering, Faculty of Engineering, Khairun University. Email: imranimonamakuimo@outlook.com
[c]Department of Civil Engineering, Faculty of Engineering, Khairun University. Email: chairul_anwar@gmail.com
[d]Department of Civil Engineering, Faculty of Engineering, Khairun University. Email: liskasan0211@gmail.com

---

Abstract

The Pumice is a bright colored butian type, containing foam made from glass-walled bubbles and usually referred to as silicate volcanic glass granules. This pumice can be used as a substitute for normal sand as fine aggregate in a mixture of concrete mix. Based on the characteristic test examination, it can be seen that in testing the characteristics of pumice to the specifications of normal sand in specific gravity testing and weight testing of quicksand obtained results that are smaller than the specifications of normal sand and absorption tests obtained results greater than specifications on normal sand. The results of the normal sand compressive strength at BN is 250.95 kg /cm^2 while the results of the floating sand concrete compressive strength on BPA is 224, 965 kg /cm^2. Based on the research, it can be concluded that with the same quality of concrete, the quality of K-250 is different in comparison to the compressive strength of concrete in normal sand and pumice concrete shows almost the same results. Therefore, a more in-depth research is needed regarding the use of pumice instead of normal sand in a mixture of concrete mix.

Keywords: Compressive strength; concrete; pumice; sand concrete

---

1. Introduction

The development of concrete is necessary to improve the field of development. The development of civil engineering is very rapid and driven by the development of concrete technology and the concrete products produced are very innovative. Concrete can be said to be the main ingredient of construction buildings in Indonesia.

Ternate City is one of the areas in North Maluku that has the availability of sand, but if it is used continuously, the amount of sand will be depleted, therefore it is necessary to have an innovation related to the use of sand. Ternate City is an area with growing and increasing population mobility which is growing quite rapidly. The development of residential areas in Ternate caused an increase in the need for sufficient facilities and infrastructure. Nowadays the use of lightweight concrete is a very good alternative because of high quality concrete that has been used as a basic material for thousands of years ago is used for application in building construction. Normal concrete density is very high, which is around 2400 kg/m^3 so that the dead load will be very large. To reduce the dead load of a concrete structure or reduce heat transfer properties, it is necessary to use lightweight concrete using floating sand with a weight between 500-900 kg/m^3. Therefore, pumice is a material that is very suitable for use in lightweight concrete mixtures because it is able to absorb water on the surface and is very resistant to heat, then the shear behavior of the beam will be examined due to the use of pumice.

Natural resources are found in the Tidore Islands, one of which is the availability of pumice that can be used to make concrete. Based on the survey, it is necessary to innovate concrete mixes using quicksand which is then compared with the results of the concrete compressive strength in normal circulation. Therefore, it is necessary to have an in-depth study of the concrete press in the quicksand and the results of the compressive strength can be accounted for. Several research on lightweight concrete have been carried out based on literature studies on the number of writings and results that have been carried out based on laboratory tests and field testing.

Throughout the knowledge of the author, similar studies have never been conducted. I Made Alit Karyawan Salain conducted a study on compressive strength and modulus of lightweight concrete elasticity using pumice aggregate and flying ash as a substitute for most portland cement and superplasticizer [1]. This research was conducted to determine the mechanical behavior of

---

*Corresponding author.
Civil Engineering Department, Khairun University,
Jl. Jusuf Abdulrahman Unkhair Gambesi
Ternate Selatan, Indonesia, 97718

Table 1. Various types of concrete and its characteristic

No	Type of lightweight concrete	Specific gravity in	Compressive	Dry	Temperature
		the air	Strenght	shrinkage	Conductivity
		(kg/m^3)	(N/mm^2)	(%)	(W/M^{0}C)
1	hardened roasted ash flour (*Lytag*)	1360-1760	14-42	0.04-0.07	0.32-0.91
2	Slate or clay developed (*Agli & Leca*)	1360-1840	14-42	0.04-0.07	0.24-0.91
3	Charcoal foam (*Foamed Slag*)	1680-2080	10.5-42	0.03-0.07	0.24-0.93
4	Pumice	720-1440	2-14	0.04-0.08	0.21-0.6
5	*Clinker* (hardened granules)	1040-960	2-7	0.04-0.18	0.35-0.67
6	Stir in cement mixed with air (*aerated*)	400-960	1.4-4.9	0.02-0.03	0.10-0.22
7	Solid concrete with gravel or	2240-2480	14-70	0.03-0.05	1.40-1.80

lightweight concrete beams including compressive strength and modulus of elasticity of lightweight concrete. Nenni Simamora dan Mukti Hamza Harahap studied the effect of styrofoam addition with toluene solvents against press strength and modulus of elasticity of lightweight concrete [2]. This study aims to determine the effect of adding Styrofoam with toluene solvents on compressive strength and modulus of elasticity of lightweight concrete. Ratna Widyawati investiagted uptake, penetration and permeability of lightweight concrete [3]. This research was conducted to find out how much the lightweight concrete porosity as one of the concrete durability benchmarks, in this study carried out absorption test, penetration, and permeability of lightweight concrete. The test results show that the absorption value, penetration and water permeability of lightweight concrete increases with the increase in the value of the cement water factor.

Moreover, Purnawan Gunawan, Slamet Prayitno, dan Aroma Isman Abdul Majid studied the effect of adding zinc fiber to lightweight concrete with foam technology against compressive strength, tensile strength [4]. This research produced lightweight fibrous foam concrete, meaning lightweight concrete (specific gravity <1900 km/m^3). Based on the results of lightweight concrete compressive strength, aluminum fiber foam can be categorized as structural concrete. Bambang Supriyadi studied the sliding behavior in the layan state and the limits of the longitudinal reinforced concrete beam [5]. This study utilizes concrete weight reduction by examining the shear behavior of the beam in the boundary conditions. Pratikto investigated the utilization of lightweight concrete superplasticizers aggregate plastic bottled waste type of poly ethylene terephthalate (PET) [6]. This study looks for the ratio of mixtures of cement, coarse, fine and water aggregate and admixture enhancer substances.

Yudi Risdiyanto researched on concrete compressive strength study with weight ratio for mass concrete production using crushed stone rough aggregate (case study on sabo dam development project) [7]. This study aims to study the concrete compressive strength of K250 with weight ratio (WR) and volume ratio (VR) using coarse aggregate Batu Merapi broke as a trial mix on the Sabo dam development project. Murdock and Brook [8] wrote in concrete materials and practices titled book that it is necessary to aggregate combinations to obtain a lower specific gravity than normal concrete density. The type of the lightweinght and characteristic can be can be seen in Table 1.

2. Experiment

This test was carried out at the Laboratory of the structure and materials of the engineering faculty of the civil engineering study program at Khairun University. In general, the design of test objects in this study are as follows:

1. The cylinder size is 30 cm high with a diameter of 15 cm.
2. Using ordinary sand fine aggregates as comparative sand or sand control
3. Using fine aggregate pumice

The tool used to test the compressive strength of the cylinder is the 2000 kN Compression Machine. This test is based on standard specifications [9] by using the following formula:

$$f'c = \frac{P}{A} \tag{1}$$

where :

$f'c$ = compressive strength (kg/cm^2)
P = maximum load (kg)
A = area (cm^2)

This test uses 2 (two) specimens of cylinders with different fine aggregates but uses the same coarse aggregate, with a height of 30 cm and a diameter of 15 cm shown in Fig. 1 and variations in test objects can be seen in Table 2.

Tabel 2. Variation of test objects

Test objects	CWF	Area (cm^2)	Number of sampels
BN	0,35	176,625	1
BP	0,35	176,625	1

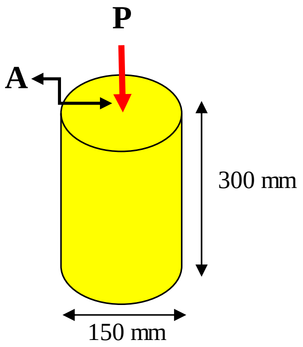

Figure 1. The Test specimens of concrete compressive strength

3. Result and Discussion

3.1. Characteristic of fine agregate

The results of the characteristics of the aggregate testing on normal sand and floating sand can be seen in Table 3. Normal sand which is used as a comparison for pumice is also tested for its characteristics so that it can be known the difference from the examination results on the two aggregates based on the specifications of the characteristic characteristics of fine aggregate according to SNI [10], to find out the testing specifications for fine aggregates. Figure 2 shows the image of fine aggregate gradation on normal sand and fine aggregate gradation on pumice.

Based on Table 3, it can be seen that the difference in the sludge level between normal sand and floating sand is 3.97%, the difference in dry weight between normal sand and floating sand is 1.92, the difference in dry weight of the saturated surface between normal sand and pumice is 2.07, the difference in apparent density between normal sand and pumice is 1.93, the difference in absorption between normal sand and pumice is 13.4%, the difference in volume weight when the solid condition between normal sand and pumice is 1, the difference in volume weight when the loose condition between normal sand and pumice is 0.94 and the difference in fine grained modulus between normal sand and pumice is 1.02.

Table 3. Characteristics of normal sand and pumice

No	**Type of testing**	**Result**	
		Normal Sand	**Pumice**
1	Sludge levels	4.5%	0.53%
2	Specific gravity		
	Bulk specificgravity	2.68	0.76
	Saturated surface dry	2.7	0.63
	Apparent specific gravity	2.75	0.82
	Absorption)	1.5%	14.98%
3	Volume weight		
	Solid condition	1.71	0.71
	Free condition	1.6	0.66
4	Analysis of filter	1.73%	2.75%


Normal Sand Pumice

Figure 2. Gradation of fine agregate

Figure 3. Gradation of coarse agregate

In Table 3, Volume weight on floating sand is lighter than normal sand specifications in SNI, in other words pumice is classified as lightweight concrete and can be used in a mixture of concrete mix. In the absorption test shown by Table 3, it is known that the absorption that occurs in floating sand is greatly increased and has a difference that is very far from absorption in normal sand, this is caused by the ability of pumice which has a very large water absorption capacity.

Based on Fig. 2, it can be seen that normal sand and quicksand in terms of texture are not much different. In terms of aggregate color, quicksand has a lighter color than the color of fine aggregate on normal sand.

This aggregate testing was carried out in the Structure and Material Laboratory of the Civil Engineering Department of the University of Khairun Ternate. In this study, there are two types of fine aggregate: normal sand fine aggregate originating from (quarry) Kalumata Village, Ternate. Other fine aggregates used in this study are quarry from Rumbune Village, Tidore. In this study, two types of fine aggregate were used because the comparison of characteristics between normal concrete and normal concrete would be compared to lightweight concrete. The results of this aggregate testing are based on SNI standards. The test results are presented in Table 3 and fine aggregate gradations are shown in Fig. 2.

This test is carried out to determine the characteristics of fine aggregates, namely normal sand is a fine aggregate originating from the Tubo Village, Ternate City and fine sand aggregate originating from the Kempland Tidore, which is then filtered to obtain sand gradation (pass No. 3 filter/8") and the next testing was carried out at the Engineering and Materials Laboratory of the Faculty of Engineering, Khairun Ternate University. This characteristic check on normal sand and floating sand is an examination of characteristics carried out with the same treatment in fine aggregates in general. In the normal sand characteristics testing, we discuss the standard parameters (specifications) that must be met by fine aggregate (normal sand) for the purpose of checking the results of testing of fine aggregates (normal sand and sand) carried out in the Laboratory. Testing Characteristics on Normal Sand (Kalumata quarry sand, Ternate is carried out as a comparison to the testing of characteristics that have been carried out on quicksand. As for the characteristics of normal sand can be seen in Table 3.

3.2. Testing concrete Compressive Strength

According to Wang and Salmon [11] the compressive strength of concrete is the magnitude of the load per unit area, which causes the concrete test object to disintegrate when a certain compressive force is generated by the press machine. The compressive strength of concrete is of paramount importance in concrete quality compared to other properties. The compressive strength of concrete is determined by the arrangement of the ratio of cement, coarse and fine aggregate, water. Comparison of cement water, the higher the compressive strength. A certain amount of water is needed to provide chemical action in hardening the concrete, excess water increases the ability of the work but decreases strength.

For testing the compressive strength of concrete that was carried out in the Structure and Civil Engineering Laboratory of Khairun Ternate University. There are two kinds of samples used in this test, namely K250 concrete quality for normal concrete and K250 concrete quality for floating sand concrete, then the two samples are mixed design with the same FAS, namely FAS 0.35. In the composition composition table for concrete quality K250 for normal concrete samples can be seen in Table 4 as follows:

Table 4 shows the results of comparison of cement water factors in normal concrete that is 0.35 with cement 627.62 kg/m^3, sand as much as 381.39 kg/m^3 with broken stones as much as 621.343 kg/m^3. The value obtained in Table 4 is the value obtained based on testing the characteristics of aggregation based on the results of the barchart aggregation between normal sand and coarse aggregate (split stone), while the results obtained from the barchart aggregation are the results obtained by using trial and error, as well as the barchart value obtained from the aggregation between quicksand and coarse aggregate. In floating sand concrete with the same water ratio of cement water factor is 0.35 with cement 585.71 kg/m^3, floating sand as much as 402.91 kg/m^3 with broken stones as much as 656.38 kg/m^3. Coarse aggregates used in normal concrete mixtures and floating sand concrete are the same coarse aggregates of the same quarry. The coarse aggregate gradations used in normal concrete and floating sand concrete are shown in Fig. 3, while the comparison composition of cement water in the concrete quality mixture K250 for floating sand concrete samples can be seen in Table 5.

Tabel 4. Cement water ratio of normal concrete

Concrete material	Weight (ton/m^3)	Ratio of cement
Cement	0.627	1.00
Split	0.381	0.61
Natural Stone	0.621	0.99
Water	0.219	0.35

Table 5. Ratio of cement water at pumice concrete

Concrete Material	Weight (ton/m^3)	Ratio of cement
Cement	0.585	1.00
Pumice	0.402	0.69
Split	0.656	1.12
Water	0.205	0.35

When testing concrete compressive strength, the first thing to do is checking the tools and materials as follows:

1. Cylinder mold, 152 mm diameter, 305 mm height;
2. Compactor stick, diameter 16 mm, length 600 mm, with rounded ends, made of clean steel and rust free;
3. Stirrer or water-resistant concrete mixing tank;
4. Scales with an accuracy of 0.3% of sample weight;
5. Press machine, capacity as needed;
6. A set of capping tools;
7. Additional equipment: bucket, shovel, spoon, leveling spoon, and talam;
8. A set of slump check tools, This test is shown in Fig.4
9. A set of concrete weight inspection equipment.

After the testing tools and materials have been prepared, the next thing that needs to be done is to do a physical examination of the material that will be used as a mixture of concrete, namely: physical examination of coarse aggregates and fine aggregates, while physical inspection of these materials must meet the specification specifications aggregates based on the specifications of the Indonesian National Standard (SNI). After carrying out a physical examination of the material both on coarse aggregates and fine aggregates, then the next is to make a concrete composition composition planning, then the next step is the manufacture of test items, the following is the procedure for making test specimens on concrete:

- Fill the mold with a mixture of concrete in 3 layers, each layer is compacted with 25 times the puncture evenly. At the time of compaction of the first layer, the compacting stick may not hit the mold base, when compaction of the second layer and the three compacting sticks may enter approximately 25.4 mm into the layer below;
- After completing compaction, tap the side of the mold slowly until the puncture cavity is closed, flatten the

Figure 4. Concrete slump testing

surface of the concrete and cover it immediately with a waterproof and rust resistant material, then leave the concrete in the mold for 24 hours and place it in a place free of vibration.

- After 24 hours, open the mold and remove the test object, to plan the concrete mixture, soak the specimen in the tank containing water at a temperature of 25 0C mentioned for curing, for the desired time, to control the concrete quality during concreting, ripening (curing) adjusted to requirements.

Then the next step is to test the compressive strength of the concrete, the following are the steps that must be followed in testing the compressive strength of the concrete:

1. Take a specimen that will determine its compressive strength from the soaking tub, then clean it from the dirt that is stuck with a damp cloth;
2. Determine the weight by means of weighing the specimen as shown in Fig. 5 and the size of the test object;
3. Capping the upper and lower surfaces of the specimen with sulfur mortar. This is done so that the surface of the test object becomes smooth and flat and facilitates the loading process on the test object until it becomes destroyed;
4. Place the test object on the machine press centricly;
5. Run the press machine with constant load increases ranging from 2 to 4 kg/cm^2 per second;
6. Perform the loading until the test is destroyed and record the maximum load that occurs during the examination of the test object.

Figure 5. Concrete weight measurement

Figure 6. Compressive strength test

After the stage of making concrete specimens, the final step is the data analysis stage, which is analyzing the results of the compressive strength that has been obtained in the tests that have been carried out in the laboratory.

Testing of concrete compressive strength is carried out when the age of concrete has reached 28 days. Histograms test results of normal concrete compressive strength and quicksand concrete can be seen in Fig. 6 as follows:

Testing of the compressive strength of the cylinder uses two samples with different fine aggregates, namely concrete that uses normal sand and concrete that uses pumice. Testing of compressive strength in normal concrete and floating sand concrete was carried out using the same variation of Cement Water Factor (FAS), namely FAS 0.35. Based on the results of the compressive strength test results obtained compressive strength in normal concrete is 252.351 kg/cm^2 and the compressive strength test results on floating sand concrete is 224.281 kg/cm^2. The quality of concrete in this normal concrete mixture is the same concrete quality as the mixture with fine aggregates that use quicksand, namely the K-250 concrete quality.

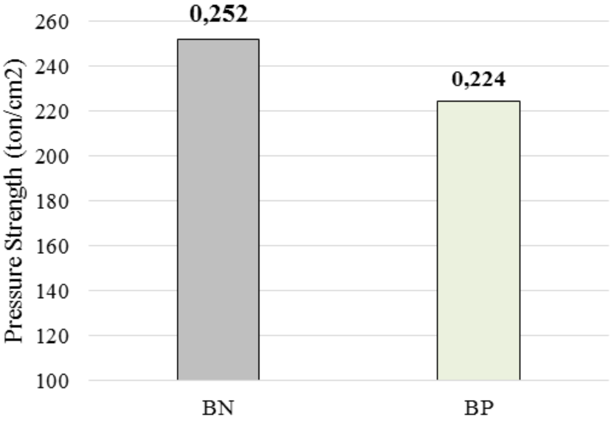

Figure 7. Histogram of testing compressive strength on concrete

4. Conclusion

Based on the results of the study, it can be concluded as follows:

1. The test results on the compressive strength of concrete that is between the normal sand and floating sand has a compressive strength that is not much different, that is the results of the normal sand concrete compressive strength at BN is 252.351 kg/cm^2 and the results of the research 224.281 kg/cm^2 and the difference in compressive strength of both samples was 28.07 kg/cm^2.
2. The use of the pumice as a mixture of concrete does not affect the quality of compressive strength in concrete.

Acknowledgement

This research is funded by the Higher Education and is part of the essay by Liska Novianti.

References

[1] Salain, I., Compressive Strength and Modulus of Elasticity of Lightweight Concrete by Using Aggregates of Pumice and Fly Ash as a Substitute for Part of Portland Cement and Superplasticizer, Proceeding of Seminar Nasional Teknik Sipil 1, 2015, 3-7. (in Bahasa)

[2] Simamora, N., Harahap, M., Effect of Addition of Stryfoam with Toluene Solvents on Compressive Strength and Modulus of Elasticity of Lightweight Concrete, Jurnal Einstein, 2015, 15-22. (in Bahasa)

[3] Widyawati, R., Absorption, Penetration and Permeability of Light Concrete, Proceeding of Seminar Nasional Sains dan Teknologi IV, Bandar Lampung, 2011, 29-33. (in Bahasa)

[4] Gunawan, P., Prayitno, S., Majid, A, I.A., The Effect of Zinc Fiber Addition on Lightweight Concrete with Foam Technology on Compressive Strength, Tensile Strength and Modulus of Elasticity, Konferensi Nasional Teknik Sipil, 2013. (in Bahasa)

[5] Supriyadi, B., et. al., Behavior of Sliding in the State of Service and Limits of Lengthy Perforated Concrete Beams, Jurnal Ilmiah Semesta Teknika, 2010, 145-154. (in Bahasa)

[6] Risdiyanto, Y., Study of Concrete Compressive Strength with a Weight Ratio for Mass Concrete Production using Coarse Aggregate of Broken Stone Merapi (Case Study on the Sabo Dam Construction Project), Civil Engineering, Universitas Negeri Yogyakarta, 2013. (in Bahasa)

[7] Pratikto, Utilization of Lightweight Concrete Superplasticizer Waste Plastic Bottle with aggregate Poly Ethylene Terephthalate (PET), Poli Teknologi Vol, 10 No. 1, 2011. (in Bahasa)

[8] Murdock, L.J., Brook, K.M., 1986, Concrete Materials and Practices, 4th Edition, Erlangga, Jakarta, 1986. (in Bahasa)

[9] BSNI, Concrete Press Strength Testing Method (SNI 03-2847-2002), Jakarta, 2002. (in Bahasa)

[10] BSNI, Methods of Testing Fine and Coarse Aggregate Filters Analysis (SNI 03-1968-1990), Jakarta, 1990. (in Bahasa)

[11] Wang., Salmon., Press Strength Testing on Concrete, Jakarta, 1990. (in Bahasa)

EPI International Journal of Engineering
Volume 2, Number 1, February 2019, pp. 67-73
DOI: 10.25042/epi-ije.022019.12

*p*ISSN 2615-5109
*e*ISSN 2621-0541

Free Vibration Analysis of L-Shaped Folded Thin Plates

Koji Sekine[a]*

[a]Mechanical Engineering, Department of Creative Engineering, National Institute of Technology, Kushiro College. Email:sekine@kushiro-ct.ac.jp

---

Abstract

Free vibration analysis of L-shaped folded thin plates having various boundary conditions is presented. Vibration properties of the folded plates are analyzed by means of the Ritz method. Displacement functions satisfying the geometric boundary conditions are assumed in the form of double power series. The interconnection of plate elements of the folded plates is defined by translational and rotational coupling springs. The generalized eigenvalue problem, which is derived by means of minimizing the energy functional, is solved to determine the natural frequencies and mode shapes. The accuracy and validity of the present solutions are demonstrated through convergence studies and comparisons with the results from the literature and FEM (finite element method) analysis solutions. Numerical results are presented for different conditions, such as width ratio, length ratio and the four types of boundary condition.

Keywords: Folded plate; natural vibration; vibration of continuous system

---

1. Introduction

Folded plates are widely used as a structural member on the fields of transportation, aerospace, ship and construction. Therefore, it is important to clarify and understand its vibration characteristics from a viewpoint of resonance problem in structural design.

Vibration problems of the folded plates have been studied extensively over the last few decades. Free vibration of a cantilever folded plate has been studied by the Ritz method [1]. Liu and Huang [2] showed the free vibration characteristics of a cantilever folded plate and a cylindrical curved plate by using the transfer matrix method. Free vibration of completely free folded plates considering rotational inertia has been investigated on the basis of finite element method [3]. Danial et al. [4] indicated the shock response of box-type beam based on finite element method. Free vibration of composite folded plates considering transverse shear deformation and rotational inertia has been analyzed by finite element method [5]. In addition, Nayaka et al. [6] presented transient response of composite sandwich folded plates by the use of finite element method. Most of these researches are analyzed by finite element method and detailed studies on the accuracy of solutions have been indicated. On the other hand, there are few examples of analysis showing the variations in the natural vibration characteristics due to the difference in dimensions and boundary conditions.

From the above review, this paper deals with the free vibration analysis of L-shaped folded plates by using Ritz method and a commercial FEM (finite element method) software, SolidWorks simulation. Practically, the strain energy and the kinetic energy of the folded plate and the elastic energy of the connecting springs are evaluated, and the frequency equation is derived by applying the minimization condition to the energy functional of the folded plate. In numerical example, accuracy and validity of solutions are shown from the convergence of solutions and the comparisons with the results in the published literature. Furthermore, the effects of dimension ratio and boundary conditions on natural vibration characteristics such as natural frequencies and vibration modes of the folded plates are illustrated and discussed.

2. Theoretical Formulation

2.1. Dimensions and displacement field of the folded plate

Figure 1 shows the dimensions and coordinate system of L-shaped folded plate composed of plate-1 and plate-2. As shown in the figure, the coordinate system o-x-y-z is taken and displacements in the x, y and z directions at arbitrary points on the folded plate are represented by u, v and w, respectively. Also, a, b and L are the length and width of plate-1 and plate-2, and h is the thickness of the plates.

As shown in Fig. 2, plate-1 and plate-2 are connected by the translational springs k_u , k_v and k_w and the rotational spring k_{rot}. Therefore, the relative translational and the relative angular displacements are constrained to zero on the connection line of plate-1 and plate-2.

---

*Corresponding author. Tel.: +81-154-57-7294
Otanoshike-Nishi 2-32-1, Kushiro, Hokkaido, Japan
084-0916

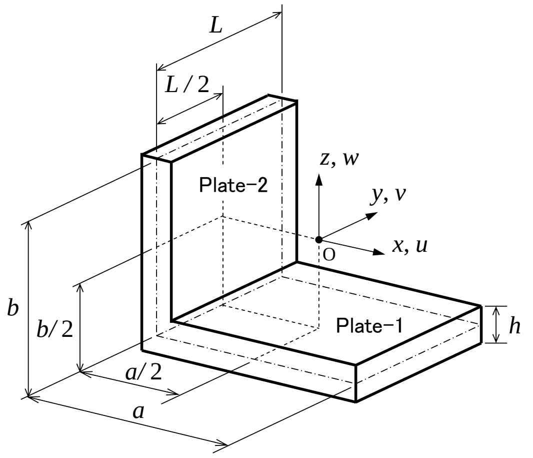

Figure 1. Dimensions and the coordinate system of L-shaped folded plate

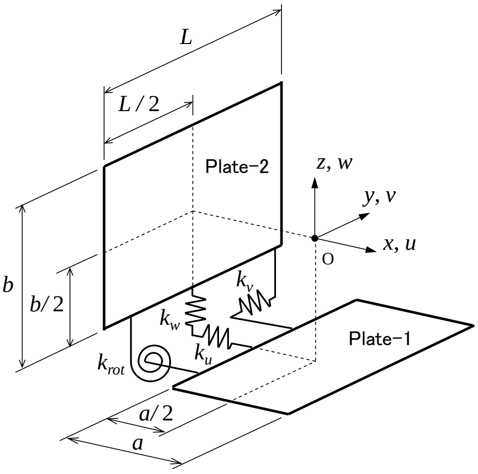

Figure 2. Connection of plate elements defined by translational and rotational springs

Kirchhoff 's assumption (Line elements perpendicular to the middle plane of the plate remain straight and perpendicular to the middle plane during deformation) is applied to the bending deformation of plate-1 and plate-2. In this case, displacements u_p, v_p and w_p (p→1: plate-1, p→2: plate-2) at arbitrary points of plate-1 and plate-2 can be written in Eq. (1), including displacement u_{p0} , v_{p0} and w_{p0} on the middle plane.

$$\begin{aligned}
&u_1(x,y,z,t) = u_{10}(x,y,t) - \left(z+\frac{b}{2}\right)\frac{\partial w_{10}(x,y,t)}{\partial x} \\
&v_1(x,y,z,t) = v_{10}(x,y,t) - \left(z+\frac{b}{2}\right)\frac{\partial w_{10}(x,y,t)}{\partial y} \\
&w_1(x,y,z,t) = w_{10}(x,y,t) \\
&u_2(x,y,z,t) = u_{20}(y,z,t) \\
&v_2(x,y,z,t) = v_{20}(y,z,t) - \left(x+\frac{a}{2}\right)\frac{\partial u_{20}(y,z,t)}{\partial y} \\
&w_2(x,y,z,t) = w_{20}(y,z,t) - \left(x+\frac{a}{2}\right)\frac{\partial u_{20}(y,z,t)}{\partial z}
\end{aligned} \tag{1}$$

2.2. Potential and kinetic energies

Assuming that the folded plate is a linear elastic body, the stress-strain relation is expressed as Eq. (2). In each subsequent equations, suffixes are replaced as p→1, r→x, s→y for plate-1 and p→2, r→y, s→z for plate-2. Also, Q_{ij} (i, j=1,2,6) in Eq. (2) is the stiffness coefficients determined by the modulus of longitudinal elasticity E and the Poisson's ratio ν, and are given by Eq. (3).

$$\begin{Bmatrix} \sigma_{rp} \\ \sigma_{sp} \\ \tau_{rsp} \end{Bmatrix} = \begin{bmatrix} Q_{11} & Q_{12} & 0 \\ Q_{12} & Q_{22} & 0 \\ 0 & 0 & Q_{66} \end{bmatrix} \begin{Bmatrix} \varepsilon_{rp} \\ \varepsilon_{sp} \\ \gamma_{rsp} \end{Bmatrix} \tag{2}$$

$$Q_{11} = Q_{22} = \frac{E}{1-\nu^2}\,,\, Q_{12} = \frac{\nu E}{1-\nu^2}\,,\, Q_{66} = \frac{E}{2(1+\nu)} \tag{3}$$

Considering the harmonic vibration driving at the angular frequency ω[rad/s] with respect to the folded plate, each displacements on the middle plane can be written as follows using the maximum amplitude U_p , V_p and W_p.

$$\begin{aligned}
&u_{p0}(r,s,t) = U_p(r,s)\sin\omega t \\
&v_{p0}(r,s,t) = V_p(r,s)\sin\omega t \\
&w_{p0}(r,s,t) = W_p(r,s)\sin\omega t
\end{aligned} \tag{4}$$

The maximum strain energy P_p of plate-1 (p→1) and plate-2 (p→2) is evaluated by Eq. (5). In the equation, [A] and [D] are extensional and bending stiffness matrix, $\{\varepsilon_p\}$ and $\{\kappa_p\}$ are strain and curvature vector, and components of the matrices and the vectors are given as Eqs. (6) and (7).

$$P_p = \frac{1}{2}\int_s\int_r \left[\{\varepsilon_p\}^{\mathrm{T}}[A]\{\varepsilon_p\} + \{\kappa_p\}^{\mathrm{T}}[D]\{\kappa_p\}\right] dr\,ds \tag{5}$$

$$\begin{gathered}
[A] = \begin{bmatrix} A_{11} & A_{12} & 0 \\ A_{12} & A_{22} & 0 \\ 0 & 0 & A_{66} \end{bmatrix},\ [D] = \begin{bmatrix} D_{11} & D_{12} & 0 \\ D_{12} & D_{22} & 0 \\ 0 & 0 & D_{66} \end{bmatrix} \\
A_{ij} = \int_{-h/2}^{h/2} Q_{ij}\,dz\,,\, D_{ij} = \int_{-h/2}^{h/2} z^2 Q_{ij}\,dz \ \ (i,j=1,2,6)
\end{gathered} \tag{6}$$

$$\begin{aligned}
&\{\varepsilon_1\} = \left\{\frac{\partial U_1}{\partial x}, \frac{\partial V_1}{\partial y}, \frac{\partial U_1}{\partial y} + \frac{\partial V_1}{\partial x}\right\}^{\mathrm{T}} \\
&\{\kappa_1\} = \left\{-\frac{\partial^2 W_1}{\partial x^2}, -\frac{\partial^2 W_1}{\partial y^2}, -2\frac{\partial^2 W_1}{\partial x \partial y}\right\}^{\mathrm{T}} \\
&\{\varepsilon_2\} = \left\{\frac{\partial V_2}{\partial y}, \frac{\partial W_2}{\partial z}, \frac{\partial V_2}{\partial z} + \frac{\partial W_2}{\partial y}\right\}^{\mathrm{T}} \\
&\{\kappa_2\} = \left\{-\frac{\partial^2 U_2}{\partial y^2}, -\frac{\partial^2 U_2}{\partial z^2}, -2\frac{\partial^2 U_2}{\partial y \partial z}\right\}^{\mathrm{T}}
\end{aligned} \tag{7}$$

Further, the maximum elastic energy P_u, P_v and P_w of the translational springs and the maximum elastic energy P_{rot} of the rotational spring can be evaluated as follows:

$$
\begin{aligned}
P_u &= \frac{k_u}{2}\int_{-L/2}^{L/2}\left(U_1\Big|_{x=-a/2} - U_2\Big|_{z=-b/2}\right)^2 dy \\
P_v &= \frac{k_v}{2}\int_{-L/2}^{L/2}\left(V_1\Big|_{x=-a/2} - V_2\Big|_{z=-b/2}\right)^2 dy \\
P_w &= \frac{k_w}{2}\int_{-L/2}^{L/2}\left(W_1\Big|_{x=-a/2} - W_2\Big|_{z=-b/2}\right)^2 dy \\
P_{rot} &= \frac{k_{rot}}{2}\int_{-L/2}^{L/2}\left(\frac{\partial W_1}{\partial x}\Big|_{x=-a/2} + \frac{\partial U_2}{\partial z}\Big|_{z=-b/2}\right)^2 dy
\end{aligned}
\tag{8}
$$

where k_u, k_v, k_w and k_{rot} represent the stiffness of the translational and rotational connecting spring distributed in the y direction. The maximum potential energy P_{max} of the folded plate is given by the following equation as the sum of the maximum strain energy of plate-1 and plate-2 and the maximum elastic energy of the connecting spring.

$$
P_{max} = P_1 + P_2 + P_u + P_v + P_w + P_{rot} \tag{9}
$$

On the other hand, the maximum kinetic energy T_p of plate-1 (p→1) and plate-2 (p→2) is evaluated by Eq. (10) with the volume density ρ of the folded plate, and the maximum kinetic energy T_{max} of the folded plate is given by Eq. (11) as the sum of the maximum kinetic energy of plate-1 and plate-2.

$$
T_p = \frac{\omega^2}{2}\int_s\int_r \rho h \left(U_p^2 + V_p^2 + W_p^2 \right) dr ds \tag{10}
$$

$$
T_{max} = T_1 + T_2 \tag{11}
$$

2.3. Derivation of the frequency equation

Displacement functions of plate-1 (p→1) and plate-2 (p→2) that satisfy the geometric boundary conditions at each edge of the folded plate are given by a series form as follows:

$$
\begin{aligned}
U_p(r,s) &= \sum_{m=0}^{I-1}\sum_{n=0}^{I-1} U_{pmn} F_{pumn}(r,s) \\
V_p(r,s) &= \sum_{m=0}^{I-1}\sum_{n=0}^{I-1} V_{pmn} F_{pvmn}(r,s) \\
W_p(r,s) &= \sum_{m=0}^{I-1}\sum_{n=0}^{I-1} W_{pmn} F_{pwmn}(r,s)
\end{aligned}
\tag{12}
$$

where U_{pmn}, V_{pmn} and W_{pmn} represent undetermined coefficients. In present analysis, the four kinds of boundary condition *Clamp-1*, *Clamp-2*, *Cantilever* and *Free* shown in Fig. 3 are taken into consideration. Also, the admissible function F_{pdmn} (d→u, v, w) in Eq. (12) is given as a power function from Eq. (13) to Eq. (16).

Clamp-1;

$$
\begin{aligned}
&F_{1umn}(x,y) = F_{1vmn}(x,y) = x^m y^n (y^2 - L^2/4) \\
&F_{1wmn}(x,y) = x^m y^n (y^2 - L^2/4)^2 \\
&F_{2umn}(y,z) = y^m z^n (y^2 - L^2/4)^2 \\
&F_{2vmn}(y,z) = F_{2wmn}(y,z) = y^m z^n (y^2 - L^2/4)
\end{aligned}
\tag{13}
$$

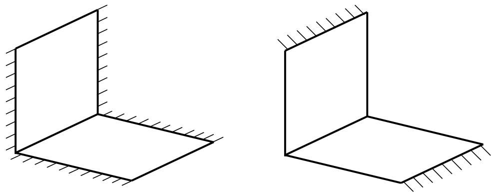

(a) Clamp-1 (b) Clamp-2

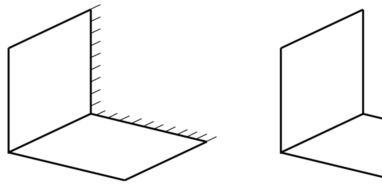

(c) Cantilever (d) Free

Figure 3. Four types of the boundary condition

Clamp-2;

$$
\begin{aligned}
&F_{1umn}(x,y) = F_{1vmn}(x,y) = x^m y^n (x - a/2) \\
&F_{1wmn}(x,y) = x^m y^n (x - a/2)^2 \\
&F_{2umn}(y,z) = y^m z^n (z - b/2)^2 \\
&F_{2vmn}(y,z) = F_{2wmn}(y,z) = y^m z^n (z - b/2)
\end{aligned}
\tag{14}
$$

Cantilever;

$$
\begin{aligned}
&F_{1umn}(x,y) = F_{1vmn}(x,y) = x^m y^n (y - L/2) \\
&F_{1wmn}(x,y) = x^m y^n (y - L/2)^2 \\
&F_{2umn}(y,z) = y^m z^n (y - L/2)^2 \\
&F_{2vmn}(y,z) = F_{2wmn}(y,z) = y^m z^n (y - L/2)
\end{aligned}
\tag{15}
$$

Free;

$$
\begin{aligned}
&F_{1umn}(x,y) = F_{1vmn}(x,y) = F_{1wmn}(x,y) = x^m y^n \\
&F_{2umn}(y,z) = F_{2vmn}(y,z) = F_{2wmn}(y,z) = y^m z^n
\end{aligned}
\tag{16}
$$

Furthermore, the displacement functions given by Eq. (12) are substituted into the maximum potential and the maximum kinetic energy described by Eqs. (9) and (11). Also, applying the minimization condition equation given by Eq. (17) to the energy functional L=$T_{\max}$−$P_{\max}$ derives the frequency equation as generalized eigenvalue problem given by Eq. (18).

$$
\frac{\partial L}{\partial U_{pmn}} = \frac{\partial L}{\partial V_{pmn}} = \frac{\partial L}{\partial W_{pmn}} = 0\,, \qquad (\,p:1,2 \qquad m,n = 0,1,2,\ldots,I-1) \tag{17}
$$

$$
\begin{aligned}
&[K]\{Q\} = \omega^2 [M]\{Q\}\,, \\
&\{Q\} = \{\,U_{1mn}, V_{1mn}, W_{1mn}, U_{2mn}, V_{2mn}, W_{2mn}\,\}^{\mathrm{T}}
\end{aligned}
\tag{18}
$$

In Eq. (18), $[K]$ and $[M]$ are the stiffness matrix and the mass matrix, respectively. By substituting the eigenvector $\{Q\}$ into the displacement function given by Eq. (12), the vibration mode of the folded plates can be obtained. In numerical example, the natural angular frequency ω[rad/s] is expressed as the dimensionless frequency Ω shown in Eq. (19).

$$
\Omega = \omega a^2 \sqrt{\frac{\rho h}{D_0}} \qquad \left(D_0 = \frac{E h^3}{12(1-\nu^2)} \right) \tag{19}
$$

3. Numerical Results and Discussions

Based on the previous analysis, numerical study will be considered on the free vibration characteristics of the L-shaped folded plate. In numerical calculation and software simulation, the longitudinal modulus of elasticity E=207GPa, Poisson's ratio ν=0.3 and the volume density ρ=7800kg/m^3 are used as the material constant of the folded plate. In addition, the analytical results by SolidWorks simulation which is a commercial FEM (finite element method) software are included within each tables and figures.

Table 1 presents the convergence study of dimensionless frequency Ω with respect to variations of the number of terms $I\times I$ of displacement functions given by Eq. (12) and the connecting spring stiffness k_u, k_v, k_w and k_{rot} for the folded plate having *Clamp-1* boundary condition. Dimensionless frequencies Ω converge with four significant figures in terms of the number of terms $I\times I$ =12×12 and spring stiffness $k_u = k_v = k_w = k_{rot} = 10^{11}$ in any mode number. Also, dimensionless frequencies Ω are consistent with the results given by SolidWorks simulation with three significant figures. Therefore, the number of terms $I\times I$=12×12 was adopted to the displacement function given by Eq. (12), and all spring stiffness were set to 10^{11} in present calculation.

Table 2 shows comparisons of dimensionless frequency Ω of the folded plate having *Cantilever* boundary condition. In the table, Irie et al. [1] show the analytical solutions by the Ritz method, Liu and Huang [2] and Haldar and Sheikh [5] give results by the finite element method. In particular, the transverse shear deformation is taken into account on the bending deformation of the folded plate in [5].

Table 1. Convergence study of dimensionless frequencies Ω
[a/b=1, L/a=1, h/a=0.01, *Clamp-1*]

Mode No.	Num.of terms $I\times I$	Spring stiffness (k_u, k_v, k_w, k_{rot})			
		10^8	10^9	10^{10}	10^{11}
1	9×9	23.362	23.373	23.374	23.374
	10×10	23.360	23.371	23.373	23.373
	11×11	23.358	23.369	23.371	23.371
	12×12	23.358	23.369	23.370	23.370
	FEM				23.366
2	9×9	23.903	23.922	23.924	23.925
	10×10	23.901	23.921	23.923	23.923
	11×11	23.899	23.918	23.921	23.921
	12×12	23.898	23.918	23.920	23.920
	FEM				23.915
3	9×9	35.415	35.554	35.570	35.572
	10×10	35.413	35.552	35.568	35.570
	11×11	35.411	35.550	35.566	35.568
	12×12	35.411	35.549	35.566	35.568
	FEM				35.548
4	9×9	39.618	39.955	39.990	39.993
	10×10	39.615	39.952	39.987	39.990
	11×11	39.614	39.951	39.985	39.989
	12×12	39.613	39.950	39.984	39.988
	FEM				39.962
5	9×9	62.845	62.881	62.886	62.886
	10×10	62.838	62.875	62.880	62.880
	11×11	62.836	62.873	62.877	62.878
	12×12	62.833	62.870	62.874	62.875
	FEM				62.852

Table 2. Comparisons of dimensionless frequencies Ω
[a/b=1, L/a=2, h/a=0.04, *Cantilever*]

Source	Mode No.				
	1	2	3	4	5
Present (Ritz)	2.12	4.21	7.727	9.050	14.95
Present (FEM)	2.12	4.21	7.722	9.042	14.95
Ritz method (1)	2.13	4.23	7.768	9.098	15.47
FEM (2)	2.13	4.20	7.734	9.024	15.41
FEM (5)	2.11	4.16	7.734	8.985	14.80

Table 3. Comparisons of dimensionless frequencies Ω
[a=0.28m, b=0.428m, L=0.215m, h=0.00121m,
ρ=7850kg/m^3, *Free*]

Source	Mode No.			
	1	2	3	4
Present (Ritz)	2.795	6.464	8.505	9.911
Present (FEM)	2.794	6.462	8.503	9.907
Exp.(3)	2.748	6.612	8.446	9.547
FEM (6)	2.832	6.468	8.630	9.937

Table 3 presents comparisons of the dimensionless frequency Ω with respect to the folded plate with *Free* boundary condition. Allman [3] gives experiment results and Nayak et al. [6] present analytical solutions by the finite element method considering transverse shear deformation and rotational inertia in free vibration analysis of the folded plates.

In Tables 2 and 3, the present solutions are in good agreement wit h the results by the references, and it is shown that connecting conditions of translation and rotation between plate-1 and plate-2 are sufficiently satisfied by using the connecting spring. Also, the accuracy and validity of the present solutions are verified through comparing with results from references.

Figures 4 and 5 show vibration modes with respect to variation in the length ratios a/b for the folded plates having *Clamp-1* and *Free* boundary conditions, respectively. Dimensionless frequency Ω_{Ritz} and Ω_{FEM} by present analysis and SolidWorks simulation are shown under each vibration modes. The folded plates having *Clamp-1* with the constraint of the edge shows higher Ω than the plates having *Free* boundary condition. In any of the boundary conditions, dimensionless frequencies Ω increase as the length ratio a/b increases. Also, vibration mode shape of the folded plate has a beam type mode when a/b=0.1, and a plate type mode when a/b=10.

Figures 6 and 7 give vibration modes with respect to variation versus the width ratio L/a for the folded plates with *Clamp-1* and *Free* boundary conditions. In the both of the boundary conditions, dimensionless frequencies Ω decrease as the width ratio L/a increases. The reduction rate of Ω with respect to the increase in the width ratio L/a is larger in the folded plate having *Clamp-1* than in the folded plate having *Free* boundary condition without constraint on the edge side. The folded plate has the beam type vibration modes when L/a=0.1 and 10, and shows the plate type vibration modes when L/a=2, because plate-1 and plate-2 become the flat plates in the case of L/a=2.

Figure 8 shows the variations of the dimensionless frequency Ω with respect to the length ratio a/b for the folded plates with *Clamp-1*, *Clamp-2*, *Cantilever* and *Free* boundary conditions. In the figure, the solid line shows the present solution, and the small circles show the solutions by SolidWorks simulation. The folded plate having *Clamp-1*, which has constraint on four sides gives high Ω. Also, in any boundary condition, Ω shows an increasing tendency as the length ratio a/b increases. In addition, the veering points which frequency curves of different modes approach each other are observed in 3rd and 4th mode of *Clamp-1*, 2nd and 3rd mode of *Clamp-2*, 4th and 5th mode of *Cantilever*, 1st and 2nd mode of *Free*.

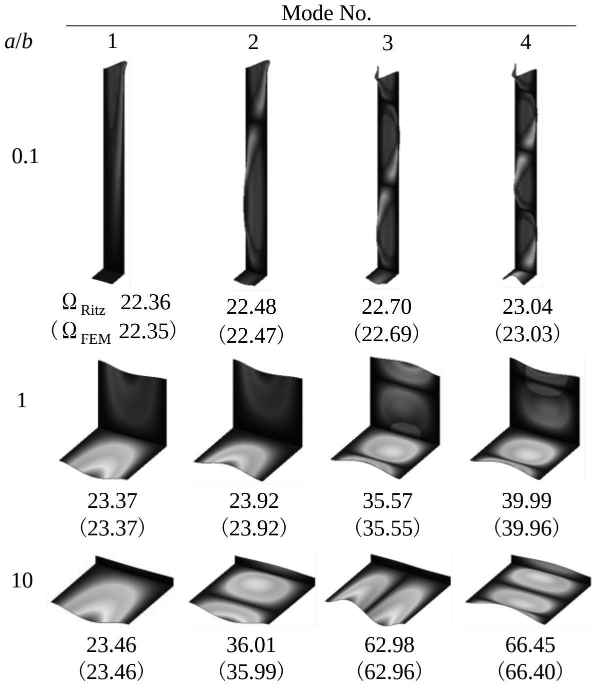

Figure 4. Vibration modes of L-shaped folded plates
[L/a =1, h/a =0.01, *Clamp-1*]

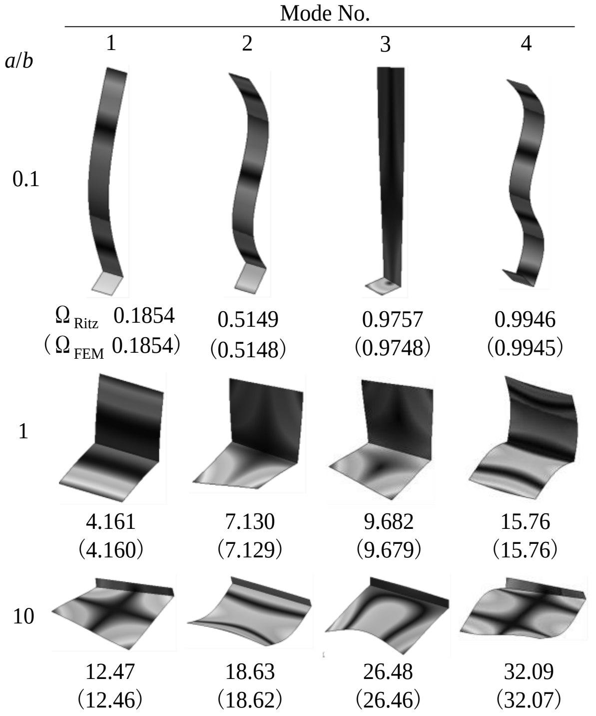

Figure 5. Vibration modes of L-shaped folded plates
[L/a =1, h/a =0.01, *Free*]

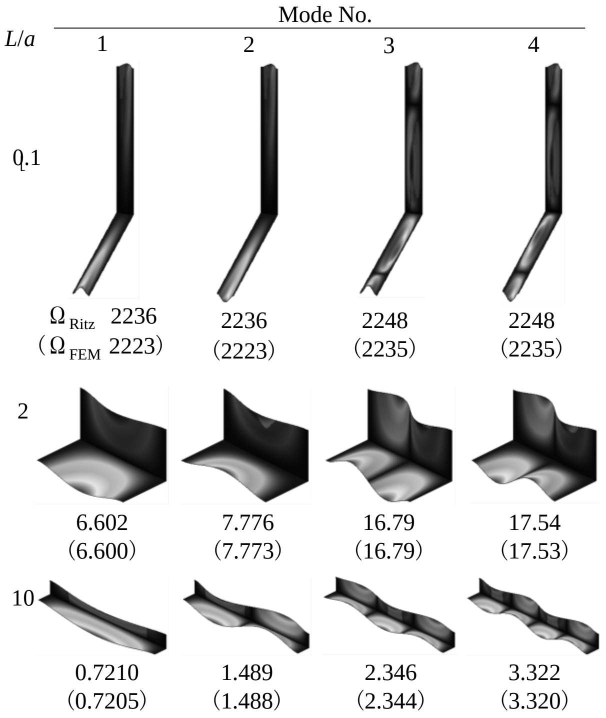

Figure 6. Vibration modes of L-shaped folded plates
[a/b =1, h/a =0.01, *Clamp-1*]

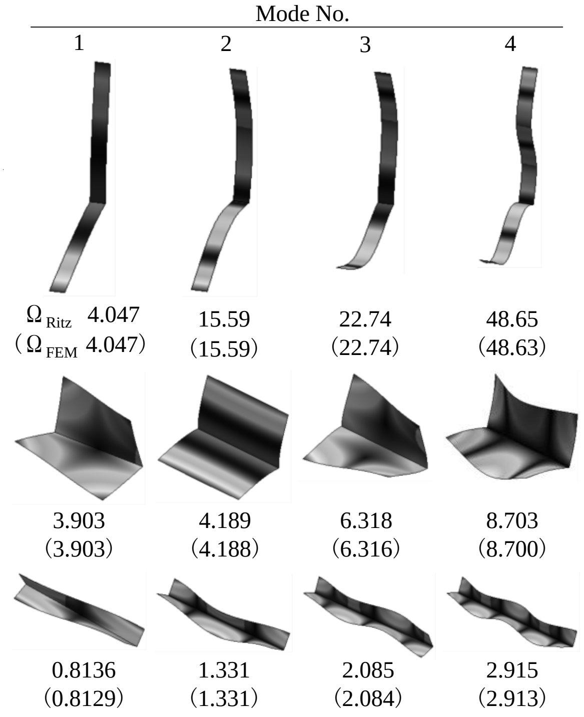

Figure 7. Vibration modes of L-shaped folded plates
[a/b =1, h/a =0.01, *Free*]

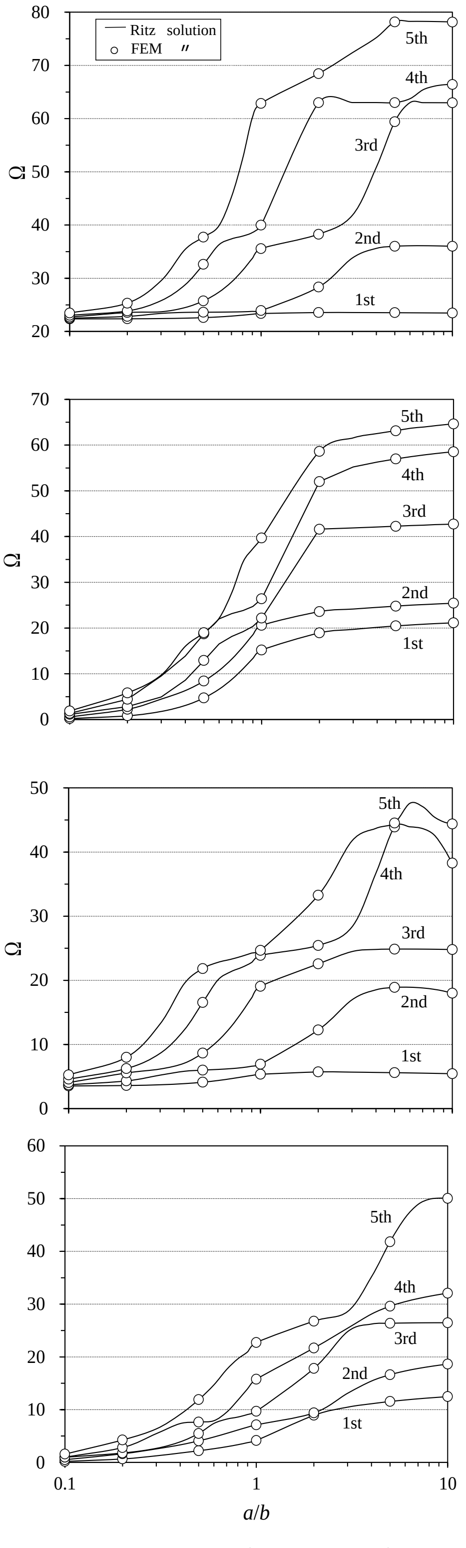

Figure 8. Variations of dimensionless frequencies Ω versus the length ratio for L-shaped folded plates
[*L*/*a*=1, *h*/*a*=0.01]

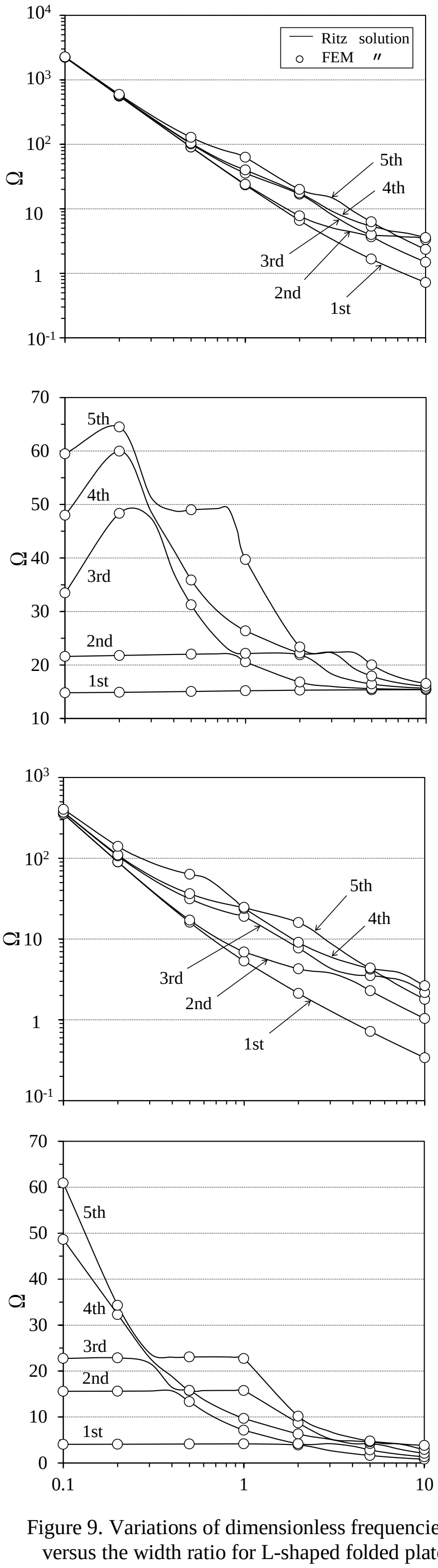

Figure 9. Variations of dimensionless frequencies Ω versus the width ratio for L-shaped folded plates
[*a*/*b*=1, *h*/*a*=0.01]

Figure 9 shows the variations of the dimensionless frequency Ω with respect to the width ratio *L*/*a* for the folded plates with the four kinds of boundary condition *Clamp-1*, *Clamp-2*, *Cantilever* and *Free*. On the folded plates having *Clamp-1* and *Cantilever*, high Ω is given in the range of the width ratio $L/a<1$. Also, in any boundary condition, Ω shows a decreasing tendency as the width ratio *L*/*a* increases. On the other hand, the variations in the fundamental frequency with respect to the width ratio *L*/*a* is scarce in *Clamp-2* and *Free* where there is no constraint on the sides.

4. Concluding Remarks

In this study, the free vibration analysis of the L-shaped folded plates has been formulated by applying the Ritz method. Several perceptions obtained through discussion considering numerical examples are as follows.

On natural frequencies of the L-shaped folded plates, accuracy and validity of present solutions were verified from the comparisons with results by FEM software and literature. Also, it was shown that connecting conditions of translation and rotation between two plates are satisfied by using the connecting spring. In addition, vibration modes of the folded plates exhibit a beam type and a plate type shape according to the length ratio and the width ratio. Regarding the variations of frequency curves, in any boundary condition, natural frequencies show an increasing as the length ratio increases and a decreasing as the width ratio increases.

It is expected that present numerical results are useful for the optimization design on vibration problems of the folded plates.

References

[1] Irie T, Yamada G, Kobayashi Y. Free vibration of a cantilever folded plate. J Acoust Soc Am 1984;6:1743-48.

[2] Liu WH, Huang CC. Vibration analysis of folded plates. J Sound Vib 1992;1:123-37.

[3] Allman DJ. Implementation of a flat facet shell finite element for applications in structural dynamics. Comput Struct 1996;4:657-63.

[4] Danial AN, Doyle JF, Rizzi SA. Dynamic analysis of folded plate structures. Trans ASME J Vib Acoust 1996;118:591-98.

[5] Haldar S, Sheikh AH. Free vibration analysis of isotropic and composite folded plates using a shear flexible element. Finite Elem Anal Des 2005; 42:208-26.

[6] Nayak AK, Shenoi RA, Blake JIR. A study of transient response of initially stressed composite sandwich folded plates. Compos B Eng 2013;44:67-76.

EPI International Journal of Engineering
Volume 2, Number 1, February 2019, pp. 74-79
DOI: 10.25042/epi-ije.022019.13

*p*ISSN 2615-5109
*e*ISSN 2621-0541

Mathematical Modeling in Combining Photovoltaic and Thermoelectric Generator Using a Spectrum Splitter

Hariyanto[a], Mustofa[b]*, Zuryati Djafar[c], Wahyu H. Piarah[d]

[a]Department of Mechanical Engineering, Engineering Faculty, Musamus University, Merauke, Indonesia. Email: hryengine@gmail.com
[b]Department of Mechanical Engineering, Engineering Faculty, Universitas Tadulako, Palu, Indonesia. Email: mustofauntad@gmail.com
[c]Department of Mechanical Engineering, Engineering Faculty, Universitas Hasanuddin, Gowa, Indonesia. Email: zuryatidjafar@unhas.ac.id
[d] Department of Mechanical Engineering, Engineering Faculty, Universitas Hasanuddin, Gowa, Indonesia. Email: wahyupiarah@unhas.ac.id

---

Abstract

The experimental stages of converting solar energy into electrical energy in Photovoltaic and Thermoelectric Generator (PV-TEG) hybrid takes a long time. Mathematical modeling is an approach to find out the initial data before conducting experiments leading to minimized design errors, time and budget. The mathematical model is created to analyze the performance of a PV-TEG hybrid module. Modeling is performed as an electrical circuit equivalent to Kirchoff's Current Law (KCL) by deriving several equations corresponding to the characteristics of each module. Type of PV is amorphous Silicon (a-Si), while TEG is Bismuth Telluride (Bi_2Te_3). The AM1.5D standard solar spectrum is split its wavelength using hot mirror, where the wavelengths of 400-690 nm are transmitted to PV and 690-1150 nm are reflected to TEG. All of the PV-TEG hybrid parameters, for example intensity, temperature, and material property are obtained from the specification data of each module. As a result, the maximum total power is 0.1710 W with 5.1% of its efficiency.

Keywords: Photovoltaic; power output; spectrum splitter; thermoelectric generator

---

1. Introduction

Solar energy is a renewable energy source that continues to be developed to meet future energy needs. The light and thermal produced by the solar energy can be used for daily living needs. Photovoltaics (PV) and thermoelectric generator (TEG) are devices whose utilization have been developed to convert light and heat into electrical energy. PV can absorb up to 80% of solar radiation, but not all can be converted into electrical energy, partly are discharged into waste heat which can increase the temperature of the cell and ultimately cause a decrease in efficiency [1]. Waste heat which is wasted due to increasing temperature can be utilized by using a thermoelectric [2]. TEG is a power generating device that converts heat energy into electrical energy due to temperature differences between the hot side and the cold side [3]. The development of research combining stacked PV-TEG integration has been done experimentally to observe the maximum work of PV and TEG [4–6], and simulations with mathematical modeling with the help of Matlab/simulink and experiments carried out by Babu and Ponnambalam [7].

While research with hybrid PV-TEG mathematical modeling that splits the light spectrum is still rarely conducted. Actually the basic idea about spectrum splitting was already introduced by Tritt et al. [8] in a bulletin, the study was expanded by Kraemer et al. [9] by varying PV in 3 types of solar cells (a-Si: H, mc-Si; H and polymer) and 1 type of TEG. Unfortunately, the radiation source that came AM1.5G was not concentrated before reaching the spectrum splitter and the type of splitter itself was not written on the specification of its light transmission power, as done Ju et al. [10]. Experimented in closed spaces, the latest research on PV-TEG hybrid using Hot mirror spectrum splitter has been carried out by Mustofa et al. [11] which utilizes artificial light spectrum radiation sources known as artificial sun, namely Xenon, Halogen and Incandescent bulbs whose lights concentrated with Fresnel lenses before reaching the splitter (Hot mirror). The concentrated light is divided according to its wavelength in order to adjust to the needs of the PV module and TEG. However, the results only described radiant heat and wavelengths of lights, while inputs from radiation and wavelengths did not describe the characteristics of each PV and TEG.

---

*Corresponding author. Tel.: +62-813-4107-4257
Palu, Sulawesi Tengah, Indonesia
94118

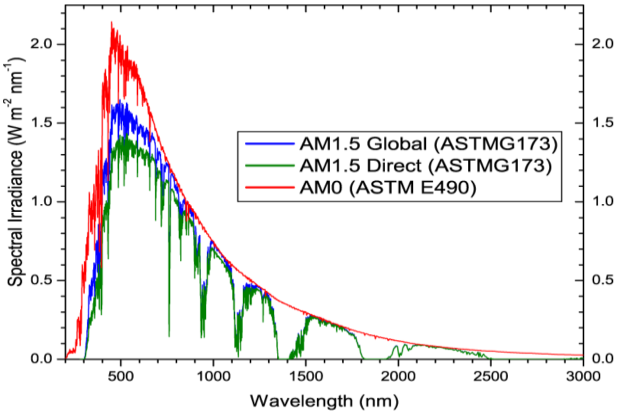

Figure 1. AM1.5 Global Sun Spectrum Measurement (ASTMG173), AM1.5 Direct (ASTMG173) and AM0 (ASTM E490) [15]

Mathematical modeling has been made to see the characteristics of PV [12, 13] and TEG has been carried out by Rukdq et al. [14], by inserting the required input parameters. Therefore, in this paper the author conducts modeling by combining the PV mathematical model and TEG which describe the characteristics of each module. The used radiation source is a standard spectrum AM1.5D (GSTM1730) with 1 Sun. The radiation that comes is focused by using Fresnel lens and then split by hot mirror. Radiation spectrum wavelengths are adjusted according to the needs of PV and TEG modules, amorphous Silicon; (a-Si) and Bismuth Telluride (Bi2Te3), respectively.

2. Spectrum AM1.5D (GSTM1730)

Figure 1 shows the data measured by the solar spectrum at STC (standard test condition). AM0 is red color (ASTM E490), AM1.5 Global blue color (ASTMG173) and AM1.5Direct is green color (ASTMG173) [15].

The AM1.5 Global (ASTMG173) spectrum is a spectrum designed for flat plate modules and has an integrated power of 1000 W/m^2. AM1.5 Direct (ASTMG173) is a spectrum designed for solar concentrators, with additional circumference and has an integrated power of 900 W/m^2. AM0 (ASTM E490) is a standard spectrum for aerospace applications with integrated power of 1366.1 W/m^2 [15].

The total power density emitted from the light source can be calculated by integrating spectral irradiation into all wavelengths or energies expressed in equation [16]:

$$H = \int_0^\infty F(\lambda)\, d\lambda \tag{1}$$

Where H is the total power density emitted from the light source in Wm^{-2}, $F(\lambda)$ is spectral radiation in units of Wm $^{-2}$ µm $^{-1}$ and $d\lambda$ is the wavelength with units of nm.

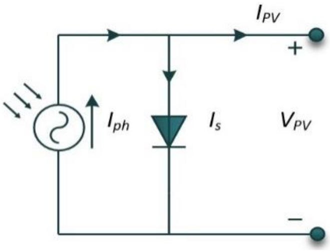

Figure 2. PV cell circuit model ideal

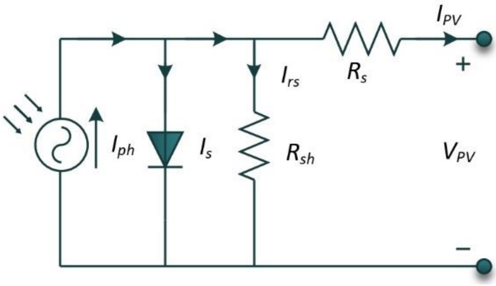

Figure 3. PV cell circuit model in one diode

3. Model of PV

The electrical circuit used to model the PV module is illustrated as shown in Fig. 2 below. The use of the equivalent KCL list (Kirchoff's Curent Law) makes it possible to create characteristic models of PV. The ideal PV cell model is a circuit model that ignores the presence of obstacles in the device, so that current flows only through ideal diodes as shown in Fig. 2 [13].

It can be seen that the ideal PV cell series model can be expressed in equation [13]:

$$I_{pv} = I_{ph} - I_s \tag{2}$$

where I_{pv} is the PV output current, I_{ph} is the current of the photon that is generated and I_s is the diode current. While the real PV cell model one diode is done by adding obstacles to the circuit. The obstacles applied to the circuit are divided into two obstacles, namely series and parallel barriers as shown in Fig. 3 [13].

The equation of the voltage current meets in Fig. 3. which represents an equivalent circuit according to Kirchoff's law and expressed as [13]:

$$I_{pv} = I_{ph} - I_s - I_{rs} \tag{3}$$

I_{rs} is the current on the added obstacle. The current of the generated photon is expressed by equation [12]:

$$I_{ph} = [I_{sc} + K_i(T - T_0)]\left(\frac{G}{G_0}\right) \tag{4}$$

I_{sc} is short circuit current, K_i is current conductivity, T is PV temperature, G is irradiation, T_0 and G_0 are temperature and irradiation at STC (Standard test Condition) based on international standard IEC (International Electrotecnical Commission). T_0 = 25 ºC and G_0 = 1000 W/m^2. The resistance current is expressed in the equation [12]:

$$I_{rs} = I_{scr}\left[\exp\left(\frac{qV_{oc}}{N_s kAT}\right)-1\right] \qquad (5)$$

I_{scr} is a standard short current current, V_{oc} is an open circuit voltage, q is an electron charge (1.602 x 10^{-19}C), N_s is the number of series cells in a PV module, k is a Boltzman constant (1.38 x 10^{-23} J), A is a factor ideal diode. While the diode current is expressed as [12]:

$$I_s = I_{rs}\left(\frac{T}{T_0}\right)^3 \exp\left[\frac{qE_g}{Ak}\left(\frac{1}{T_0}-\frac{1}{T}\right)\right] \qquad (6)$$

E_{gp} is the band gap energy, so equation (2) becomes [12]:

$$I_{pv} = N_p I_{ph} - N_p I_d\left[\exp\left(\frac{qV_{vp}+I_{pv}R_s}{N_s kAT}\right)-1\right] - \frac{V_{vp}+I_{pv}R_s}{R_h} \qquad (7)$$

R_s is the series resistance and R_h is a parallel resistance. The parameters A, I_{ph}, I_d, R_s, R_h, are called PV cell internal parameters. The PV module consists of PV cells that are connected and can be arranged in series, parallel and combination.

Input power due to irradiation from light sources can be calculated by the following equation [13]:

$$P_{in} = GA_{pv} \qquad (8)$$

A_{pv} is the surface area of a PV module. To evaluate the quality of PV cells in the filling factor with the equation [13]:

$$FF = \frac{I_{MP}V_{MP}}{I_{sc}V_{oc}} \qquad (9)$$

I_{MP} is the current at maximum power, V_{MP} voltage at maximum power. While the maximum efficiency of PV is expressed as an equation [13]:

$$\eta_{pv} = \frac{I_{MP}V_{MP}}{GA_{pv}} \qquad (10)$$

In general, the characteristics of PV can be seen in the I-V current and voltage curves, using the maximum power I-V curve can be determined at the maximum power point and voltage at the maximum power point. As shown in Fig. 4. The red I-V curve and the blue P-V curve [17].

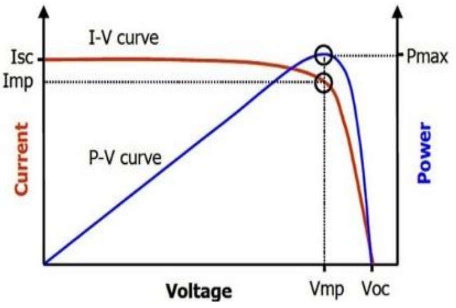

Figure 4. PV curve : I-V (*red*) dan P-V(*blue*) curve [17]

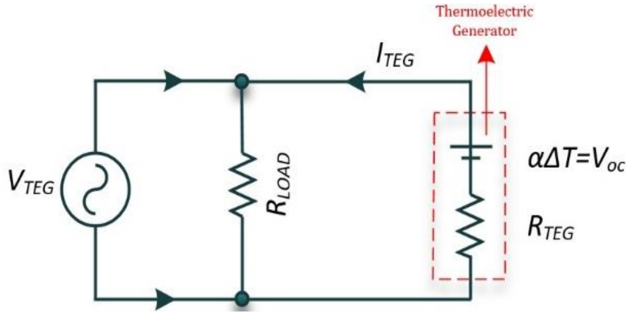

Figure 5. TEG circuit model

4. Model of PV

The model for measuring electrical power in TEG can be described by V_{oc} open circuit voltage and the value of TEG electrical resistance. Internal resistance is determined in maximized electrical power as shown in Fig. 5 [18].

Based on Fig. 5, Voltage is generated by the Seebeck effect on TEG. The heat absorbed is expressed as an equation [14]:

$$Q_H = \alpha IT_H + K(T_H - T_C) - 0.5RI^2 \qquad (11)$$

Where α is the Seebeck coefficient, R is the internal resistance, K is thermal conductivity. While for the calculation of voltage current is expressed as [14]:

$$V_{OC} = \alpha\Delta T \qquad (12)$$

Where V_{oc} is the open circuit voltage, α is the Seebeck coefficient of semiconductor material and ΔT is the temperature between the hot side and the cold side of TEG. The currents generated from TEG are expressed as equations [14]:

$$I_{TEG} = \frac{\alpha\Delta T}{R_{TEG}+R_{LOAD}} \qquad (13)$$

where R_{TEG} is an internal TEG obstacle and R_{LOAD} external constraints are given.

If $V_{TEG} = I_{TEG}R_{TEG}$ then :

$$V_{TEG} = \frac{\alpha\Delta T}{R_{TEG}+R_{LOAD}}R_{LOAD} \qquad (14)$$

So that the power that can be generated by TEG [14]:

$$P_{TEG} = V_{TEG} I_{TEG} \tag{15}$$

Efficiency can be calculated by equation [14]:

$$\eta_{TEG} = \frac{V_{TEG} I_{TEG}}{Q_H} \tag{16}$$

5. PV-TEG Performance

The types of devices used are commercial amorphous silicon (a-Si) PV [19], TEG type Bismuth Telluride (Bi2Te3) [20] and hot mirror 40x40 mm from Edmund optic, where the specifications are shown in Table 1-3. Furthermore, the schematic calculation of the PV-TEG hybrid can be seen in Fig. 6.

For determining PV-TEG hybrid output power can be referred to Babu and P. Ponnambalam [7] as follows:

$$P_{PV-TEG} = P_{PV} + P_{TEG} \tag{17}$$

Where P_{PV} is the output power of PV and P_{TEG} is the output power of TEG, while its efficiency is:

$$\eta_{PV-TEG} = \eta_{PV} + \eta_{TEG} \tag{18}$$

Where η_{PV} and η_{TEG} are the efficiency of PV and TEG module, respectively.

Figure 6 shows the scheme and stages of PV-TEG hybrid mathematical modeling calculations. Power output and overall efficiency are the sum of PV output with TEG output.

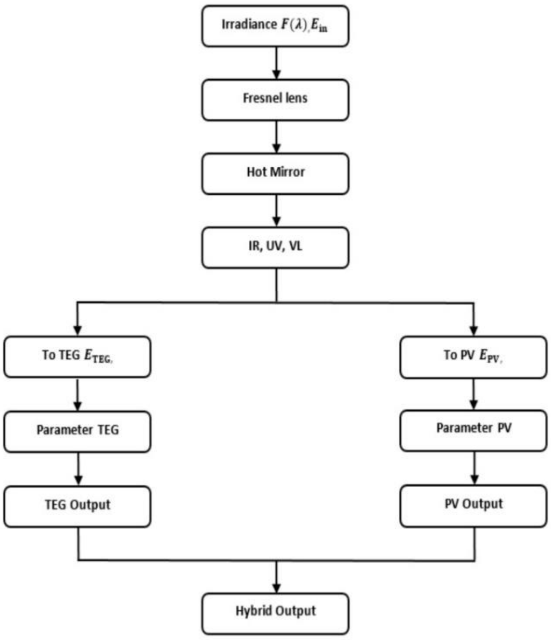

Figure 6. Schematic Calculation of PV-TEG hybrids

Figure 7 shows the results of the AM1.5D data spectrum calculation (ASTMG173) after illuminating the hot mirror. The solar spectrum transmitted in the form of visible (Vis) and ultraviolet (UV) lights to PV is = 362.93 W/m^2 (at 400-690 nm) and reflected in the form of near-infrared (Nir) and infrared (IR) spectrums to TEG are = 311.62 W/m^2 (at 690-1150 nm). PV in the form of photons with low temperatures needs Vis and UV, while TEG needs NIR or IR in the form of thermal at high temperatures.

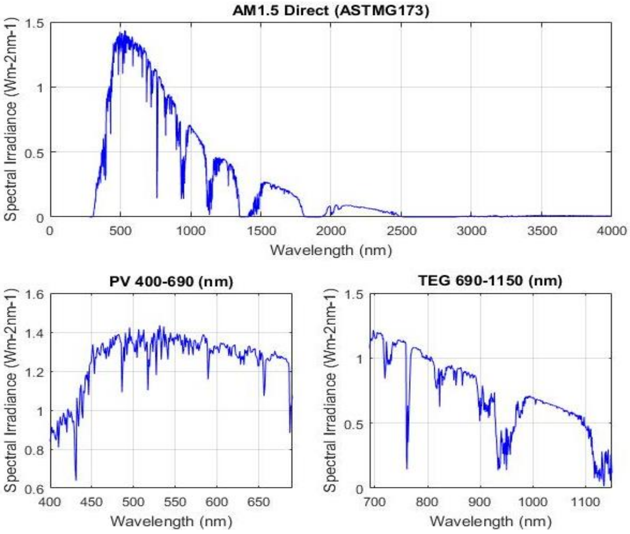

Figure 7. AM1.5D spectrum wavelength passes through a hot mirror

Table 1. Data Specifications of ASC 4040 [19]

Parameter	Value
Maximum Power (P)	0.082 W
Maximum Power voltage V_{MP}	1.85 V
Maximum Power current I_{MP}	0.044 A
Open circuit voltage (V_{oc})	2.4 V
Short circuit current (I_{sc})	0.054 A
Dimensions (L*W*H)	40*40*2 mm

Material : Amorphous silicon (a-Si)
Electrical specifications at standard test conditions; irradiance of 1000 W/m^2, spectrum of 1.5 air mass and cell temperature of 25° C.

Table 2. Data Spesifikasi SP1848-27145 [20]

Parameter	Value
Voltage open circuit (Voc)	0.97 V
Current (I)	0.225 A
Resistance	2.4 Ohm
Hot side temperature (T_H)	50 °C
Cold side temperature (T_C)	30 °C
Dimensions (L*W*H)	40*40*3.4 mm

Table 3. Data Specifications Hot Mirror [21]

Parameter	Value
Angle of incident (ºC)	45
>90% Transmission from (nm)	400-690
>95% Reflections from (nm)	710-1150
Dimensions (L*W*H)	40*40*1 mm

6. Result and Discussion

The calculation results of the hybrid PV-TEG mathematical model based on equation (1-16) using the initial parameters of the specification data in Table 1-3 which can be seen in Figs. 8 and 9 in the form of I-V and P-V curves. Figure 8 shows the calculation results on the I-V curve in the PV module. The power transmitted from the hot mirror to PV is used as input to the irradiation value (G) = 362.93 W/m^2, resulting in a value of I_{sc} = 0.019 A and V_{oc} = 1.952 V.

Figure 9 shows the results of calculations on the P-V curve in the PV module. The power value is obtained by multiplying the voltage and current values. While constant values include: Boltzman constant (k) = 1.38 x 10^{-23}, Electron charge (q) =1.602 x 10^{-19}, ideality factor diode (A) = 1, Energy gap E_{gp}) = 1.5, Temperature (T) = 25ºC and produce I_{MP} = 0.015 A, V_{MP} = 1.394 V and P_{MP} = 0.021 W. While the efficiency produced is 3.6%. This result can also illustrate that the output value and efficiency of PV cells are very dependent on the value of the intensity and temperature given.

Figure 10 shows the calculation results on the I-V curve in the TEG module. The magnitude reflected from the hot mirror to TEG 311.62 W m^2 is assumed to provide thermal with a maximum value of ΔT of 30ºC. Under conditions of T_H = 60ºC, T_C = 30ºC, R_{TEG} = 3.7Ω and R_{LOAD} = 1-10Ω, produce I_{sc} = 0.404 A and V_{oc} = 0.967 V.

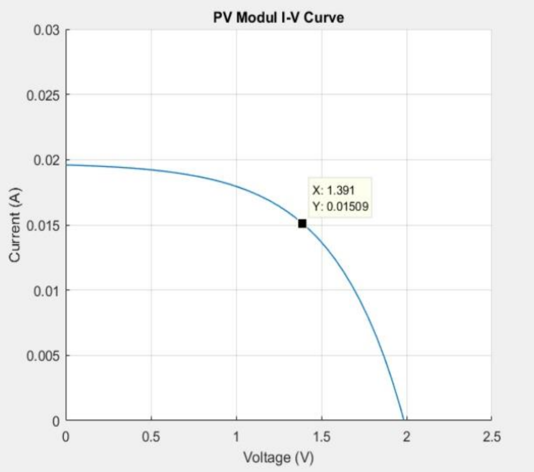

Figure 8. PV Modul I-V Curve

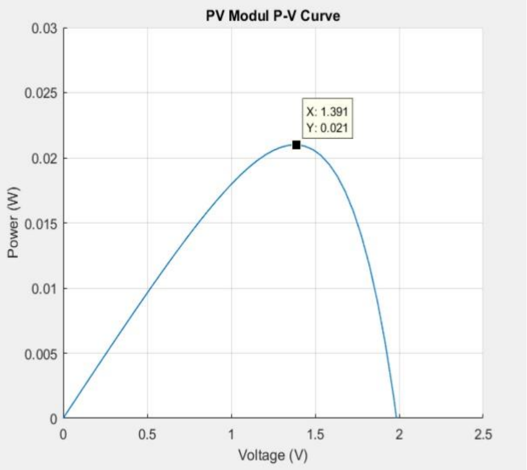

Figure 9. PV Modul P-V Curve

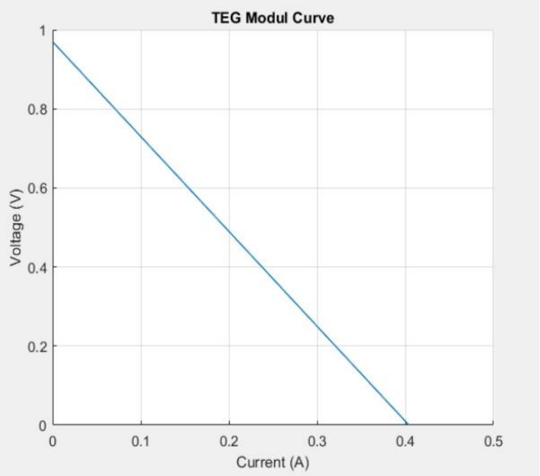

Figure 10. TEG Modul I-V Curve

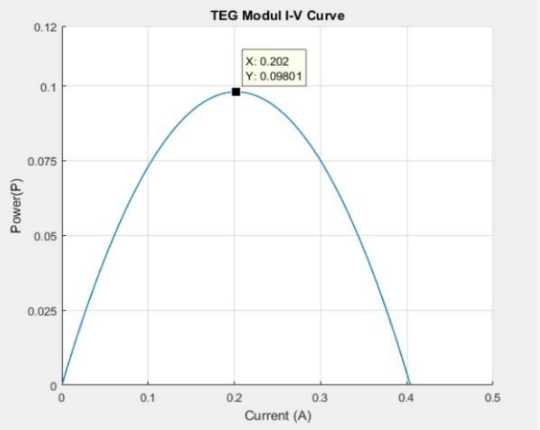

Figure 11. TEG Modul I-P Curve

Figure 11 displays the results of calculations on the I-P curve. The maximum power value is obtained by multiplying the voltage and current values in the quadratic function. Resulting in the value I_{MP} = 0.202 A, V_{MP} = 0.073 V dan P_{MP} = 0.098 W. While the efficiency produced is 1.502 %. The characteristics of TEG as a power plant have quite important parameters that determine output power and efficiency including temperature differences between hot and cold sides, voltage and load [7]. The total output power and efficiency of Hybrid PV-TEG is the sum of the total power and efficiency produced by PV and TEG by P_{hybrid} = 0.1710 W and η_{hybrid} = 5.1 %.

7. Conclusion

The new mathematical modeling that characterizes PV-TEG hybrid using wavelength spectrum splitter of a hot mirror is presented. From the modeling results produce PV values; I_{MP} = 0.015 A, V_{MP} = 1.394 V and P_{MP} = 0.021 W and values at TEG I_{MP} = 0.202 A, V_{MP} = 0.073 V dan P_{MP} = 0.098 W. Total maximum power generated is 0.1710 W with an efficiency of 5.1%. The power output and efficiency of the hybrid PV are greatly influenced by irradiation and the temporal temperature in TEG is only influenced by differences in hot side temperature and cold side. The magnitude of the AM1.5 D spectrum that can be utilized with the use of hot mirrors is only 674.55 W/m^2 at wavelengths of 400-690 (visible light and UV) and 690-1150 (NIR and IR). The total total power is 900 W/m^2 and is 225.45 W/m^2 wasted environment. The choice of construction and material both PV and TEG needs to be considered because it influences internal factors such as material resistivity and thermal conductivity. This modeling still needs to be developed with other types of PV and TEG material to see the best ratio of output power and efficiency.

Acknowledgements

Thank you to the BUDI-DN 2016 affirmation scholarship organizers and Musamus University (UNMUS), Merauke as a sponsor of this research.

References

[1] A. Makki, S. Omer, and H. Sabir, “Advancements in hybrid photovoltaic systems for enhanced solar cells performance,” *Renew. Sustain. Energy Rev.*, vol. 41, pp. 658–684, 2015.

[2] A. Kane and V. Verma, “Performance Enhancement of Building Integrated Photovoltaic Module using Thermoelectric Cooling,” vol. 3, no. 2, 2013.

[3] U. Syamsuddin, Z. Djafar, T. Tjandinegara, Z. Djafar, and W. H. Piarah, “Heat Utilization of Incinerator Chimneys as Mini Power Generator Based on Thermoelectric,” *EPI Int. J. Eng.*, vol. 1, no. August 2018, pp. 51–58, 2018.

[4] H. Chang, M. Kao, K. Cho, S. Chen, K. Chu, and C. Chen, “Integration of CuO thin fi lms and dye-sensitized solar cells for thermoelectric generators,” *Curr. Appl. Phys.*, vol. 11, no. 4, pp. S19--S22, 2011.

[5] H. Chang and Z. Yu, “Integration of Dye-Sensitized Solar Cells , Thermoelectric Modules and Electrical Storage Loop System to Constitute a Novel Photothermoelectric Generator,” vol. 12, no. 8, pp. 6811–6816, 2012.

[6] Y. Li, S. Witharana, H. Cao, M. Lasfargues, Y. Huang, and Y. Ding, “Wide spectrum solar energy harvesting through an integrated photovoltaic and thermoelectric system,” *Particuology*, vol. 15, pp. 39–44, 2014.

[7] C. Babu and P. Ponnambalam, “The theoretical performance evaluation of hybrid PV-TEG system,” *Energy Convers. Manag.*, vol. 173, no. April, pp. 450–460, 2018.

[8] T. M. Tritt, H. Böttner, and F. Institut, “Thermoelectrics : Direct Solar Thermal Energy Conversion,” vol. 33, no. APRIL, pp. 366–368, 2008.

[9] D. Kraemer, L. Hu, A. Muto, X. Chen, G. Chen, and M. Chiesa, “Photovoltaic-thermoelectric hybrid systems: A general optimization methodology,” *Appl. Phys. Lett.*, vol. 92, no. 24, pp. 23–25, 2008.

[10] X. Ju, Z. Wang, G. Flamant, P. Li, and W. Zhao, “Numerical analysis and optimization of a spectrum splitting concentration photovoltaic – thermoelectric hybrid system,” *Sol. Energy*, vol. 86, no. 6, pp. 1941–1954, 2012.

[11] Mustofa, Z. Djafar, Syafaruddin, and W. H. Piarah, “A new hybrid of photovoltaic-thermoelectric generator with hot mirror as spectrum splitter,” *J. Phys. Sci.*, vol. 29, pp. 63–75, 2018.

[12] K. Nakagawa, T. Tanaka, and T. Suzuki, “Modelling of Photovoltaic Module Using Matlab Simulink.”

[13] Y. Belkassmi, A. Rafiki, K. Gueraoui, L. Elmaimouni, O. Tata, and N. Hassanain, “Modeling and simulation of photovoltaic module based on one diode model using Matlab/Simulink,” *Proc. - 2017 Int. Conf. Eng. MIS, ICEMIS 2017*, vol. 2018–Janua, pp. 1–6, 2018.

[14] F. Rukdq *et al.*, “Modeling and Simulation of Thermo Electrical Generator with MPPT,” *ICRERA*, vol. 6, pp. 855–860, 2017.

[15] C. Honsber and S. Bowden, “Standard Solar Spectra,” *pveducation*, 2018. [Online]. Available: https://www.pveducation.org/pvcdrom/appendices/standard-solar-spectra. [Accessed: 11-Nov-2018].

[16] C. Honsberg and S. Bowden, “Properties of Light,” *pveducation*, 2018. [Online]. Available: https://www.pveducation.org/pvcdrom/properties-of-sunlight/properties-of-light.

[17] B. Schweber, “Solar cells and power, Part 2 – power extraction,” *powerelectronictips*, 2017. [Online]. Available: https://www.powerelectronictips.com/solar-cells-power-part-2-power-extraction/.

[18] R. Mawi and Y. Kazuz, “Hybrid Solar Thermo-Electric Systems for Combined Heat and Power,” no. September, 2014.

[19] alibaba.com, “Data Sheet of PV ASC 4040,” *alibaba.com*. [Online]. Available: https://www.alibaba.com/product-detail/1W-small-size-customized-amorphous-silicon_60159308905.html?spm=a2700.7724857.normalList.49.3a24696eEpoJ6S. [Accessed: 11-Nov-2018].

[20] alibaba.com, “Data Sheet of TEG SP1848-27145,” *alibaba.com*, 2018. [Online]. Available: https://www.alibaba.com/product-detail/Thermoelectric-Power-Generator-Peltier-Module-TEG_60707268580.html?spm=a2700.7724838.2017115.34.3c8d392fDqYIMv. [Accessed: 11-Nov-2018].

[21] Edmund Optics, “Data Sheet of Hot Mirror,” *Edmund Optics*, 2016. [Online]. Available: https://www.edmundoptics.com/f/high-performance-hot-mirrors/13824/.

EPI International Journal of Engineering
Volume 2, Number 1, February 2019, pp. 80-83
DOI: 10.25042/epi-ije.022019.14

*p*ISSN 2615-5109
*e*ISSN 2621-0541

Harmonic Response Analysis of Strut Fin on Planar Motion Mechanism

Kusnindar Priohutomo[a]*, Danang Ariyanto[b]

[a]Indonesian Hydrodynamics Laboratory, Agency for the Assessment and Application of Technology (BPPT), Indonesia.
Email:kusnindar.priohutomo@gmail.com
[b]Indonesian Hydrodynamics Laboratory, Agency for The Assessment and Application of Technology (BPPT), Indonesia.
Email:kusnindar.priohutomo@gmail.com

Abstract

In a material selection, the design that will be used is one important step because by selecting the right material with the appropriate material properties, the harmonic response value of the structure can be seen. By knowing the value of harmonic response in a structure, at the time of testing, damage to the structure can be avoided. In this study, the material used for Fin Planar Motion Mechanism (PMM) is Stainless Steel 304 (SS 304). To calculate the harmonic response, the SPSS (square root) method is used. From the research results, in the range 1-100 Hz the displacement value is still below the limit with a maximum value of 2.50E-12 mm and a maximum stress value of 2.95E-05 Pa.

Keywords: Finite element method; harmonic response; natural frequency; strut fin; planar motion mechanism

1. Introduction

Strut Fin on Planar Motion Mechanism (PMM) is used as a ship model holder and as a load cell stand that will measure the forces acting during the test. PMM was first designed by Gertler and Goodman et al. [1] installed on David Taylor Model Basin (DTMB) in 1960, which later made improvement in measurement captive model test. From PMM, it can be produced pure sway ship motion, pure yaw ship motion, and combination sway and yaw ship. A load cell is used to measure forces resulting from strut fin movement which is in front and behind the PMM in oscillation motion (See Fig.1).

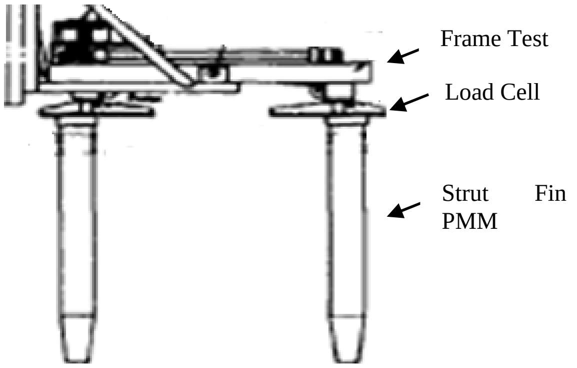

Figure 1. Planar Motion Mechanism in TT

The PMM equipment is used on the carriage Towing Tank (TT) that belongs BTH-BPPT. With this combination of tests, needed Strut Fin PMM design is strong and lightweight so that the frequency produced by the motor at the time of testing does not affect the reading of the load cell on Strut Fin PMM.

In the design stage of a structure, the natural frequency is one of the points that must be considered. Because by knowing the natural frequency, it can be used to calculate the value of the failure rate and the level of damage from a structure. Many studies have been conducted to calculate the value of natural frequency, including research on reference [2]. This study discusses the effect of crack produced using a natural frequency approach to structural materials that have a beam type. In this study, the natural frequency analysis uses the help of ANSYS FEM software. The results of this study were to determine the location of cracks in structures with crack depths around 1-3 mm. The effects of natural crack frequency are analyzed as health structures using mode 1 to mode 4.

The next study in [3] discusses experimental modal analysis (EMA) to analyze the crack that occurs in the beam. Where natural frequency mode 1 used as a reference for detecting the occurrence of a crack in the structure. The intersection of the three contours provides information on the location of the crack and depth of the crack. The results of the case study show the ability and efficiency of the method developed.

---

*Corresponding author. Tel.: +62-315948060
Jl. Hidrodinamika, Kompleks ITS, Sukolilo
Surabaya, Indonesia, 60112

Another research in [4] discusses failure modes dan buckling loads of composite plate under uniformly distributed loading and deflection is investigated by using analytical and theoretical approaches. Conclusion in this research is that the composite plate carries out the theoritical and the FEM results and is found to be around 8-10% difference. The achieved deflection factor is 5.4 against 4.6 in FEM. However, the results of FEM show close agreement with theoritical results.

Another study in [5] discusses a relation which describes the influence of discontinuities on the dynamic response of prismatic cantilever beams. The relation providing the natural frequencies of weak-axis bending vibration modes of damaged beams was contrived by considering the continous model in a global approach, opposite to researches presented in the literature involving mainly models based on two segments linked by a rotational spring and focusing on the local effect of the discontinuity.

From some of the studies that have been mentioned, the authors conducted research on natural frequencies in Strut Fin PMM with various types of material used and analyzed using modal analysis method assisted by Finite Element Method software (FEM).

2. Method

The research method was developed to be able to calculate the natural frequency Strut Fin PMM where steps in the research method can be explained as follows:

2.1. Material type

The choice of material type is the first thing in predicting the natural frequency of a structure. In this study, the material chosen was Stainless Steel 304 (SS304). Stainless steel 304 (SS304) is one of the stainless steel that is often used in the design industry. Because SS304 has advantages such as having resistance to corrosion against a variety of good environmental conditions [6-9]. SS304 has chemical properties shown in Table 1 and material properties shown in Table 2.

Table 1. Chemical Properties

Properties	Composition
C	0.05
Si	1.08 - 1.49
Mn	0.35
P	0.038
S	0.001
Ni	8.5 - 10.6
Cr	18.65 - 21.20
Fe	66.4

Table 2. Mechanical Properties

Properties	
Density	1.08-1.49
Tensile Strength (Yield)	215 MPa
Tensile Strength (Ultimate)	505 MPa
Modulus of Elasticity	193-200 GPa
Poisson Ratio	0.29
Shear Modulus	86 GPa

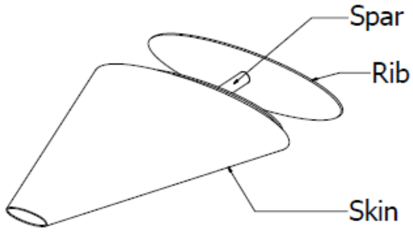

Figure 2. Design Strut Fin PMM

2.2. Strut fin PMM design

The components of the Strut Fin PMM compiler are components that are commonly used in structural design. Where consists of ribs arranged into 5 parts from the largest to the smallest. Rib Strut Fin PMM is made from SS304 material. Whereas for reinforcement is given an amplifier in the form of a spar that is connected from the largest rib to the smallest rib. The spar is mounted in the middle position of the rib. Spar is connected with Rib using the welding method so that it becomes the main structure Strut Fin PMM. Spar Strut Fin PMM is made of SS304 material. The skin has a thickness of 10mm and is used to make the flow of fluid passing through it smooth during the test (See Fig. 2).

2.3. Model Analysis

The calculation method used to analyze the natural frequency of Strut Fin PMM is Modal Analysis. Modal analysis is used to analyze natural frequencies because using the method modal analysis can find out natural mode (change the shape of a structure), calculate natural frequency, calculate the response of each mode, calculate the response in each mode if the system is loaded. The natural frequency of a system depends on the stiffness and mass of a structure, does not depend on the load received by the system. The results of the natural frequency are in the form of structure. Based on the results of natural frequency, vibration analysis can be calculated to avoid or reduce the excitation effect of the largest frequency. The kinematic equation of the free vibration on the structure is a simple harmonic vibration, which means that the displacement meets the sine.

$$x(t) = c_1 \cos(\omega t) + c_2 \sin(\omega t) \tag{1}$$

Equation 1 can be written

$$x(t) = A\cos(\omega t - \varphi) \tag{2}$$

where:

$$\omega = \sqrt{\frac{k}{m}}\ ,\ A = \sqrt{C1^2 + C2^2}\ ,\ \tan\varphi = \frac{C2}{C1}$$

ω = angular frequency
A = amplitude
φ = phase

2.4. Harmonic response analysis

Harmonic response analysis using finite element models SPSS (square root method), harmonic response analysis based on Response Spectrum. In this study, the frequency given to PMM Strut Fin is 1-100 Hz. Harmonic response analysis used in this study was analyzed under no load conditions. The no-load condition is defined as the condition when the Strut Fin PMM attaches to the Towing Tank carriage without the load of the ship model below it. To assist the calculation of harmonic response using FEM software [10-13].

3. Results Analysis and Discussion

Deformation occurs due to natural frequencies that affect the structure of the Strut Fin PMM. By using FEM software, the maximum value and minimum deformation values that occur in the PMM Strut Fin are obtained. The natural frequency that occurs is shown in Table 3.

Table 3. Mode vs Frequency vs Displacement

Mode	Natural Frequency (Hz)	Max. Displ. (m)
1	0.0371	0.0532
2	433.339	0.1148
3	502.121	0.0899
4	776.368	0.0353
5	867.883	0.0469

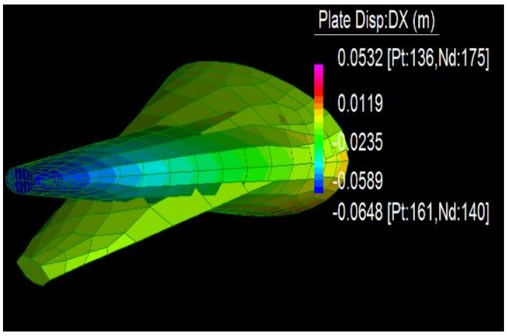

Figure 3. First Mode

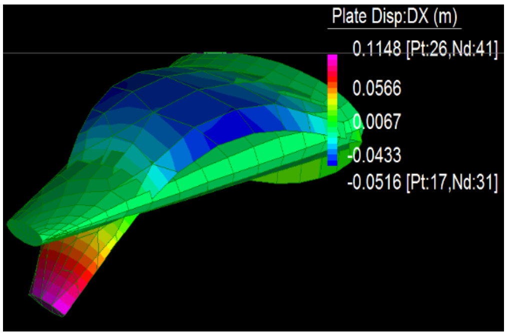

Figure 4. Second Mode

Table 4. Frequency vs Displacement vs Pressure

Freq. (Hz)	Displ. (mm)	Pressure (Pa)	Freq. (Hz)	Displ. (mm)	Pressure (Pa)
1	2.50E-12	2.95E-05	51	6.64E-16	1.38E-05
2	6.24E-13	1.69E-05	52	6.28E-16	1.38E-05
3	2.77E-13	1.51E-05	53	5.93E-16	1.38E-05
4	1.56E-13	1.45E-05	54	5.61E-16	1.38E-05
5	9.95E-14	1.42E-05	55	5.30E-16	1.38E-05
6	6.90E-14	1.41E-05	56	5.01E-16	1.38E-05
7	5.06E-14	1.40E-05	57	4.73E-16	1.38E-05
8	3.87E-14	1.39E-05	58	4.47E-16	1.38E-05
9	3.05E-14	1.39E-05	59	4.22E-16	1.38E-05
10	2.47E-14	1.38E-05	60	3.98E-16	1.38E-05
11	2.03E-14	1.38E-05	61	3.75E-16	1.38E-05
12	1.70E-14	1.38E-05	62	3.54E-16	1.38E-05
13	1.45E-14	1.38E-05	63	3.34E-16	1.38E-05
14	1.24E-14	1.38E-05	64	3.14E-16	1.38E-05
15	1.08E-14	1.38E-05	65	2.96E-16	1.38E-05
16	9.45E-15	1.38E-05	66	2.78E-16	1.38E-05
17	8.34E-15	1.38E-05	67	2.61E-16	1.38E-05
18	7.41E-15	1.37E-05	68	2.45E-16	1.38E-05
19	6.62E-15	1.37E-05	69	2.29E-16	1.38E-05
20	5.94E-15	1.37E-05	70	2.14E-16	1.38E-05
21	5.36E-15	1.37E-05	71	2.00E-16	1.38E-05
22	4.86E-15	1.37E-05	72	1.86E-16	1.38E-05
23	4.42E-15	1.37E-05	73	1.73E-16	1.38E-05
24	4.04E-15	1.37E-05	74	1.61E-16	1.38E-05
25	3.70E-15	1.37E-05	75	1.49E-16	1.39E-05
26	3.40E-15	1.37E-05	76	1.37E-16	1.39E-05
27	3.13E-15	1.37E-05	77	1.26E-16	1.39E-05
28	2.89E-15	1.37E-05	78	1.15E-16	1.39E-05
29	2.67E-15	1.37E-05	79	1.05E-16	1.39E-05
30	2.48E-15	1.37E-05	80	9.49E-17	1.39E-05
31	2.30E-15	1.37E-05	81	8.54E-17	1.39E-05
32	2.14E-15	1.37E-05	82	7.62E-17	1.39E-05
33	2.00E-15	1.37E-05	83	6.73E-17	1.39E-05
34	1.86E-15	1.37E-05	84	5.87E-17	1.39E-05
35	1.74E-15	1.37E-05	85	5.05E-17	1.39E-05
36	1.63E-15	1.37E-05	86	4.25E-17	1.39E-05
37	1.53E-15	1.37E-05	87	3.48E-17	1.39E-05
38	1.43E-15	1.37E-05	88	2.74E-17	1.39E-05
39	1.35E-15	1.38E-05	89	2.02E-17	1.39E-05
40	1.26E-15	1.38E-05	90	1.32E-17	1.39E-05
41	1.19E-15	1.38E-05	91	6.51E-18	1.39E-05
42	1.12E-15	1.38E-05	92	1.11E-20	1.39E-05
43	1.05E-15	1.38E-05	93	6.28E-18	1.39E-05
44	9.94E-16	1.38E-05	94	1.24E-17	1.39E-05
45	9.37E-16	1.38E-05	95	1.83E-17	1.39E-05
46	8.84E-16	1.38E-05	96	2.40E-17	1.39E-05
47	8.34E-16	1.38E-05	97	2.95E-17	1.40E-05
48	7.88E-16	1.38E-05	98	3.49E-17	1.40E-05
49	7.44E-16	1.38E-05	99	4.01E-17	1.40E-05
50	7.03E-16	1.38E-05	100	2.84E-14	8.78E-03

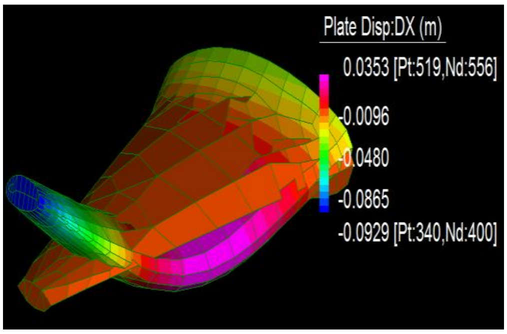

Figure 5. Third Mode

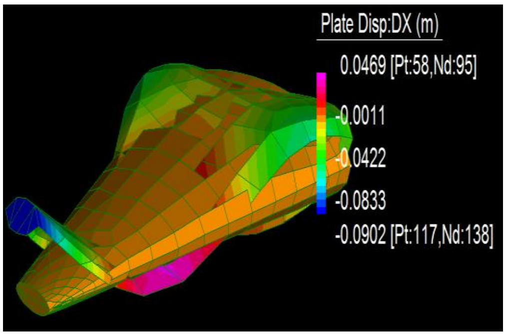

Figure 6. Fourth Mode

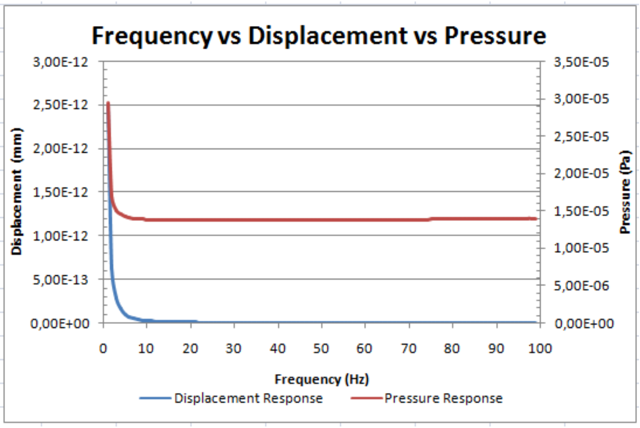

Figure 7. Frequency vs Displacement vs Pressure

After knowing the natural frequency value, the value is used to input the harmonic response analysis, where the harmonic response of the spectrum value is 1 to 100 Hz, the results from the three spectra are shown in Table 4.

Figure 7 shows that at a frequency of 1 Hz Strut Fin PMM displacement of 2.50E-12 mm, the displacement value the higher the frequency decreases in the sense that the resonance structure of the Strut Fin PMM at very high frequencies is very small. While for stress at a frequency of 1 Hz is 2.95E-05 Pa. The value of stress the higher the frequency decreases to a frequency of 18 Hz - 38 Hz with a value of 1.37E-05 Pa, after that the value of pressure increases again but the value is small at 100 Hz.

4. Conclusion

In a structure, one of the factors that cause failure is the resonance of the structure. By knowing the resonance value, in this case, the natural frequency of Strut Fin PMM, it can avoid natural frequencies which can endanger the structure. In the Strut Fin PMM structure with variations in frequency between 1 - 100 Hz the displacement value that occurs is still within normal limits. Largest displacement value occurs at a high frequency of 1 Hz and the lowest displacement value at a frequency of 100 Hz. For the highest stress value at a frequency of 1 Hz. In the frequency range that has been studied, it becomes a reference when designing the motor needs for Strut Fin PMM drive, so that when testing the motor frequency is in the range of 0-100 Hz, thus the deformation that occurs is still within normal limits

Acknowledgments

The authors highly appreciates to Center of Technology for Maritime Industrial Engineering BPPT who have allowed using software FEM Strand 7.

References

[1] M. Gertler, "The DTMB Planar Motion Mechanism System," no. July 1967, 1967.

[2] S. U. Sawant, S. J. Chauhan, and N. N. Deshmukh, "Effect of crack on natural frequency for beam type of structures," *AIP Conf. Proc.*, vol. 1859, pp. 1–7, 2017.

[3] A. V Deokar and V. D. Wakchaure, "Experimental Investigation of Crack Detection in Cantilever Beam Using Natural Frequency as Basic Criterion," *Int. Conf. Curr. Trends Technol.*, pp. 8–10, 2011.

[4] A. S. Kumar, "Modeling and Analysis of a Composite Wing for Missile Structure," vol. 8, no. 6, pp. 338–347, 2017.

[5] G. R. Gillich, P. F. Minda, Z. I. Praisach, and A. A. Minda, "Natural Frequencies of Damaged Beams - A New Approach," *Rom. J. Acoust. Vib.*, vol. 9, no. 2, pp. 101–108, 2012.

[6] N. Mubarok, H. A. Notonegoro, K. A. Z. Thosin, and A. Manaf, "The Effect of Mechanical Deformation to The Magnetic Properties of Stainless Steel 304," *J. Phys. Conf. Ser.*, vol. 776, no. 1, pp. 8–11, 2016.

[7] G.-Y. Kim, M. Koç, and J. Ni, "Experimental and Numerical Investigations on Microcoining of Stainless Steel 304," *J. Manuf. Sci. Eng.*, vol. 130, no. 4, p. 41017, 2008.

[8] N. Mubarok, H. A. Notonegoro, and K. A. Z. Thosin, "Comparative Mechanical Improvement of Stainless Steel 304 Through Three Methods," *IOP Conf. Ser. Mater. Sci. Eng.*, vol. 367, no. 1, pp. 1–6, 2018.

[9] M. Shukla, P. Agarwal, M. K. Pradhan, and S. K. Dhakad, "Experimental Investigation of EDM Parameters on Al-LM6/SiC/B4C Hybrid Composites," *Appl. Mech. Mater.*, vol. 877, no. 8, pp. 149–156, 2018.

[10] H. J. Hu, "Simulations of Isothermal ECAE for Magnesium Alloy using FEM Software and Experimental Validations," *J. Manuf. Process.*, vol. 14, no. 3, pp. 181–187, 2012.

[11] G. Liu, C. Huang, R. Su, T. Özel, Y. Liu, and L. Xu, "3D FEM Simulation of The Turning Process of Stainless Steel 17-4PH with Differently Texturized Cutting Tools," *Int. J. Mech. Sci.*, vol. 155, no. November 2018, pp. 417–429, 2019.

[12] J. Klon, J. Sobek, and V. Veselý, "Spatial Modeling of Wedge-Splitting Test on Cylindrical Specimens Using FEM Software," *Procedia Eng.*, vol. 190, pp. 427–432, 2017.

[13] G. Ortiz-De-Zarate *et al.*, "Experimental and FEM Analysis of Surface Integrity when Broaching Ti64," *Procedia CIRP*, vol. 71, pp. 466–471, 2018.

EPI International Journal of Engineering
Volume 2, Number 1, February 2019, pp. 84-90
DOI: 10.25042/epi-ije.022019.15

*p*ISSN 2615-5109
*e*ISSN 2621-0541

Renewable Energy Developments in Indonesia; Opportunities for Improving Local Production Energy for Local Consumption

Muhammad Zulkifli[a]*, Ryuji Tohyama[b], Tomohiro Tohyama[c], Kazuyuki Maeda[d]

[a]Prospec AZ, Inc Japan. Email: m-zulkifli@prospec-az.com
[b]Prospec AZ, Inc Japan. Email: r-tohyama@prospec-az.com
[c]Prospec AZ, Inc Japan. Email: info@prospec-az.com
[d]Professor Emeritus, National Fisheries University, Japan. Email: k2y2t-kazu@jcom.home.ne.jp

Abstract

Replacing consumption of fossil fuel with renewable energy is an important way in reducing carbon emission and one of effective solution facing issues of electricity in Indonesia. In light of the perspective of promoting the renewable energy, we plan to use palm oil as biofuels for power generation activities that will help to supply electricity for local community in Indonesia. This paper is a preliminary study that aims to overview the current progress of renewable energy development in Indonesia, also to introducing background of our planning as one of solution in dealing with Indonesia`s current renewable energy usage. Based on expected outputs of our planning, this study attempts to discuss our concept which is to promote of Local Production Energy for Local Consumption and its application which will lead to development of one Smart Energy Community, as one of the key points to developing Smart City.

Keywords: Local production energy; palm oil; renewable energy; smart energy

1. Introduction

Indonesia's economy is the largest in Southeast Asia and one of world fastest growing countries in terms of energy consumption. Data Report by IRENA (International Renewable Energy Agency) in 2017 shows that between 2000 and 2014, consumption increased by nearly 65% and it is predicted grow up to 80% by 2030, mainly transport and industry sector shown the fastest growth [1]. Based on Annual Energy Forecast from Indonesia`s Agency for the Assessment and Application of Technology (BPPT), transport fuel consumption will increase on average 5% per year through 2050, as shown in Fig.1 [2].

Nowadays, although there is a trend of decreasing, the majority demand of energy is still covered by fossil fuels which is about 42% of Indonesia's total energy consumption based on oil. Unfortunately, the domestic production oil is only around 825,000 barrel per day on the other hand, oil demand reaches 1,200,000 barrel per days, as shown in Fig.2. Therefore, deficit is covered by import and makes Indonesia is one of net oil importing countries [3].

Based on data Indonesia's Ministry of Energy and Mineral Resources (MEMR), Indonesia has coal resources at around 120.5 billion tons, proven oil resources at around 3.69 billion barrels, and proven natural gas reserves at around 101.54 trillion cubic feet. This translates into about 12 remaining years of oil reserves, 39 years of gas, and 146 years of coal at current production rates. Indonesia's renewable energy sources are also considerable. The country is endowed with significant potential for hydropower (75,000 MW), micro and mini hydropower (1,013 MW), solar (4.80 kilowatt-hours per square meter per day), biomass (32,654 MW), and wind (3 to 6 meters per second), and holds 40% of the world's geothermal reserves (28,000 MW) [4].

Therefore, nowadays Indonesia have been promoting renewable energy to secure stable sources of energy. The goal is not only to reduce the country's dependence on oil imports, but also to increase concern of the global warming aspect. In here, renewable energy having significant role and positive trend of usage by significantly, as shown in Fig. 3.

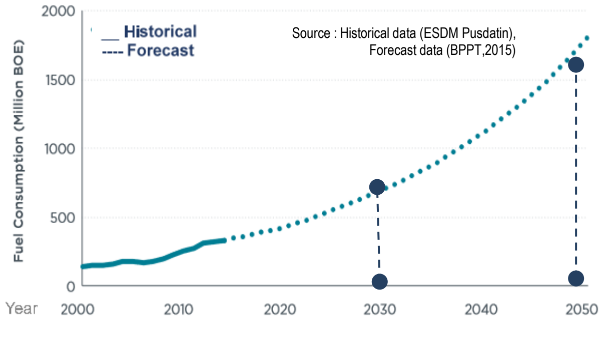

Figure 1. Indonesia transport fuel consumption [2]

---

*Corresponding author. Tel.: +81-3-6551-2441
Tokyo, Japan 100-0006

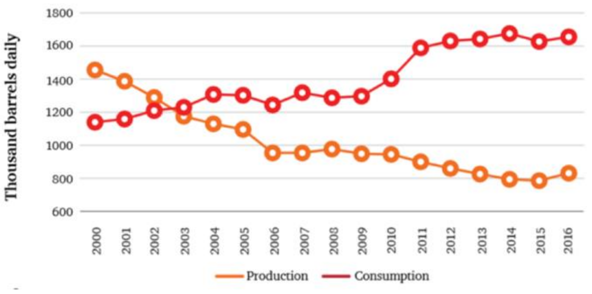

Source :
* Oil Production and Consumption 2000-2005: BP Statistical Review 2015.
* Oil Production 2006-2015: SKK Migas, MoEMR, Oil Production 2016 : Press Release of MoEMR
* Oil Consumption 2016 : EIA/BMI

Figure 2. Oil production versus consumption in Indonesia [3]

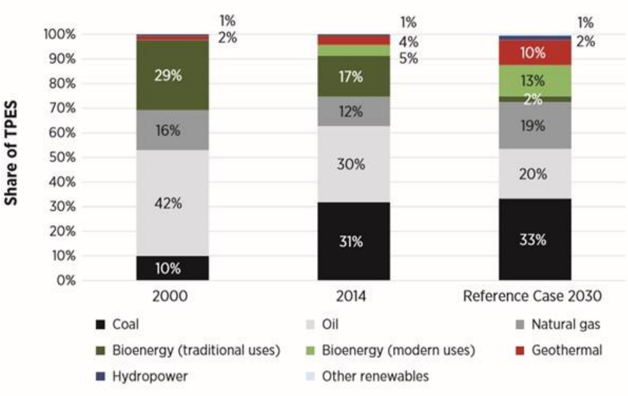

TPES : Total Primary Energy Supply

Figure 3. Fuel mix in primary energy supply in 2000, 2014 and in the Reference Case for 2030 [1]

Geothermal is predicted will be increased to 10% in 2030, from 4% in 2014. Bioenergy modern is predicted will be increased from 5% in 2014 to be 13% in 2030. Bioenergy in here refers to the renewable energy of biomass for electricity and heat or to produce liquid for fuels (e.g. bioethanol or biodiesel) for transport use. One interesting to note that bioenergy in term of traditional also has significant usage in Indonesia especially in rural areas which used by 24.5 million households in 2014 [1]. Traditional uses in here in term of using fuel wood or other bioenergy for home cooking and it plays important role in rural areas.

The target of Government of Indonesia for biofuels in 2025 is reach 30% to be mixed with fossil fuels in the transport's energy supply, so level of fossil fuels consumption can be reduced. However, because the slow growth of biofuels development, almost 40% of diesel fuels is still imported [2]. This condition make Government of Indonesia still continue to support palm oil as biodiesel, which this source having highest potential sources in Indonesia especially on the Kalimantan and Sumatera Island.

2. Purpose and Method

This study aims to discuss opportunities to improve renewable energy development in Indonesia. There are three focus for this study; *Firstly*, the study will begin with a review the progress of renewable energy development in Indonesia for identifying existing condition of energy issues in the country. *Secondly*, this study will try to discuss our thinking way through overview plan for develop power generation that promoting the usage of palm oil as biofuels for power generation in Indonesia. *Thirdly*, based on expected output from the plan, this study introducing our concepts for developing a more sustainable energy community which can improve and strengthen the concept for "Local energy production for local consumption" which based on local potential sources of energy.

To deal with expected purposes above, we also conduct of literature review as a method through reviewing the previous studies and published research which come from some sources such as Report of Indonesia`s Ministry of Energy and Mineral Resources Ministry, Report of Indonesia Energy by Asian Development Bank, report by The International Renewable Energy Agency (IRENA) and some published research related with the study.

This paper is a preliminary study of a comprehensive planning for promoting one of solutions for sustainable development that can be applied in Indonesia. Therefore, the results also can be integrated with the concept of smart city with based on improving a smart energy community.

3. Results and Discussion

3.1. Overview of electrification and Indonesia`s national renewable energy initiatives

Indonesia has many islands, rural areas, unique demography, geographical and diverse social culture with difference level of economy and living standard. This is will be related to the characteristic of level of electrification as shown in Fig.4. Despite being a growing global economic power, Indonesia's energy consumption is considered low. Electricity consumption in 2017 was 1.02 MWh per capita, which was relatively lower than neighboring economies [5]. Electrification ratio in the western part of the country is as high as 99.99% (DKI Jakarta, Jabar, Banten, DIY Kaltim and Babel). Electrification ratio is defined as the ratio of the number of households with access to electricity to the total number of households.

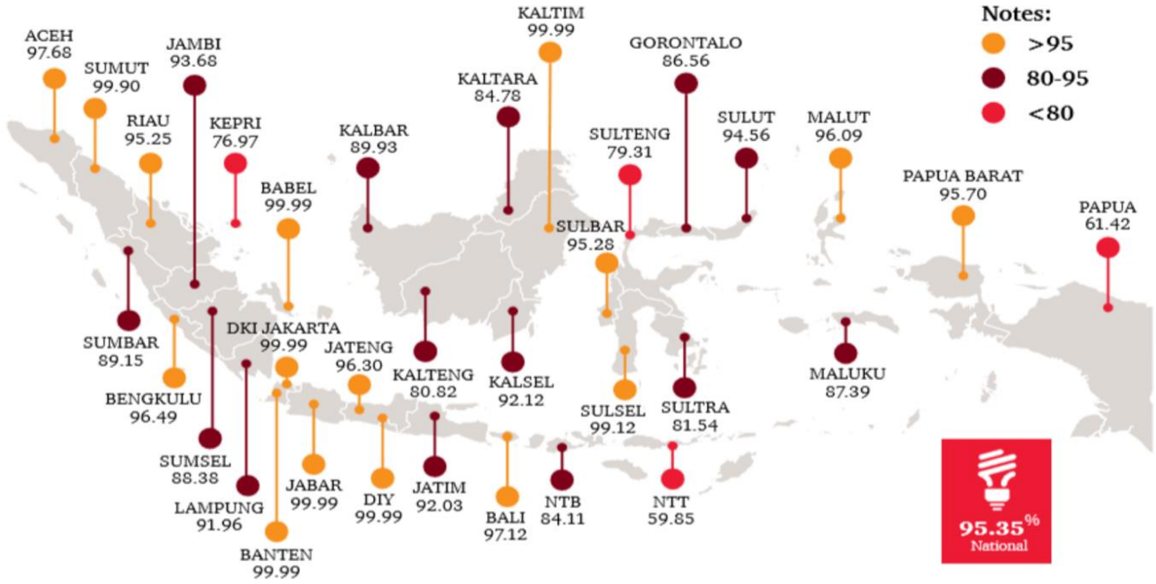

Figure 4. Ratio electrification of Indonesia [5]
(Source: 2017 Performance Report of MoEMR)

(1) Based on data by the Minister of Energy and Mineral Resources 2017, current national electrification rate in Indonesia is 95,35 % is as shown in Fig. 4 [5]. Electrification ratio herein is a measure of the prevalence of households with electricity access in a country. In general, electrification ratio is defined as the ratio of the number of households with access to electricity to the total number of households. Province of Papua and Nusa Tenggara Timur which identified has the lowest level of ratio of 50 – 70%.

(2) Analysis of survey by Asian Development Bank based on Electrification ratio 2013 by Directorate General of Electricity shows that the level of electrification ratios is not related with level per capita GDP of area in Indonesia [6]. As shown in Fig.5, Kalimantan Timur (East Kalimantan) has the second-highest per capita GDP in Indonesia, but an electrification ratio below the national average.

(3). Analysis of survey also shows that Electrification has not lagged in eastern Indonesia due to lower population densities [6]. Based on this analysis, changes in population density account for only 18% of the differences in electrification ratios. For example, though West Nusa Tenggara (Nusa Tenggara Barat) has higher population density than most provinces in Indonesia, it has one of the lowest electrification ratios.

(4) Within next 5 years, the growth demand of electricity will be predicted about 8,6% per year, therefore Government of Indonesia already set target of electrification ratio to 97,4% in 2019 and 100% in 2020. In order to achieve all those targets, Government of Indonesia recognize that government budget will not be sufficient to cover all the cost in rural areas. The cost of electrification in rural area will be more expensive, especially in some islands that having less infrastructure. Therefore, smaller scale of hydropower, wind, solar and bioenergy projects provided by private sector investment on renewable energy is expected to play a much greater role for the future.

(5) Government of Indonesia also identified renewable energy as one of solutions to cover the growth of electricity demand which access to electricity in rural areas where the national electricity grid is not yet available. The government's strategy is outlined in the Presidential Decree No. 5/2006 on National Energy Policy (KEN) which emphasized diversification, environmental sustainability, and maximum use of domestic energy resources. KEN set a compatible target energy mix of oil 25%, coal 30%, gas 22% and renewable energy 23% by 2025, as shown in Fig.7. For Electricity Generation Mix, Draft RUKN 2015 sets a target of renewable energy as 25 % in 2025 [7].

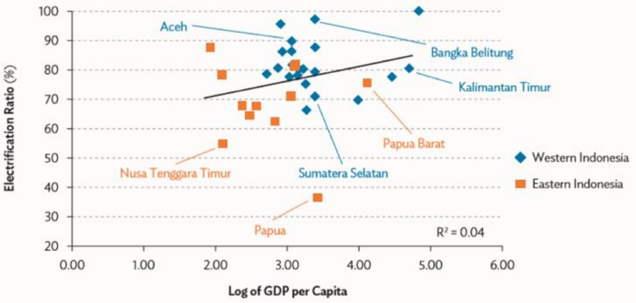

Note: "Eastern Indonesia" here refers to the islands of Sulawesi, Maluku, Papua, and Nusa Tenggara

Figure 5. Electrification ratio and per capita GDP [6]

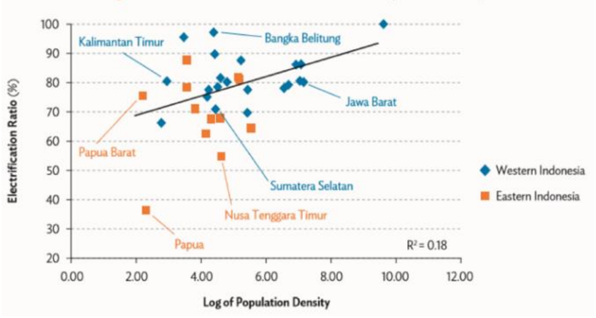

Note: "Eastern Indonesia" here refers to the islands of Sulawesi, Maluku, Papua, and Nusa Tenggara.

Figure 6. Electrification and population density [6]

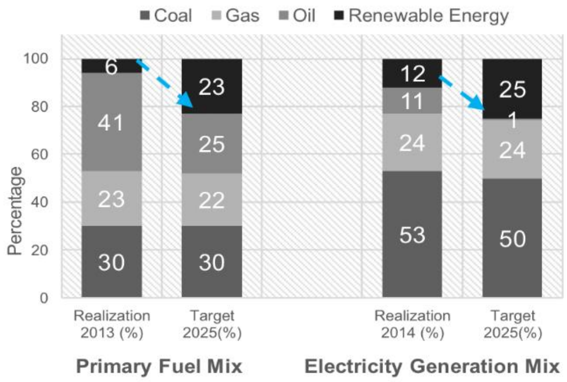

Figure 7. Primary fuel mix and electricity generation mix (2014 and Target 2025)

To achieve the target, the country also issues regulations that recommend that all diesel fuel used for land vehicles must have 20% of bio content by 2018, and then the mandate will increase to be 30% of bio content by 2020 [7]. The biodiesel Indonesia uses to meet its mandate comes exclusively from palm oil sources. Base on this mandate, it is predicted that Bioenergy will continue to play significant role in the renewable energy development in Indonesia for the future.

3.2. Highlight of our activities on bioenergy development in Japan and Indonesia

Government of Indonesia also issued several key strategies to maximize the usage of renewable energy sources such as for electricity generation and biodiesel for transportation. However, because the slow growth of biofuels development, almost still 40% of diesel fuels is still imported. This condition makes government continuing to support research and projects related with biofuels, which include palm oil which having high potential resources in Indonesia.

The fuel for the diesel engine generated from the plant etc. is called biodiesel. It is necessary to do chemical processing and reforming processing to use biodiesel for the diesel engine for transportation. Figure 8 shows process for biodiesel made of waste cooking oil. Thus, it is necessary to turn on a large amount of energy and the cost to manufacture biodiesel. It is necessary to consider the cost that requires it to process the by-product in additionally.

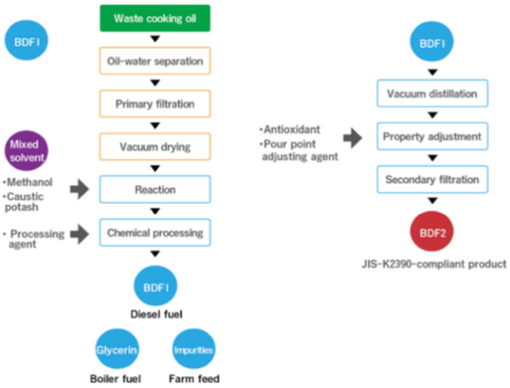

Figure 8. Process for biofuel from waste oil from cooking

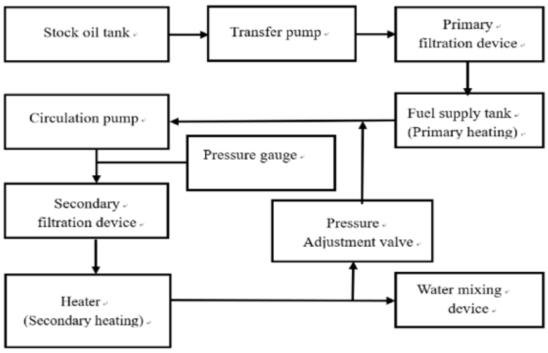

Figure 9. Block diagram of a biofuel production device

(1) Recently, we have conducted research and developed biomass fuel (biofuel) in province of Aichi, Japan. The fuel is a resource recycling type fuel which based on reuses waste cooking oil. This is an alternative fuel to gas oil. Our research using process used oil from tempura fried food (waste cooking oil) into fuel for diesel engines and generator of electricity. Figure 9 shows the concept for block diagram of a biofuel production device. Because it doesn't need chemical processing and reforming processing in the process of manufacturing the fuel as shown in this figure, energy and the cost can be greatly reduced. This is based on our joint research with the National Fisheries University of National Research and Development Agency, Japan Fisheries Research and Education Agency.

As the output of the research, we developed New Clean Fuels for generator of electricity. The developed fuel also has impact on reducing emission such as CO_2, NOx and BC.

(2) As next work to renewable energy development, based on the research in Japan, we plan for develop power generation in Indonesia. For this project, we use palm oil as biofuels for power generation activities that will help to supply electricity for the local community consumption in Indonesia. The planned location for plant projects is South Kalimantan, a province of Indonesia located in Kalimantan island. The planned areas have possible connections to palm oil production regarding considering that South Kalimantan has long history of oil palm plantation area.

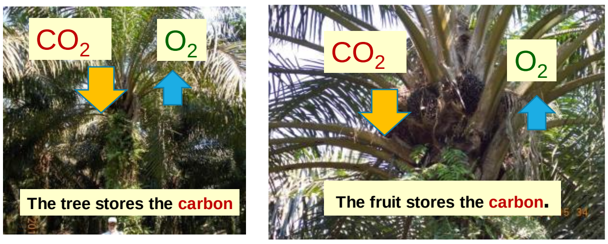

Figure 10. Process of carbon stored in palm oil

3.3 *Expected output and exploring the concept of local production energy for local consumption*

(1) Promoting biofuels from palm oil sources to reducing negative Impact of emission

The study having three reasons using palm oil as fuel. *Firstly*, one of the important problems faced by Indonesia and the world today is global warming. Palm oil tree is sources of low emission carbon in the growth process as shown in Fig.10 [8]. Since the vegetable fuel is renewable energy as carbon neutral, CO2 emissions will be zero in essentially. However, harvest fruits from palm oil and carry it to the factory, energy required to manufacture fuel from palm oil at the factory are added.

Secondly, it is realistic to restrain the use of fossil fuels by using Biofuels for diesel engine in order to reducing the effect of emission. Results of study by S. Nishio, et al [9]. which conducted experiment on combustion and exhaust characteristics of 4 stroke cycle medium speed marine diesel engine using gas oil and biofuel (used vegetable oil and palm oil) have been shown that the CO emissions of biofuels without esterification are lower than that of gas oil or MDO at high load condition, as shown in Fig. 11 [9].

Thirdly, In the rate of heat release on the 75% load, ignition time of FAME is the earliest and next is that of gas oil. Though MDO, rapeseed oil, palm oil, UVO are the same ignition time mostly, the difference appears at the peak of the premixed combustion. That of MDO is the highest, and those of rapeseed oil and UVO are high next and overlap, as shown in Fig.12 [9]. For relation between Thermal Efficiency and Engine load, the result is shown in Fig.13 [9].

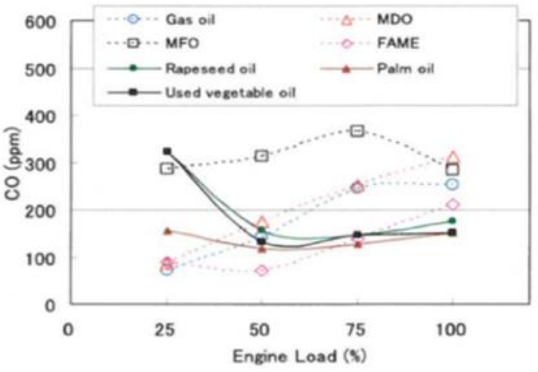

Figure 11. Relation between CO and engine load for palm oil [9]

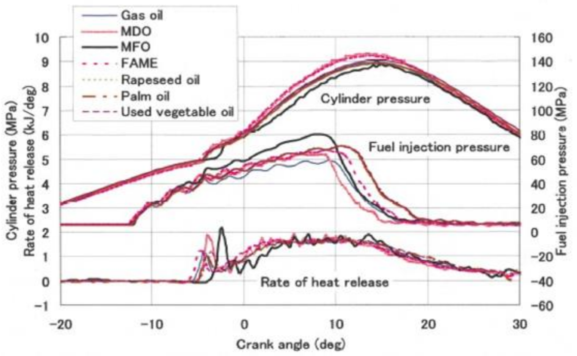

Figure 12. Comparison of cylinder pressure, fuel injection and rate of heat release (75% engine load) [9]

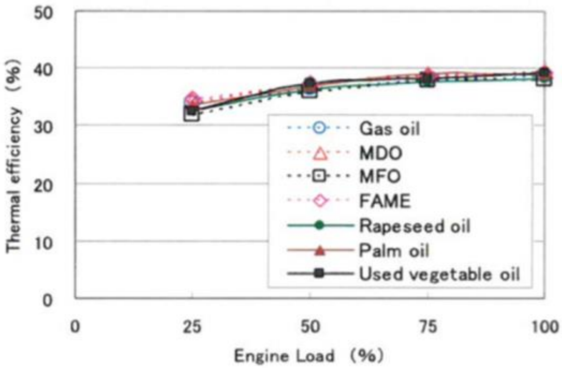

Figure 13. Relation between thermal efficiency and engine load [9]

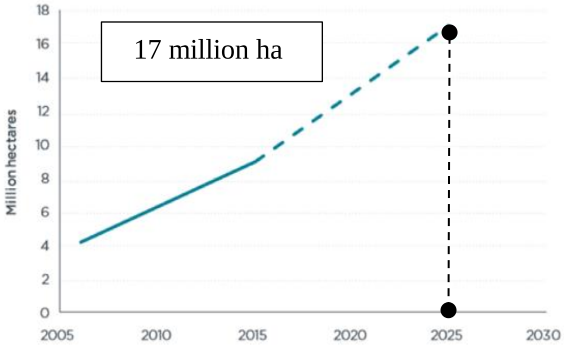

Figure 14. History and projection of palm oil plantation in Indonesia [2]

(2) Promoting energy system through using local potential natural resources

Indonesia is one of most potential supplier countries of biofuels, especially oil palm biodiesel. In 2015 the country is contributed 46% of world total palm oil plantation. Total harvested oil palm area in Indonesia 8.9 million ha in 2015 and is projected to reach 17 million ha by 2025 as shown in Fig. 14 [2].

Majority of Indonesia's population is located in rural areas which agriculture having significant in rural employment. Significant growth in the palm oil industry becoming component of economic and reducing level of poverty. Through maximize natural resources palm as energy, will provides many people with a sustainable income, especially in Sumatera and Kalimantan which having a significant percent of rural poor. In here, new energy system requires rethinking the energy management by maximize the potential sources. The solutions for the new smart energy system are sustainable, stable for supply demand, cost-effective and should having significant impact on reduction of rural poverty.

(3) Promoting local education on maintain renewable energy for people of community.

We will provide training for local engineers to ensure the process of maintenance of power generation, through transfer techniques which accumulated in the local area. It will create new jobs and transfer of knowledge for local human resource.

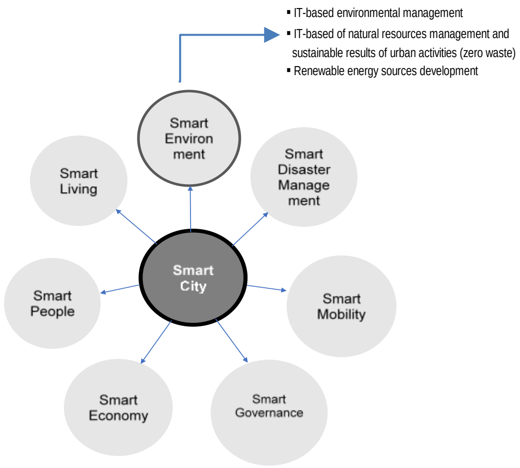

Figure 15. Smart City Components
(National Urban Development Policies and Strategies) [10].

3.4. Enhancing the value of local renewable energy and opportunities to develop smart energy community based on our PR-AZ Smart City Concept

Smart city is an urban concept that can provide a high quality of life through sustainable resource management by implementation technologies to transform the urban existing systems, operations and services through participatory of resident and governance. Indonesia government having the concept for enhancing Smart City Components through BAPPENAS National Urban Development Policies and Strategies, as shown in Fig.15 [10]. Renewable Energy sources development is key urgent point to develop platform of Smart Environment.

In relation to the energy management concepts, there are four of our PR-AZ concepts in order to reach possibility of developing smart city, i.e. Low Carbon Society, Regional Recycling based on agriculture society, Local Production for Local Consumption and Stable Supply of Electricity, as shown in Fig. 16.

A smart city must have comprehensive solution to develop an energy system to be smarter and efficient on cost. The platforms to reach for Smart Energy City can be achieved by several ways and one of the important key points is enhancing local production energy for sustainable local energy system. Therefore, the implementation of the smart energy system which using local potential sources and transform it into energy is needed, to fulfill energy demand and stable supply for the area on the overall. Concept of Smart City is to construct the power generating system that doesn't rely on a large-scale power plant. Therefore, it will be achieved by generating electricity by solar, wind power, and biomass for the community at the town [8].

Based on expected results which as stated before, this study promotes the concepts to break away from current condition of energy consumption which to depend on fossil fuels and shift to the local production energy of biofuels palm oil for local energy consumption. The current system needs the changes from traditional energy form which energy and fuels are supplied from out of region, shift to be the new energy system where the demand and supply are balanced, and sources of fuels come from local renewable sources in the regions. The system will promote many values benefits that will be circulated in the local community.

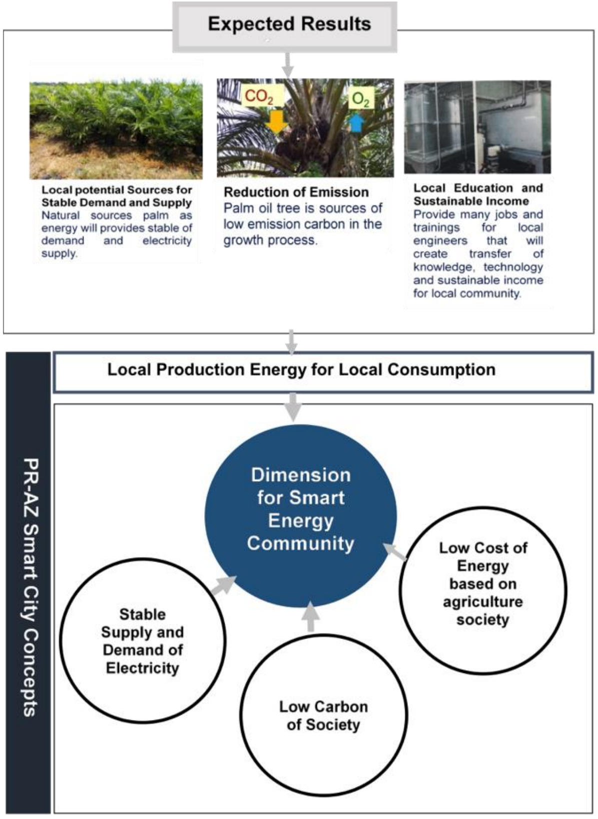

Figure 16. Opportunities to develop smart energy community based on expected results of project

4. Conclusion and Further Steps

There are three urgent points which are highlighted in this study, as follows:

1) Recently Indonesia has been improving the use of renewable energy as one of alternative sources of energy in order to reduce the country's dependence on imported fuel fossil, also to reduce environmental impact of carbon emission. In here, this study tries to develop a planning for comprehensive renewable energy program with more enhancing the local potential sources.
2) This study gives an overview of the concepts for `Local Production Energy for Local Consumption' which addressed its application to develop more smart energy community that related with key points development of Smart City. To reach this, based on our research in Japan, we introducing our planning for the usage of palm oil as biofuels for power generation activities which produced energy will be allocated for local community in the region.
3) Based on expected results of the planning, the study promotes our comprehensive concepts to break away from current condition of energy consumption which depending on fossil fuels shift to be the new energy system where the demand and supply are balanced, and fuels come from local renewable sources. The system

also will promote low carbon society, sustainable income and many values benefits that will be circulated in the local community.

The purpose of this paper is the preliminary study to discuss the highlight and background of our activity on renewable development. As further steps, this study will continue to explore various condition related to technical steps and details process of implementation. As the final goal, this study aims to provide a comprehensive concept of how it can be implemented in order to promote the 'Local Production Energy for Local Consumption' which is urgently need to be applied in Indonesia.

References

[1] The International Renewable Energy Agency (IRENA); Executive Summary of Renewable Energy Prospects Indonesia, March 2017. https://www.irena.org

[2] A. Kharina, C. Malins, S. Searle; Biofuels Policy in Indonesia. Overview and Status Report, International Council of Clean Transportation, August 2016. https://www.theicct.org

[3] PricewaterhouseCoopers Indonesia Reports; Oil and Gas in Indonesia (Investment and Taxation Guide), May 2017. https://www.pwc.com

[4] Energy Sector Assessment, Strategy and Road Map; Asian Development Bank, 2017. https://www.adb.org

[5] PricewaterhouseCoopers Indonesia Reports; Alternating Currents: Indonesian Power Industry Survey 2018, July 2018. https://www.pwc.com

[6] Asian Development Bank; Achieving universal electricity access in Indonesia, 2016. https://www.adb.org

[7] B.Saril ; Renewable Energy in Indonesia, Institute of Energy Economics Japan, February 2018.

[8] K. Maeda. Power-generation Activities that Use Palm Oil ; Smart City Plan for the future after 100 years, Asean Japan Business Meeting, 2018.

[9] S. Nishio, Z. Xu, M.Ikame, T. Kishi, M. Kuwabara ; Combustion and Exhaust Characteristics of Bio-Fuels in Marine Diesel Engine, Proceedings of the International Symposium on Marine Engineering (ISME), October 2011.

[10] Ministry of National Development Planning/National Development Planning Agency Indonesia; Installation of Smart Street Lighting in Indonesia, Asia Smart City Conference 2018, Yokohama Japan; November 2018.